Title

Colloidal Synthesis of Ge Nanocrystals and Bi2Te3, Sb2Te3 and Bi2Se3 Nanoplates

Permalink

Author

Ju, Zheng

Publication Date

2021

Colloidal Synthesis of Ge Nanocrystals and Bi_2Te_3, Sb_2Te_3 and Bi_2Se_3 Nanoplates

By

ZHENG JU

DISSERTATION

Submitted in partial satisfaction of the requirements for the degree of

DOCTOR OF PHILOSOPHY

in

Chemistry

in the

OFFICE OF GRADUATE STUDIES

of the

UNIVERSITY OF CALIFORNIA

DAVIS

Approved:

Susan M. Kauzlarich, Chair

Dong Yu

Yayoi Takamura

Committee in Charge

2021

ProQuest LLC.
789 East Eisenhower Parkway
P.O. Box 1346
Ann Arbor, MI 48106 - 134

Colloidal Synthesis of Ge Nanocrystals and Bi_2Te_3, Sb_2Te_3 and Bi_2Se_3 Nanoplates

Abstract

Colloidally synthesized nanocrystals (NCs) play important roles in research studies and industry. Nanotechnology as a field of research has provided new materials for various applications due to their electrical, optical, and magnetic properties which depend on their size and shape. For example, nanoparticles are a wide class of materials whose dimensions are less than 100 nm and spherical in shape. Many nanoparticles are of interest for their optical or optoelectronic properties. Nanoplates are 2D materials that have anisotropic properties that may be of importance for electronic, magnetic, and thermal properties. During my PhD, different studies have been carried out on optimizing the colloidal synthesis of Ge NCs, exploring the synthesis and thermoelectrical properties of Bi_2Te_3/Sb_2Te_3 core-shell nanoplates, and discovering the ambipolar effect on solution-synthesized Sb-doped Bi_2Se_3 nanoplates with high carrier mobility. Both fundamental and advanced reaction principles and characterizations were investigated.

Chapter 1 provides an overview of fundamental concepts in the synthesis, nucleation, growth processes, and composition manipulation of NCs and a summary of Ge NCs. Fundamental concepts of property measurements of thermoelectric materials and topological insulators are also briefly discussed.

Chapter 2 presents a two-step microwave-assisted reaction that produced single crystalline and monodispersed Ge NCs. The as-synthesized Ge NCs showed high crystallinity with single crystal nature as indicated by powder X-ray diffraction, selected area electron diffraction and high-resolution transmission electron microscopy. The Tauc plot derived from photothermal deflection spectroscopy of Ge NCs thin films showed an increased bandgap of the Ge NCs obtained from GeI_2 compared with that from GeI_4 with similar particle size, indicating the single crystal nature of the particles prepared *via* a two-step reaction from GeI_4. Solutions involved in this two-step reaction were investigated with ^1H NMR spectroscopy, high-resolution mass spectrometry (MS). One possible reaction pathway is proposed to unveil the details of the reaction involved GeI_4 and oleylamine (OAm). This two-step synthesis produced high quality Ge NCs and provided new insight on nanoparticle synthesis of covalently bonding semiconductors.

Chapter 3 discusses the thermoelectric properties of successfully synthesized Bi_2Te_3/Sb_2Te_3 (BTST) nanostructured heterojunctions *via* a two-step solution route. Samples with different Sb_2Te_3 to Bi_2Te_3 ratios could be synthesized by controlling the reaction precursors. Scanning electron microscopy (SEM), transmission electron microscopy (TEM) and energy dispersive X-ray spectroscopy were used to study the nanostructure and composition. The powder samples were pressed into pellets by spark plasma sintering (SPS). Thermoelectric properties were measured with two different directions, in-plane and out-of-plane, and show anisotropic properties due to the nanostructure alignment of the nanoplates within the pellets. The highest overall zT was observed with BTST1-3 (1-3 represents the ratio of Bi_2Te_3 (BT) to Sb_2Te_3 (ST)) sample in the out-of-plane direction at 500 K.

Chapter 4 presents a solution-synthesized Sb-doped Bi_2Se_3 nanoplate with enhanced electronic transport properties. Sb doping was used to suppress the bulk carriers, and an atomic percentage ~ 6% of Sb was demonstrated by energy dispersive X-ray spectroscopy (EDS). The 2D electron carrier concentration for Sb-doped Bi_2Se_3 nanoplates was lowered to 5.5×10^{12} cm^{-2}, reducing the concentration by a factor of 3 compared to the undoped Bi_2Se_3 nanoplate sample with an average 2D carrier concentration of 16×10^{12} cm^{-2}. At 2 K, pronounced ambipolar field effect was observed on the low-carrier-density Sb-doped Bi_2Se_3 nanoplates, further demonstrating the flexible manipulation of carrier type and concentration for these single-crystal nanoplates.

Dedication

Dedicated to:

To my beloved Father, Yiyun Ju

To my beloved Mother, Juxiu Wang

"I do not know what I may appear to the world; but to myself I seem to have been only like a boy playing on the seashore, and diverting myself in now and then finding a smoother pebble or a prettier shell than ordinary, whilst the great ocean of truth lay all undiscovered before me."

-Isaac Newton

Acknowledgements

My PhD life at the University of California, Davis would not have been better without the incredible help and support that I received from my principal investigator, committee members, my dear parents, and my friends. I sincerely appreciate their valuable and precious dedication and encouragements through all these years.

I would like to dedicate my dissertation to my dear parents, Yiyun Ju and Juxiu Wang. Without their unconditional love and support, I would never reach this stage in my life. Thanks for being such amazing parents, not only raising me up with love and patience but teaching and encouraging me to think and live independently and guiding me with correct directions in my life.

I am sincerely grateful to my PhD advisor, principal investigator, Professor Susan M. Kauzlarich. I gained a lot from her abundant knowledge, clear instructions, and philosophy of life. I joined her group in 2016 with a background in nano synthesis and photocatalysts. I was attracted by the research topics on colloidal synthesis of nanocrystals and also her personality. During these years, her encouragement and passion on research and providing conferences opportunities enabled me to solve the problems from various perspectives. Susan cares for her research and the group, and more, that the students succeed in their life. She provided me an internship opportunity at Applied Materials by connecting me with one of her former students, Nasrin Kazem, in 2020, which absolutely broadened my perspectives. Besides her great role in my academic achievement, her supportive personality and her philosophy of life also affected me with great impact. I could not be luckier to have her as my advisor.

I acknowledge my great committee members, Professor Dong Yu, and Professor Yayoi Takamura for their great and valuable support. Professor Yu is from Department of Physics, and we collaborated and published a paper in 2019. I really appreciate all his instructions and efforts on this project. Professor Takamura is from the Department of Materials Science and Engineering. She was one of my committee members in my qualifying exam and provided me with suggestions and support. I also took one of her classes, EMS 298, and learned a lot of material characterization methods.

I would like to thank all my past and present lab members, especially Dr. Katayoun Tabatabaei, Dr. Christopher Perez and Xiao Qi for the wonderful friendly lab environment and sharing their expertise and experiences through all these years. Even after graduation, they still provided me with help on research and job hunting. I would also like to express my thanks to my friends at UC Davis, Wen Fu, Allan He, Robert Zhu and Wenxing Zou. I am fortunate to have such good friends during my PhD life in Davis and the friendships are priceless.

Table of Contents

List of Figures

List of Tables

Chapter 1

Introduction

Section 1.3 resulted in one review article that has been accepted for publication to RSC Chemical Society Review in 2021. I contributed to the section on germanium nanocrystals which is included in this chapter.

S. M. Kauzlarich, Z. Ju, E. Tseng, J. Lundervold, "Recent developments in germanium containing clusters in intermetallics and nanocrystals." *RSC Chem. Soc. Rev.* **2021**, DOI: 10.1039/d1cs00538c.

1.1. Overview

Colloidally synthesized nanocrystals (NCs) play important roles in many applications, both in fundamental research and industrial applications such as electronics, coatings, catalysis, biomedicine and biotechnology. Nanotechnology impacts various fields of study such as chemistry, physics, environmental engineering and biomedical engineering. Colloidal synthesized NCs also show great potential as biosensors, and in drug delivery and bioimaging.

During my PhD, different studies have been carried out optimizing the colloidal synthesis of Ge NCs, exploring the synthesis and thermoelectrical properties of Bi_2Te_3/Sb_2Te_3 core-shell nanoplates, and uncovering the ambipolar effects of solution-synthesized Sb-doped Bi_2Se_3 nanoplates with high carrier mobility. Detailed characterization, along with fundamental and advanced principles of transport behavior were investigated.

In this chapter, four foundational topics will be introduced to provide a framework for the understanding of the synthesis and properties described in the following chapters. The foundational topics include nucleation principles; opportunities and challenges with colloidal synthesized Ge NCs; introduction of thermoelectricity and V_2VI_3 materials; and introduction of a topological insulator and Bi_2Se_3.

1.2. Nucleation

1.2.1. Introduction to Nucleation

Nucleation is the process of forming a new thermodynamic phase or a new structure. It can happen in gas, liquid, or solid phase. In nucleation theory, clusters of crystalline atoms (or particles or molecules) of any size are treated as a macroscopic object, which is a homogeneous crystalline phase separated from a surrounding liquid phase by a thin interface. This apparently trivial assumption is known as the capillarity approximation. According to the capillarity approximation, crystal nucleation can be fully described by the combination of the interfacial free energy, γ_s, and the difference in free energy between the liquid and the crystal, $\boldsymbol{\Delta\mu_v}$. The free energy of crystal nucleation of a spherical particle with a radius of $\boldsymbol{r}$ can be described as:

$$\boldsymbol{\Delta G = 4\pi r^2 \cdot \gamma_s - \frac{4}{3}\pi r^3 \cdot \Delta\mu_v} \qquad \textbf{Equation 1.1}$$

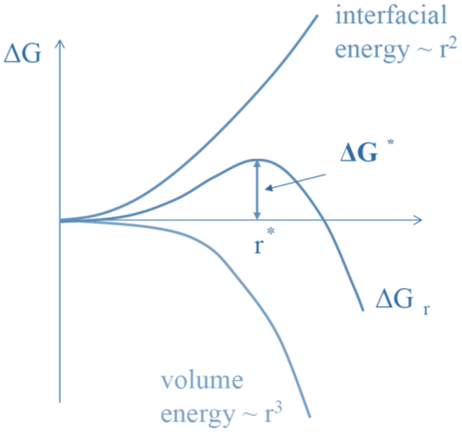

Figure 1.1 Schematic illustrating the change of total free energy as a function of the nuclei radius.

From Figure 1.1, we can see the newly formed nucleus is stable when its radius is larger than the critical size **r***. A nucleus smaller than **r*** will dissolve back into the solution to reduce the overall free energy. When it exceeds **r***, the nucleus can keep growing to reduce the overall free energy. At the critical point, $\frac{d\Delta G}{dr} = 0$, so $r * = \frac{2\gamma_s}{\Delta\mu_v}$ and $\Delta G * = \frac{16\pi{\gamma_s}^3}{3\Delta{\mu_v}^2}$, where$\Delta G$ $*$is the energy barrier that a nucleation process must overcome.[1,2]

The interfacial free energy, γ_s, is assumed depend linearly on temperature, whereas the free energy difference between the liquid and solid phases, $\boldsymbol{\Delta\mu_v}$ is proportional to the supercooling, $\Delta T = T_m - T$ (or the supersaturation) and has the form:

$$\Delta\mu_v = \frac{\Delta H_m \cdot \Delta T}{T_m} \qquad \textbf{Equation 1.2}$$

where $\mathbf{H_m}$ is the latent heat of melting. Therefore,

$$r * = (\frac{2\gamma_s \cdot T_m}{\Delta H_m})\frac{1}{\Delta T} \qquad \textbf{Equation 1.3}$$

and

$$\Delta G * = (\frac{16\pi {\gamma_s}^3 {T_m}^2}{3\Delta {H_m}^2}) \cdot \frac{1}{\Delta T^2} \qquad \textbf{Equation 1.4}$$

Both of **r*** and $\Delta G\ *$decrease with increasing undercooling as shown in Figure 1.2. In other words, the furthest temperature (T_2) from the melting temperature T_m (or more supersaturated), the larger the thermodynamic driving force for nucleation is.

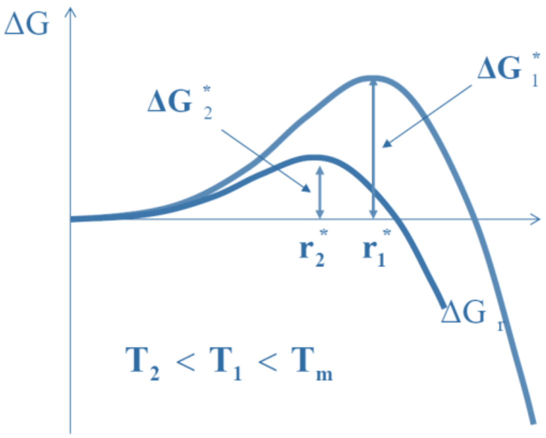

Figure 1.2 Schematic illustrating the relation of $\Delta G\ *$ and r * with different undercooling temperatures, T_1 and T_2.

Normally, nucleation can be categorized into two types: heterogeneous nucleation and homogeneous nucleation. Heterogeneous nucleation occurs at nucleation sites on surfaces contacting the liquid or vapor or on suspended particles or minute bubbles. Homogeneous nucleation normally occurs spontaneously and randomly without preferential nucleation sites, but it requires superheating or supercooling of the medium.[1,3,4]

1.2.2. Heterogeneous Nucleation

When nucleation occurs on account of the presence of a foreign phase, it is called heterogeneous nucleation. Compared with homogeneous nucleation, heterogeneous nucleation has a lower free energy barrier $\Delta G *_{het}$ because of the presence of foreign substances in contact with the liquid. Specifically,

$$\boldsymbol{\Delta G *_{het} = \Delta G *_{homo} \cdot S(\theta)} \qquad \textbf{Equation 1.5}$$

where the $S(\theta) \leq 1$ is the shape factor.

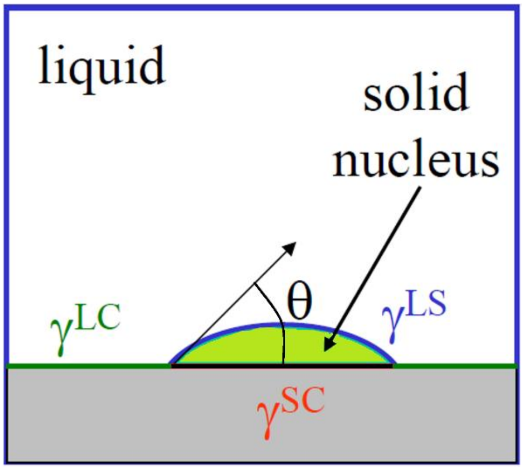

Figure 1.3 Heterogeneous nucleation occurring on the container surface.

Consider a basic situation of heterogeneous nucleation with a spherical capped nucleus on a wall of a container. There will be three interfacial energies: liquid-container interface $\boldsymbol{\gamma_{lc}}$, liquid-solid interface $\boldsymbol{\gamma_{ls}}$, and solid-container interface $\boldsymbol{\gamma_{sc}}$ **as shown in Figure 1.3**. Balancing the interfacial tensions in the plane of the container wall gives

$$\boldsymbol{\gamma_{lc} = \gamma_{sc} + \gamma_{ls} \cdot cos(\theta)} \qquad \textbf{Equation 1.6}$$

(Young's equation) and the wetting angle θ is defined by

$$\boldsymbol{cos(\theta) = (\gamma_{lc} - \gamma_{sc})/\gamma_{ls}.} \qquad \textbf{Equation 1.7}$$

The formation of the nucleus leads to a Gibbs free energy change of:

$$\boldsymbol{\Delta G_{het} = -Vs \cdot \Delta\mu_v + A_{sl} \cdot \gamma_{sl} + A_{sc} \cdot \gamma_{sc} - A_{sc} \cdot \gamma_{lc}} \qquad \textbf{Equation 1.8}$$

Here, $Vs = \pi r^3(2 + cos(\theta))(1 - cos(\theta))^2/3,\ A_{sl} = 2\pi r^2(1 - cos(\theta))$, and $A_{sc} = \pi r^2\, sin^2(\theta)$.

Thus, $\boldsymbol{\Delta G_{het} = (4\pi r^2 \cdot \gamma_{sl} - \frac{4}{3}\pi r^3 \cdot \Delta\mu_v) \cdot S(\theta) = \Delta G_{hom\,o} \cdot S(\theta)},$ **Equation 1.9**

$$\boldsymbol{S(\theta) = (2 + cos\,\theta)(1 - cos\,\theta)^2/4 \leq 1.} \qquad \textbf{Equation 1.10}$$

At the critical point, $\frac{d\Delta G}{dr} = 0$, so $r* = \frac{2\gamma_s}{\Delta\mu_v}$, which is the same as for homogeneous nucleation, and $\Delta G*_{het} = \frac{16\pi{\gamma_s}^3}{3{\Delta\mu_v}^2} \cdot S(\theta) = \Delta G*_{hom\,o} \cdot S(\theta)$. In other words, as shown in Figure 1.4, heterogeneous nucleation occurs at a lower undercooling temperature or lower supersaturation, but with the same critical size as homogeneous nucleation. In addition, in most cases, the shape of the nucleus will not be spherical, but have more complicated geometries. Typically, many different nucleation sites with different morphologies exist on the same impurity.

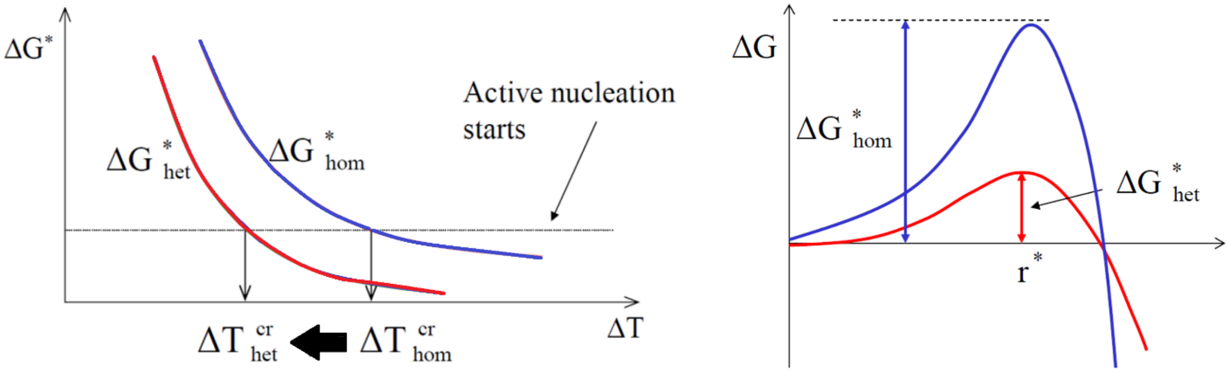

Figure 1.4 Heterogeneous nucleation starts at a lower undercooling temperature with lower critical overall free energy, but the same critical size compared with homogeneous nucleation.

1.2.3. Homogeneous Nucleation in Nanoparticle Synthesis

For the formation of nanoparticles by homogeneous nucleation, a supersaturated solution is required. A reduction of temperature of an equilibrium mixture would lead to supersaturation. The more common method is to generate supersaturation through chemical reactions by converting highly soluble chemical reagents to less soluble chemical products. A solution with the solute exceeding supersaturation will produce a high Gibbs free energy which will be reduced by the nucleation of the solute from the solution into solid particles. This reduction of free energy is the driving force for both nucleation and growth.[5] The free energy per unit volume depends on the concentration of the solute:

$$\boldsymbol{\Delta\mu_v = \frac{-kT}{\Omega} ln(\frac{C}{C_0}),} \qquad \textbf{Equation 1.11}$$

where C is the concentration of the solute, C_0 is the equilibrium concentration, k is the Boltzmann constant, T is the temperature, Ω is the atomic volume. If the nucleation particle is spherical, the total free energy change can be described as $\Delta G = 4\pi r^2 \cdot \gamma_s - \frac{4}{3}\pi r^3 \cdot \Delta\mu_v$ (same as discussed in part 1), except here $\Delta\mu_v$ depends on the concentration of solute rather than on the undercooling temperature. Therefore, the critical size can be described as $r* = \frac{2\gamma_s}{\Delta\mu_v}$ and $\Delta G* = \frac{16\pi\gamma_s{}^3}{3\Delta\mu_v{}^2}$. To reduce the particle size, one should increase the change of free energy, $\Delta\mu_v$, and reduce the surface energy of the new phase γ_s. Equation $\Delta\mu_v = \frac{-kT}{\Omega} ln(\frac{C}{C_0})$ indicates that $\Delta\mu_v$ can be increased by increasing the supersaturation. Temperature can significantly affect the supersaturation and also the surface energy. With higher temperature, supersaturation becomes more difficult and surface energy also increases which lead to larger critical size and total free energy. As shown in Figure 1.5, fast reduction induces a rapid buildup of supersaturation. If the concentration of solute is considered as a function of time, then nucleation will happen when the supersaturation reaches the critical point as $\Delta G * = \frac{16\pi{\gamma_s}^3}{3\Delta{\mu_v}^2}$, after which the concentration will decrease. When the concentration drops below the critical point, no more nuclei would form, but the growth will continue until the concentration attained the equilibrium concentration.[6]

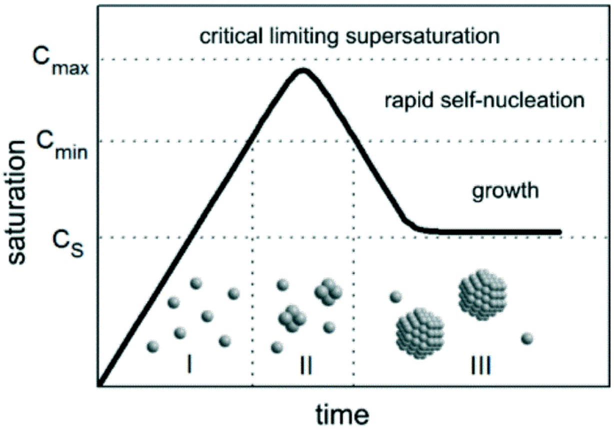

Figure 1.5 Schematic illustrating the process of nucleation and subsequent growth. Adapted with permission from (*CrystEngComm*, **2015**, *17*, 6809-6830).[7] Copyright (2015) Royal Society of Chemistry.

Aside from these thermodynamic considerations, nucleation is also controlled by kinetic parameters. The rate of nucleation $\mathbf{R_{nuc}}$ is proportional to the probability **P** that a nucleation event can happen with a critical free energy ΔG^*, the number of growth species per unit volume that can be utilized **n** (in homogeneous nucleation, **n** equals to the initial concentration $\mathbf{C_0}$), and the frequency of growth species Γ that successfully overcome the energy barrier. So, the probability **P** can be given as

$$\boldsymbol{P = exp(\frac{-\Delta G*}{kT})} \qquad \textbf{Equation 1.12}$$

k is Boltzmann constant, and T is the temperature. $\Gamma = \frac{kT}{3\pi\lambda^3\eta}$, where λ is the diameter of the growth species and η is the viscosity of the solution. Thus, in total the rate of nucleation $\mathbf{R_{nuc}}$ can be described as $R_{nuc} = nP\Gamma = (\frac{C_0 kT}{3\pi\lambda^3\eta}) \cdot exp(\frac{-\Delta G*}{kT})$. From this equation we can conclude that higher starting concentration, low viscosity and low critical energy barrier favor higher nucleation speed. For a given concentration, a larger number of nuclei means smaller size.[8,9]

1.3. Overview of Colloidal Synthesized Ge Nanocrystals

1.3.1. Introduction of Ge

A tremendous amount of effort has been put into the studies of conventional compound semiconductor nanomaterials. Nanostructures of group IV (Si and Ge) semiconducting materials are of significant interest due to their promising properties in a broad range of applications.[10–13] Compared with metal chalcogenides and group III-V quantum dots, Ge NCs are less toxic alternatives and have been widely studied by different research groups with a goal of tuning their optical and electronic properties by controlling size, morphology, surface functionality and compositions.[11,12,14–22] However, optimization and design of improved synthesis protocols are still required to achieve well-defined and high-quality Ge nanostructures for the targeted applications.

Ge, with its narrow bulk bandgap of 0.67 eV, can be tuned through the quantum confinement effect by controlling the particle size and has been investigated broadly over decades.[13,18,23] High carrier mobilities, large absorption coefficient and exciton Bohr radius (~24 nm) makes nanostructured Ge a promising candidates for solar energy conversion,[12,17,24,25] an anode material in lithium ion batteries,[19,20] and in optoelectronics[26–28] and bioimaging.[22] Another important outcome of research on Ge NCs is the fact that they could have many of the important near-IR (near-infrared) emission capabilities that are demonstrated in the heavy element, such as Pb, Hg, or Cd, or As containing nanocrystals without the environmental hazards. Demonstration of multielectron generation in Ge nanostructures (Ge NCs embedded in silica) suggests that with the proper surface capping, Ge NCs may provide a new generation of highly efficient detectors or photovoltaics.[29] Nanoscale Ge also has shown a high capacity for energy storage (4.4 Li per Ge and 1 Na per Ge).[30,31] Ge NCs have great potential with a large absorption coefficient (~2 x 10^5 cm^{-1} at 2 eV) and large exciton Bohr radius (25 nm) that provides strong confinement and a large tunable bandgap. With effective capping, Ge NCs show near-IR photoluminescence.[32]

As a result, many methods have been developed to optimize synthesis conditions with the goal of producing Ge NCs with uniform size, shape, and surface-ligand distribution. Previous review articles on the colloidal synthesis of Ge NCs have included reduction of Ge halide precursors, metathesis reactions of Ge Zintl salts, thermal decomposition of organogermane precursors, and one-pot methods.[11,28,31,33] The synthesis of Ge NCs through the reduction of organogermanium precursors and via microwave-assisted reduction will be briefly highlighted.

1.3.2. Colloidal Chemistry of Ge Nanocrystals

1.3.2.1. Reduction of organogermanium precursors

Organogermanium precursors for the synthesis of Ge nanoparticles have relied on the thermal reduction of these precursors. Here, the term nanoparticle will be employed to indicate amorphous or mixed amorphous and crystalline forms of Ge nanoparticles. Since most of these reagents contain Ge in the highest oxidation state, Ge(IV), decomposition of the organogermanium precursor typically involves temperatures above 300 ˚C. In order to obtain better control of the size and crystallinity of these nanoparticles, the organometallic Ge(IV) precursors—Ph_2GeCl_2, Ph_3GeCl, and Ph_3GeBr—were reduced at a temperature of 300°C by employing sulfur as the reducing agent to produce Ge nanoparticles.[33] The effect of solvent, either oleylamine (OAm) or hexadecylamine (HDA), as the primary amine solvent provided some control over crystallinity. Amorphous nanoparticles ranging from 3.5 to 8.2 nm in diameter, depending on the sulfur concentration, were prepared with OAm as the solvent. Synthesis in HDA yielded crystalline diamond structured Ge nanoparticles ranging from 7 to 16 nm in diameter, depending on the sulfur concentration (Figure 1.6). It was proposed that sulfur radicals were important for the crystalline formation and that in HDA a $[Ph_3Ge(IV)NH_2R]^+Cl^-$ species interacts with H_2S, reducing the species from IV to II, $Ph_2Ge(II)$, and at temperatures above 140˚C, spontaneous disproportionation to Ge(0) and Ge(IV) with the formation of Ge NCs.[33] In OAm, sulfur leads to polymeric products that were confirmed by NMR and therefore does not provide a crystalline product.

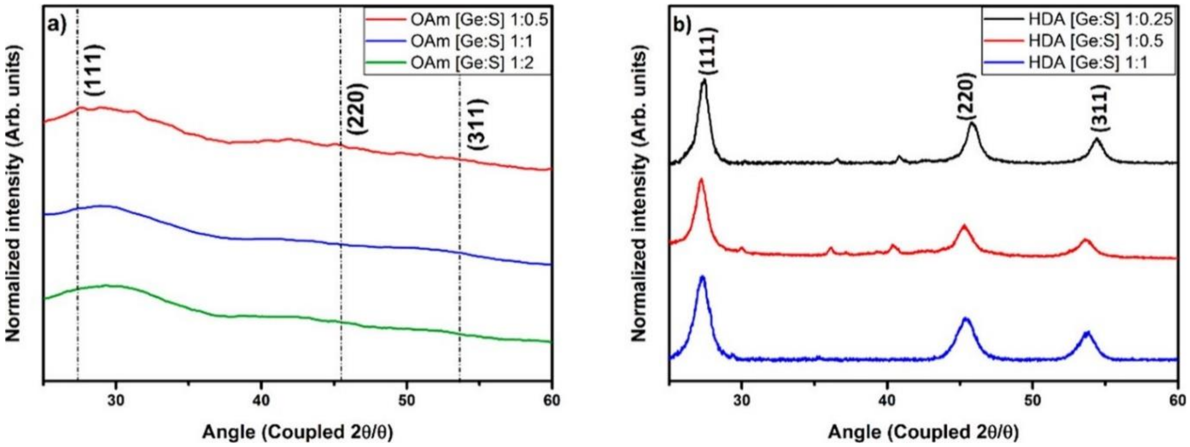

Figure 1.6 X-ray powder diffraction patterns for Ge nanoparticle samples prepared with three [Ge:S] molar ratios in oleylamine (OAm) (a) and hexadecylamine (HDA) (b). The nanoparticles prepared in OAm are amorphous and those in HDA are crystalline. The Bragg peaks for diamond structured Ge are indicated by dashed-dotted lines and Miller indexes in (a). Reprinted with permission from (*Inorg. Chem.* 2019, 58, 8, 4802–4811). Copyright (2019) American Chemical Society.

1.3.2.2.Microwave-assisted synthesis

Microwave-assisted synthesis has become a more common method for the preparation of semiconductor nanomaterials.[34–37] Microwave heating requires either a microwave absorbing solvent or polar reagents and provides rapid heating with little temperature gradient and can provide high quality nanomaterials.[36] The importance of microwaves to the crystallinity of the final product is shown by carrying out identical reactions by conventional thermal heating.[38] Samples prepared via microwave are crystalline and that those via conventional heat treatment at the same temperature (210 ˚C) are not as indicated by powder X-ray diffraction.[38] This difference is attributed to local heating of polar and ionic species in the solution by microwaves along with the fact that Ge has a high dielectric constant. Once the Ge particles nucleate, the high dielectric constant of Ge allows the nuclei to absorb electromagnetic radiation and gives rise to additional local heating. Microwaves interact directly with the reaction solution where the energy transfers more efficiently than with conventional heating techniques such as conduction or radiation and convection heating. The conventional heating generally relies on the thermal conductivity, where the heat transfers firstly from the source to the container and then from the container to the reaction solution. This process is slow and less efficient, taking longer to reach thermal equilibrium. Figure 1.7 shows a schematic comparison of conventional and microwave heating.

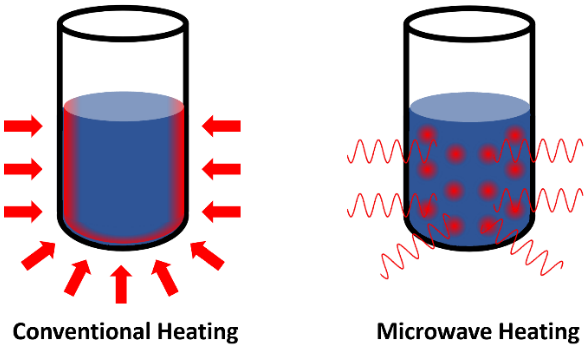

Figure 1.7 Scheme of conventional heating *vs.* microwave heating. The arrows stand for the direct heating transfer by conventional heating, and the wavy lines represent the microwave heats the solution directely.

It has been shown that oleylamine will reduce Ge^{2+} ions and multi-valent precursors (GeI_2/GeI_4) or halogen concentration can be used to gain control over nucleation and subsequent growth of Ge NCs.[23,38,39] Oleylamine is a reducing agent for the preparation of a number of transition/noble metal and main group element nanocrystals.[40–42] Oleylamine serves a triple function of solvent, binding ligand, and reducing agent for both Ge(II) and Ge(IV) containing precursors.[38] There are two important recent advances in amine reduction synthesis: (1) employing organic bases[42] and (2) the effect of an amide promotor.[43] The application of microwaves[34] provide an efficient route to Ge NCs and recent publications demonstrated that Ge amide intermediates are initially formed in this reaction and that when Ge NCs are nucleated, hydrogen and ammonia gas are simultaneously formed.[39,44] Figure 1.8 shows typical sizes of oleylamine-capped Ge NCs obtained from a microwave reaction at 210 ˚C. Thiol ligands (dodecanethiol) provide stable Ge nanocrystal colloids.[23] Thiol-capped Ge NCs are stable when exposed to air and moisture for weeks whereas the oleylamine-capped nanocrystals prepared at 210˚C degrade within 24 h upon ambient exposure. Preparing Ge NCs at slightly higher temperatures in the microwave provide more efficiently capped nanocrystals.[45] NMR spectroscopy show that there are two types of ligands associated with the surface: oleylamide ligands that are strongly bound and can be characterized as covalent X-type bonds and or physisorbed, weakly bound, oleylamine. The weakly bound ligand can freely exchange with the solution, oleylamine. As the reaction temperature increases the amount of X-type bound oleylamide ligands increases and provides better colloidal stability of the nanocrystals. Thiol and carboxylic acid ligands were also investigated and at room temperature, there was no NMR evidence for binding to the Ge nanocrystal surface. These more acidic ligands only showed exchange at higher temperatures and only with either the weakly bound oleylamine or open surface sites.[45] This NMR study confirm earlier electrochemical experiments[46] that showed that the Ge NCs prepared from the microwave reaction are not fully passivated.

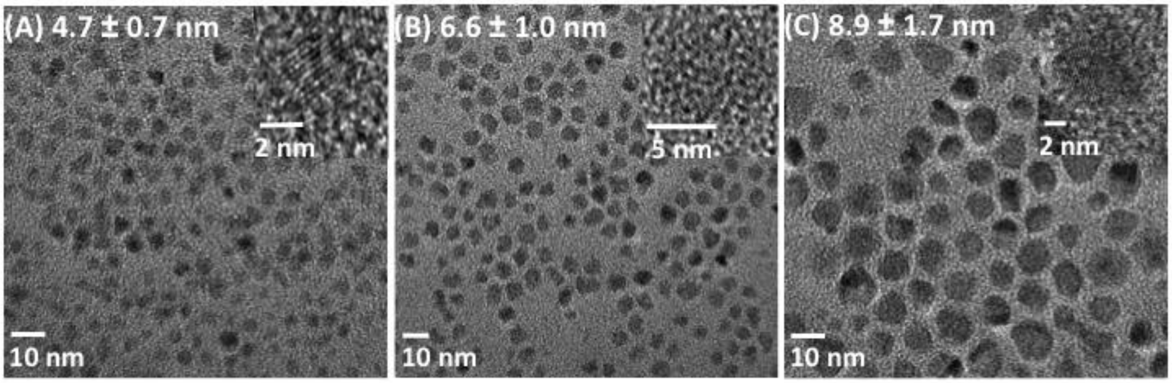

0.4 mmol GeI_2

0.35 mmol GeI_2, 0.05 mmol GeI_4

0.3 mmol GeI_2, 0.1 mmol GeI_4

Figure 1.8 Ge NCs prepared via microwaves at 210 ˚C with a heating time of 60 minutes with varying GeI_4/GeI_2 precursor ratios. Insets show HRTEM of a single particle with lattice fringes. Adapted with permission from (Chemistry of Materials 2013, 25 (8), 1416-1422). Copyright (2013) American Chemical Society.

1.3.2.3. Multimetallic Ge Nanocrystals

Incorporation of other atoms into the structure of semiconducting nanoparticles can result in changes in the crystal structure as well as the electronic and optical properties.[47–51] Expanding the range of dopants and substitutions that can be incorporated in the structure can be extremely useful and may enhance the ability to apply these nanoparticles to a range of applications such as photovoltaics, energy storage, and biological probes.[30,48,51–53] Literature of doped and alloyed Ge offer a wide range of synthesis techniques and elements, including alloy nanostructures,[49,51,54] transition metal doped Ge nanoparticles,[58] and binary phase transition metal-Ge intermetallic nanocrystals.[55,56]

Intentional impurities in a structure can result in changes in properties of the material, including optical, electronic, and magnetic properties; however, there are many challenges for enabling this new functionality with semiconductor nanoparticles.[57] The addition of an element with one less valence electron than that of the semiconductor is a *p*-dopant, while an element with one more valence electron is an *n*-dopant. More electrons or holes in a semiconductor can greatly influence the band structure of the material. In conjunction with size and shape control, dopants can aid in tuning the bandgap. Similarly, alloy structures can result in changes to properties through the introduction of another element. In some examples, metastable new compositions can be obtained.[49,50,58,59]

Traditional dopants such as boron and phosphorus can be incorporated into Ge NCs through a nonthermal plasma approach.[60–62] A variety of other dopants, such as antimony, aluminum, indium, and gallium, have also been reported with between 1.5 and 0.41 mol % dopant inclusion into Ge NCs prepared via a colloidal route in oleylamine.[63] McLeod *et al.* reported a simple and versatile solution method on synthesis of transition metal (Cu, Ni, Co, Mn) doped Ge NCs.[58] In the study on transition metal dopants, $NaBH_4$ is used as the reducing agent. The incorporated transition metal dopant amount was characterized by energy dispersive spectroscopy (EDS). X-ray diffraction patterns confirmed that the nanocrystals are diamond structured Ge with diameters of 18-20 nm with no evidence for intermetallic phases or impurities. Elemental mapping with EDS can determine the composition of a nanocrystal and in turn determine the distribution of a dopant or other element. EDS is used with either transmission electron microscopy (TEM) or scanning transmission electron microscopy (STEM). Both types of microscopies can be used to examine the size, shape, and distribution of nanocrystals. Figure 1.9(A) shows a schematic reaction of the synthesis, and Figure 1.9(B-F) show the EDS mapping of pristine Ge and transition metal doped Ge NCs. With the two-step synthesis employed here the transition metal atoms are more possible to be deposited on the surface of the nanocrystals rather than incorporated in the interior of the nanocrystals. EDS mapping and elemental analysis shows the highest dopant amount with Ni which may be attributed to the comparatively higher diffusion rate of Ni compared with other first-row transition metals.[58]

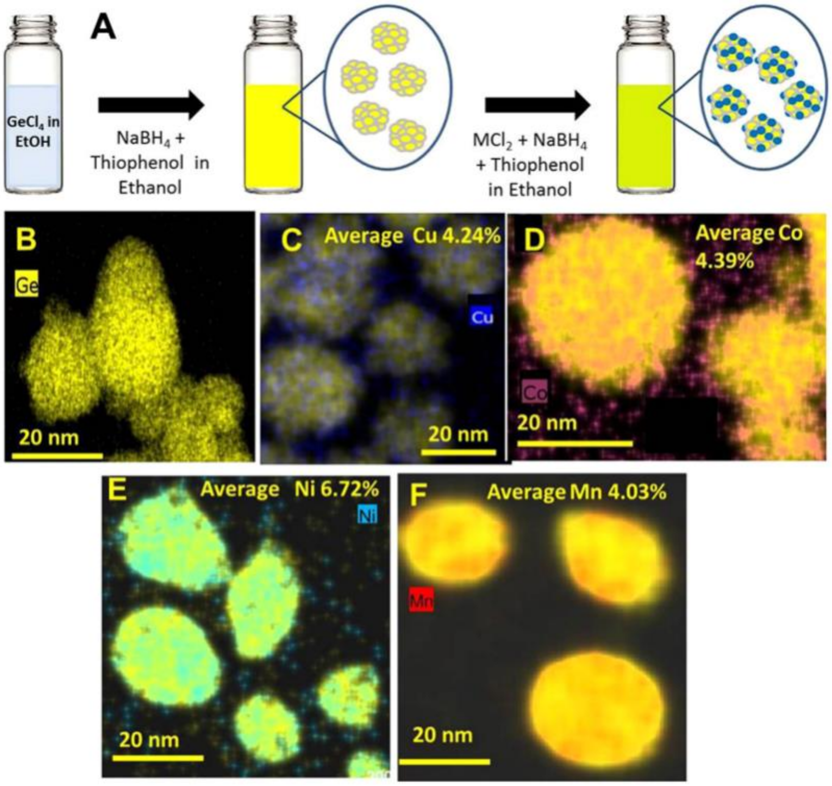

Figure 1.9 Schematical synthesis route of pristine and transition metal doped Ge NCs, A. EDS mapping of plain Ge and Cu, Co, Ni and Mn doped Ge NCs, B-F. Reproduced with permission from (*J. Phys. Chem. C* **2019**, 123, 1477−1482). Copyright (2019) American Chemical Society.

Semi-metal-doped, Bi and Sb, Ge NCs were obtained from solution using a microwave assisted heating method.[59,64] Figure 1.10 shows a HRTEM image of the Bi-doped Ge NCs with an inset showing the fast Fourier transform (FFT) of the particle outlined in red. The calculation based on the FFT gives an average lattice parameter of 0.320 nm which corresponds very well with that of XRD refinement for these Bi-doped Ge NCs. The highest incorporation of Bi was 1.46 mol % Bi which was confirmed through inductively coupled plasma- mass spectrometry (ICP-MS). As the amount of Bi precursor added increased, the size of the Bi-doped NCs also increased and resulted in a wider size distribution of size of the resulting nanocrystals. The bandgap of the nanocrystals also decreased with increasing Bi concentration.[50] Figure 1.11 shows the EDS for Bi doped Ge NCs.

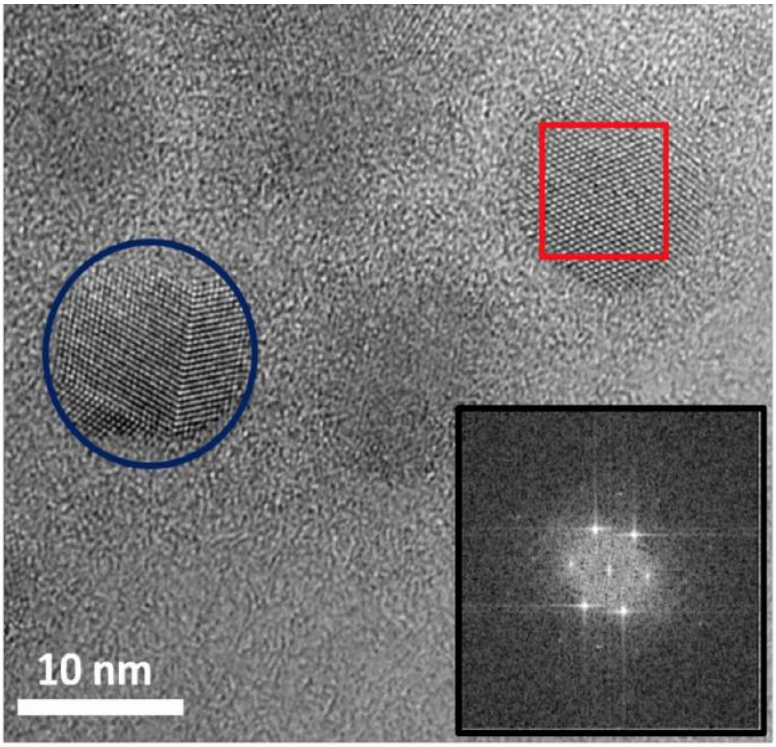

Figure 1.10 An HRTEM image of Bi-doped Ge NCs prepared from a microwave-assisted route with crystalline particles indicated by the blue circle and red square. The average incorporation of Bi was approximately 1.5 mol% and the inset shows the FFT form of the area indicated with the red square, consistent with diamond structured Ge. Reprinted with permission from (*Chem. Mater.* 2017, 29, 17, 7353–7363). Copyright (2017) American Chemical Society.

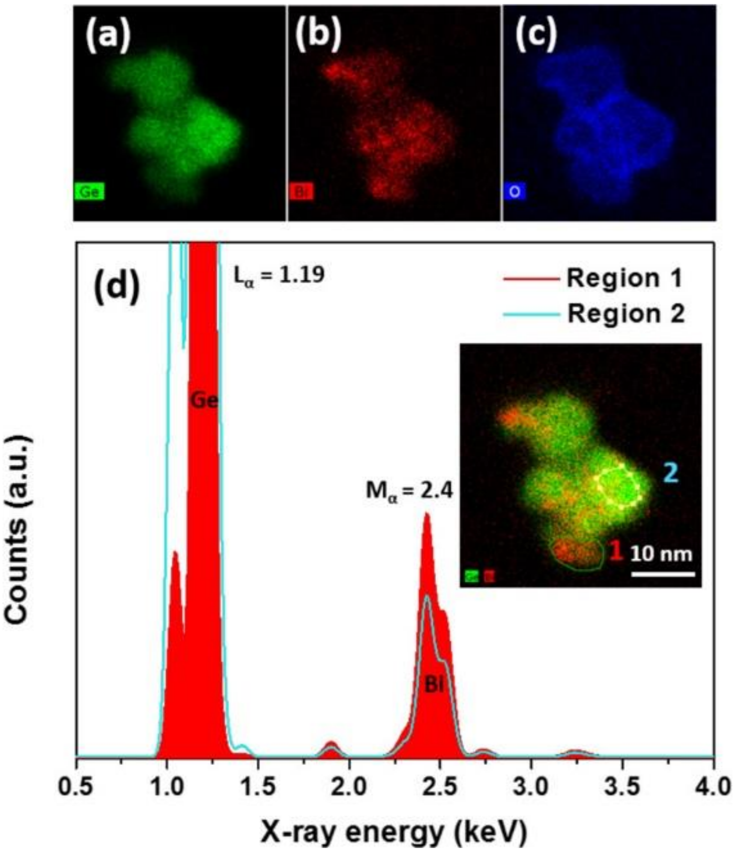

Figure 1.11 STEM-EDS images of Ge, Bi, and oxygen (a-c) from an agglomeration of Bi-doped Ge NCs. Integrated EDS spectra color coded for the two regions extracted from the inset (d). Reprinted with permission from (*Chem. Mater*. 2017, 29, 17, 7353–7363). Copyright (2017) American Chemical Society.

While doped and alloyed nanoparticles can be prepared, these nanomaterials face challenges in structural characterization which originate from disorder. The large surface-to-volume relationship in nanocrystals makes surface states dominate as the particle becomes smaller. Dopants of significantly different size compared to the host structure can introduce strain further impacting the electronic properties and details of the density of states. Structural characterization is a necessary component for providing insight into the electronic properties. Powder X-ray diffraction can provide changes in lattice parameters and confirm the crystal system. EDS can provide the information concerning the distribution of dopants. However, HRTEM images with great quality are required; however, HRTEM also has limitations that limit the unveiling of details important for bonding and structure information. Extended X-ray Absorption Fine Structure (EXAFS) Spectroscopy can be an important tool for characterizing structures. This technique can distinguish local structure and can be sensitive to very low levels of dopant and therefore is ideal for investigating the structure of Bi and Sb doped Ge NCs.[16,64] There are two major parameters that are obtained from the EXAFS analysis, that is the peak shift (r-shift) due to backscattering of the photoelectrons which informs on the distance between the absorbing atom the near neighbors and amplitude which informs on the number of nearest neighbors. Table 1.1 summarizes the reported number of near-neighbors (NN) determined from the Ge K edge for Ge NCs with different dopants.[16,64,65] The Sn-alloyed Ge NCs have the highest 1st Ge-Ge NN which is close to bulk Ge. This result indicates a successful synthesis of a diamond structured Ge-Sn solid solution without creating vacancies. The Sn-alloyed Ge NCs at the reaction temperature of 250˚C shows a high number of NN from the 2nd Ge-Ge distance. While the Sn-alloyed Ge NCs made at lower temperatures show a higher Sn content, they are likely less crystalline as the NN numbers, especially for the 2nd NN are low. Other data will be discussed in the following sections.

Table 1.1 Number of Neighbors around Ge from Fits to the Ge K Edge for Bulk Ge and OAm - Capped Pure and Doped Ge NCs from References[16,64,65]

Dopant/ Alloy Element (E)	Reaction Temperature (°C)	E mol % in Ge NCs	Crystallite Size^a (nm)	Ge-Ge (1st NN)^b	Ge-Ge (2nd NN)^b
Ge (bulk)	-	-	Bulk Ge	4.0	12
Pristine Ge (NCs)	250	0.00	3.4	3.0	6.5
	250	0.00	3.5	3.3	6.8
	250	0.00	3.9	3.4	7.2
	250	0.00	9.7	3.6	8.4

Bi	250	0.50	3.5	3.2	6.9
	250	1.0	5	3.5	8.2
	250	1.5	8.6	3.4	8.8
Sb	250	0.50	3.1	2.6	4.8
	250	1.5	4.4	2.8	5.1
Sn	250	13.9	4.6	3.7	7
	240	16.2	4.0	3.7	4
	230	16.7	3.3	3.8	2

[a] Crystallite sizes are calculated based on the Scherrer method employing the (220) reflection.

[b] Errors on the number of neighbors are 15%.

1.3.2.4.Structural Characterization of Multimetallic Ge Nanoparticles

While Sb is a well-known dopant in Ge, Bi has no solubility in bulk Ge, yet can be kinetically stabilized in Ge nanoparticles and remain in the structure even after hydrazine treatment and ligand exchange.[16,59] Similarly, Sn, another element that has no solubility in bulk Ge, can be introduced in fairly high amounts in Ge NCs.[24,49,50,66] Powder X-ray diffraction is consistent with an increasing lattice parameter with Bi, Sb, and Sn incorporation into Ge NCs.[16,24,49,50,59,65,66] EXAFS characterization of Bi and Sb doped Ge NCs shows that there is expansion in the first NN bond distances, consistent with the larger sized dopant atom.[16]

For Bi-doped Ge, smaller peak shift in EXAFS is observed while the distance between dopant and the second and the third neighbor increased.[16] The peak shifts of the Bi-Ge path for Bi-doped Ge NCs with different doping percentage (0.5% - 1.5%) and capping ligand (oleylamine-trioctylphosphine mixtures and dodecanethiol) were analyzed in the work. A large r-shift of 0.28 Å to 0.29 Å from the fitted first peak in the EXAFS matches the covalent radius difference between

Bi and Ge of 0.28 Å. The r-shift decreases for the second and third peak indicates the distortion induced by Bi in the nanocrystal relaxes with increased distance to Ge. The large r-shift of the first peak and less shift for the second and third peaks suggests that the Bi dopants are mostly incorporated on (or near) the surface of Ge NCs.

The small amplitude of the Bi near neighbors provides additional evidence supporting the model where Bi is on or near the surface of the nanocrystal. As reported in Table 1.1, the amplitude values (number of neighbors) are significantly smaller than that of bulk Ge.[16] Compared with interior atoms, surface atoms should have roughly half the neighboring atoms and that is consistently observed in the analysis. Due to the high surface-to-volume nature of nanocrystals, the effect of the surface atoms is not negligible. With the large size of Bi atoms and the lack of incorporation in bulk Ge, it is likely that Bi is only incorporated near or at the surface of the Ge NCs. This result is also confirmed by the STEM-EDS data shown in Figure 1.11, where the Bi signals are mostly distributed on the edges. A simulation of the first and the second nearest neighbor number with the nanocrystal size is shown in Figure 1.12. The calculated amplitudes of the Ge edges of pure and doped samples are overlaid and follow the trend of the simulated amplitudes (the green curve). This result indicates the size difference of Bi vs Ge atoms on the EXAFS amplitude is significant. Another reason for the low amplitude is that Bi atoms may provide a significant amount of disorder to the structure. The Bi atoms could be incorporated in an amorphous phase which is commonly observed on the surface of Ge NCs, providing a small and broadened EXAFS signal for the first peak and will have no significant contribution to further peaks. The relatively high amplitudes calculated for the first shell neighbors of Ge edges in Figure 1.12 indicates that the maximum amount of an amorphous contribution is less than 20%.[16]

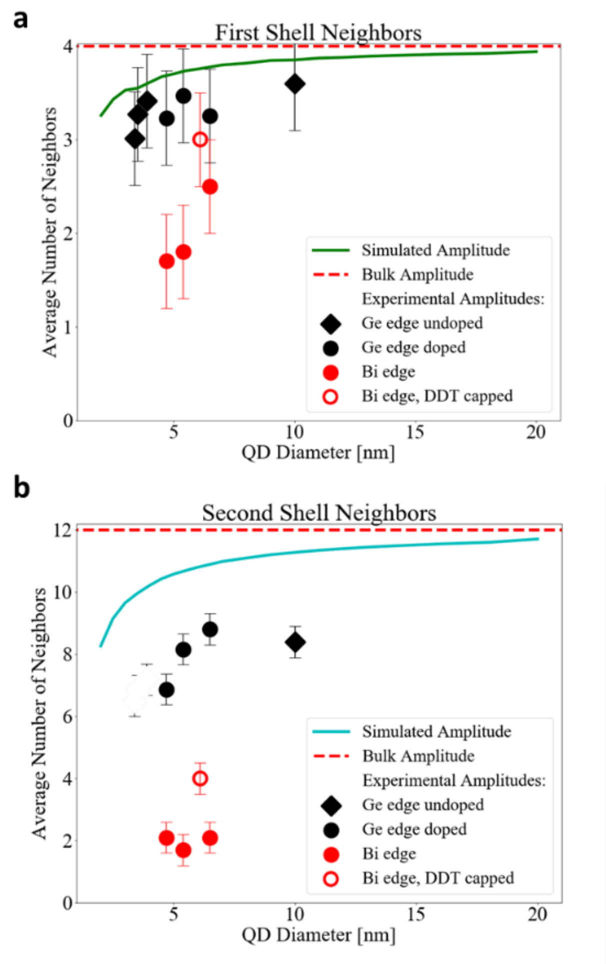

Figure 1.12 First shell (a) and second shell (b) amplitudes for simulated spherical distorted Bi-doped Ge NCs (quantum dots, QDs) of different sizes. Adapted with permission from (*ACS Applied Nano Materials* **2020,** *3* (6), 5410-5420). Copyright (2020) American Chemical Society.

Sb is another element from Group 15 that has been successfully incorporated in Ge NCs by colloidal synthesis with a percentage up to 1.5%.[64] Similar to Bi-doped Ge NCs, EXAFS of the Ge edge of Sb-doped Ge NCs showed lower peak amplitudes (number of nearest neighbors) compared with that of bulk Ge as shown in Table 1.1. The ratio of first to second nearest neighbor amplitude is calculated and compared among bulk and synthesized pristine and Sb-doped Ge NCs. Pristine Ge NCs show a ratio of 0.43-0.49 while bulk Ge has a ratio of 0.33. The ratio of first to second nearest neighbor amplitude decreases with an increase of the Ge particle size and becomes closer to that of bulk Ge. These results confirm the idea that bigger nanocrystals have lower surface-to-volume ratio and allow a better opportunity to separate the effect of the surface from location of the dopant. Sb-doped Ge NCs have much higher calculated ratios of 0.54-0.60. What is more, the second nearest neighbor amplitudes of doped Ge NCs are lower than that of pristine Ge. Both results indicate high disorder for the site occupation for Sb in Ge NCs.[64]

To understand the details of the Sb incorporation in Ge NCs, different structural models were tested to fit the Sb K-edge EXAFS data. The model that put the Sb atom off center in the diamond structure within the crystallite and adjacent to a vacancy provided the best fit. This Sb-vacancy defect pair (*E* center) has been reported in thin films.[67] Figure 1.13 shows a simplified illustration of this model. Different paths of the second near neighbors are shown in different colors. In this model, Sb-vacancy pairs contribute to the lower amplitude and broadening of the EXAFS peaks. The data indicates that with increasing particle size and Sb dopant concentration, that the fraction of Sb atoms on the surface also increases, although modeling the amount of the surface *vs* Sb-vacancy pairs with the current data was not possible.[64]

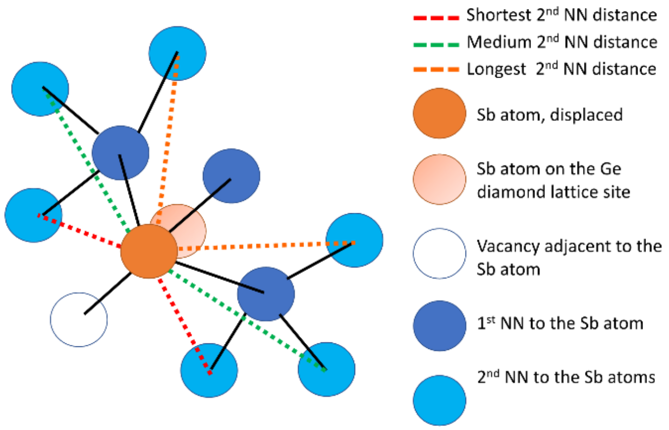

Figure 1.13 Illustration showing the splitting of the EXAFS functions for an Sb atom located within the Ge lattice and adjacent to a vacancy, with first and second near neighbor (NN) distances indicated. Adapted with permission from (*ACS Nano* **2021,** *15* (1), 1685-1700).[64] Copyright (2021) American Chemical Society.

Unlike the dopants, Sb and Bi, which can only be incorporated into Ge NCs in a small amount (≤ 2 mol %), group 14 Sn has been reported to alloy successfully into Ge NCs with various percentages that span 0-95%. The incorporation of Sn in a cubic $Ge_{1-x}Sn_x$ alloy structure is expected to result in an indirect-to-direct bandgap crossover.[49,68–70]

Ramasamy and coworkers reported a solution synthesis on Sn_xGe_{1-x}.[24] In this work, GeI_2 and Bis[bis(trimethylsilyl)amino]tin(II), $Sn(HDMS)_2$, were used as the precursors in a colloidal synthesis of $Ge_{1-x}Sn_x$ nanocrystals. It was reported that no reductant was required in the synthesis of Sn_xGe_{1-x} with x below 0.18. With the assistance of n-BuLi, the alloy percentage of Sn increased to 42 %. STEM−EDS element mapping was utilized to scope the homogeneity of the as-synthesized Sn_xGe_{1-x} nanocrystals, as shown in Figure 1.14 a-c. In a later work, Ramasamy reported another solution synthesis route on Sn_xGe_{1-x} with the assist of n-BuLi.[71] Sn_xGe_{1-x} nanocrystals with a compositional range of $0 < x < 0.95$ have been successfully synthesized. XRD and TEM-EDS were used to characterize the as-synthesized Sn_xGe_{1-x} NCs. A shift of XRD peak to the smaller angle indicates the incorporation between Sn and Ge as shown in Figure 1.14d. The authors also found that instead of altering the precursor ratios, the composition was easier to be controlled by reaction temperature and the durations. The composition percentage of Sn decreased with higher temperature or longer reaction duration time. A similar compositional trend was observed in microwave assisted reaction reported by Newton *et al*.[65]

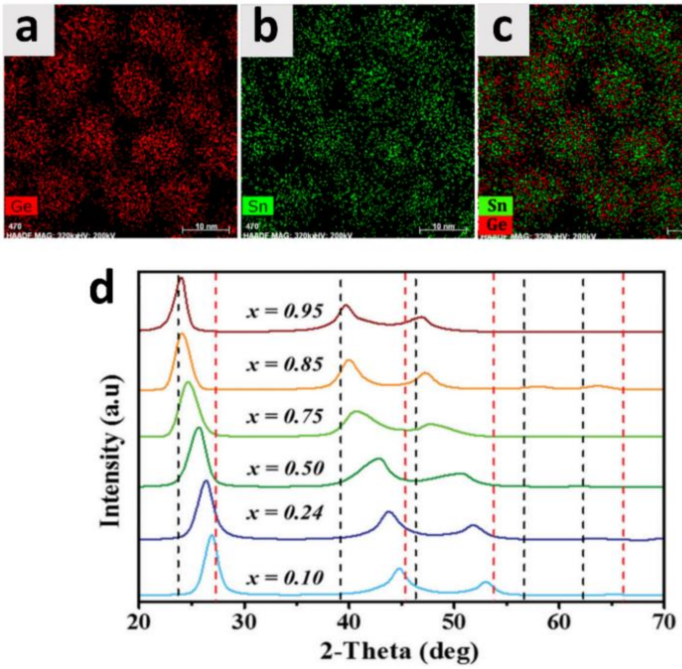

Figure 1.14 a-c. EDS mapping of solution synthesized Sn$_x$Ge$_{1-x}$ NCs with an x of 0.36. d. XRD patterns of Sn$_x$Ge$_{1-x}$ NCs with different compositions. Adapted with permission from (*Chem. Mater*. **2015,** *27* (13), 4640-4649.) copyright (2015) American Chemical Society.

The refinement of the EXAFS data on microwave synthesized GeSn nanocrystals prepared at different temperatures of capped with dodecanethiol is also provided in Table 1.1.[65] In this study, EXAFS of dodecanethiol-capped GeSn alloy nanocrystals made at three different temperatures (230 °C, 3.5 Å, 14 % Sn; 240 °C, 5.1 Å, 17.9 % Sn; and 250 °C, 5.1 Å, 15.4 % Sn; reaction temperature, nanocrystal diameter, nanocrystal Sn composition; respectively) were compared and analyzed. The distance of the second near neighbors of the Ge-Ge pair (4.04 Å-4.07 Å) from the Ge edge and Sn-Ge pair (4.03 Å-4.04 Å) from the Sn edge are almost the same. This observation is in great agreement with the average distance of second near neighbor reported for GeSn thin alloy films.[72] However, the first near neighbor distances are quite different for Ge-Ge and Sn-Ge, suggesting that the Sn is alloyed in Ge structure by local bond changing.

The second near neighbor distances from both Ge and Sn edges are much smaller than that of pristine Ge sample, indicating significant disorder beyond the first nearest neighbors in the GeSn nanocrystal alloy. Of the GeSn alloy nanocrystals prepared at the three different temperatures, the sample prepared at 250 °C gives the largest amplitude for the second nearest neighbor, suggesting the least disorder within the structure.[65]

Figure 1.15 shows a comparison of the bond expansion (*r*) for incorporation of the Bi, Sb and Sn atoms in Ge NCs. The bond expansions of Bi and Sb match the differences of covalent radius of the dopant indicates the dopant atoms are located on a Ge site in the diamond structure. As discussed above, Bi atoms are incorporated mostly on the surface of Ge NCs which minimizes the expansion and disorders of the Ge lattice. Sb doping introduces vacancies into the crystals and causes the disorder of the structure that is noted in the fitting of the peak of second and third near neighbors. Different from Bi and Sb, the bond expansion of the GeSn alloys is only 0.1 Å. However, this number is much smaller than the expected expansion of 0.14-0.19 Å, calculated form the ionic and covalent radius. This may attribute to the high Sn incorporation in the Ge NCs (as high as 15 %), at which the Sn alloyed lattice is expected to result in not only Sn-Ge bonding but also Sn-Sn bonding (0.6 out of 4).[65]

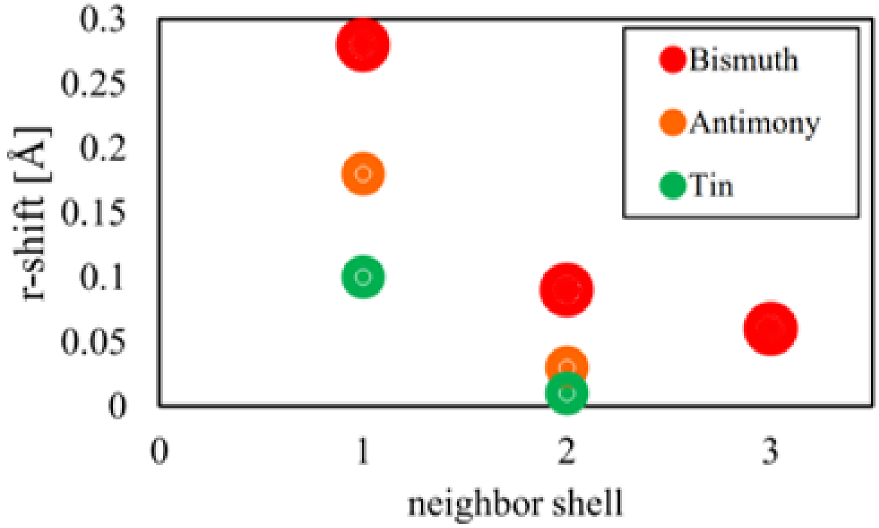

Figure 1.15 The bond expansion (r-shift) for Bi, Sb and Sn atoms in Ge NCs. Reprinted with permission from Sully, H. R., Structure, and Disorder of Large Dopants in Colloidal Germanium Quantum Dots. *Ph.D. Dissertation UC Santa Cruz,* **2020**.

Bi, Sb doped, and Sn alloyed Ge NCs are of great interest with unique properties and no bulk analogue. XRD and STEM-EDS mapping provides information about the incorporation and homogeneity. EXAFS analysis on doped and alloyed Ge NCs fills the gap of the knowledge about the local structures of the particles and sheds a light on the future direction for colloidal synthesis of Ge NCs. Here, we summarized some solution synthesized doped or alloyed Ge NCs in Table 1.2. The incorporation of heteroatoms in Ge structure could significantly modify the photoelectronic and electric properties. Several comprehensive review papers present and discuss Ge and the Ge-Sn system.[11,50,65] However, the limited number of examples of aliovalent doping that have been reported on points towards new avenues of exploration.

Table 1.2 Overview of Solution Synthesized Ge NCs with Different Dopant or Alloy.

Dopant or Alloyed Element	Solvent	Reducing agent	Doping (Alloy) percentage		Particle size (nm)	Ref.
Bi	OAm	OAm	Up to 2 %		4.6-9.4	59
Sb	OAm	OAm	Up to 2 %		3-5.9	64
Al, P, Ga, As, In, Sn, and Sb	OAm	n-BuLi in 1-octadecene	Al	0.51	3.3-4.1	63
			P	1.1		
			Ga	0.46		
			As	1.2		
			In	1.1		
			Sn	0.91		
			Sb	1.4		
Cu, Co, Ni and Mn	EtOH	$NaBH_4$	Cu	1.46;4.24	18.7-22.1	58
			Co	1.76; 4.39		
			Ni	2.05; 6.71		
			Mn	1.32; 4.03		
Sn	OAm	OAm	0~18		4.4-11.9	24
		n-BuLi	18~42			

Sn	OAm	n-BuLi	0~95	5-16	71
Sn	OAm	n-BuLi in 1-octadecene	0~23.6	Small: 1-3 Large polydispersed: 5-20	73
Sn	OAm	n-BuLi in 1-octadecene	0~27.9	Small: 3.4-4.6 Large polydispersed: 15-23	66
Sn	OAm	OAm	11.8-17.9	3.5-5.9	65

1.3.2.5. Conclusion

Ge NCs with different dopants have been discussed here with insights into the structures of NCs. However, solution synthesis on Ge NCs usually provides polycrystalline or amorphous structures which limits the properties of Ge NCs. In Chapter 2, we are going to discuss a two-step microwave assisted solution synthesis that provides monodispersed highly single-crystalline Ge NCs.

1.4. Thermoelectric Materials, Bi_2Te_3 and Sb_2Te_3

1.4.1. Introduction of Thermoelectric Properties

Thermoelectric materials enable direct energy conversion between heat and electricity and hold promising capabilities of increasing the energy waste harvesting and developing sustainable energy utilization. Thermoelectric effects can be used as temperature sensing, solid-state cooling, and solid-state heat-electricity generation. The energy conversion efficiency of thermoelectric device is expressed as dimensionless thermoelectric figure of merit:

$$zT = \frac{\sigma \cdot S^2}{\kappa} T \qquad \textbf{Equation 1.13}$$

where S is the Seebeck coefficient, σ the electrical conductivity, κ the total thermal conductivity (including contributions from lattice, κ_{lat}, and electrons, κ_e) and T the absolute temperature. In general, materials with peak zT values above 1 are superior for thermoelectric applications. Although a lot of effort has been put into improving and discovering thermoelectric materials, the max zT that has been achieved to date is 2.6.[74,75]

The figure of merit, zT, reflects the metric of the material properties to thermoelectric performance. However, S, σ, and electronic component of κ are inter-related through carrier concentration. It is disappointedly difficult to manipulate these interrelated properties, and to optimize the overall zT of a material. The relationship of Seebeck and carrier concentration n is described in Equation 1.14, where m^* is effective mass.[76]

$$\boldsymbol{S = \frac{8\pi^2 k_B^2}{3eh^2} m^* T (\frac{\pi}{3n})^{\frac{2}{3}}} \qquad \textbf{Equation 1.14}$$

Electrical conductivity and carrier concentration also related, as seen in Equation 1.15, where μ is carrier mobility.[76]

$$\boldsymbol{\sigma = ne\mu} \qquad \textbf{Equation 1.15}$$

Carrier concentration also plays a role in the electronic component of the thermal conductivity, shown in Equations 1.16 and 1.17, where the L is the Lorenz number.[76]

$$\boldsymbol{\kappa = \kappa_{electronic} + \kappa_{lattice}} \qquad \textbf{Equation 1.16}$$

$$\boldsymbol{\kappa_{electronic} = L\sigma T = Lne\mu T} \qquad \textbf{Equation 1.17}$$

Thermoelectric devices consist of two types of semiconducting materials, one is p-type whose major carriers are holes, and the other electrons (n-type). Once the two types of materials are connected into a circuit in series, and a heat gradient is applied, carriers in the two types of materials would be thermally activated and diffuse from the hot side to the cold side, which generates a current through the circuit.[77–79] This is schematically shown in Figure 1.16.

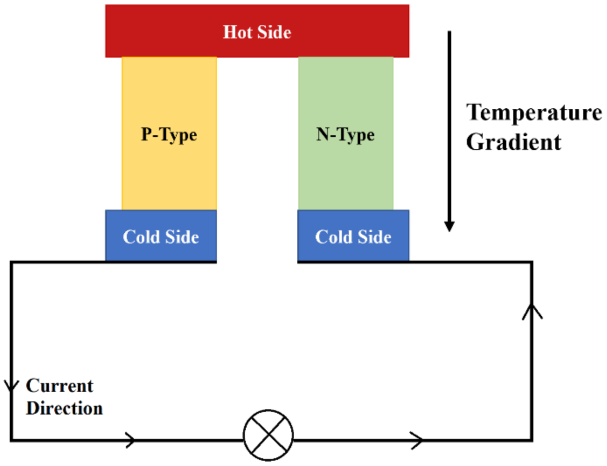

Figure 1.16 A scheme of a thermoelectric device consists of a p-type semiconductor leg and a n-type. While the temperature gradient is applied, the carriers in these two types of semiconductors move along the gradient and provide electricity.

Waste heat energy is usually a byproduct of many industrial productions and accounts for a large portion of the energy loss. Internal combustion engines and turbines convert thermal energy produced from chemical energy to mechanical work. However, only a fraction of thermal energy can be converted, and the rest is rejected as waste heat. Thermoelectric generators are useful in different applications to recover the energy in the heat waste as they have no moving parts and are quiet in comparison to other generators. Due to the diverse applications of thermoelectric generators and the potential to reutilize the waste heat, a need exists for discovering new materials and improving the properties to access higher zT across many temperature ranges.

To enhance the overall zT, according to the Equation 1.13, the Seebeck coefficient and electrical conductivity could be increased, and the thermal conductivity reduced. The power factor, a parameter describes the efficiency of energy generation, is the product of the squared Seebeck coefficient and the electrical conductivity. However, as described in Equation 1.14 and 1.15, the

Seebeck coefficient and electrical conductivity are inversely related through carrier concentration. Thus, an optimum carrier concentration needs to be reached which allows for maximizing the power factor.

The other approach to enhance overall *zT* is minimizing the thermal conductivity. Some materials have inherently low thermal conductivity due to structure complexity, such $Yb_{14}MnSb_{11}$,[80] which has a large molecular weight and can reduce the number of phonon modes which carry heat. Another way is utilizing nanostructuring and alloying, as previously discussed in Equation 1.16, thermal conductivity has two components, the lattice, and the electronic components. The electronic term is related to electrical conductivity inherently (Equation 1.17) and will always increase with increasing electrical conductivity. However, researchers still have some room to optimize lattice thermal conductivity, which is the only parameter not relevant with the electronic structure. By alloying or nanostructuring materials, more interfaces that potentially scatter phonons are introduced into the system, and in turn, reduce the thermal conductivity and improve the overall *zT*.

1.4.2. Bi_2Te_3 and Sb_2Te_3 as Thermoelectric Materials

Bi_2Te_3 and Sb_2Te_3 are two small bandgap semiconductors discovered decades ago since 1960,[81–83] and are still two of the best room-temperature thermoelectric materials. Over the decades, efforts have been devoted to enhancing the *zT* of these materials. For instance, using nanostructured Bi_2Te_3 (nanoparticles,[84] nanowires[85] and nanoplates[86]) decreased the thermal conductivity with enhanced phonon scattering and increased the Seebeck effect by quantum confinement effect.[87,88] Nanopores formed in Bi_2Te_3 may reduce the thermal conductivity.[89] Doping Bi_2Te_3 with Se,[90–94] and Sb_2Te_3 with Bi[95,96] modified the band structure and increased the carrier concentrations, leading to an improvement of overall *zT*. Dispersing nanoparticles in Bi_2Te_3[97] or Sb_2Te_3[98,99] matrix suppressed grain growth and created new interfaces and defects, which reduced thermal conductivity and enhanced Seebeck coefficient at higher temperature due to carrier filtering effect. Se-doped Bi_2Te_3 with their enhanced properties are shown in Figure 1.17. While the doping system efficiently modifies the electronic structure, the nanostructuring and anisotropy of the as-prepared device provide further decrease on thermal conductivity and enhance the overall *zT*. Figure 1.18 shows the decreased thermal conductivity in the direction parallel to the pressing direction.

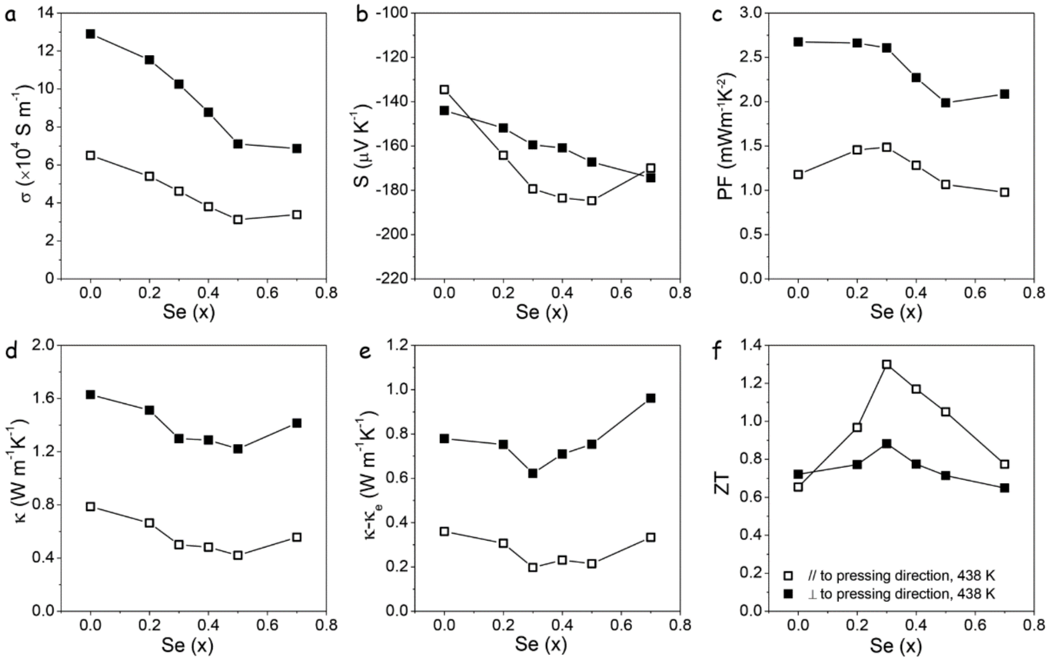

Figure 1.17 Properties with different Se concentration (x) (a) the electrical conductivity, (b) Seebeck coefficient, S; (c) power factor PF; (d) total thermal conductivity κ; (e) thermal conductivity after subtraction of electronic component, $\kappa - \kappa_e$; and (f) overall figure of merit zT, of $Bi_2Te_{3-x}Se_x$ pellets measured in the two directions, parallel (∥) (open symbols, □) and normal (⊥) (solid symbols, ■) to the pressing direction at 438 K. Adapted with permission from (*ACS Nano*. **2018,** *12* (7), 7174-7184) copyright (2018) American Chemical Society.

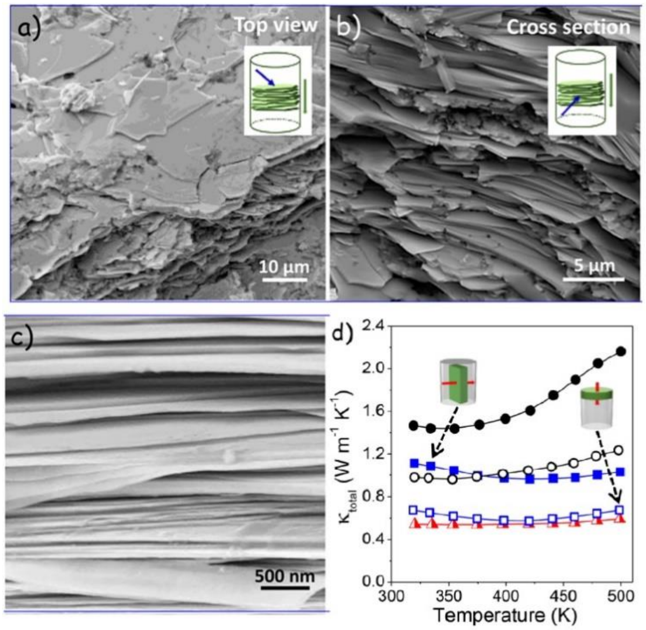

Figure 1.18 (a) Top-view SEM image of a $Bi_xSb_{2-x}Te_3$ pellet produced at 480 °C. (b) Cross-section SEM image of the pellet. (c) SEM image of detailed cross-section. (d) Thermal conductivity of $Bi_{0.5}Sb_{1.5}Te_3$ nanomaterial hot pressed at 480 °C (blue squares) measured in two directions, parallel (open squares) and normal (solid squares) to the press axis; $Bi_{0.5}Sb_{1.5}Te_3$ nanomaterial hot pressed at 300 °C (red triangles); and a commercial ingot (black circles) measured in two directions, parallel (solid circles) and normal (open circles) to the cleavage direction. Adapted with permission from (*Nano Lett.* **2018,** *18* (4), 2557-2563) copyright (2018) American Chemical Society.

In recent years, nanostructured heterojunction structures combined these benefits together with enhanced thermoelectric properties by even stronger energy filtering effect and phonon scattering.[88,100,101] Different Bi_2Te_3-based heterojunction systems have been studied and showed improvement on *zT*.[102–107] In previous work, Bi_2Te_3 and Bi_2Se_3 core shell heterojunction structure has been successfully synthesized by a solution method, highly improved the power factor ($S^2\sigma$), and reduced thermal conductivities.[108] Even though there are several studies of the effect on thermoelectric properties by heterojunction structures, very few p-n junctions (PNJ) have been reported. PNJ is seldom considered a promising way to improve *zT* since the potential of detrimental σ and S. However, introducing appropriate PNJ could also be beneficial to thermoelectric properties by manipulating carrier concentration to an optimal range. The PNJ also potentially performs energy filtering effect which could amplify the Seebeck coefficient and reduce the lattice thermal conductivity (κ_{lat}) by introducing interfaces. Bi_2Te_3 and Sb_2Te_3 bulk alloy demonstrated an enhancement on zT with reduced thermal conductivity and enhanced Seebeck coefficient.[109] Figure 1.19 provides the evidence of increased Seebeck coefficient and decreased electrical conductivity of the alloyed Bi_2Te_3 and Sb_2Te_3. High resolution transmission electron microscopy image clearly shows the interfaces between these two materials. The authors attributed the enhancement of the Seebeck coefficient to the filtering effect across the interfaces.[109]

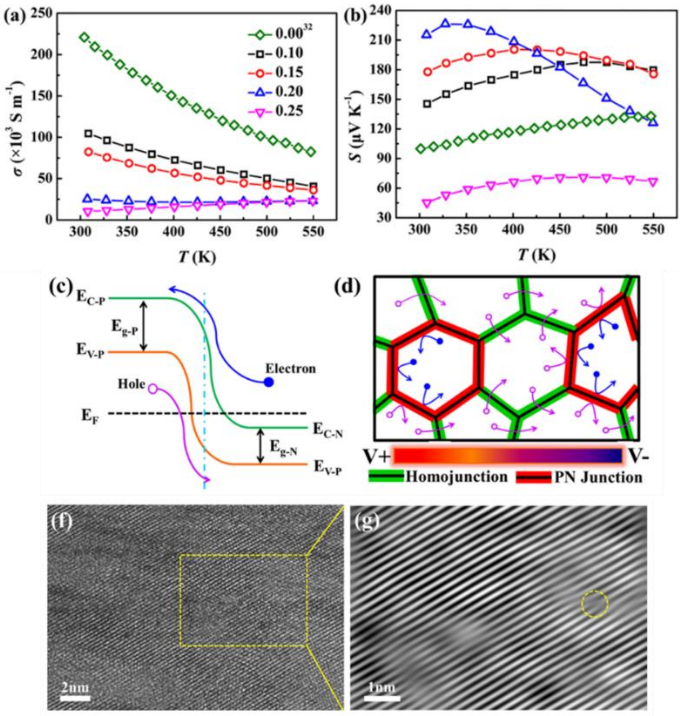

Figure 1.19 (a) Electrical conductivity and (b) Seebeck coefficient of as-sintered samples $(Bi_2Te_3)_x-(Sb_2Te_3)_{1-x}$ (x = 0.00, 0.10, 0.15, 0.20, and 0.25). (c) Band alignment at the interface between p-type Sb_2Te_3 and n-type Bi_2Te_3. (d) Scheme of transports for electrons and holes. (f) HRTEM image of the p-type Sb_2Te_3 matrix in the composite of $(Bi_2Te_3)_{0.15}-(Sb_2Te_3)_{0.85}$. (g) IFFT image of the box area in (f). Adapted with permission from (*Nano Lett.* **2018,** *18* (4), 2557-2563) copyright (2018) American Chemical Society.

In Chapter 3, I will discuss the solution synthesized Bi_2Te_3/Sb_2Te_3 core shell nanostructures and the corresponding thermoelectric properties.

1.5. Topological Insulators and Bi_2Se_3

Topological insulators (TIs) are a class of materials that can exhibit robust spin polarization at surfaces, and as one of the most promising candidate materials for constructing new spintronic circuits have attracted much attention. Charge transport and spin generation in TIs differ significantly from traditional three-dimensional (3D) or two-dimensional (2D) electronic systems, due to the robust topological order protected by time-reversal symmetry.

1.5.1. Introduction to Topological Insulators

Topological phases in condensed matter physics have been studied over decades.[110,111] TIs were firstly predicted by theorists with topologically protected surface states that have strong spin-orbit coupling.[112,113] The spins of the Dirac fermions on the TI surface are tightly locked with their momentum, thus the elastic backscattering of nonmagnetic impurities is prohibited. In other words, topological insulators are semiconducting materials that have a bandgap but have protected conducting states on their edges or surfaces.[112] Due to the combination of spin-orbit interactions and time-reversal symmetry, topological insulating states are possible. Novel spin-polarized 2D Dirac fermions exist on a three-dimensional (3D) topological insulator surface.

1.5.2. Bi_2Se_3 as Topological Insulator

In recent years, a lot of TIs have been predicted and discovered,[114–116] one of which is Bi_2Se_3. Bi_2Se_3 has been studied as a thermoelectric material[117–120] and a near infrared transparent conductor[121,122] and more recently as a topological insulator.[116,123] Bi_2Se_3 is of interest because of its simple surface state with a well-defined single Dirac cone and a wide bulk bandgap of 0.34 eV compared with other TIs, and thus is most promising to achieve room temperature spintronic devices. Bi_2Se_3, shown in Figure 1.20, has a rhombohedral crystal structure of space group $R\bar{3}m$ ($a = b = 4.140$ Å and $c = 28.636$ Å; JCPDF #33-0214) that can be described as a layered structure where the covalently bonded Bi_2Se_3 sheets are arranged in planar quintuple layers (QLs) of Se(1)-Bi-Se(2)-Bi-Se(1) atoms (with each QL approximately 1 nm thick). The QLs are stacked and connected by weak van der Waals interactions along the *c*-axis.

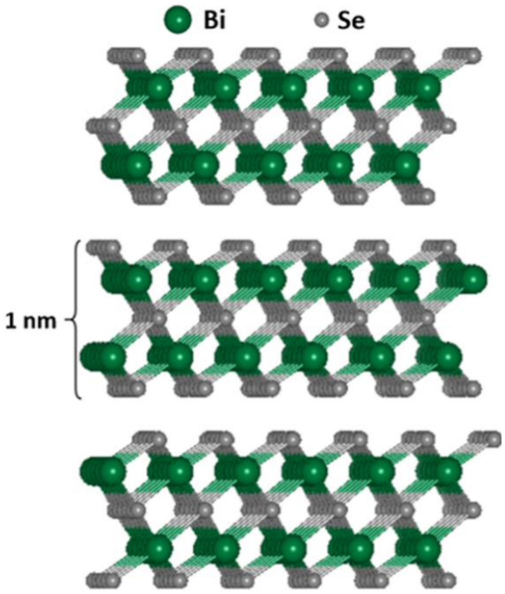

Figure 1.20 A view of the layered rhombohedral structure of Bi_2Se_3 showing the quintuple layers (QLs) of Se(1)-Bi-Se(2)-Bi-Se(1) with a thickness around 1 nm.

To date, existing theories often only consider charge/spin transport at the TI surface at the low impurity density limit. However, high density defects naturally occur in some TI materials, such as Se vacancies and interfacial defects due to surface oxidation of Bi_2Se_3.[124,125]

Due to the different atomic radii of Bi, Sb, Se and Te, 3D TI compounds of Bi_2Se_3, Sb_2Te_3 and Bi_2Te_3 have different defect types, which make them inherently n-doped or p-doped. In order to eliminate the possible doping and defects, Bi_2Se_3, Bi_2Te_3 and Sb_2Te_3 were alloyed together to neutralize these defects while maintaining the fundamental properties of a 3D TI.[126–129]

3D TIs have typically been prepared by chemical and physical vapor deposition (CVD and PVD),[130–135] molecular beam epitaxy (MBE)[136–139] and solvothermal methods.[129,140–142] However, TIs prepared by CVD or PVD methods normally contain excessive bulk carriers with a comparatively higher thickness (over 30 nm).[127,136,137,143] Thinner TI nanostructures have been synthesized by solvothermal routes with small lateral sizes (less than 5 μm). The small thickness (6 - 15 quintuple layers) reduces the bulk conductivity and allows stronger gate tunability of the Fermi level. To further suppress the bulk conductivity, Bi_2Se_3 is doped with Sb to compensate the excess electrons. Sb has been confirmed as an effective dopant which can significantly reduce carrier concentration without disrupting the topological surface state.[129,132,144] In Chapter 4, a mild solution reaction was carried out and synthesized significant amount of Sb doped Bi_2Se_3 with pronounced ambipolar field effect.

1.6. Conclusion

This Chapter describes the overall structure of this dissertation, and provides some fundamental principles of nucleation; opportunities and challenges with colloidal synthesized Ge NCs; introduction of thermoelectricity and V_2VI_3 materials; and introduction of a topological insulator and Bi_2Se_3.

1.7. References of Chapter 1

(1) Cao, G. *Nanostructures and Nanomaterials*; PUBLISHED BY IMPERIAL COLLEGE

PRESS AND DISTRIBUTED BY WORLD SCIENTIFIC PUBLISHING CO., 2004. https://doi.org/10.1142/p305.

(2) Sosso, G. C.; Chen, J.; Cox, S. J.; Fitzner, M.; Pedevilla, P.; Zen, A.; Michaelides, A. Crystal Nucleation in Liquids: Open Questions and Future Challenges in Molecular Dynamics Simulations. *Chem. Rev.* **2016**, *116* (12), 7078–7116. https://doi.org/10.1021/acs.chemrev.5b00744.

(3) Loh, N. D.; Sen, S.; Bosman, M.; Tan, S. F.; Zhong, J.; Nijhuis, C. A.; Král, P.; Matsudaira, P.; Mirsaidov, U. Multistep Nucleation of Nanocrystals in Aqueous Solution. *Nat. Chem.* **2017**, *9* (1), 77–82. https://doi.org/10.1038/nchem.2618.

(4) Privman, V. Mechanisms of Diffusional Nucleation of Nanocrystals and Their Self-Assembly into Uniform Colloids. *Ann. N. Y. Acad. Sci.* **2009**, *1161* (1), 508–525. https://doi.org/10.1111/j.1749-6632.2008.04323.x.

(5) Thanh, N. T. K.; Maclean, N.; Mahiddine, S. Mechanisms of Nucleation and Growth of Nanoparticles in Solution. *Chem. Rev.* **2014**, *114* (15), 7610–7630. https://doi.org/10.1021/cr400544s.

(6) Van Embden, J.; Sader, J. E.; Davidson, M.; Mulvaney, P. Evolution of Colloidal Nanocrystals: Theory and Modeling of Their Nucleation and Growth. *J. Phys. Chem. C* **2009**, *113* (37), 16342–16355. https://doi.org/10.1021/jp9027673.

(7) Polte, J. Fundamental Growth Principles of Colloidal Metal Nanoparticles – a New Perspective. *CrystEngComm* **2015**, *17* (36), 6809–6830. https://doi.org/10.1039/C5CE01014D.

(8) Xia, Y.; Xia, X.; Peng, H. C. Shape-Controlled Synthesis of Colloidal Metal Nanocrystals: Thermodynamic versus Kinetic Products. *J. Am. Chem. Soc.* **2015**, *137* (25), 7947–7966. https://doi.org/10.1021/jacs.5b04641.

(9) Lee, J.; Yang, J.; Kwon, S. G.; Hyeon, T. Nonclassical Nucleation and Growth of Inorganic Nanoparticles. *Nat. Rev. Mater.* **2016**, *1* (8), 1–16. https://doi.org/10.1038/natrevmats.2016.34.

(10) Holman, Z. C.; Liu, C. Y.; Kortshagen, U. R. Germanium and Silicon Nanocrystal Thin-

Film Field-Effect Transistors from Solution. *Nano Lett.* **2010**, *10* (7), 2661–2666. https://doi.org/10.1021/nl101413d.

(11) Carolan, D. Recent Advances in Germanium Nanocrystals: Synthesis, Optical Properties and Applications. *Prog. Mater. Sci.* **2017**, *90*, 128–158. https://doi.org/10.1016/j.pmatsci.2017.07.005.

(12) Vörös, M.; Wippermann, S.; Somogyi, B.; Gali, A.; Rocca, D.; Galli, G.; Zimanyi, G. T. Germanium Nanoparticles with Non-Diamond Core Structures for Solar Energy Conversion. *J. Mater. Chem. A* **2014**, *2* (25), 9820–9827. https://doi.org/10.1039/c4ta01543f.

(13) Ruddy, D. A.; Johnson, J. C.; Smith, E. R.; Neale, N. R. Size and Bandgap Control in the Solution-Phase Synthesis of near-Infrared-Emitting Germanium Nanocrystals. *ACS Nano* **2010**, *4* (12), 7459–7466. https://doi.org/10.1021/nn102728u.

(14) Hu, J.; Lu, Q.; Wu, C.; Liu, M.; Li, H.; Zhang, Y.; Yao, S. Synthesis of Fluorescent and Water-Dispersed Germanium Nanoparticles and Their Cellular Imaging Applications. *Langmuir* **2018**, *34* (30), 8932–8938. https://doi.org/10.1021/acs.langmuir.8b01543.

(15) Chou, N. H.; Oyler, K. D.; Motl, N. E.; Schaak, R. E. Colloidal Synthesis of Germanium Nanocrystals Using Room-Temperature Benchtop Chemistry. *Chem. Mater.* **2009**, *21* (18), 4105–4107. https://doi.org/10.1021/cm902088y.

(16) Sully, H. R.; Tabatabaei, K.; Hellier, K.; Newton, K. A.; Ju, Z.; Knudson, L.; Zargar, S.; Wang, M.; Kauzlarich, S. M.; Bridges, F.; Carter, S. A. Characterizing Bismuth Doping of Colloidal Germanium Quantum Dots for Energy Conversion Applications. *ACS Appl. Nano Mater.* **2020**, *3* (6), 5410–5420. https://doi.org/10.1021/acsanm.0c00709.

(17) Nozik, A. J. Nanoscience and Nanostructures for Photovoltaics and Solar Fuels. *Nano Lett.* **2010**, *10* (8), 2735–2741. https://doi.org/10.1021/nl102122x.

(18) Pillarisetty, R. Academic and Industry Research Progress in Germanium Nanodevices. *Nature*. 2011, pp 324–328. https://doi.org/10.1038/nature10678.

(19) Chockla, A. M.; Klavetter, K. C.; Mullins, C. B.; Korgel, B. A. Solution-Grown Germanium Nanowire Anodes for Lithium-Ion Batteries. *ACS Appl. Mater. Interfaces*

2012, *4* (9), 4658–4664. https://doi.org/10.1021/am3010253.

(20) Yuan, F. W.; Yang, H. J.; Tuan, H. Y. Alkanethiol-Passivated Ge Nanowires as High-Performance Anode Materials for Lithium-Ion Batteries: The Role of Chemical Surface Functionalization. *ACS Nano* **2012**, *6* (11), 9932–9942. https://doi.org/10.1021/nn303519g.

(21) Tallapally, V.; Nakagawara, T. A.; Demchenko, D. O.; Özgür, Ü.; Arachchige, I. U. Ge1-:XSnx Alloy Quantum Dots with Composition-Tunable Energy Gaps and near-Infrared Photoluminescence. *Nanoscale* **2018**, *10* (43), 20296–20305. https://doi.org/10.1039/c8nr04399j.

(22) Fan, J.; Chu, P. K. Group IV Nanoparticles: Synthesis, Properties, and Biological Applications. *Small* **2010**, *6* (19), 2080–2098. https://doi.org/10.1002/smll.201000543.

(23) Muthuswamy, E.; Zhao, J.; Tabatabaei, K.; Amador, M. M.; Holmes, M. A.; Osterloh, F. E.; Kauzlarich, S. M. Thiol-Capped Germanium Nanocrystals: Preparation and Evidence for Quantum Size Effects. *Chem. Mater.* **2014**, *26* (6), 2138–2146. https://doi.org/10.1021/cm4042154.

(24) Ramasamy, K.; Kotula, P. G.; Fidler, A. F.; Brumbach, M. T.; Pietryga, J. M.; Ivanov, S. A. SnxGe1-x Alloy Nanocrystals: A First Step toward Solution-Processed Group IV Photovoltaics. *Chem. Mater.* **2015**, *27* (13), 4640–4649. https://doi.org/10.1021/acs.chemmater.5b01041.

(25) Wheeler, L. M.; Nichols, A. W.; Chernomordik, B. D.; Anderson, N. C.; Beard, M. C.; Neale, N. R. All-Inorganic Germanium Nanocrystal Films by Cationic Ligand Exchange. *Nano Lett.* **2016**, *16* (3), 1949–1954. https://doi.org/10.1021/acs.nanolett.5b05192.

(26) Kamata, Y. High-k/Ge MOSFETs for Future Nanoelectronics. *Materials Today*. 2008, pp 30–38. https://doi.org/10.1016/S1369-7021(07)70350-4.

(27) Seino, M.; Henderson, E. J.; Puzzo, D. P.; Kadota, N.; Ozin, G. A. Germanium Nanocrystal Doped Inverse Crystalline Silicon Opal. *J. Mater. Chem.* **2011**, *21* (40), 15895–15898. https://doi.org/10.1039/c1jm13172a.

(28) Vaughn, D. D.; Schaak, R. E. Synthesis, Properties and Applications of Colloidal

Germanium and Germanium-Based Nanomaterials. *Chem. Soc. Rev.* **2013**, *42* (7), 2861–2879. https://doi.org/10.1039/c2cs35364d.

(29) Saeed, S.; De Weerd, C.; Stallinga, P.; Spoor, F. C.; Houtepen, A. J.; Siebbeles, L. D. A.; Gregorkiewicz, T. Carrier Multiplication in Germanium Nanocrystals. *Light Sci. Appl.* **2015**, *4* (2), 1–6. https://doi.org/10.1038/lsa.2015.24.

(30) Loaiza, L. C.; Monconduit, L.; Seznec, V. Si and Ge-Based Anode Materials for Li-, Na-, and K-Ion Batteries: A Perspective from Structure to Electrochemical Mechanism. *Small* **2020**, *16* (5). https://doi.org/10.1002/smll.201905260.

(31) Pescara, B.; Mazzio, K. A. Morphological and Surface-State Challenges in Ge Nanoparticle Applications. *Langmuir* **2020**, *36* (40), 11685–11701. https://doi.org/10.1021/acs.langmuir.0c01891.

(32) Guo, Y.; Rowland, C. E.; Schaller, R. D.; Vela, J. Near-Infrared Photoluminescence Enhancement in Ge/CdS and Ge/ZnS Core/Shell Nanocrystals: Utilizing IV/II-VI Semiconductor Epitaxy. *ACS Nano* **2014**, *8* (8), 8334–8343. https://doi.org/10.1021/nn502792m.

(33) Pescara, B.; Mazzio, K. A.; Lips, K.; Raoux, S. Crystallinity and Size Control of Colloidal Germanium Nanoparticles from Organogermanium Halide Reagents. *Inorg. Chem.* **2019**, *58* (8), 4802–4811. https://doi.org/10.1021/acs.inorgchem.8b03157.

(34) Zhu, J.; Palchik, O.; Chen, S.; Gedanken, A. Microwave Assisted Preparation of CdSe, PbSe, and Cu2-XSe Nanoparticles. *J. Phys. Chem. B* **2000**, *104* (31), 7344–7347. https://doi.org/10.1021/jp001488t.

(35) Panda, A. B.; Glaspell, G.; El-Shall, M. S. Microwave Synthesis of Highly Aligned Ultra Narrow Semiconductor Rods and Wires. *J. Am. Chem. Soc.* **2006**, *128* (9), 2790–2791. https://doi.org/10.1021/ja058148b.

(36) Gerbec, J. A.; Magana, D.; Washington, A.; Strouse, G. F. Microwave-Enhanced Reaction Rates for Nanoparticle Synthesis. *J. Am. Chem. Soc.* **2005**, *127* (45), 15791–15800. https://doi.org/10.1021/ja052463g.

(37) Atkins, T. M.; Thibert, A.; Larsen, D. S.; Dey, S.; Browning, N. D.; Kauzlarich, S. M.

Femtosecond Ligand/Core Dynamics of Microwave-Assisted Synthesized Silicon Quantum Dots in Aqueous Solution. *J. Am. Chem. Soc.* **2011**, *133* (51), 20664–20667. https://doi.org/10.1021/ja207344u.

(38) Muthuswamy, E.; Iskandar, A. S.; Amador, M. M.; Kauzlarich, S. M. Facile Synthesis of Germanium Nanoparticles with Size Control: Microwave versus Conventional Heating. *Chem. Mater.* **2013**, *25* (8), 1416–1422. https://doi.org/10.1021/cm302229b.

(39) Tabatabaei, K.; Holmes, A. L.; Newton, K. A.; Muthuswamy, E.; Sfadia, R.; Carter, S. A.; Kauzlarich, S. M. Halogen-Induced Crystallinity and Size Tuning of Microwave Synthesized Germanium Nanocrystals. *Chem. Mater.* **2019**, *31* (18), 7510–7521. https://doi.org/10.1021/acs.chemmater.9b02225.

(40) Carenco, S.; Boissière, C.; Nicole, L.; Sanchez, C.; Le Floch, P.; Mézailles, N. Controlled Design of Size-Tunable Monodisperse Nickel Nanoparticles. *Chem. Mater.* **2010**, *22* (4), 1340–1349. https://doi.org/10.1021/cm902007g.

(41) Wang, C.; Yin, H.; Chan, R.; Peng, S.; Dai, S.; Sun, S. One-Pot Synthesis of Oleylamine Coated AuAg Alloy NPs and Their Catalysis for CO Oxidation. *Chem. Mater.* **2009**, *21* (3), 433–435. https://doi.org/10.1021/cm802753j.

(42) He, M.; Protesescu, L.; Caputo, R.; Krumeich, F.; Kovalenko, M. V. A General Synthesis Strategy for Monodisperse Metallic and Metalloid Nanoparticles (In, Ga, Bi, Sb, Zn, Cu, Sn, and Their Alloys) via in Situ Formed Metal Long-Chain Amides. *Chem. Mater.* **2015**, *27* (2), 635–647. https://doi.org/10.1021/cm5045144.

(43) Yarema, O.; Perevedentsev, A.; Ovuka, V.; Baade, P.; Volk, S.; Wood, V.; Yarema, M. Colloidal Phase-Change Materials: Synthesis of Monodisperse GeTe Nanoparticles and Quantification of Their Size-Dependent Crystallization. *Chem. Mater.* **2018**, *30* (17), 6134–6143. https://doi.org/10.1021/acs.chemmater.8b02702.

(44) Bernard, A.; Zhang, K.; Larson, D.; Tabatabaei, K.; Kauzlarich, S. M. Solvent Effects on Growth, Crystallinity, and Surface Bonding of Ge Nanoparticles. *Inorg. Chem.* **2018**, *57* (9), 5299–5306. https://doi.org/10.1021/acs.inorgchem.8b00334.

(45) Smock, S. R.; Tabatabaei, K.; Williams, T. J.; Kauzlarich, S. M.; Brutchey, R. L. Surface

Coordination Chemistry of Germanium Nanocrystals Synthesized by Microwave-Assisted Reduction in Oleylamine. *Nanoscale* **2020**, *12* (4), 2764–2772. https://doi.org/10.1039/c9nr09233a.

(46) Holmes, A. L.; Hütges, J.; Reckmann, A.; Muthuswamy, E.; Meerholz, K.; Kauzlarich, S. M. Probing Electronics as a Function of Size and Surface of Colloidal Germanium Nanocrystals. *J. Phys. Chem. C* **2015**, *119* (10), 5671–5678. https://doi.org/10.1021/jp511929v.

(47) Norris, D. J.; Efros, A. L.; Erwin, S. C. Doped Nanocrystals. *Science (80-.).* **2008**, *319* (5871), 1776–1779. https://doi.org/10.1126/science.1143802.

(48) Kagan, C. R. Flexible Colloidal Nanocrystal Electronics. *Chem. Soc. Rev.* **2019**, *48* (6), 1626–1641. https://doi.org/10.1039/c8cs00629f.

(49) Barth, S.; Seifner, M. S.; Maldonado, S. Metastable Group IV Allotropes and Solid Solutions: Nanoparticles and Nanowires. *Chem. Mater.* **2020**, *32* (7), 2703–2741. https://doi.org/10.1021/acs.chemmater.9b04471.

(50) Doherty, J.; Biswas, S.; Galluccio, E.; Broderick, C. A.; Garcia-Gil, A.; Duffy, R.; O'Reilly, E. P.; Holmes, J. D. Progress on Germanium-Tin Nanoscale Alloys. *Chem. Mater.* **2020**, *32* (11), 4383–4408. https://doi.org/10.1021/acs.chemmater.9b04136.

(51) Kirmani, A. R.; Luther, J. M.; Abolhasani, M.; Amassian, A. Colloidal Quantum Dot Photovoltaics: Current Progress and Path to Gigawatt Scale Enabled by Smart Manufacturing. *ACS Energy Lett.* **2020**, *5* (9), 3069–3100. https://doi.org/10.1021/acsenergylett.0c01453.

(52) Stroyuk, O.; Raevskaya, A.; Gaponik, N. Solar Light Harvesting with Multinary Metal Chalcogenide Nanocrystals. *Chem. Soc. Rev.* **2018**, *47* (14), 5354–5422. https://doi.org/10.1039/c8cs00029h.

(53) Cassette, E.; Helle, M.; Bezdetnaya, L.; Marchal, F.; Dubertret, B.; Pons, T. Design of New Quantum Dot Materials for Deep Tissue Infrared Imaging. *Adv. Drug Deliv. Rev.* **2013**, *65* (5), 719–731. https://doi.org/10.1016/j.addr.2012.08.016.

(54) Cho, Y. J.; Kim, C. H.; Im, H. S.; Myung, Y.; Kim, H. S.; Back, S. H.; Lim, Y. R.; Jung,

C. S.; Jang, D. M.; Park, J.; Lim, S. H.; Cha, E. H.; Bae, K. Y.; Song, M. S.; Cho, W. Il. Germanium-Tin Alloy Nanocrystals for High-Performance Lithium Ion Batteries. *Phys. Chem. Chem. Phys.* **2013**, *15* (28), 11691–11695. https://doi.org/10.1039/c3cp51366a.

(55) Vaughn, D. D.; Sun, D.; Moyer, J. A.; Biacchi, A. J.; Misra, R.; Schiffer, P.; Schaak, R. E. Solution-Phase Synthesis and Magnetic Properties of Single-Crystal Iron Germanide Nanostructures. *Chem. Mater.* **2013**, *25* (21), 4396–4401. https://doi.org/10.1021/cm402795r.

(56) Lim, S. C.; Hsiao, M. C.; Lu, M. De; Tung, Y. L.; Tuan, H. Y. Synthesis of Germanium-Platinum Nanoparticles as High-Performance Catalysts for Spray-Deposited Large-Area Dye-Sensitized Solar Cells (DSSC) and the Hydrogen Evolution Reaction (HER). *Nanoscale* **2018**, *10* (35), 16657–16666. https://doi.org/10.1039/c8nr03983f.

(57) Makkar, M.; Viswanatha, R. Frontier Challenges in Doping Quantum Dots: Synthesis and Characterization. *RSC Adv.* **2018**, *8* (39), 22103–22112. https://doi.org/10.1039/c8ra03530j.

(58) McLeod, M.; Tabor, C. Tunable Conductivity of Germanium Thin Films Fabricated via Doped Colloidal Nanoparticle Sintering. *J. Phys. Chem. C* **2019**, *123* (2), 1477–1482. https://doi.org/10.1021/acs.jpcc.8b10300.

(59) Tabatabaei, K.; Lu, H.; Nolan, B. M.; Cen, X.; McCold, C. E.; Zhang, X.; Brutchey, R. L.; Van Benthem, K.; Hihath, J.; Kauzlarich, S. M. Bismuth Doping of Germanium Nanocrystals through Colloidal Chemistry. *Chem. Mater.* **2017**, *29* (17), 7353–7363. https://doi.org/10.1021/acs.chemmater.7b02241.

(60) Gao, Y.; Pi, X.; Wang, X.; Yuan, T.; Jiang, Q.; Gresback, R.; Lu, J.; Yang, D. Structures, Oxidation, and Charge Transport of Phosphorus-Doped Germanium Nanocrystals. *Part. Part. Syst. Charact.* **2016**, *33* (5), 271–278. https://doi.org/10.1002/ppsc.201600016.

(61) Yuan, T. H.; Pi, X. D.; Yang, D. Nonthermal Plasma Synthesized Boron-Doped Germanium Nanocrystals. *IEEE J. Sel. Top. Quantum Electron.* **2017**, *23* (5). https://doi.org/10.1109/JSTQE.2017.2654058.

(62) Zhi, B.; Yang, Y.; Hudson-Smith, N. V.; Kortshagen, U. R.; Haynes, C. L. Bacterial

Toxicity of Germanium Nanocrystals Induced by Doping with Boron and Phosphorus. *ACS Appl. Nano Mater.* **2019**, *2* (8), 4744–4755. https://doi.org/10.1021/acsanm.9b00525.

(63) Ruddy, D. A.; Erslev, P. T.; Habas, S. E.; Seabold, J. A.; Neale, N. R. Surface Chemistry Exchange of Alloyed Germanium Nanocrystals: A Pathway toward Conductive Group IV Nanocrystal Films. *J. Phys. Chem. Lett.* **2013**, *4* (3), 416–421. https://doi.org/10.1021/jz3020875.

(64) Tabatabaei, K.; Sully, H. R.; Ju, Z.; Hellier, K.; Lu, H.; Perez, C. J.; Newton, K. A.; Brutchey, R. L.; Bridges, F.; Carter, S. A.; Kauzlarich, S. M. Structural Insights on Microwave-Synthesized Antimony-Doped Germanium Nanocrystals. *ACS Nano* **2021**, *15* (1), 1685–1700. https://doi.org/10.1021/acsnano.0c09352.

(65) Newton, K. A.; Sully, H. R.; Bridges, F.; Carter, S. A.; Kauzlarich, S. M. Structural Characterization of Oleylamine- And Dodecanethiol-Capped Ge1- XSnxAlloy Nanocrystals. *J. Phys. Chem. C* **2021**, *125* (11), 6401–6417. https://doi.org/10.1021/acs.jpcc.0c11637.

(66) Esteves, R. J. A.; Ho, M. Q.; Arachchige, I. U. Nanocrystalline Group IV Alloy Semiconductors: Synthesis and Characterization of Ge1- XSnx Quantum Dots for Tunable Bandgaps. *Chem. Mater.* **2015**, *27* (5), 1559–1568. https://doi.org/10.1021/cm503983b.

(67) Markevich, V. P.; Peaker, A. R.; Litvinov, V. V.; Emtsev, V. V.; Murin, L. I. Electronic Properties of Antimony-Vacancy Complex in Ge Crystals. *J. Appl. Phys.* **2004**, *95* (8), 4078–4083. https://doi.org/10.1063/1.1669059.

(68) Moontragoon, P.; technology, Z. I.-… science and; 2007, undefined. Band Structure Calculations of Si–Ge–Sn Alloys: Achieving Direct Band Gap Materials. *iopscience.iop.org* **2007**. https://doi.org/10.1088/0268-1242/22/7/012.

(69) Lee, M. H.; Liu, P. L.; Hong, Y. A.; Chou, Y. T.; Hong, J. Y.; Siao, Y. J. Electronic Band Structures of Ge1-XSnx Semiconductors: A First-Principles Density Functional Theory Study. *J. Appl. Phys.* **2013**, *113* (6), 063517/1-063517/5. https://doi.org/10.1063/1.4790362.

(70) Gupta, S.; Chen, R.; Huang, Y. C.; Kim, Y.; Sanchez, E.; Harris, J. S.; Saraswat, K. C.

Highly Selective Dry Etching of Germanium over Germanium-Tin (Ge 1-XSnx): A Novel Route for Ge1-XSnx Nanostructure Fabrication. *Nano Lett.* **2013**, *13* (8), 3783–3790. https://doi.org/10.1021/nl4017286.

(71) Ramasamy, K.; Kotula, P. G.; Modine, N.; Brumbach, M. T.; Pietryga, J. M.; Ivanov, S. A. Cubic SnGe Nanoalloys: Beyond Thermodynamic Composition Limit. *Chem. Commun.* **2019**, *55* (19), 2773–2776. https://doi.org/10.1039/c8cc07570k.

(72) Gencarelli, F.; Grandjean, D.; Shimura, Y.; Vincent, B.; Banerjee, D.; Vantomme, A.; Vandervorst, W.; Loo, R.; Heyns, M.; Temst, K. Extended X-Ray Absorption Fine Structure Investigation of Sn Local Environment in Strained and Relaxed Epitaxial Ge1-XSnx Films. *J. Appl. Phys.* **2015**, *117* (9). https://doi.org/10.1063/1.4913856.

(73) Esteves, R.; Hafiz, S.; … D. D.-C.; 2016, U. Ultra-Small Ge 1− x Sn x Quantum Dots with Visible Photoluminescence. *Chem. Commun.* **2016**, *52* (78), 11665–11668.

(74) Zhao, L. D.; Tan, G.; Hao, S.; He, J.; Pei, Y.; Chi, H.; Wang, H.; Gong, S.; Xu, H.; Dravid, V. P.; Uher, C.; Snyder, G. J.; Wolverton, C.; Kanatzidis, M. G. Ultrahigh Power Factor and Thermoelectric Performance in Hole-Doped Single-Crystal SnSe. *Science (80-.).* **2016**, *351* (6269), 141–144. https://doi.org/10.1126/science.aad3749.

(75) Majumdar, A.; Chowdhury, S.; Ahuja, R. Ultralow Thermal Conductivity and High Thermoelectric Figure of Merit in Two-Dimensional Thallium Selenide. *ACS Appl. Energy Mater.* **2020**, *3* (9), 9315–9325. https://doi.org/10.1021/acsaem.0c01658.

(76) Tan, G.; Zhao, L. D.; Kanatzidis, M. G. Rationally Designing High-Performance Bulk Thermoelectric Materials. *Chem. Rev.* **2016**, *116* (19), 12123–12149. https://doi.org/10.1021/acs.chemrev.6b00255.

(77) Disalvo, F. J. Thermoelectric Cooling and Power Generation. *Science (80-.).* **1999**, *285* (5428), 703–706. https://doi.org/10.1126/science.285.5428.703.

(78) Zhang, Q. H.; Huang, X. Y.; Bai, S. Q.; Shi, X.; Uher, C.; Chen, L. D. Thermoelectric Devices for Power Generation: Recent Progress and Future Challenges. *Adv. Eng. Mater.* **2016**, *18* (2), 194–213. https://doi.org/10.1002/adem.201500333.

(79) Kauzlarich, S. M.; Zevalkink, A.; Toberer, E.; Snyder, G. J. Zintl Phases: Recent

Developments in Thermoelectrics and Future Outlook. *RSC Energy Environ. Ser.* **2017**, *2017-Janua* (17), 1–26. https://doi.org/10.1039/9781782624042-00001.

(80) Brown, S. R.; Kauzlarich, S. M.; Gascoin, F.; Jeffrey Snyder, G. Yb 14MnSb 11: New High Efficiency Thermoelectric Material for Power Generation. *Chem. Mater.* **2006**, *18* (7), 1873–1877. https://doi.org/10.1021/cm060261t.

(81) Smith, G. E.; Wolfe, R. Thermoelectric Properties of Bismuth-Antimony Alloys. *J. Appl. Phys.* **1962**, *33* (3), 841–846. https://doi.org/10.1063/1.1777178.

(82) Bergvall, P.; Beckman, O. Thermoelectric Properties of Non-Stoichiometric Bismuth-Antimony-Telluride Alloys. *Solid State Electron.* **1963**, *6* (2), 133–136. https://doi.org/10.1016/0038-1101(63)90006-6.

(83) Walker, P. A. The Thermal Conductivity and Thermoelectric Power of Bismuth Telluride at Low Temperatures. *Proc. Phys. Soc.* **1960**, *76* (1), 113–126. https://doi.org/10.1088/0370-1328/76/1/314.

(84) Scheele, M.; Oeschler, N.; Meier, K.; Kornowski, A.; Klinke, C.; Weller, H. Synthesis and Thermoelectric Characterization of Bi2Te 3 Nanoparticles. *Adv. Funct. Mater.* **2009**, *19* (21), 3476–3483. https://doi.org/10.1002/adfm.200901261.

(85) Zhang, G.; Kirk, B.; Jauregui, L. A.; Yang, H.; Xu, X.; Chen, Y. P.; Wu, Y. Rational Synthesis of Ultrathin N-Type Bi 2Te 3 Nanowires with Enhanced Thermoelectric Properties. *Nano Lett.* **2012**, *12* (1), 56–60. https://doi.org/10.1021/nl202935k.

(86) Son, J. S.; Choi, M. K.; Han, M. K.; Park, K.; Kim, J. Y.; Lim, S. J.; Oh, M.; Kuk, Y.; Park, C.; Kim, S. J.; Hyeon, T. N-Type Nanostructured Thermoelectric Materials Prepared from Chemically Synthesized Ultrathin Bi 2Te 3 Nanoplates. *Nano Lett.* **2012**, *12* (2), 640–647. https://doi.org/10.1021/nl203389x.

(87) Nielsch, K.; Bachmann, J.; Kimling, J.; Böttner, H. Thermoelectric Nanostructures: From Physical Model Systems towards Nanograined Composites. *Advanced Energy Materials*. 2011, pp 713–731. https://doi.org/10.1002/aenm.201100207.

(88) Zhang, G.; Yu, Q.; Wang, W.; Li, X. Nanostructures for Thermoelectric Applications: Synthesis, Growth Mechanism, and Property Studies. *Adv. Mater.* **2010**, *22* (17), 1959–

1962. https://doi.org/10.1002/adma.200903812.

(89) Wu, Z.; Mu, E.; Che, Z.; Liu, Y.; Sun, F.; Wang, X.; Hu, Z. Nanoporous (00l)-Oriented Bi2Te3 Nanoplate Film for Improved Thermoelectric Performance. *J. Alloys Compd.* **2020**, *828*, 154239. https://doi.org/10.1016/j.jallcom.2020.154239.

(90) Hong, M.; Chasapis, T. C.; Chen, Z. G.; Yang, L.; Kanatzidis, M. G.; Snyder, G. J.; Zou, J. N-Type Bi2Te3-XSex Nanoplates with Enhanced Thermoelectric Efficiency Driven by Wide-Frequency Phonon Scatterings and Synergistic Carrier Scatterings. *ACS Nano* **2016**, *10* (4), 4719–4727. https://doi.org/10.1021/acsnano.6b01156.

(91) Liu, Y.; Zhang, Y.; Lim, K. H.; Ibáñez, M.; Ortega, S.; Li, M.; David, J.; Martí-Sánchez, S.; Ng, K. M.; Arbiol, J.; Kovalenko, M. V.; Cadavid, D.; Cabot, A. High Thermoelectric Performance in Crystallographically Textured N-Type Bi2Te3- XSex Produced from Asymmetric Colloidal Nanocrystals. *ACS Nano* **2018**, *12* (7), 7174–7184. https://doi.org/10.1021/acsnano.8b03099.

(92) Yan, X.; Poudel, B.; Ma, Y.; Liu, W. S.; Joshi, G.; Wang, H.; Lan, Y.; Wang, D.; Chen, G.; Ren, Z. F. Experimental Studies on Anisotropic Thermoelectric Properties and Structures of N-Type Bi2Te2.7Se0.3. *Nano Lett.* **2010**, *10* (9), 3373–3378. https://doi.org/10.1021/nl101156v.

(93) Soni, A.; Yanyuan, Z.; Ligen, Y.; Aik, M. K. K.; Dresselhaus, M. S.; Xiong, Q. Enhanced Thermoelectric Properties of Solution Grown Bi 2Te 3-XSe x Nanoplatelet Composites. *Nano Lett.* **2012**, *12* (3), 1203–1209. https://doi.org/10.1021/nl2034859.

(94) Li, D.; Qin, X. Y.; Liu, Y. F.; Wang, N. N.; Song, C. J.; Sun, R. R. Improved Thermoelectric Properties for Solution Grown Bi2Te 3-XSex Nanoplatelet Composites. *RSC Adv.* **2013**, *3* (8), 2632–2638. https://doi.org/10.1039/c2ra22562j.

(95) Blank, V. D.; Buga, S. G.; Kulbachinskii, V. A.; Kytin, V. G.; Medvedev, V. V.; Popov, M. Y.; Stepanov, P. B.; Skok, V. F. Thermoelectric Properties of Bi 0.5Sb 1.5Te 3/C 60 Nanocomposites. *Phys. Rev. B - Condens. Matter Mater. Phys.* **2012**, *86* (7), 75426. https://doi.org/10.1103/PhysRevB.86.075426.

(96) Liu, Y.; Zhang, Y.; Ortega, S.; Ibáñez, M.; Lim, K. H.; Grau-Carbonell, A.; Martí-

Sánchez, S.; Ng, K. M.; Arbiol, J.; Kovalenko, M. V.; Cadavid, D.; Cabot, A. Crystallographically Textured Nanomaterials Produced from the Liquid Phase Sintering of BixSb2-XTe3 Nanocrystal Building Blocks. *Nano Lett.* **2018**, *18* (4), 2557–2563. https://doi.org/10.1021/acs.nanolett.8b00263.

(97) Zhang, Q.; Ai, X.; Wang, L.; Chang, Y.; Luo, W.; Jiang, W.; Chen, L. Improved Thermoelectric Performance of Silver Nanoparticles-Dispersed Bi2Te3 Composites Deriving from Hierarchical Two-Phased Heterostructure. *Adv. Funct. Mater.* **2015**, *25* (6), 966–976. https://doi.org/10.1002/adfm.201402663.

(98) Ko, D. K.; Kang, Y.; Murray, C. B. Enhanced Thermopower via Carrier Energy Filtering in Solution-Processable Pt-Sb2Te3 Nanocomposites. *Nano Lett.* **2011**, *11* (7), 2841–2844. https://doi.org/10.1021/nl2012246.

(99) Li, J.; Tan, Q.; Li, J. F.; Liu, D. W.; Li, F.; Li, Z. Y.; Zou, M.; Wang, K. BiSbTe-Based Nanocomposites with High ZT: The Effect of SiC Nanodispersion on Thermoelectric Properties. *Adv. Funct. Mater.* **2013**, *23* (35), 4317–4323. https://doi.org/10.1002/adfm.201300146.

(100) Choi, J.; Lee, J. Y.; Lee, S. S.; Park, C. R.; Kim, H. High-Performance Thermoelectric Paper Based on Double Carrier-Filtering Processes at Nanowire Heterojunctions. *Adv. Energy Mater.* **2016**, *6* (9). https://doi.org/10.1002/aenm.201502181.

(101) Mehta, R. J.; Karthik, C.; Singh, B.; Teki, R.; Borca-Tasciuc, T.; Ramanath, G. Seebeck Tuning in Chalcogenide Nanoplate Assemblies by Nanoscale Heterostructuring. *ACS Nano* **2010**, *4* (9), 5055–5060. https://doi.org/10.1021/nn101322p.

(102) Zhang, G.; Fang, H.; Yang, H.; Jauregui, L. A.; Chen, Y. P.; Wu, Y. Design Principle of Telluride-Based Nanowire Heterostructures for Potential Thermoelectric Applications. *Nano Lett.* **2012**, *12* (7), 3627–3633. https://doi.org/10.1021/nl301327d.

(103) Cheng, L.; Chen, Z. G.; Yang, L.; Han, G.; Xu, H. Y.; Snyder, G. J.; Lu, G. Q.; Zou, J. T-Shaped Bi2Te3-Te Heteronanojunctions: Epitaxial Growth, Structural Modeling, and Thermoelectric Properties. *J. Phys. Chem. C* **2013**, *117* (24), 12458–12464. https://doi.org/10.1021/jp4041666.

(104) Wang, W.; Lu, X.; Zhang, T.; Zhang, G.; Jiang, W.; Li, X. Bi2Te3/Te Multiple Heterostructure Nanowire Arrays Formed by Confined Precipitation. *J. Am. Chem. Soc.* **2007**, *129* (21), 6702–6703. https://doi.org/10.1021/ja070976c.

(105) Fang, H.; Feng, T.; Yang, H.; Ruan, X.; Wu, Y. Synthesis and Thermoelectric Properties of Compositional-Modulated Lead Telluride-Bismuth Telluride Nanowire Heterostructures. *Nano Lett.* **2013**, *13* (5), 2058–2063. https://doi.org/10.1021/nl400319u.

(106) Zhang, G.; Wang, W.; Li, X. Enhanced Thermoelectric Properties of Core/Shell Heterostructure Nanowire Composites. *Adv. Mater.* **2008**, *20* (19), 3654–3656. https://doi.org/10.1002/adma.200800162.

(107) Min, Y.; Roh, J. W.; Yang, H.; Park, M.; Kim, S. Il; Hwang, S.; Lee, S. M.; Lee, K. H.; Jeong, U. Surfactant-Free Scalable Synthesis of Bi 2 Te 3 and Bi 2 Se 3 Nanoflakes and Enhanced Thermoelectric Properties of Their Nanocomposites (Adv. Mater. 10/2013) . *Adv. Mater.* **2013**, *25* (10), 1424–1424. https://doi.org/10.1002/adma.201370066.

(108) Min, Y.; Park, G.; Kim, B.; Giri, A.; Zeng, J.; Roh, J. W.; Kim, S. Il; Lee, K. H.; Jeong, U. Synthesis of Multishell Nanoplates by Consecutive Epitaxial Growth of Bi2Se3 and Bi2Te3 Nanoplates and Enhanced Thermoelectric Properties. *ACS Nano* **2015**, *9* (7), 6843–6853. https://doi.org/10.1021/nn507250r.

(109) Wang, X. Y.; Wang, H. J.; Xiang, B.; Fu, L. W.; Zhu, H.; Chai, D.; Zhu, B.; Yu, Y.; Gao, N.; Huang, Z. Y.; Zu, F. Q. Thermoelectric Performance of Sb2Te3-Based Alloys Is Improved by Introducing PN Junctions. *ACS Appl. Mater. Interfaces* **2018**, *10* (27), 23277–23284. https://doi.org/10.1021/acsami.8b01719.

(110) Ando, T.; Matsumoto, Y.; Uemura, Y. Theory of Hall Effect in a Two-Dimensional Electron System. *J. Phys. Soc. Japan* **1975**, *39* (2), 279–288. https://doi.org/10.1143/JPSJ.39.279.

(111) Laughlin, R. B. Quantized Hall Conductivity in Two Dimensions. *Phys. Rev. B* **1981**, *23* (10), 5632–5633. https://doi.org/10.1103/PhysRevB.23.5632.

(112) Bernevig, B. A.; Zhang, S. C. Quantum Spin Hall Effect. *Phys. Rev. Lett.* **2006**, *96* (10). https://doi.org/10.1103/PhysRevLett.96.106802.

(113) Bernevig, B. A.; Hughes, T. L.; Zhang, S. C. Quantum Spin Hall Effect and Topological Phase Transition in HgTe Quantum Wells. *Science (80-.).* **2006**, *314* (5806), 1757–1761. https://doi.org/10.1126/science.1133734.

(114) Fu, L.; Kane, C. L.; Mele, E. J. Topological Insulators in Three Dimensions. *Phys. Rev. Lett.* **2007**, *98* (10). https://doi.org/10.1103/PhysRevLett.98.106803.

(115) Hsieh, D.; Qian, D.; Wray, L.; Xia, Y.; Hor, Y. S.; Cava, R. J.; Hasan, M. Z. A Topological Dirac Insulator in a Quantum Spin Hall Phase. *Nature* **2008**, *452* (7190), 970–974. https://doi.org/10.1038/nature06843.

(116) Zhang, H.; Liu, C. X.; Qi, X. L.; Dai, X.; Fang, Z.; Zhang, S. C. Topological Insulators in Bi 2 Se 3, Bi 2 Te 3 and Sb 2 Te 3 with a Single Dirac Cone on the Surface. *Nat. Phys.* **2009**, *5* (6), 438–442. https://doi.org/10.1038/nphys1270.

(117) Wang, S.; Sun, Y.; Yang, J. J.; Duan, B.; Wu, L.; Zhang, W.; Yang, J. J. High Thermoelectric Performance in Te-Free (Bi,Sb)2Se3: Via Structural Transition Induced Band Convergence and Chemical Bond Softening. *Energy Environ. Sci.* **2016**, *9* (11), 3436–3447. https://doi.org/10.1039/c6ee02674e.

(118) Ghaemi, P.; Mong, R. S. K.; Moore, J. E. In-Plane Transport and Enhanced Thermoelectric Performance in Thin Films of the Topological Insulators Bi2Te3 and Bi 2Se3. *Phys. Rev. Lett.* **2010**, *105* (16), 166603. https://doi.org/10.1103/PhysRevLett.105.166603.

(119) Tretiakov, O. A.; Abanov, A.; Murakami, S.; Sinova, J. Large Thermoelectric Figure of Merit for Three-Dimensional Topological Anderson Insulators via Line Dislocation Engineering. *Appl. Phys. Lett.* **2010**, *97* (7), 073108. https://doi.org/10.1063/1.3481382.

(120) Kong, D.; Cui, Y. Opportunities in Chemistry and Materials Science for Topological Insulators and Their Nanostructures. *Nat. Chem.* **2011**, *3* (11), 845–849. https://doi.org/10.1038/nchem.1171.

(121) Lin, Z.; Chen, Y.; Yin, A.; He, Q.; Huang, X.; Xu, Y.; Liu, Y.; Zhong, X.; Huang, Y.; Duan, X. Solution Processable Colloidal Nanoplates as Building Blocks for High-Performance Electronic Thin Films on Flexible Substrates. *Nano Lett.* **2014**, *14* (11),

6547–6553. https://doi.org/10.1021/nl503140c.

(122) Peng, H.; Dang, W.; Cao, J.; Chen, Y.; Wu, D.; Zheng, W.; Li, H.; Shen, Z. X.; Liu, Z. Topological Insulator Nanostructures for Near-Infrared Transparent Flexible Electrodes. *Nat. Chem.* **2012**, *4* (4), 281–286. https://doi.org/10.1038/nchem.1277.

(123) Xia, Y.; Qian, D.; Hsieh, D.; Wray, L.; Pal, A.; Lin, H.; Bansil, A.; Grauer, D.; Hor, Y. S.; Cava, R. J.; Hasan, M. Z. Observation of a Large-Gap Topological-Insulator Class with a Single Dirac Cone on the Surface. *Nat. Phys.* **2009**, *5* (6), 398–402. https://doi.org/10.1038/nphys1274.

(124) Yashina, L. V.; Sánchez-Barriga, J.; Scholz, M. R.; Volykhov, A. A.; Sirotina, A. P.; Neudachina, V. S.; Tamm, M. E.; Varykhalov, A.; Marchenko, D.; Springholz, G.; Bauer, G.; Knop-Gericke, A.; Rader, O. Negligible Surface Reactivity of Topological Insulators Bi 2Se3 and Bi2Te3 towards Oxygen and Water. *ACS Nano* **2013**, *7* (6), 5181–5191. https://doi.org/10.1021/nn400908b.

(125) Kong, D.; Cha, J. J.; Lai, K.; Peng, H.; Analytis, J. G.; Meister, S.; Chen, Y.; Zhang, H. J.; Fisher, I. R.; Shen, Z. X.; Cui, Y. Rapid Surface Oxidation as a Source of Surface Degradation Factor for Bi2Se3. *ACS Nano* **2011**, *5* (6), 4698–4703. https://doi.org/10.1021/nn200556h.

(126) Singh, R.; Gangwar, V. K.; Daga, D. D.; Singh, A.; Ghosh, A. K.; Kumar, M.; Lakhani, A.; Singh, R.; Chatterjee, S. Unusual Negative Magnetoresistance in Bi2Se3-YSy Topological Insulator under Perpendicular Magnetic Field. *Appl. Phys. Lett.* **2018**, *112* (10), 102401. https://doi.org/10.1063/1.5019235.

(127) Andzane, J.; Kunakova, G.; Charpentier, S.; Hrkac, V.; Kienle, L.; Baitimirova, M.; Bauch, T.; Lombardi, F.; Erts, D. Catalyst-Free Vapour-Solid Technique for Deposition of Bi2Te3 and Bi2Se3 Nanowires/Nanobelts with Topological Insulator Properties. *Nanoscale* **2015**, *7* (38), 15935–15944. https://doi.org/10.1039/c5nr04574f.

(128) Lee, J.; Park, J.; Lee, J. H.; Kim, J. S.; Lee, H. J. Gate-Tuned Differentiation of Surface-Conducting States in Bi 1.5Sb0.5Te1.7Se1.3 Topological-Insulator Thin Crystals. *Phys. Rev. B - Condens. Matter Mater. Phys.* **2012**, *86* (24), 245321.

https://doi.org/10.1103/PhysRevB.86.245321.

(129) Kong, D.; Koski, K. J.; Cha, J. J.; Hong, S. S.; Cui, Y. Ambipolar Field Effect in Sb-Doped Bi2Se3 Nanoplates by Solvothermal Synthesis. *Nano Lett.* **2013**, *13* (2), 632–636. https://doi.org/10.1021/nl304212u.

(130) Kong, D.; Dang, W.; Cha, J. J.; Li, H.; Meister, S.; Peng, H.; Liu, Z.; Cui, Y. Few-Layer Nanoplates of Bi2Se3 and Bi 2Te3 with Highly Tunable Chemical Potential. *Nano Lett.* **2010**, *10* (6), 2245–2250. https://doi.org/10.1021/nl101260j.

(131) Cao, H.; Venkatasubramanian, R.; Liu, C.; Pierce, J.; Yang, H.; Zahid Hasan, M.; Wu, Y.; Chen, Y. P. Topological Insulator Bi 2Te 3 Films Synthesized by Metal Organic Chemical Vapor Deposition. *Appl. Phys. Lett.* **2012**, *101* (16), 162104. https://doi.org/10.1063/1.4760226.

(132) Hong, S. S.; Cha, J. J.; Kong, D.; Cui, Y. Ultra-Low Carrier Concentration and Surface-Dominant Transport in Antimony-Doped Bi 2 Se 3 Topological Insulator Nanoribbons. *Nat. Commun.* **2012**, *3*, 757. https://doi.org/10.1038/ncomms1771.

(133) Guo, Y.; Aisijiang, M.; Zhang, K.; Jiang, W.; Chen, Y.; Zheng, W.; Song, Z.; Cao, J.; Liu, Z.; Peng, H. Selective-Area van Der Waals Epitaxy of Topological Insulator Grid Nanostructures for Broadband Transparent Flexible Electrodes. *Adv. Mater.* **2013**, *25* (41), 5959–5964. https://doi.org/10.1002/adma.201302661.

(134) Brom, J. E.; Ke, Y.; Du, R.; Won, D.; Weng, X.; Andre, K.; Gagnon, J. C.; Mohney, S. E.; Li, Q.; Chen, K.; Xi, X. X.; Redwing, J. M. Structural and Electrical Properties of Epitaxial Bi 2Se 3 Thin Films Grown by Hybrid Physical-Chemical Vapor Deposition. *Appl. Phys. Lett.* **2012**, *100* (16), 162110. https://doi.org/10.1063/1.4704680.

(135) Xu, Z.; Guo, X.; Yao, M.; He, H.; Miao, L.; Jiao, L.; Liu, H.; Wang, J.; Qian, D.; Jia, J.; Ho, W.; Xie, M. Anisotropic Topological Surface States on High-Index Bi2Se 3 Films. *Adv. Mater.* **2013**, *25* (11), 1557–1562. https://doi.org/10.1002/adma.201202936.

(136) Liu, X.; Smith, D. J.; Fan, J.; Zhang, Y. H.; Cao, H.; Chen, Y. P.; Leiner, J.; Kirby, B. J.; Dobrowolska, M.; Furdyna, J. K. Structural Properties of Bi2Te3 and Bi 2Se3 Topological Insulators Grown by Molecular Beam Epitaxy on GaAs(001) Substrates. *Appl. Phys. Lett.*

2011, *99* (17), 171903. https://doi.org/10.1063/1.3655995.

(137) Schreyeck, S.; Tarakina, N. V.; Karczewski, G.; Schumacher, C.; Borzenko, T.; Brüne, C.; Buhmann, H.; Gould, C.; Brunner, K.; Molenkamp, L. W. Molecular Beam Epitaxy of High Structural Quality Bi2Se 3 on Lattice Matched InP(111) Substrates. *Appl. Phys. Lett.* **2013**, *102* (4), 041914. https://doi.org/10.1063/1.4789775.

(138) Zhang, Y.; He, K.; Chang, C. Z.; Song, C. L.; Wang, L. L.; Chen, X.; Jia, J. F.; Fang, Z.; Dai, X.; Shan, W. Y.; Shen, S. Q.; Niu, Q.; Qi, X. L.; Zhang, S. C.; Ma, X. C.; Xue, Q. K. Crossover of the Three-Dimensional Topological Insulator Bi 2 Se 3 to the Two-Dimensional Limit. *Nat. Phys.* **2010**, *6* (8), 584–588. https://doi.org/10.1038/nphys1689.

(139) Li, Y. Y.; Wang, G.; Zhu, X. G.; Liu, M. H.; Ye, C.; Chen, X.; Wang, Y. Y.; He, K.; Wang, L. L.; Ma, X. C.; Zhang, H. J.; Dai, X.; Fang, Z.; Xie, X. C.; Liu, Y.; Qi, X. L.; Jia, J. F.; Zhang, S. C.; Xue, Q. K. Intrinsic Topological Insulator Bi 2 Te 3 Thin Films on Si and Their Thickness Limit. *Adv. Mater.* **2010**, *22* (36), 4002–4007. https://doi.org/10.1002/adma.201000368.

(140) Yang, L.; Chen, Z. G.; Hong, M.; Han, G.; Zou, J. Enhanced Thermoelectric Performance of Nanostructured Bi2Te3 through Significant Phonon Scattering. *ACS Appl. Mater. Interfaces* **2015**, *7* (42), 23694–23699. https://doi.org/10.1021/acsami.5b07596.

(141) Zhang, G.; Wang, W.; Lu, X.; Li, X. Solvothermal Synthesis of V-VI Binary and Ternary Hexagonal Platelets: The Oriented Attachment Mechanism. *Cryst. Growth Des.* **2009**, *9* (1), 145–150. https://doi.org/10.1021/cg7012528.

(142) Liu, X.; Xu, J.; Fang, Z.; Lin, L.; Qian, Y.; Wang, Y.; Ye, C.; Ma, C.; Zeng, J. One-Pot Synthesis of Bi2Se3 Nanostructures with Rationally Tunable Morphologies. *Nano Res.* **2015**, *8* (11), 3612–3620. https://doi.org/10.1007/s12274-015-0861-4.

(143) Kunakova, G.; Galletti, L.; Charpentier, S.; Andzane, J.; Erts, D.; Léonard, F.; Spataru, C. D.; Bauch, T.; Lombardi, F. Bulk-Free Topological Insulator Bi2Se3 Nanoribbons with Magnetotransport Signatures of Dirac Surface States. *Nanoscale* **2018**, *10* (41), 19595–19602. https://doi.org/10.1039/c8nr05500a.

(144) Zhang, Y.; Chang, C. Z.; He, K.; Wang, L. L.; Chen, X.; Jia, J. F.; Ma, X. C.; Xue, Q. K.

Doping Effects of Sb and Pb in Epitaxial Topological Insulator Bi_2Se_3 Thin Films: An in Situ Angle-Resolved Photoemission Spectroscopy Study. *Appl. Phys. Lett.* **2010**, *97* (19), 194102. https://doi.org/10.1063/1.3516160.

Chapter 2

Single Crystalline Germanium Nanocrystals via a Two-step Microwave-assisted Colloidal Synthesis from GeI_4

Zheng Ju,[1] Xiao Qi,[1] Roy Sfadia,[2] Minyuan Wang,[1] Emily Tseng,[1] Sue A. Carter,[2] and Susan M. Kauzlarich[1]*

[1]Department of Chemistry, University of California, Davis, One Shields Ave., Davis, CA 95616, USA

[2]Department of Physics, University of California, Santa Cruz, CA 95064, USA

This work has resulted in one publication that has been submitted to ACS Chemistry of Materials Au. I performed all the synthesis and most of the characterization of the germanium nanocrystals. Collaborators at UC Santa Cruz performed the conductivity measurements. Transmission electron microscopy at the Molecular Foundry was performed by Xiao Qi from UC Davis.

Abstract

Colloidal germanium (Ge) nanocrystals (NC) are of great interest with possible applications for photovoltaics and near-IR detectors. In many examples of colloidal reactions Ge(II) precursors are employed and NCs of diameter ~3 – 10 nm have been prepared. Herein, we employ a two-step microwave-assisted reduction of GeI_4 in oleylamine to prepare monodispersed Ge NCs with a size of 18.9 ± 1.84 nm. More importantly, the as-synthesized Ge NCs showed high crystallinity with single crystal nature as indicated by powder X-ray diffraction, selected area electron diffraction and high-resolution transmission electron microscopy. The Tauc plot derived from photothermal deflection spectroscopy measurement on Ge NCs thin films shows an increased bandgap of the Ge NCs obtained from GeI_4 compared with that from GeI_2 with similar particle size, indicating higher crystallinity of the samples prepared with the two-step reaction from GeI_4. The calculated Urbach energy indicates less disorders in larger NCs. This disorder might correlate with the fraction of surface states associated with decreased particle size, or with the increased molar ratio of ligands to germanium. Solutions involved in this two-step reaction were investigated with ^1H NMR spectroscopy, high-resolution mass spectrometry (MS). Two possible reaction pathways are proposed to unveil the details of the reaction involved GeI_4 and oleylamine (OAm). Overall, this two-step synthesis produces high quality Ge NCs and provides new insight on nanoparticle synthesis of covalently bonding semiconductors.

2.1. Introduction

Ge, with its narrow bulk bandgap of 0.67 eV, can be tuned with the quantum confinement effect by controlling the particle size, has been investigated broadly over decades.[1–3] High carrier mobilities, large absorption coefficient and exciton Bohr radius (~24 nm) make nanostructured Ge a promising candidate for solar energy conversion,[4–7] anode material in lithium batteries,[8,9] optoelectronics[10–12] and bioimaging.[13]

Colloidal methods have been developed for the synthesis of Ge NCs in the past decades. However, a solution-based method with precise control on Ge NCs size and morphology is still a challenge compared with noble metal nanocrystals and Cd- and Pd- based semiconductors, because of the high crystallization temperature required for the formation of diamond structured Ge.[12,14,15] As a result, some of the solution routes reported to date produce amorphous particles or particles with amorphous surfaces that are easily oxidized. To avoid amorphous products, highly reactive reducing agents such as $LiAlH_4$, $NaBH_4$, hydrazine and n-BuLi can be employed to produce crystalline Ge NPs.[12,16–19] The disadvantage of using strong reducing agents is complexity of the synthesis and for those employing a hydride reagent, toxic byproducts.

Ge NCs have been successfully prepared from GeI_2 via a microwave-assisted route that has been shown to be a highly reproducible method.[2,20,21] While size control by employing the mixed halides, GeI_2 and GeI_4, or GeI_2 and halogens has been demonstrated,[3,20,21] the microwave-assisted synthesis of Ge NCs directly from Ge(IV) halides as the single source has not been well-studied to date. This is largely due to the different reduction potential of Ge(II) compared with Ge(IV). The two-electron reduction potential of Ge (II) to Ge (0) is +0.247 V and is easily reduced under mild conditions. On the other hand, the four-electron reduction potential of Ge (IV) to Ge (0) is +0.124 V, suggesting that it is more difficult to reduce and requires more extreme conditions.[3,22]

Even though great progress has been made on the size control of Ge NCs, the crystallinity is not as well developed because of the strong covalent nature of the Ge-Ge bond. The crystallite size calculated from X-ray diffraction (XRD) is commonly reported to be significantly smaller than the particle size measured from transmission electron microscopy (TEM) images.[20,23–27] This observation may be attributed to an amorphous Ge surface giving rise to a larger particle size in TEM images as well as the polycrystalline nature of the NCs. Ge NCs with high crystallinity should be well capped with surface ligands providing fewer defects at the surface and enhancing carrier mobility and photoluminescence and may be further beneficial to the application of various electronics.

Herein, a two-step microwave-assisted solution synthesis route is designed and processed. Pristine Ge NCs with different sizes were synthesized from GeI_4 and investigated with temperature, reaction duration and concentration. As-synthesized Ge NCs are characterized by powder XRD, TEM, scanning transmission electron microscopy (STEM) and selected area electron diffraction (SAED). NMR spectroscopy, high-resolution mass spectrometry (HRMS), and gas chromatography (GC) were applied to analyze and understand the liquid and gas phases of the reaction. This work demonstrates a new route synthesizing single crystalline Ge NCs with enhanced quality which could be further developed for applications. The studies on the two-step reaction provide insight to improve the nanocrystal synthesis not only for Ge but also for other metal or semimetals.

2.2. Experimental Methods:

2.2.1. Chemicals

Germanium (IV) and (II) iodides, GeI_4, and GeI_2, were purchased from Prof. Richard Blair's laboratory (University of Central Florida) and confirmed to be phase pure from powder XRD.[21] Oleylamine (OAm, (Z)- octadec-9-enylamine, technical grade, >50%, TCI America) was degassed under vacuum for longer than 2 hours at 150 °C before use. Methanol, toluene (HPLC grade, Fisher Scientific) were purified using a solvent purification system and stored in a glovebox under argon.

2.2.2. Two-step Synthesis of Ge NCs

Microwave heating was applied to all Ge NCs reactions by employing a CEM microwave reactor (Discover SP) under dynamic mode. GeI_4 stock solution (35 mM) was prepared by dissolving 1.2 g (2.1 mmol) of GeI_4 in 60 mL OAm and stirring in an Ar-filled glove box for a few days. The as-made colorless solution was kept in the glove box until used in reactions. Different concentration stock solutions were prepared following the same process.

In a typical synthesis of OAm-capped Ge NCs, 6 ml of the prepared GeI_4 stock solution was transferred into a 35 mL borosilicate microwave tube (purchased from CEM Corporation). In the first step of a reaction, the microwave tube with the solution, sealed with a CEM Teflon cap, was removed from the glove box and heated to 250 °C in the microwave reactor with a maximum heating power of 150 W. After 40 min at 250 °C, the microwave tube was automatically cooled to 60 °C by the reactor and a clear light-yellow solution was observed. Since the microwave cap is not fully airtight, to avoid any contamination with the air, the tube with the as-made yellow solution was parafilmed and transferred into the glove box. Parafilm is moisture resistant but has gas permeability. Thus, during the vacuum, the gases in the headspace should be removed. The microwave tube cap was removed, and 2 mL of the as-prepared yellow solution was transferred to a clean and dry microwave tube. The 2 mL yellow solution was then transferred out and heated to 260 °C for 30 min also with a maximum power of 150 W to finish the synthesis. A caramel brown colored solution was obtained. Samples for device fabrication were synthesized slightly different as described in the following section. To isolate the Ge NCs, the microwave tube containing the final product was transferred to an argon-filled glovebox.

In the glove box, the brown colored solution was transferred into a 50 mL centrifuge tube and 2 mL of anhydrous toluene and 3 ml of anhydrous methanol as an antisolvent were added. For the samples with smaller particle size, a total of 10 ml of anhydrous methanol was required for the isolation. The solution in the centrifuge tube was taken out and centrifuged at 5000 rpm at room temperature for 3 min, then the tube was transferred back into the glove box and the pale yellow or pale brown supernatant was discarded. This wash process was carried out two more times in order to fully remove extra free OAm ligands and other impurities. The final precipitation was well dispersed in 1 ml toluene and kept in the glove box for further characterizations. For some characterization, the supernatant after the second step was acquired. After reacted at 260 ^{o}C, the as-prepared brown colored solution was directly transferred into centrifuge tube in the glove box and then transferred out and centrifuged at 5000 rpm for 5 min. The Ge NCs could be precipitated, and a pale-yellow solution was obtained for further characterization.

GeI_2-reduced Ge NCs (10 nm). The method was modified from previous work.[21,23] 0.2 mmol of GeI_2 was dissolved in 6 ml of degassed OAm by stirring in the glove box overnight. A yellow solution was obtained once the GeI_2 fully dissolved. The obtained solution was then microwave heated to 260 ^{o}C with 150 W applied power. After 60 min reaction, the obtained dark brown colored solution was isolated by the method described above.

GeI_4-reduced Ge NCs (10-nm). 6 ml of as-prepared 35 mM GeI_4/OAm stock solution was transferred into a 35 ml microwave tube. The solution went through a two-step reaction as described above except a set temperature of 240 ^{o}C was applied for the second step. A selective isolation was carried out. In the glove box, the as-obtained brown solution was transferred to a centrifuge tube without adding any solvents. The centrifuge tube was pumped out and centrifuged at 3000 rpm for 3 min followed with the same isolation as described above.

GeI_4-reduced Ge NCs (18-nm). 6 ml of as-prepared 35 mM GeI_4/OAm stock solution followed the procedure above for the two-step reaction. We kept the volume as 6 ml for the second step at 260 °C for 30 min. The same isolation process was carried out.

2.2.3. Characterization

Ge NCs products were characterized by XRD, TEM, STEM, selected area electron diffraction (SAED), NMR spectroscopy, high-resolution mass spectrometry (HRMS) and gas chromatography (GC). The Ge NCs were prepared into thin films and measured with photothermal deflection spectroscopy (PDS) and photo current.

X-ray Diffraction (XRD). XRD patterns were obtained by drop-casting and drying the toluene dispersion of prepared Ge NCs on quartz substrate holder. The obtained dark brown thin film was then scanned using Bruker D8 Advance diffractometer (Cu-Kα, 40 kV, 40 mA, $\lambda = 1.5418$ Å) with a two theta range of 10° – 80°.

Transmission Electron Microscopy (TEM) and Dark-field Scanning Transmission Electron Microscopy (DF-STEM). Both TEM and DF-STEM samples were prepared by drop-casting the dilute dispersion of Ge NCs in toluene onto lacey carbon supported by a 400 mesh copper grid (Ted Pella). The grids were dried completely to avoid carbon contamination of the vacuum chamber during electron beam irradiation. TEM/DF-STEM images were acquired using a FEI ThemIS 60−300 STEM/TEM (Thermo Fisher Scientific, US) operated at 300 kV at the National Center for Electron Microscopy within the Molecular Foundry in Lawrence Berkeley National Laboratory. The ThemIS is equipped with image aberration corrector optics, and a Ceta2 camera (4k × 4k pixels, and 14-bit dynamic range).

NMR Spectroscopy. Samples for ^{1}H NMR were prepared by transferring 50 µL of sample solution and mixing with 600 µL of $CDCl_3$ solvent under an inert atmosphere. ^{1}H NMR spectra were obtained at room temperature on a 400 MHz Bruker Advance IIIHD Nanobay Spectrometer. Chemical shifts were referenced to residual undertreated $CHCl_3$ (7.26 ppm).

Gas Chromatography (GC). A Varian 3800 GC was used to identify the gases produced during the reaction. The instrument is equipped with a thermal conductivity detector and a Carboxen 1010 PLOT fused silica column (30 m × 0.53 mm) (Supelco) using nitrogen (99.999%, Praxair) as the carrier gas. The microwave tubes were parafilmed. 2 µL of gas was taken and injected into the GC by a borosilicate glass syringe.

High-Resolution Mass Spectrometry (HRMS). As prepared solvents or solutions were analyzed by flow-injection analysis into a Q-Exactiv HF Orbitrap (Bremen, Germany) operated in the centroid mode. Samples were injected into a mixture of 50% methanol and 0.1% formic acid/H2O at a flow of 200 µL/min. Source parameters were 4.5 kV spray voltage, the capillary temperature of 275 °C, and sheath gas setting of 20. Spectral data were acquired at a resolution setting of 100,000 FWHM with the lock mass feature, which typically results in a mass accuracy <2 ppm.

Photothermal Deflection Spectroscopy (PDS). Samples were prepared in a nitrogen glovebox. Thin-film samples were prepared by spin-coating the Ge NC colloidal solution on a glass substrate, at 400-1000 RPM for 60 s. While details of this system are similar to previously reported procedures,[23,37] what follows is a brief description of this spectroscopy technique. The thin-film was placed securely in a quartz cuvette filled with Fluorinert FC-72 (3M). Light from a tungsten halogen arc lamp was used to pump the sample. The light was chopped at 5 Hz and scanned from 2.1 eV to 0.6 eV, in steps of 0.01 eV, by using a Princeton Instruments Acton monochromator, resulting in a pumping signal with a full-width-half-maximum of 15 nm. Using a beam splitter, this pumping light was partially sent into a reference detector, for signal scaling purposes, and partially made to be incident on the sample, normal to the substrate. A 2 mW He–Ne 633 nm laser (JDSU) was aligned parallel to the surface of the sample and used as a probe beam. As the modulated pump beam excites the sample, heat from nonradiative relaxation causes the probe beam to be deflected. The deflection was registered with a Thorlabs PDP90 position-sensitive detector, whose signal was read by a lock-in amplifier to reduce noise and allow for high-sensitivity absorption measurements The absorbance is given by the expression

$$\boldsymbol{\alpha = -\frac{1}{d}\ln\left(1 - \frac{V_{sig}}{V_{ref}} C_{norm}\right)} \qquad \textbf{Equation 2.1}$$

where α is the absorption coefficient, d is the sample thickness, V_{sig} is the signal amplitude from the PSD, V_{ref} is the signal from the reference detector, and C_{norm} is a normalization constant. Bandgap estimates were made through linear fits on the Tauc plot $(\alpha\cdot E)^{1/n}$ vs E, where E is the photon energy, and n is a constant that is ½ for direct semiconductors and 2 for indirect semiconductors. The x-intercept of the linear fit of the mid-gap region provides an estimate of the bandgap energy. Urbach energy, a characterization of the collective disorder in the system, was found by fitting to the relation $\alpha \sim \exp(\frac{E}{E_{Urbach}})$ in the mid-gap region. In practice, the Urbach energy is obtained through a linear fit of $\ln(\alpha)$ vs E, where the best-fit slope is $1/E_{Urbach}$.

Device Fabrication and Photo-current Measurement. All devices were prepared indium tin oxide-patterned glass substrates (Thin Film Devices, Inc.). Substrates were cleaned with alconox and deionized water before being placed in fifteen-minute sonication baths of first acetone and then isopropyl alcohol. The compact blocking-layer TiO_2 layer (Solaronix, Ti-nanoxide BL150/SP) was doctor bladed onto the ITO. It was then dried on a 115 ^{o}C hot plate for five minutes before being sintered in an oven at 500 ^{o}C for 30 min. Next, the mesoporous TiO_2 layer (Solaronix, Ti-nanoxide T165/SP) was applied, dried, and sintered in the same manner. Next, the Ge NCs solutions were spin-coated atop the TiO_2 layers in a nitrogen-filled glovebox at 400 RPM for 45 s. After being dried on a hot plate at 60 – 80 C for 5 min, the devices were placed in a thermal evaporation chamber built into the glovebox to avoid oxygen exposure. Approximately 60 – 80 nm of Ag (Kurt J. Lesker) was patterned on our devices at a rate of 1 Å/s. Current density-voltage measurements awerere made using a Keithley 2400 source meter. During light measurements, devices were exposed to light from a solar simulator (Oriel) passing through an AM1.5 filter. All device measurements were made in the glovebox.

2.3. Results and discussions:

2.3.1. Syntheses and characterizations

OAm, a primary unsaturated amine with a high boiling point of 350 ^{o}C, is widely applied in the synthesis of various nanomaterials.[28] It is a versatile solvent that can serve as both a reducing agent and passivating ligands. Compared with shorter chain amines, one advantage of OAm is that it stays in liquid form at room temperature which simplifies the purification process after the synthesis.[28] While the as-received OAm may contain trans isomers over 43 %,[29] in this work, there were no noticeable differences in products obtained using OAm with different grades of purity.[21] Herein, we used OAm of over 50 % purity with a further degassing process. Ge NCs have been successfully synthesized through a variety of colloidal routes, most of which employ the reduction of Ge(II) containing molecules, mostly the halides.[3,20,30] OAm can reduce GeI_2 to form Ge NCs at temperatures slightly above 200 °C.[3,20] However, to my knowledge, no studies to date have demonstrated a successful reduction of Ge(IV) reagents with OAm alone to form Ge NCs.

In this work, we designed a two-step microwave assisted colloidal reaction to prepare highly crystallized Ge NCs by the reaction of OAm and GeI_4. In a typical synthesis of Ge NCs, 6 ml stock solution (35 mM) was firstly heated by CEM microwave at 250 °C for 40 minutes. A power of 150 W was applied on both steps to provide a moderate ramping rate. A pressure of 40 psi was detected in the microwave tube indicating the formation of gases during the synthesis process. We noticed the pressure produced is correlated with the process of this step. A light-yellow solution obtained after the first step indicated the possible formation of a Ge(II) species. We didn't observe significant Tyndall effect nor any nucleation of Ge particles under TEM.

The yellow solution was pumped in and out of the glove box and then microwave heated to 260 °C and held for various lengths of time. After cooling to room temperature, a brown colored solution indicated the successful formation of Ge NCs. The product was isolated by the widely used solvent/nonsolvent method as described in the experimental methods section. The precipitated product is dispersed in toluene for further characterization.

Reactions were stopped at 5, 15 and 30 min at 260 ^{o}C in the second step to determine the growth process. Brown colored products were obtained in all reactions. Representative dark-field STEM (DF-STEM) images of different reaction times are shown in Figure 2.1a-2.1c. The particles size becomes larger and size distribution smaller with longer reaction time in the second step. At the early stage (5 min reaction), both small (~6 nm) and large (~18 nm) particles were observed which indicates the growth process is in progress and nucleation happens immediately. With a longer reaction time (15 min and 30 min), there are large particles while the amount of the small particles decreased. The uniformity and size all increased as the reaction proceeds while the small particles (<10 nm) disappeared. This result indicates an Ostwald ripening process where the large particles grow at the cost of the small ones. No small particles observed after 30 minutes indicating the nucleation process was terminated at certain point during the reaction. Over 200 Ge NCs were selected randomly to calculate the size distribution histograms of these three different stages as shown in Figure 2.2. The 30-min reaction gave a large average size and narrow dispersity range of 18.9 ± 1.84 nm. The as-synthesized NCs show explicit particle edges in the DF-STEM image. The quality of these images is significantly improved compared with our previously published work where NCs obtained by reducing GeI_2 in OAm. Particles prepared wth GeI_2 in OAm show vague edges around the particles in the DFTEM images which can be attributed to the amorphous layer on the surface of the NCs.[23,24,30] Similar results are also reported in several other studies on solution synthesized Ge NCs, demonstrating the difficulties of making Ge NCs with high crystallinity.[3,31] The corresponding selected area electron diffraction (SAED) pattern (inset of Figure 2.1c) matches the expected pattern for the crystalline diamond cubic structure of Ge. The high intensity of the SAED rings further verifies the high crystallinity of the NCs. High resolution transmission electron microscopy (HRTEM) (Figure 2.1d) shows clear lattice fringes on several NCs without any interfaces indicating the single-crystal nature and the d-spacing was calculated to be 0.335 nm which is consistent with the lattice spacing of diamond cubic Ge (111) phase. Atomic resolution TEM image (inset of Figure 2.1d) of one Ge NC also demonstrates the high crystallinity and single crystal nature. Other high resolution TEM images are provided in Figure 2.3. Most of the as-synthesized Ge NCs are single crystal with some NCs showing lattice interfaces indicating a possible twin defect in the NC.

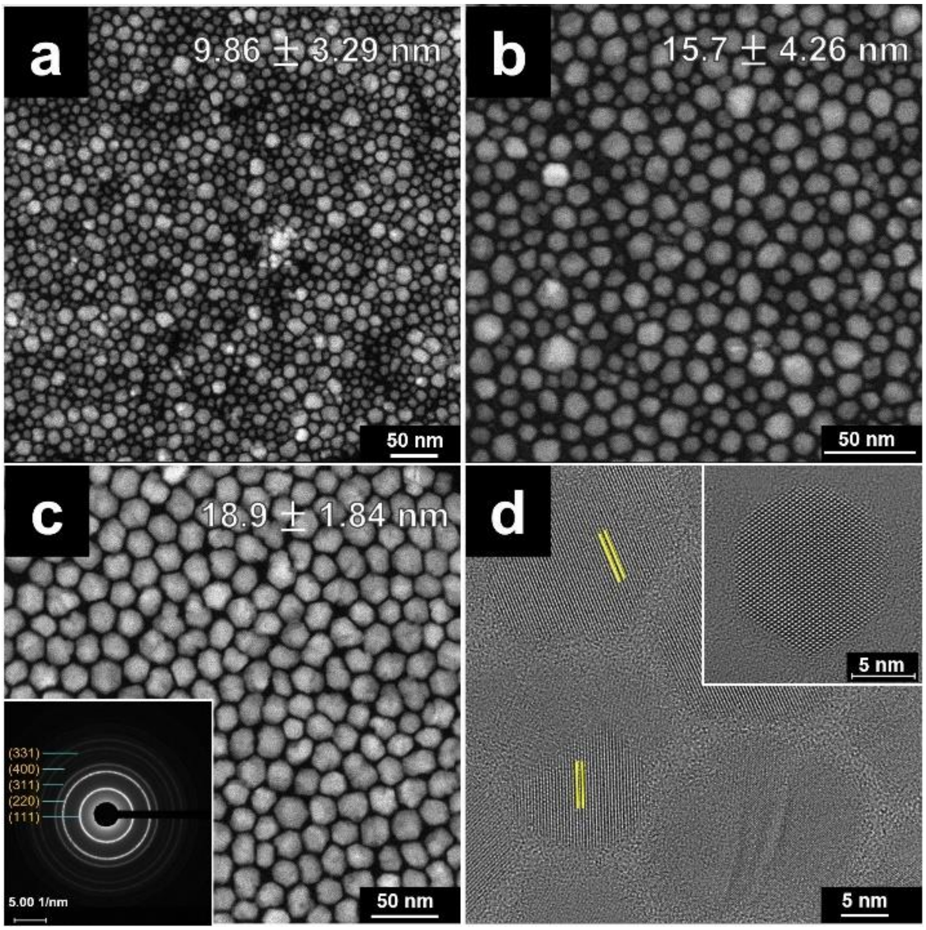

Figure 2.1 DF-STEM images of two-step reactions stopped at different time at the second step, (a) 5min, (b) 15 min, (c) 30 min. Inset of (c) is the SAED image of Ge NCs, sharp diffractions are assigned to the cubic Ge phase. (d) HRTEM image of 30 min reaction shows high crystallinity and single crystal nature of as-synthesized Ge NCs. Inset is an atomic resolution image. Upper right corner of panels in (a)-(c) show the particle size and standard deviation of the statistics over 200 particles.

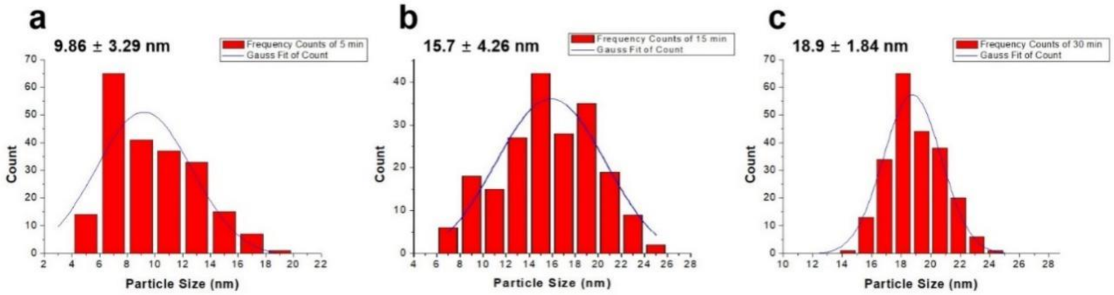

Figure 2.2 Size distribution histograms for two-step reactions stopped at different time at the second step, (a) 5min, (b) 15 min, (c) 30 min.

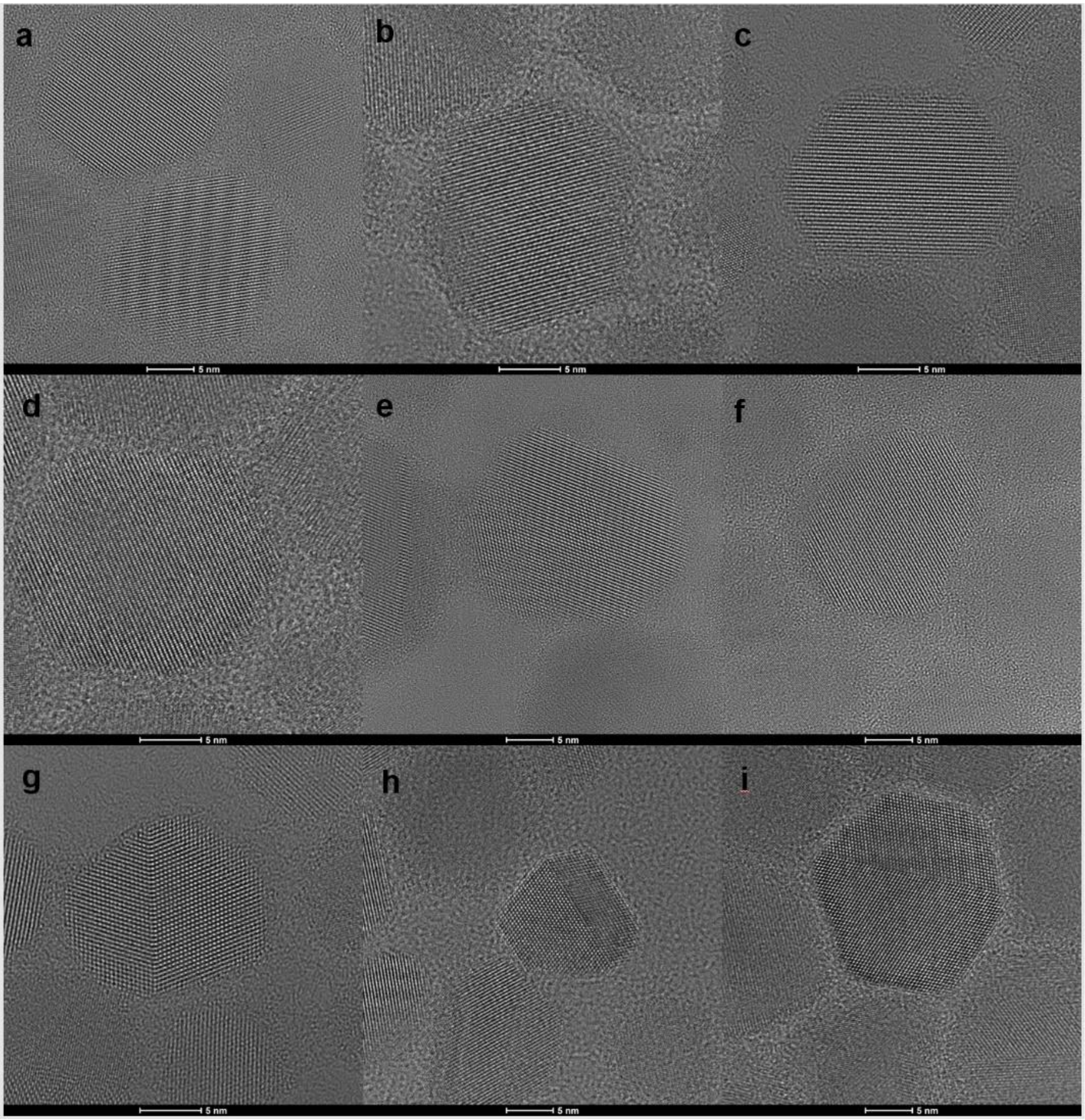

Figure 2.3. High resolution TEM images of Ge NCs by a two-step reaction. (a)-(f) images show the single crystal nature of the as-synthesized Ge NCs. (g)-(i) Some NCs also show a twin defect within the lattice.

The PXRD pattern (Figure 2.4) shows a pure phase of cubic diamond structured Ge NCs. Diffraction peaks at 27.3, 45.4, 53.8, 66.1 and 72.9° two-theta correspond to the (111), (220), (311), (400) and (331) lattice planes, respectively. The sharp peaks and high signal to noise ratio indicate the high crystallinity of the as-synthesized Ge NCs. The crystallite size is calculated by Scherrer Equation on the peak broadening of (220) peak instead of (111) to eliminate errors from peak asymmetry and background removal.[21,32] A crystallite size of 16.5(3) nm obtained by Scherrer equation is very similar as the particle size calculated by TEM. As the Scherrer equation tends to underestimate the particle size when prominent size dispersions exist, the similar particle sizes calculated by two different methods indicates the high crystallinity and monodispersity of the Ge NCs prepared by this method.[32,33]

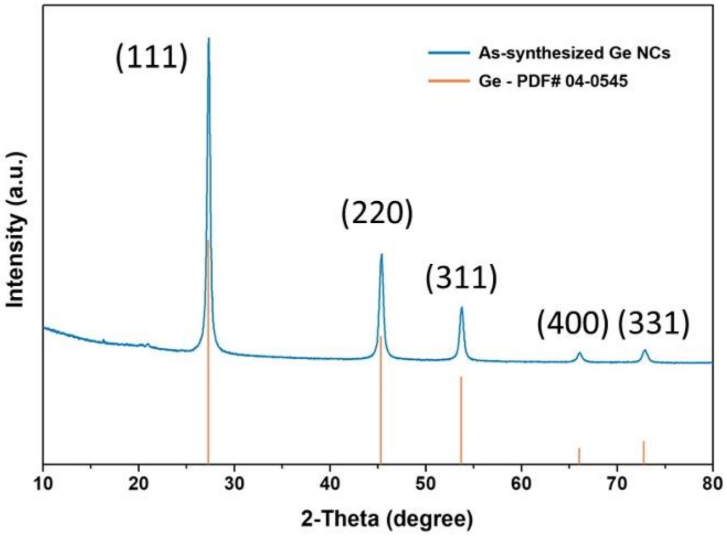

Figure 2.4. PXRD pattern of the Ge NCs synthesized at 260 °C for 30 minutes compared to the reference pattern (PDF #04- 0545) showing the (111), (220), (311), (400), and (331) reflections of cubic Ge.

To compare with the two-step reactions, a one-step reaction of the same amount of GeI_4 stock solution was carried out by microwave-heating at 250 °C. After one-hour holding at the set-temperature, dark brown to black colored product was obtained. This reaction shows that GeI_4 can be reduced by OAm without the assistance of any other reducing agents. The dark color indicates a large particle size of the Ge NCs. The same isolation process as described above was followed. Rather than well dispersed NCs, the TEM images of the product (Figure 2.5a) show agglomerates of around 100 nm in diameter. The as-synthesized sample is unable to form a stable colloidal solution which is attributed to the poor ligand capping and thereby formation of agglomerates. The agglomerates are formed with many small crystalline nanoparticles as shown in Figure 2.5b. This suggests a fast nucleation process as well as poor ligand capping. While the reaction happens in a short period with continuous heating, the small Ge NCs formed at the early stage aggregate together directly rather than continuing to grow into larger NCs. Similar results were reported in other work involving GeI_4.[3,21] The advantage of the two-step reaction is that it prevents the uncontrolled aggregation and provides a homogenous Ge NCs colloid.

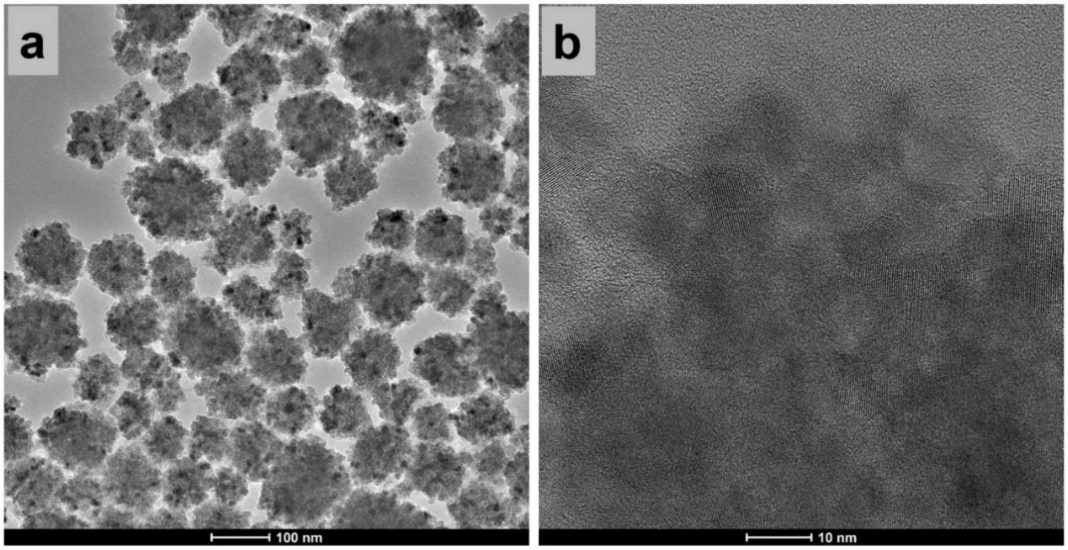

Figure 2.5. (a) TEM image of a one-step reaction with GeI_4 and OAm shows large agglomerates with a size around 100 nm. (b) HRTEM image of (a) shows the large agglomerate is formed by the aggregation of highly crystalline small particles.

To investigate the relationship between concentration and particle growth various concentrated stock solutions (17.5, 35, and 70 mM) were prepared as described in the Experimental Section. The same reaction process was carried out on these different concentrated stock solutions. The reactions were all held at the set temperature for 30 min for the second step. We noticed that with higher concentration, it took shorter time to reach the set temperature in both steps. The relation of time required to reach the set temperature *versus* the solution concentration of both first and second steps are plotted in Figure 2.6a. Heating profiles of these reactions are plotted in Figure 2.6b. It has been shown that the nonpolar OAm is a poor microwave absorber.[20,21] The heating rate of the solution relies on the type and concentration of precursors and the volume of solution. GeI_4 has been observed to be a better microwave absorber than GeI_2 due to the formation of ionic and possibly polar species. In this work, the same volume of OAm solvent is used in all parallel reactions and GeI_4 serves as the single Ge source. Thus, the heating rate is controlled by precursor concentrations.

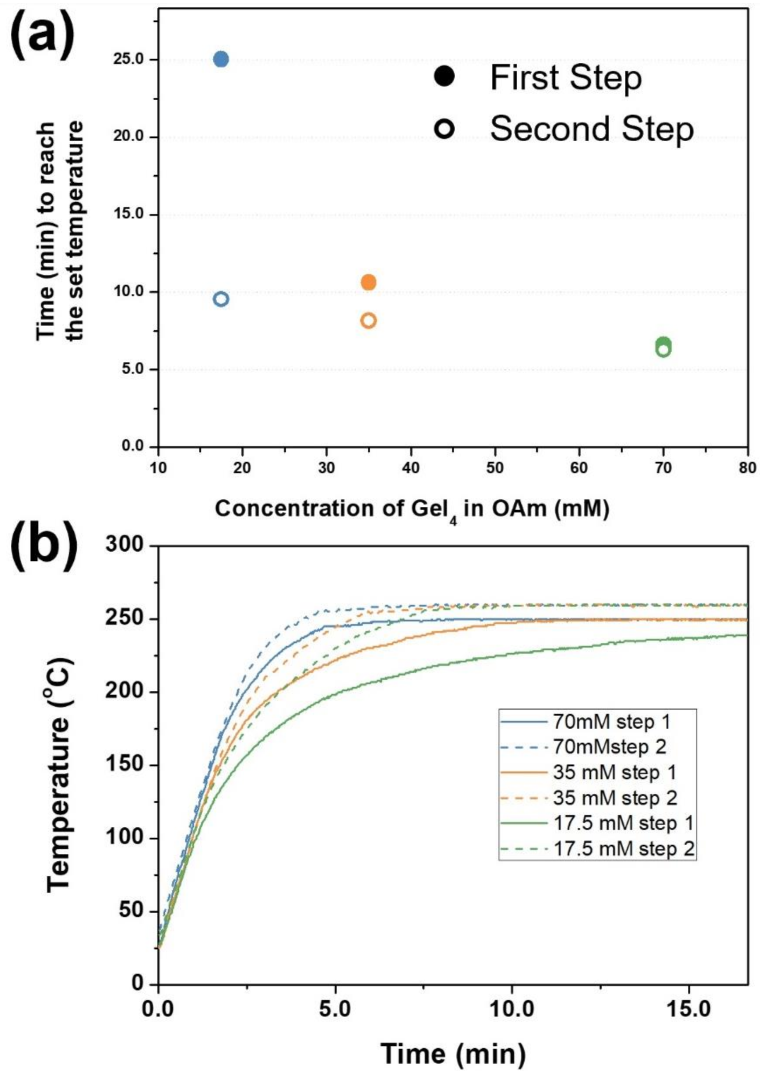

Figure 2.6. (a) Time required to reach 250 °C for the first step and 260 °C for the second step versus different concentrations of GeI_4 OAm solution. (b) Temperature profiles for microwave heating of reactions with different concentrations of GeI_4.

To obtain a yellow solution after the first step, we noticed different holding times are required for different concentrated solutions. Holding times of 20 minutes, 40 minutes, and 80 minutes were applied on double (70 mM), standard (35 mM) and half concentrated (17.5 mM) solutions during the first step of the reaction. As shown in Figure 2.7, the as-prepared solutions show color differences from dark to light yellow with decreasing stock solution concentration. The yellow solutions were transferred into the glove box and 2 ml of the obtained yellow solution was transferred out in a capped microwave tube for the next reaction step.

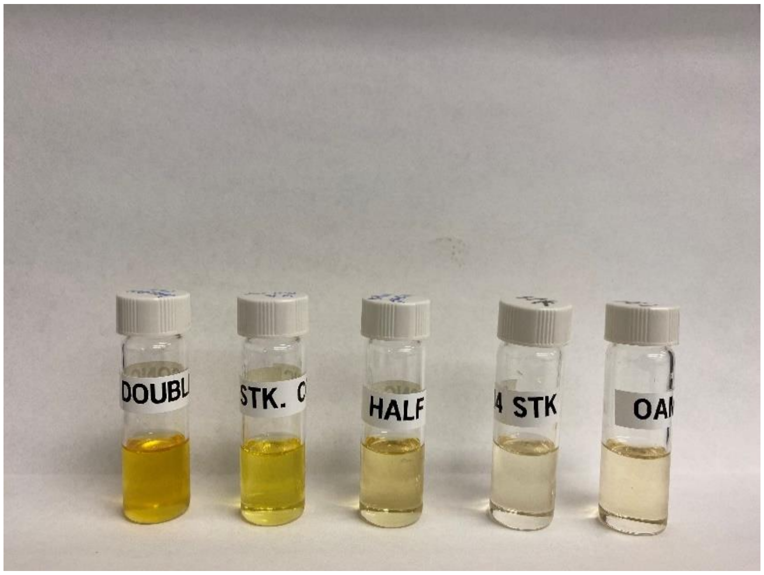

Figure 2.7. Solutions from left to right: double concentrated GeI_4 solution after first-step reaction; standard concentrated GeI_4 solution after first-step reaction; half concentrated GeI_4 solution after first-step reaction; a GeI_4 stock solution and a degassed OAm solvent as references.

The tubes were microwave-heated and held at 260 °C for 30 min, and products were synthesized and isolated from all three concentrations. Figure 2.8 displays the DF-STEM images of Ge NCs synthesized with different GeI_4 concentration stock solutions after the second step. Statistic histograms are reported in the Figure 2.9. Half concentrated stock solution (17.5 mM) gave a NCs average size of 11.9 ± 1.89 nm, much smaller than that of standard concentrated (35 mM) solution (18.9 ± 1.84 nm). This result suggests that the lower concentration solution contains less molecular precursors which reduces the growth rate and in turn limits the particle size. With the same reaction time of the second step, the particle size distribution range of the sample prepared from the half-concentrated solution is wider than that from the standard concentration. This observation on the sample prepared from the half-concentrated solution indicates that the growth process is slow and not finished after 30 minutes due to the low concentration of molecular precursors. We extended the reaction time to 45 minutes for the second step of the half-concentrated sample. The NC size increased to 14.5 nm, and the size dispersity also improved to a narrower range indicating an Ostwald ripening process in this step. The DF-STEM image and corresponding histogram were shown in Figure 2.10. Interestingly, the particles from the double concentrated (70 mM) solution were aggregated together (Figure 2.8c) and shows a similar structure and morphology to that of particles synthesized by one-step reaction (Figure 2.5a). High concentration stock solution kinetically improved the reaction rate. However, a fast nucleation and growth rate caused the particles formed with poor lattice alignment and ligand capping. And the small particles aggregated to make large agglomerates with sizes over hundreds of nanometers.

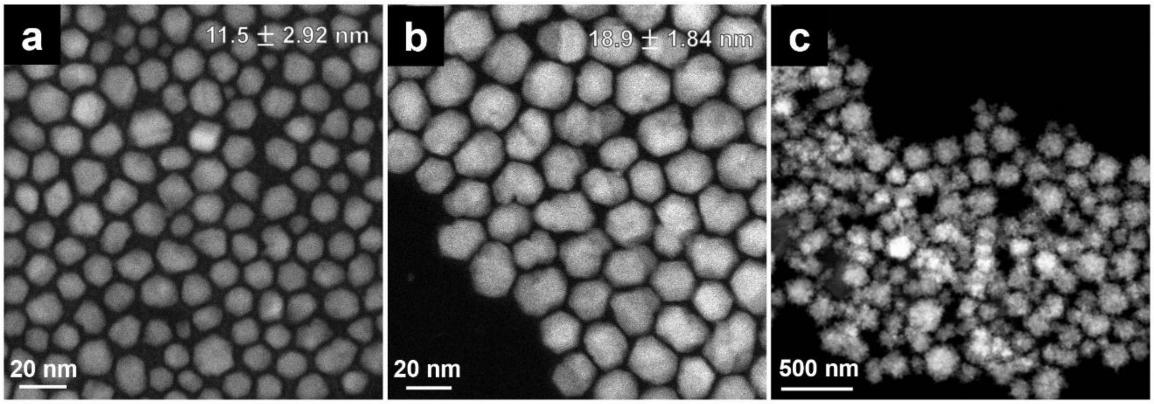

Figure 2.8. The DF-STEM images of Ge NCs synthesized with different GeI_4 concentration stock solutions after the second step at 260°C for 30 minutes. Stock solutions with GeI_4 concentration of (a) 17.5 mM, (b) 35 mM and (c) 70 mM.

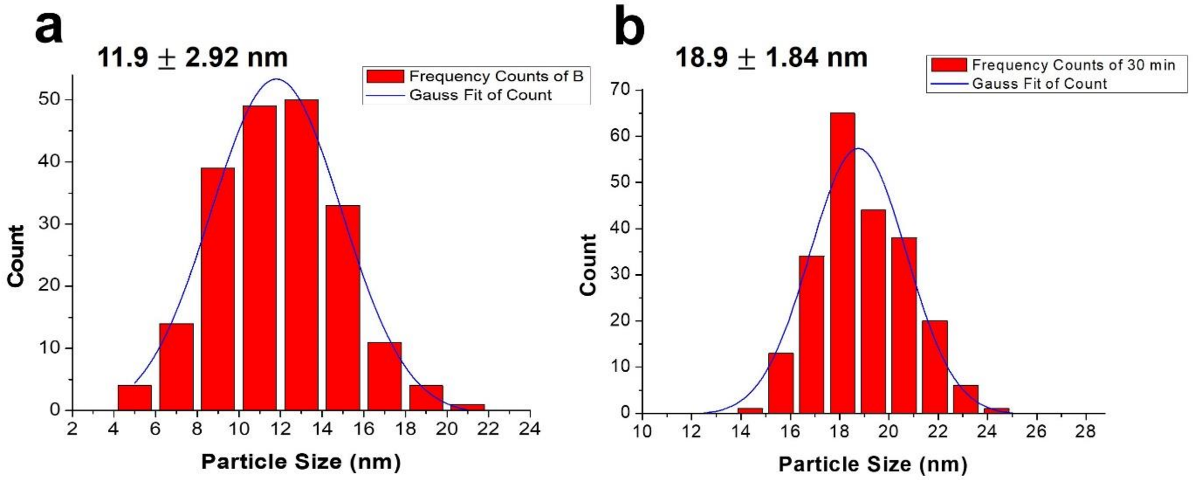

Figure 2.9. Size distribution histograms for Ge NCs synthesized with different GeI_4 concentration stock solutions after the second step at 260°C for 30 minuntes. (a) 0.2 mmol of GeI_4 in 6 ml OAm. (b) 0.4 mmol of GeI_4 in 6 ml OAm.

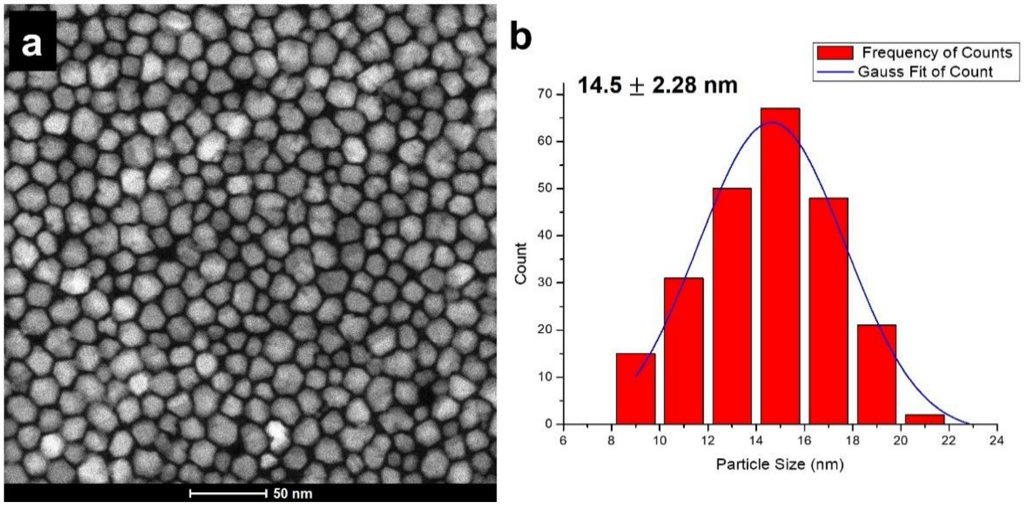

Figure 2.10. The (a) DF-STEM image and (b) corresponding histogram of the half concentrated GeI_4 solution running with an extended second step of 45 minutes.

Reactions with different times and concentration were explored as discussed above. Increasing the reaction time for a solution with a suitable concentration moderated the growth and ripening of the Ge NCs. Another factor that may affect the growth of the nanoparticle is the temperature. Here, different reaction temperatures for the second step were investigated to further understand the nucleation and growth process. Besides 260 ^{o}C, reactions were carried out at 240^{o}C, 220 ^{o}C, 200 ^{o}C, 180 ^{o}C and 160 ^{o}C for the second step. In order to provide enough reaction time for particle ripening at lower temperatures, samples were all held 45 minutes for these temperatures. Brown colored products were all successfully obtained indicating the nucleation and growth could happen at temperatures as low as 160 ^{o}C. However, the yield of Ge NCs after 45 min at 160 ^{o}C is very low. This low temperature for nanoparticle formation was also recently reported for the thermolysis of a bis(amidinato)germylene(II) complex and suggests that these species might be present in the reaction mixture after the initial heat treatment.[34] To our knowledge, this is the first example of Ge NCs being prepared at a temperature lower than 200 ^{o}C without any additional reducing agents in solution and suggests further research to determine whether small molecular clusters may be participating in this reaction as is noted for other semiconductor nanoparticle growth, such as the case of InP.[35]

Figure 2.11 displays Ge NCs synthesized at different temperatures with corresponding histograms shown in Figure 2.12. The particle size increases with higher heating temperature. When the temperature is lower than 220 ^{o}C, aggregation occurs as shown in Figure 2.11c and 2.11d, which is attributed to the poor surface capping of OAm. The capping of OAm on Ge has been studied by NMR and OAm on the surface of Ge is transformed from an L-type amine ligand to the stronger X-type of oleylamide, the fraction of which increases with increasing temperatures.[36] The stronger binding X-type ligands result in more stable capped NCs and colloidal suspensions. The particle boundaries became indistinct at low temperatures indicating that either insufficient heating produced an amorphous Ge surface, or possibly that the dative bonding of the L-type ligand allows for surface reconstruction by reaction with oxygen/water and thereby amorphization. The NCs synthesized at 240 and 220 ^{o}C show high crystallinity and single crystal nature as shown in the inset images. With a different reaction temperature for the second step, we can tune and control the size of the synthesized particles.

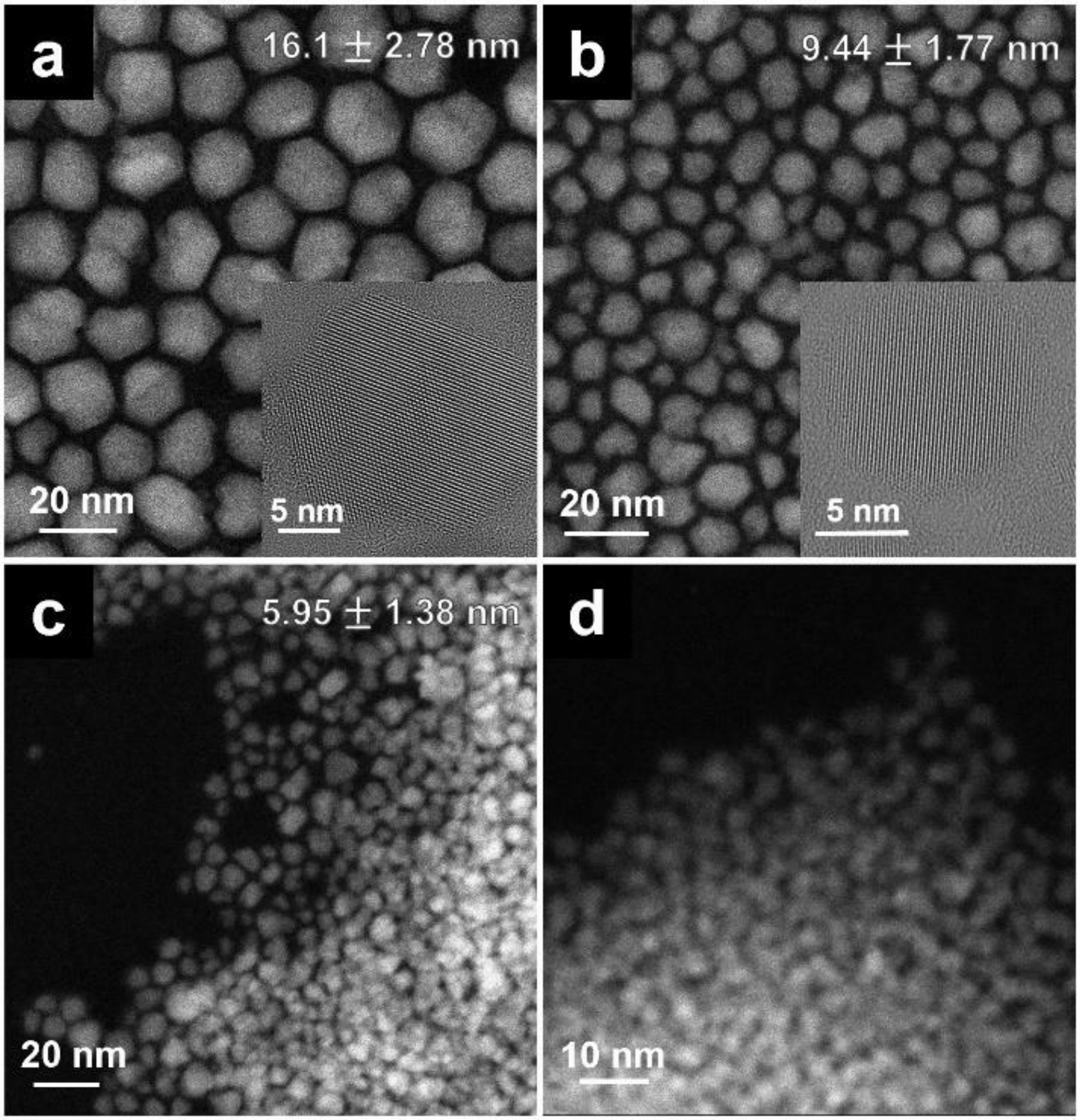

Figure 2.11. The DF-STEM images of Ge NCs synthesized at different temperature for the second step. (a) 240 °C. (b) 220 °C. (c) 200 °C. (d) 180 °C.

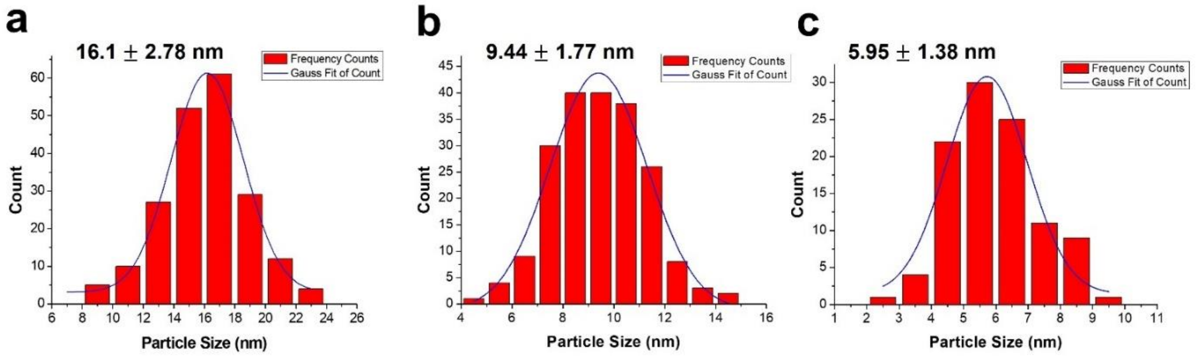

Figure 2.12. Size distribution histograms of Ge NCs synthesized at different temperature for the second step. (a) 240 °C. (b) 220 °C. (c) 200 °C.

2.3.2. Photothermal Deflection Spectroscopy (PDS) and Photocurrent Measurements

Photothermal deflection spectroscopy (PDS) is used as a sensitive measurement of band-to-band absorbance. In brief, the thin-film is placed securely in a quartz cuvette filled with Fluorinert FC-72 (3M).[23,37] The sample's surface is then aligned with the probing beam of a 2 mW He-Ne laser. Normal to the surface, the sample is pumped by monochromatic light modulated at 5 Hz. This modulation allows the sample's optically excited charge carriers to non-radiatively relax and release heat. This heat is absorbed by the Fluorinert, which is known for having an index of refraction that is sensitive to temperature. Therefore, the heat released by increased absorbance leads to the probing beam's path through the cuvette deviating further from a straight line, and this deviation is measured by a position sensitive light detector. This allows for an indirect measurement of absorption, without interference from reflected or scattered light.

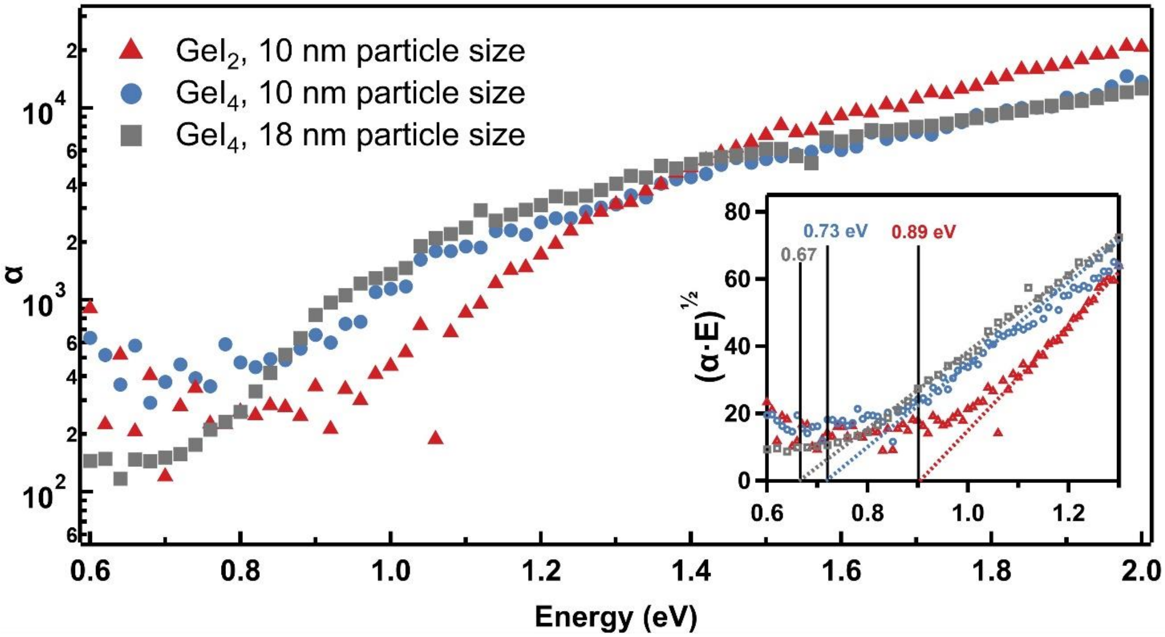

Figure 2.13. PDS measurements of 10 nm GeI_2-reduced, 10 nm GeI_4 reduced and 18 nm GeI_4 reduced Ge NCs. Inset is the Tauc plot with the estimation of indirect bandgaps of these three Ge samples.

To investigate how improved crystallinity affects the optoelectronic properties of the Ge NCs, neat thin-films of GeI_2-reduced NCs and GeI_4-reduced NCs were prepared for photothermal-deflection spectroscopy (PDS), as shown in Figure 2.13. The GeI_2-reduced NCs with an average size of 9.76 ± 1.98 nm were synthesized following published work and described with details in Experimental Section.[20,23] The GeI_4-reduced NCs were synthesized *via* the two-step reaction reported in this work. Two samples of GeI_4-reduced NCs were measured to be 10.2 ± 2.21 nm and 18.1 ± 1.78 nm, respectively. The DF-STEM images of Ge NCs measured with PDS are shown in Figure 2.14. Corresponding XRD patterns of these three samples were presented in Figure 2.15 and the crystal sizes were calculated with Scherrer Equation. Even the 10 nm Ge NCs from GeI_2 and GeI_4 gave a similar particle size, the broader peaks in the XRD pattern of GeI_2 sample indicates a possible smaller overall crystal size or more defects in the NCs. This result could be attributed to a higher degree of the amorphization of the Ge NCs surface of GeI_2 sample.

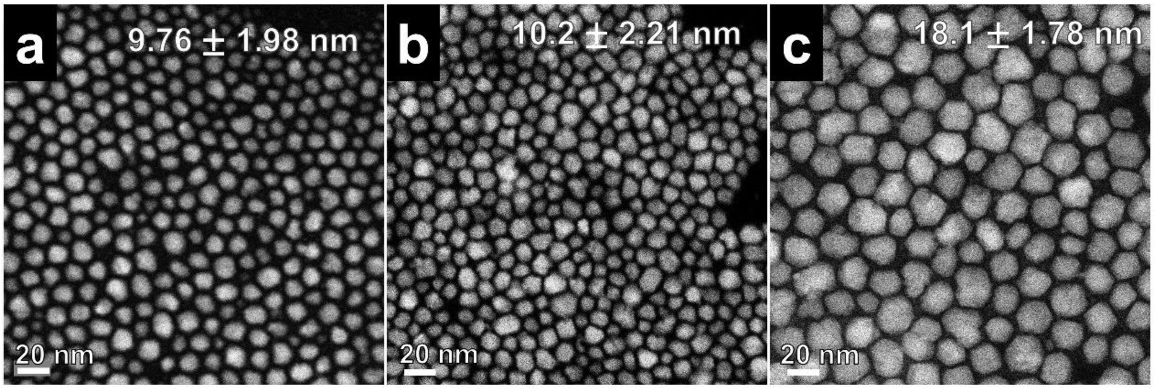

Figure 2.14. HR-STEM images of (a) 10 nm GeI_2-reduced Ge NCs from a modified one step reaction and (b) 10 nm GeI_4 reduced and (c) 18 nm GeI_4 reduced Ge NCs synthesized by the two-step reaction reported in this work.

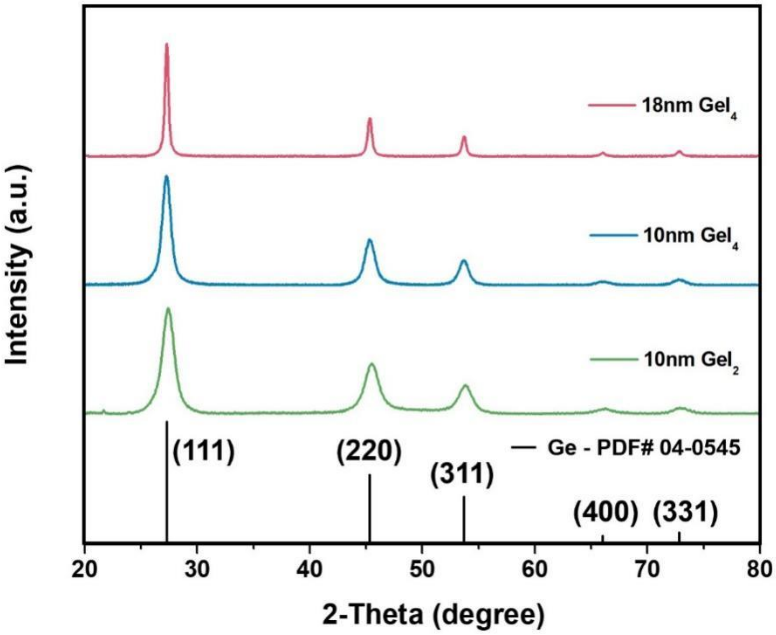

Figure 2.15. XRD patterns of 10 nm Ge NCs reduced from GeI_2 and GeI_4 and 18 nm Ge NCs reduced from GeI_4. the corresponding crystal sizes are 7.2 nm, 9.1 nm and 17 nm, respectively from the Scherrer equation.

Bandgap estimates were made through linear fits of a Tauc plot by $(\alpha \cdot E)^{1/2}$ for indirect semiconductors. The x-intercept of the linear fit of the mid-gap region provides an estimate of the bandgap energy. Fits to Tauc plots indicate the energetic bandgap to be 0.89 ± 0.05 eV for GeI_2 NCs and 0.73 ± 0.03 eV for GeI_4 NCs with similar particle sizes around 10 nm (Figure 2.13 inset). The simulated bandgap of Ge NCs from GeI_2 matches well with the reported data of Ge NCs with similar sizes.[23,38] While the particle sizes in each sample were similar, the GeI_2 NCs have a smaller crystalline core which is attributed to the less crystallinity and amorphous layer on the surface, decreasing the effective confined space an electron experiences and thus increasing the bandgap in the material. The more bulk-like bandgap of the GeI_4 NCs indicates that the quantum confinement effects associated with NCs is strongly dependent on the crystallite size, as measured by XRD, rather than the particle size measured in TEM. Tauc fits to the larger 18 nm GeI_4 samples show a more bulk-like bandgap of 0.67 eV ± 0.02 eV. The increased accuracy for our larger-sized samples is likely due to the narrower size distribution found above, as described above. *Ruddy et al.* showed similar bandgap trends with increasing particle size, though direct comparisons are difficult, as they did not estimate the size of their crystalline core.[3]

The Urbach energy of a sample is a measure of disorder, and may be due to surface states, structural disorder, or doping. Additional disorder in NC and quantum dot (QD) systems is consequent from the increased surface area and size dispersion. For reference, crystalline silicon has been measured to have $E_{Urbach} < 20$ meV, amorphous silicon ~ 45 meV, and up to 200 meV for CdSe QDs.[39,40] This disorder results in energy states available below the band edge, represented by an exponentially decreasing absorption coefficient $\alpha \sim \alpha_0 \, \mathrm{Exp}(E/E_{Urbach})$ below the bandgap edge. As shown in Figure 2.16, Urbach energies for the similarly sized GeI_2 and GeI_4 were both 145 ± 5 meV, while the 18 nm GeI_4 sample have a smaller Urbach energy of 95 meV ± 5 meV. This indicates that disorder might correlate with the fraction of surface states associated with decreased particle size, or perhaps the increased molar ratio of ligands to germanium, rather than the crystallinity of the individual nanocrystal.

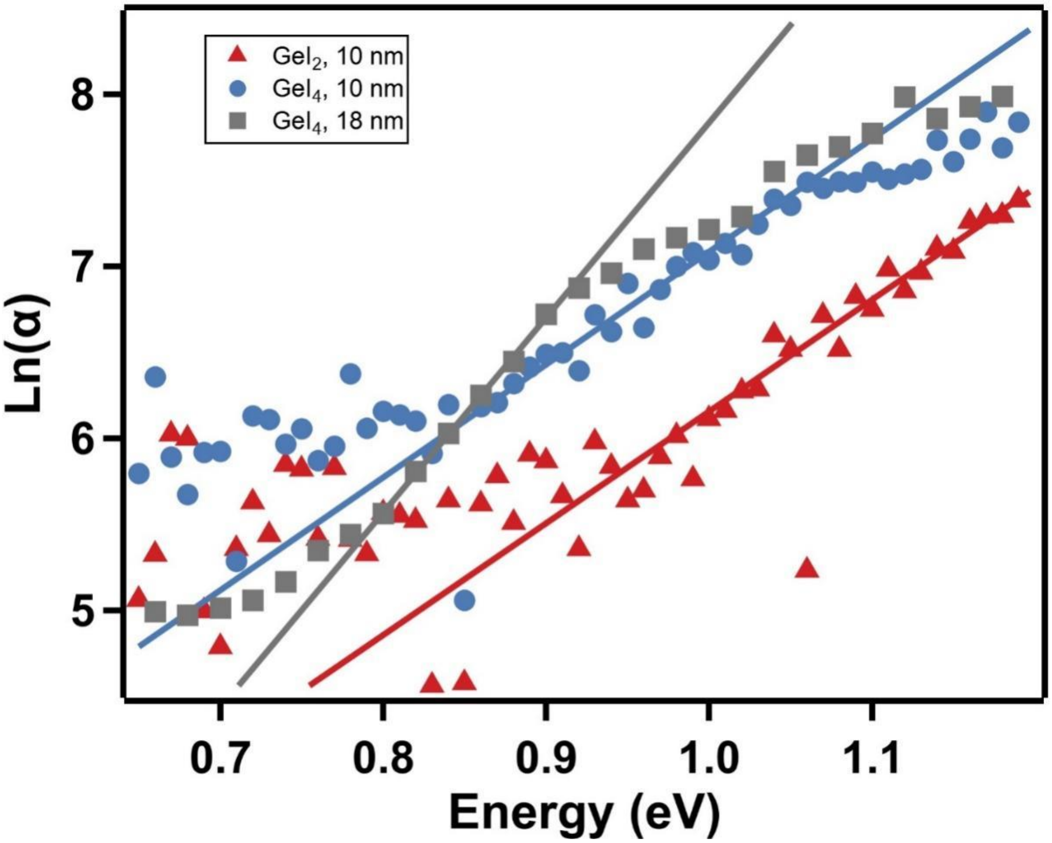

Figure 2.16. Urbach energy from a linear fit of ln(α) vs E with the best fit slope is $1/E_{Urbach}$.

To investigate our synthesis method's impact on conductivity, we fabricated heterojunction thin-film optoelectronic devices, using either GeI_2 QDs or GeI_4 NCs as the active layer. To control for interparticle spacing, both NC samples were prepared to have an average particle size of about 10 nm. All devices used a compact blocking TiO_2 layer (c-TiO_2), followed by a mesoporous TiO_2 layer (m-TiO_2) that aids in electron extraction. NCs solutions were spin-coated atop these layers, with Ag capping the devices (Figure 2.17 inset). Figure 2.17 shows average photocurrent for a set of GeI_2 and GeI_4 devices, with the inset displaying semi-log plots of both photocurrent and dark currents. A comparison of the average photocurrents extracted from our devices suggests increased performance in conductivity. It has been shown in perovskite heterojunction planar devices that increased crystallinity of the active layer leads to increases in photocurrent.[41] Similarly, the improved crystallinity in the GeI_4 samples likely leads to a reduction in trap states and an overall improvement in charge extraction. Photocurrents showed a five-decade change in magnitude in comparison to dark currents, a favorable characteristic for photodetectors.

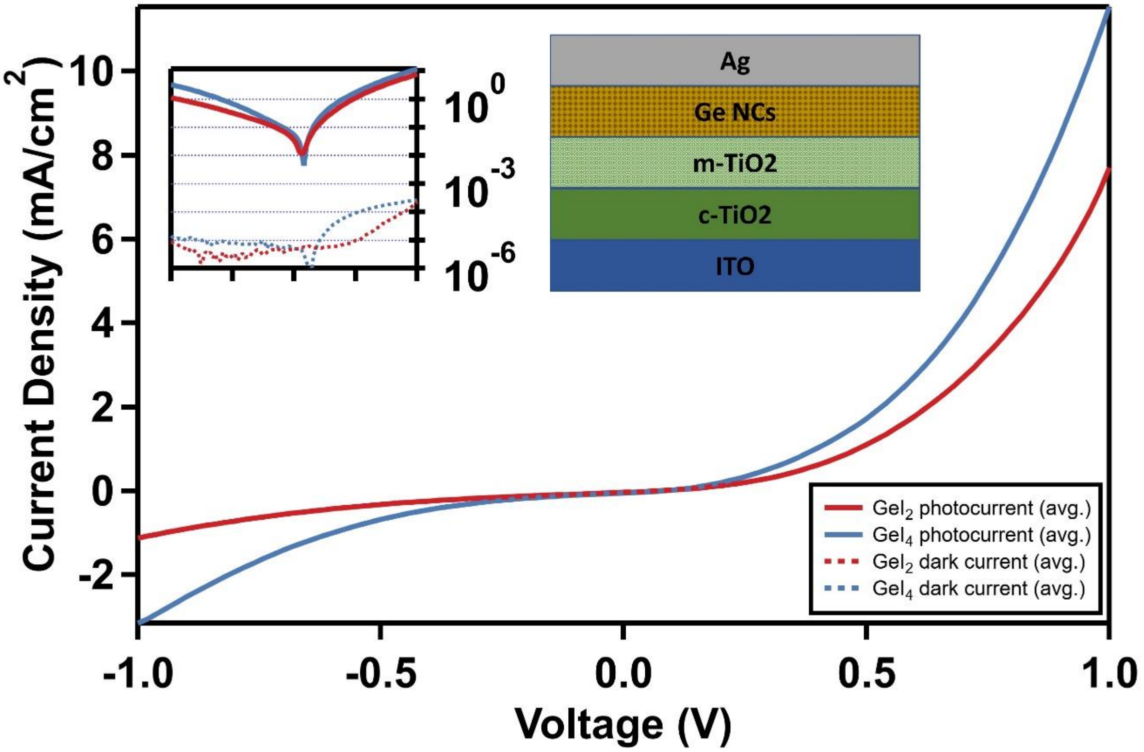

Figure 2.17. Average photocurrents for a set of GeI_2 and GeI_4 devices made of Ge NCs with similar average sizes. The inset displays the semi-log plots of both photocurrent and dark currents. A schematic image of the as-fabricated device presents as the right inset.

2.3.3. Investigation of the two-step reaction

OAm is a widely employed capping ligand that prevents aggregation, coalescence and termination of particle growth.[3,20,21,36,42] As mentioned previously, Smock *et al.* systematically studied the surface of solution synthesized Ge NCs by NMR and concluded that the strongly bound native ligands are X-type Ge-NHR covalent bonds whose fraction increased with higher reaction temperature.[36] When it comes to redox mechanisms involving OAm, different viable pathways have been proposed.[3,28,31,43,44] It has been reported that when OAm is the only reducing agent in the reaction, the lone pair of electrons in the amine group is necessary for the reduction process[45] and the carbon double bond in OAm does not play a significant role in the reactions.[46] In some syntheses of metal nanoparticles involving OAm and a metal oxide precursor, a catalytic hydrodenitrogenation reaction occurs and results in a cleavage of C-N bond of the amine.[44] Amino radicals formed at a relatively high temperature and could transform to imine or nitrile through deprotonation reaction.[43] Tabatabaei *et al.* proposed a different pathway for the reducing process to form Ge NCs by OAm with the formation of hydrogen gas. Supported with FT-IR and NMR, evidence was observed for the existence of imine nor nitrile groups to serve as capping ligands on the surface of Ge NCs.[21]

Ruddy *et al.* reduced mixed valence Ge precursors, GeI_2 and GeI_4, to synthesize Ge NCs with the assistance of reducing agent, BuLi.[3] It was proposed Ge(IV) could also be reduced to Ge^0 at a relatively high temperature (> 250 ^oC).[3] In this work, another pathway was discovered showing that Ge(IV) can be reduced to Ge(II) which is then further reduced to Ge^0. We investigated possible mechanisms behind the reactions of germanium precursors with OAm employing MS, GC, and NMR.

High-resolution mass spectrometry (HRMS), Figure 2.18 shows OAm, the GeI_4 stock solution, GeI_2 stock solution and these solutions after the first microwave heating, the GeI_4 stock solution after the second heating, along with an OAm + I_2 solution after heating. The OAm solution shows a typical mass spectrum with the main peak at 268.30 *m/z*. The GeI_4 stock solution shows the OAm peak and two new peaks: an exact mass of 663.5 amu which could be assigned to an ammonium-Iodide complex $((RNH_3)_2I)^+$ and 516.55 amu which could be assigned to an imine group R'-CH=N-CH2-R'. Here, R' is $CH_3(CH_2)_7CH=CH(CH_2)_7$- as the same carbon chain in OAm without NH_2CH_2- group. These two peaks are also seen in a GeI_2 stock solution at room temperature, as shown in Figure 2.18c. It is unexpected that an imine formed at room temperature in the GeI_4 stock solution. The possibility should be considered that the imine could be produced during the MS process in an intense gas phase.[47] However, after the first heating of the either the GeI_4 stock solution, a peak with 518.56 *m/z* arises, indicating the presence of the product of the dimerization of OAm, $((CH_3(CH_2)_7CH=CH(CH_2)_7CH_2-)_2NH)$. During the heating reaction, ammonia gas is produced, identified by GC, see below. The peak intensity of the 518.56 *m/z* increased dramatically after the second heating process (Figure 2.18e) demonstrating a higher degree of dimerization. The same MS peak (518.56 *m/z*) was reported for a GeI_2 microwave reaction.[21] All MS peak and possible species are summarized in Table 2.1. The MS signal provides evidence that Ge(IV)/I^- ions might play an important role in the formation of imine group at room temperature, and the I^- ion triggers the dimerization reaction of amines.

Table 2.1. High-resolution mass spectrometry peaks and possible species. Here, R' is $CH_3(CH_2)_7CH=CH(CH_2)_7$-.

m/z; z=1	Empirical Formula	Formula change from parent	Possible species

268.2998	$C_{18}H_{38}N$	OAm	R’-CH_2-NH_2
516.5506	$C_{36}H_{70}N$	2*OAM - NH_3-2*H	R’-CH=N-CH_2-R’
518.5617	$C_{36}H_{72}N$	2*OAM - NH_3	R’-CH_2-NH-CH_2-R’
663.5053	$C_{36}H_{78}N_2I$	2*OAM+I+2*H	$((RNH_3)_2I)^+$

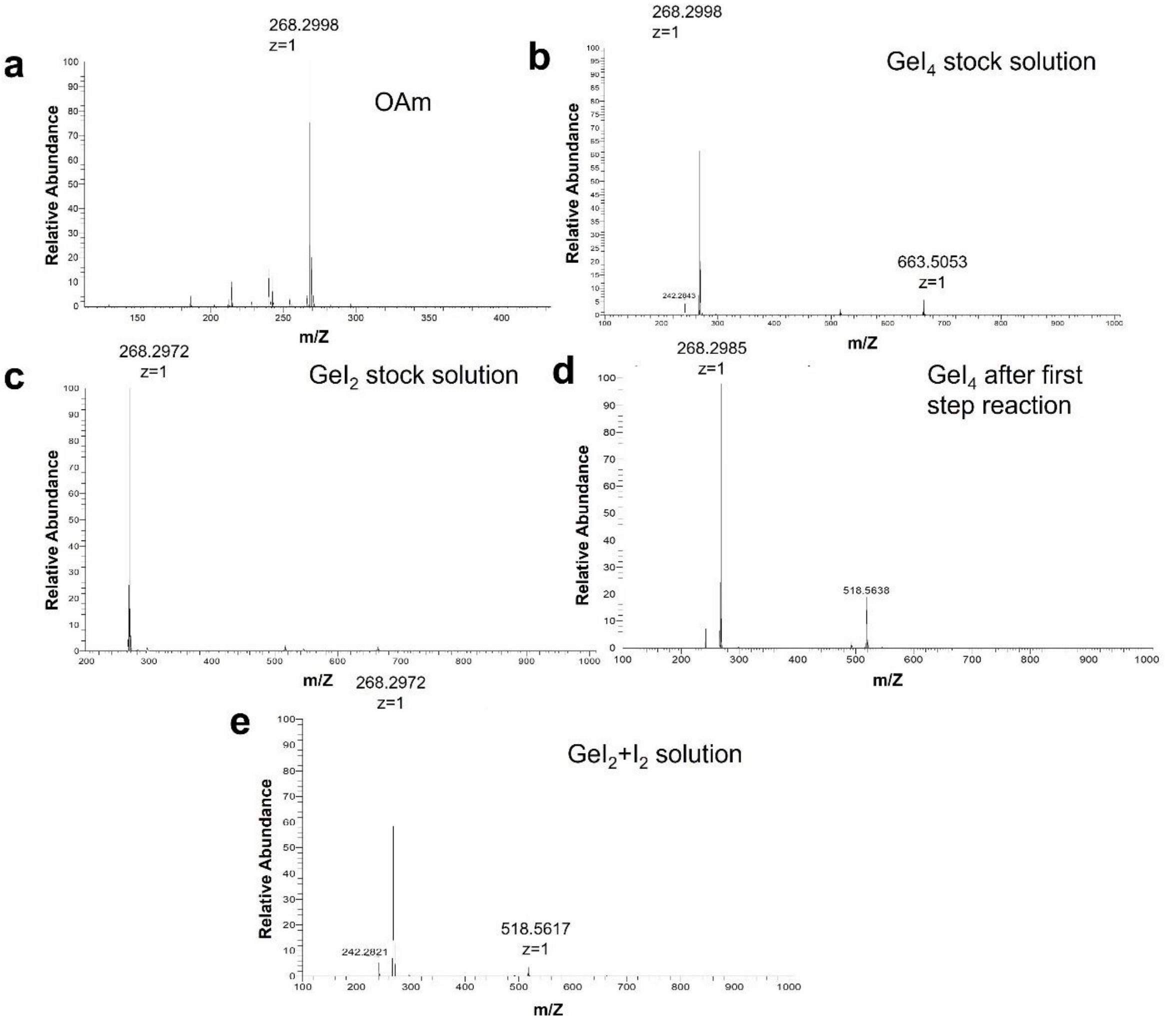

Figure 2.18. HRMS spectra of (a) degassed OAm, (b) GeI_4 stock solution, (c) GeI_2 stock solution, (d) GeI_4 stock solution after first step heating at 250 °C for 40 min. (e) Supernatant of GeI_4 stock solution after second step heating at 260 °C for 30 min. All the reaction mixtures were analyzed as prepared with no additional work up.

Gas chromatography (GC) was also used to qualitatively determine the gases produced during both steps of the reaction by injecting the gas taken from the headspace of the sealed microwave tubes. In both steps, H_2 and NH_3 gas were detected, confirmed by the pure gas injection as a comparison (Figure 2.19). The formation of NH_3 is consistent with the MS data of the formation of the OAm dimer. The pathway of the production of H_2 gas during the reaction is still unsolved. One possible hypothesis is that H_2 is released from the deprotonation reaction of OAm induced by I^-.[21] Another possible pathway is that the amine could undergo a nucleophilic substitution reaction with protonated amine (ammonium), followed with a dehydrogenation reaction.[47] Both NH_3 and H_2 gases were produced in this process.

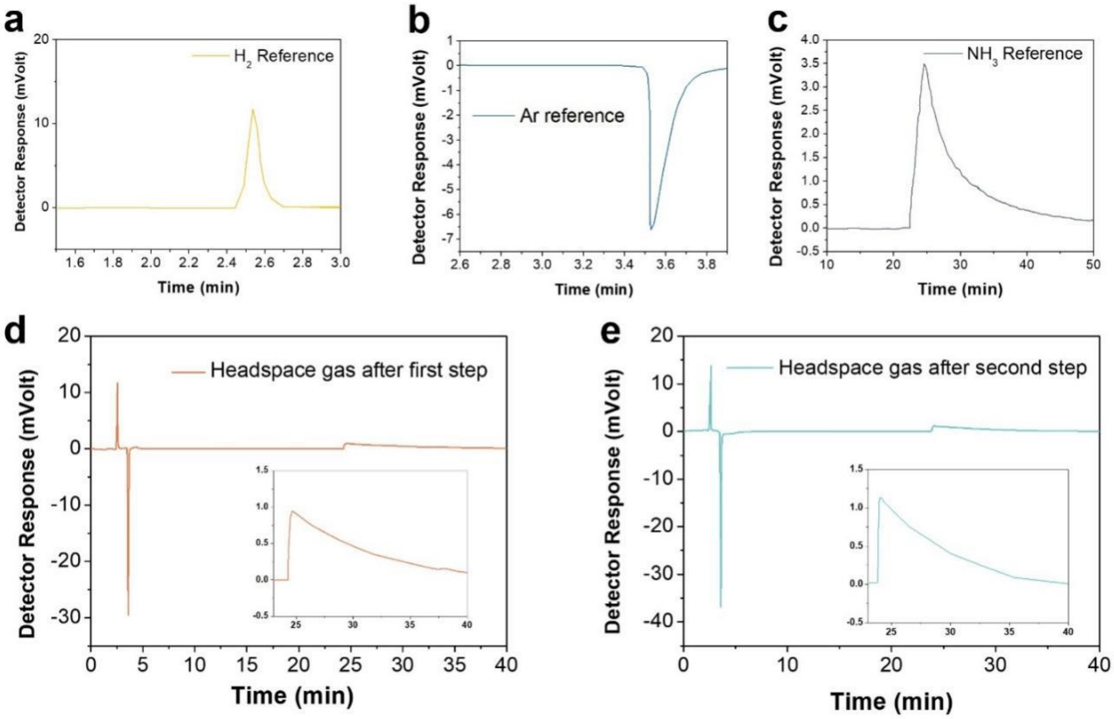

Figure 2.19. Gas chromatography spectra of (a) hydrogen gas injection as reference, (b)argon gas reference and (c) NH_3 gas reference. Gas injection of the head space of the microwave tube after (d) the first step reaction and (e) the second step reaction of GeI_4/OAm solution. The insets in (d) and (e) show the expansion regions for the elution of NH_3.

The function of H_2 gas in the reaction was investigated by running a reaction with conventional heating. The yellow solution obtained after the first-step microwave heating was transferred into a flask. The flask was heated by a heating mantle and assembled with argon gas flow to remove the produced gases. After 30 min holding at 260 °C, a brown solution was obtained, demonstrating the formation of Ge NCs. As indicated previously, while GC shows the production of H_2(g), it is not the reducing agent for the formation of Ge nanoparticles.[21]

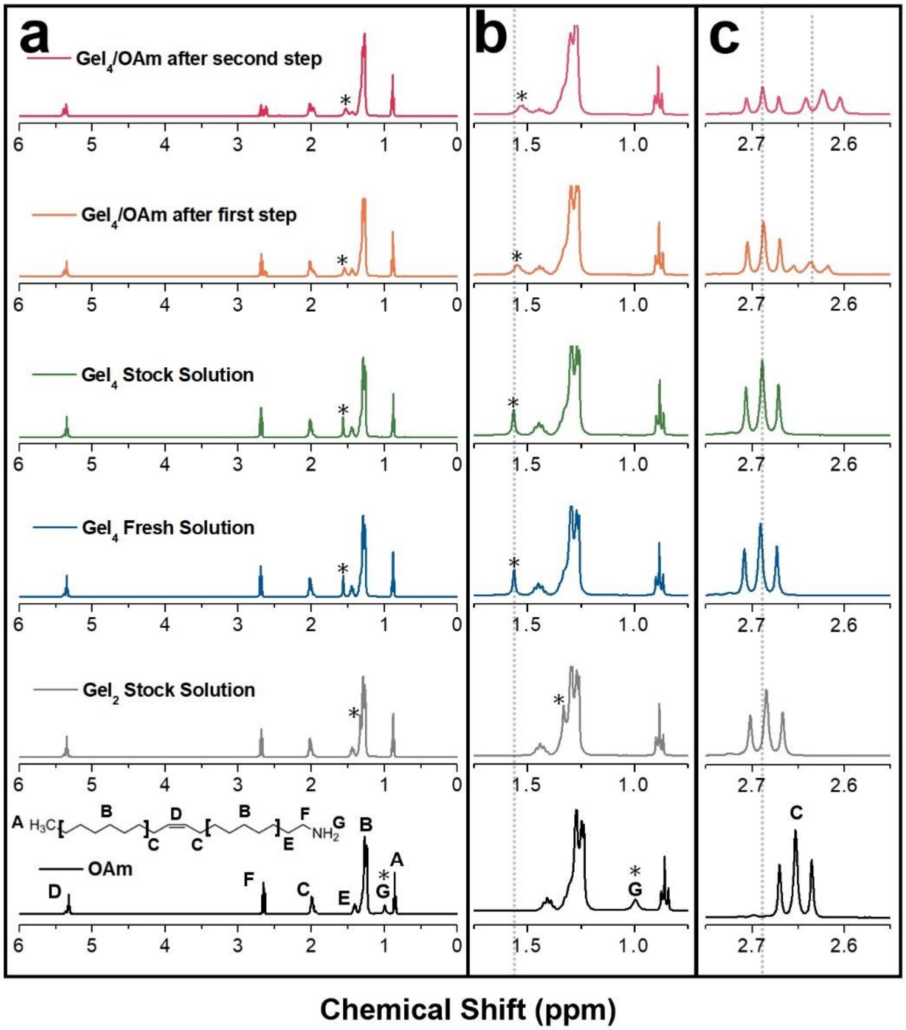

Figure 2.20. (a) Overall NMR spectra of degassed OAm, GeI_2 stock solution, GeI_4 fresh solution and stock solution and the supernatant of GeI_4/OAm after first and second steps of reaction. (b) Enlarged spectra with the range of 0.75 – 1.75 ppm. (c) Enlarged spectra with the range of 2.55 – 2.75 ppm.

^{1}H NMR spectra (Figure 2.20a) was obtained from different solutions to study the chemical changes during the reaction. The spectra of the GeI_2 and GeI_4 stock solutions, freshly prepared GeI_4 solution and GeI_4 solution after first and second reaction steps are compared with OAm in Figure 2.20b. In the order of OAm, GeI_2 stock and GeI_4 stock solutions, the peak corresponding to the amine proton (labelled with $*$) moves downfield. Shifting of the amine protons with protonation has been observed previously, for example, in a mixture of sulfur and octylamine assigned to the formation of $(RNH_3^+)(RNH\text{-}S_8^-)$.[48] The amine group of OAm has been reported to serve as an electron donor (L-type) ligand and coordinates with transition metal ions to form a reactive precursor.[49,50] Ge(IV) is a hard Lewis acid according to the hard and soft acid and base (HSAB) theory. Iodide, I^-, compared with an amine group, is soft. Thus, when GeI_4 dissolved in OAm, I^- ligands are partially substituted by OAm and $[Ge(OAm)_xI_{4-x}]^{x+}$ forms. In the presence of I^-, the amines could undergo a protonation process and form oleylammonium iodide as indicated by the shifting of amine proton peak in the NMR. GeI_2 in OAm undergoes the same process. However, compared with Ge(IV), Ge(II) is comparatively soft due to the larger atomic radius, and only possesses two coordinative positions and hence a lower degree of protonation. The peak shift in ^{1}H NMR also correlates with the existence and intensity of the protonated amine peak observed in the MS (Figure 2.18b). Compared with the OAm reference, the amine proton peak is sharper in precursor stock solutions attributed to the coordination between Ge(IV) and OAm that reduces the amine-amine interaction. The protonation is a fast process as the amine proton peak of a freshly prepared GeI_4 solution shows the same chemical shift as that of the GeI_4 stock solution.

An extra peak with small upfield shift from the original position of OAm is clearly exhibited in the enlarged range 2.5 – 2.8 ppm in the NMR (Figure 2.20c). The new peak with an upfield shift that is smaller than 0.1 ppm are likely from a derivative product of OAm such as the dioleylamine that is identified by MS. The increasing intensity of this NMR peak correlates with the increasing amount of dioleylamine after the two-step reaction. The proton peaks of the amine broaden and shift slightly upfield after the two-step heating. The broadening is caused by multiple environments of amine. The shifting is attributed to the formation of dioleylamine which has a more shielded amine group. Detected and presumed species are summarized in Table 2.2 according to MS, GC, and NMR.

Table 2.2. Summary of detected and presumed complexes and species from NMR, MS and GC.

	NMR	**MS**	**GC**
GeI_4 stock solution	$[Ge(OAm)_xI_{4-x}]^{x+}$; RNH_3^+	R’-CH=N-CH2-R’; $((RNH_3)_2I)^+$	-
GeI_4/OAm after first step	Dioleylamine	Dioleylamine	NH_3; H_2
GeI_4/OAm after second step	Dioleylamine	Dioleylamine	NH_3; H_2

Based on the summarized species, we propose a possible mechanism for the reduction of Ge(IV) to Ge(II) in OAm. It was reported decades ago that Ge(IV) can be easily reduced by different amines such as ethylamine and aniline.[51–53] The reactions pathways are listed below in Equation 2.2, 2.3. Followed with the disproportion reaction (Equation 2.4), Ge undergoes nucleation and growth under the control of the concentration of Ge(IV).

$$[\mathbf{Ge(NH_2CH_2R')_4}]^{4+} + 4\ \mathbf{NH_2CH_2R'} \longrightarrow \mathbf{Ge(NHCH_2R')_4} + 4\ \mathbf{(NH_3CH_2R')^{+}}$$ **Equation 2.2**

$$\mathbf{Ge(NHCH_2R')_3} \longrightarrow \mathbf{Ge(N = CHR)_2} + \mathbf{2NH_2CH_2R'}$$ **Equation 2.3**

$$\mathbf{Ge(II)} \leftrightharpoons \mathbf{Ge^0} + \mathbf{Ge(IV)}$$ **Equation 2.4**

The proposed reduction mechanism is similar to that reported in Nam's work on synthesis of cobalt nanoparticles.[44] The possible reaction pathways are shown in Figure 2.21. The OAm deprotonates to form a stronger coordinating ligand, oleylamide. The α-carbon atom of the coordinated oleylamide ligand on Ge(IV) interacts with the relatively electronegative nitrogen atom in another oleylamide ligand binding on the same center Ge atom. This results in the cleavage of N-C bond, also known as denitrogenation reaction. The subsequent reaction undergoes a β-hydride elimination which forms an imine and Ge hydride bond. The Ge(IV)-amine-hydride complex will be quickly reduced to Ge(II) with the formation of NH_3 gas which is observed in GC. While the imine could react with the observed H_2 gas and form the dioleylamine (R-NH-R) observed in the MS, the Ge(II) species undergoes a disproportion reaction and gives Ge^0 and Ge(IV) as shown in Equation 2.4. In this proposed mechanism, the NH_3 gas is formed from the fast reductive elimination reaction. Several germanium-amine-hydride complexes have been successfully prepared and stabilized by bulky coordinates.[54] These Ge-amine-hydride complexes are confirmed by single crystal XRD and further efforts on short chain amines might provide further insight.[54]

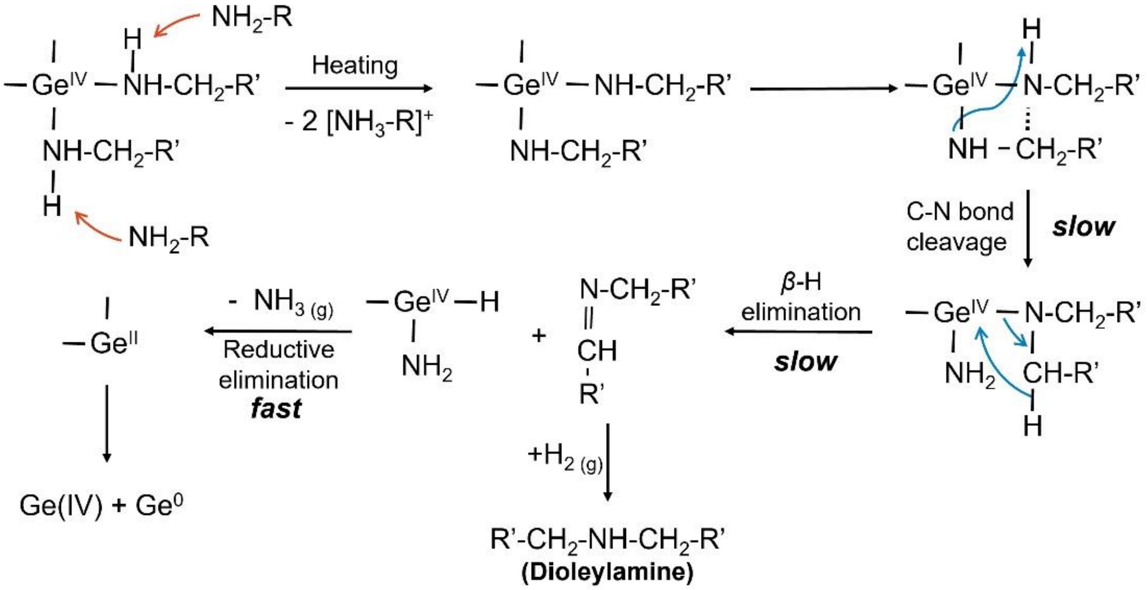

Figure 2.21. Proposed reaction pathways for the reduction of Ge(IV) to Ge(II) by OAm. Ge(IV) is reduced to Ge(II) by oleylamide from the deprotonation of OAm, with the formation of NH_3 and dioleylamine.

In this work, a two-step reaction was carried out to synthesize Ge NCs from GeI_4. In the synthesis section, different reactions demonstrates that the reaction rate is responsible for the nucleation, growth and dispersion of synthesized Ge NCs. In a prepared GeI_4/OAm solution, the ligands exchange and form $[Ge(OAm)_xI_{4-x}]^{x+}$. When the solution is heated up, binding ligands change from L-type oleylamine to stronger X-type oleylamide (Ge-NHR). Oleylamide is a long chain bulky ligand with strong binding affinity.[36] These two factors decelerate the reaction rate of the center atom, Ge(IV) and control the nucleation and growth of Ge NCs.[28,55,56]

Mixed valent Ge precursors have been employed to control size and improve the crystallinity of Ge NCs. It was believed that Ge^0 nucleated from Ge(II) reduction and grew from Ge(IV) reduction at a high temperature.[3] However, in our work, we confirmed that Ge(IV) can be reduced to Ge(II) and then undergo the well-documented disproportion reaction at microwave temperatures of 260

˚C and lower providing Ge^0 and presumably Ge(IV) as shown in Equation 2.4. High concentration of Ge(IV) in the solution further slowdown the disproportional reaction and result in the highly crystalline nature of Ge NCs.

2.4. Conclusions

A two-step microwave-assisted solution method was designed to synthesis Ge NCs from GeI_4 as the single Ge precursor. The process was investigated with different reaction time, temperatures, and concentrations. Monodispersed Ge NCs with a large average particle size of 18.9 ± 1.84 nm have been successfully produced through this two-step reaction. Both XRD and HRTEM images showed the high crystallinities of the as-synthesized Ge NCs. A high concentration of GeI_4 precursor or a low temperature of reaction results in large aggregations of small Ge nuclei. Urbach energies and optoelectronic properties of 10 nm Ge NCs prepared from GeI_4 by this two-step method was compared with that synthesized from GeI_2 by a reported method and showed higher crystallinities and better electrical conductivity. The reaction process was investigated by NMR, MS, and GC. A possible mechanism was proposed based on the detected species by these characterizations. Overall, a new method on Ge NCs synthesis was studied and showed improved qualities of produced Ge NCs. The synthesis could be further modified and applied on not only Ge based nanostructures but other metal and semimetal nanocrystals. The exploration of the possible mechanisms involved in this reaction provides new insights on nanoparticle synthesis of covalently bonding semiconductors.

2.5. Acknowledgements

This work was supported by the National Science Foundation CHE-1710110. TEM was collected at the Advanced Materials Characterization and Testing Laboratory at UC Davis and the National Center for Electron Microscopy within the Molecular Foundry in Lawrence Berkeley National Laboratory.

2.6. References of Chapter 2

(1) Pillarisetty, R. Academic and Industry Research Progress in Germanium Nanodevices. *Nature*. 2011, pp 324–328. https://doi.org/10.1038/nature10678.

(2) Muthuswamy, E.; Zhao, J.; Tabatabaei, K.; Amador, M. M.; Holmes, M. A.; Osterloh, F. E.; Kauzlarich, S. M. Thiol-Capped Germanium Nanocrystals: Preparation and Evidence for Quantum Size Effects. *Chem. Mater.* **2014**, *26* (6), 2138–2146. https://doi.org/10.1021/cm4042154.

(3) Ruddy, D. A.; Johnson, J. C.; Smith, E. R.; Neale, N. R. Size and Bandgap Control in the Solution-Phase Synthesis of near-Infrared-Emitting Germanium Nanocrystals. *ACS Nano* **2010**, *4* (12), 7459–7466. https://doi.org/10.1021/nn102728u.

(4) Nozik, A. J. Nanoscience and Nanostructures for Photovoltaics and Solar Fuels. *Nano Lett.* **2010**, *10* (8), 2735–2741. https://doi.org/10.1021/nl102122x.

(5) Vörös, M.; Wippermann, S.; Somogyi, B.; Gali, A.; Rocca, D.; Galli, G.; Zimanyi, G. T. Germanium Nanoparticles with Non-Diamond Core Structures for Solar Energy Conversion. *J. Mater. Chem. A* **2014**, *2* (25), 9820–9827. https://doi.org/10.1039/c4ta01543f.

(6) Ramasamy, K.; Kotula, P. G.; Fidler, A. F.; Brumbach, M. T.; Pietryga, J. M.; Ivanov, S. A. SnxGe1-x Alloy Nanocrystals: A First Step toward Solution-Processed Group IV Photovoltaics. *Chem. Mater.* **2015**, *27* (13), 4640–4649. https://doi.org/10.1021/acs.chemmater.5b01041.

(7) Wheeler, L. M.; Nichols, A. W.; Chernomordik, B. D.; Anderson, N. C.; Beard, M. C.; Neale, N. R. All-Inorganic Germanium Nanocrystal Films by Cationic Ligand Exchange. *Nano Lett.* **2016**, *16* (3), 1949–1954. https://doi.org/10.1021/acs.nanolett.5b05192.

(8) Chockla, A. M.; Klavetter, K. C.; Mullins, C. B.; Korgel, B. A. Solution-Grown Germanium Nanowire Anodes for Lithium-Ion Batteries. *ACS Appl. Mater. Interfaces* **2012**, *4* (9), 4658–4664. https://doi.org/10.1021/am3010253.

(9) Yuan, F. W.; Yang, H. J.; Tuan, H. Y. Alkanethiol-Passivated Ge Nanowires as High-Performance Anode Materials for Lithium-Ion Batteries: The Role of Chemical Surface Functionalization. *ACS Nano* **2012**, *6* (11), 9932–9942. https://doi.org/10.1021/nn303519g.

(10) Kamata, Y. High-k/Ge MOSFETs for Future Nanoelectronics. *Materials Today*. 2008, pp 30–38. https://doi.org/10.1016/S1369-7021(07)70350-4.

(11) Seino, M.; Henderson, E. J.; Puzzo, D. P.; Kadota, N.; Ozin, G. A. Germanium Nanocrystal Doped Inverse Crystalline Silicon Opal. *J. Mater. Chem.* **2011**, *21* (40), 15895–15898. https://doi.org/10.1039/c1jm13172a.

(12) Vaughn, D. D.; Schaak, R. E. Synthesis, Properties and Applications of Colloidal Germanium and Germanium-Based Nanomaterials. *Chem. Soc. Rev.* **2013**, *42* (7), 2861–2879. https://doi.org/10.1039/c2cs35364d.

(13) Fan, J.; Chu, P. K. Group IV Nanoparticles: Synthesis, Properties, and Biological Applications. *Small* **2010**, *6* (19), 2080–2098. https://doi.org/10.1002/smll.201000543.

(14) Carolan, D. Recent Advances in Germanium Nanocrystals: Synthesis, Optical Properties and Applications. *Prog. Mater. Sci.* **2017**, *90*, 128–158. https://doi.org/10.1016/j.pmatsci.2017.07.005.

(15) Lu, X.; Ziegler, K. J.; Ghezelbash, A.; Johnston, K. P.; Korgel, B. A. Synthesis of Germanium Nanocrystals in High Temperature Supercritical Fluid Solvents. *Nano Lett.* **2004**, *4* (5), 969–974. https://doi.org/10.1021/nl049831j.

(16) McVey, B. F. P.; Prabakar, S.; Gooding, J. J.; Tilley, R. D. Solution Synthesis, Surface Passivation, Optical Properties, Biomedical Applications, and Cytotoxicity of Silicon and

Germanium Nanocrystals. *Chempluschem* **2017**, *82* (1), 60–73. https://doi.org/10.1002/cplu.201600207.

(17) Chou, N. H.; Oyler, K. D.; Motl, N. E.; Schaak, R. E. Colloidal Synthesis of Germanium Nanocrystals Using Room-Temperature Benchtop Chemistry. *Chem. Mater.* **2009**, *21* (18), 4105–4107. https://doi.org/10.1021/cm902088y.

(18) Jeon, Y.; Lee, G. H.; Park, J.; Kim, B.; Chang, Y. Magnetic Properties of Monodisperse NiHx Nanoparticles and Comparison to Those of Monodisperse Ni Nanoparticles. *J. Phys. Chem. B* **2005**, *109* (25), 12257–12260. https://doi.org/10.1021/jp050489o.

(19) Hu, J.; Lu, Q.; Wu, C.; Liu, M.; Li, H.; Zhang, Y.; Yao, S. Synthesis of Fluorescent and Water-Dispersed Germanium Nanoparticles and Their Cellular Imaging Applications. *Langmuir* **2018**, *34* (30), 8932–8938. https://doi.org/10.1021/acs.langmuir.8b01543.

(20) Muthuswamy, E.; Iskandar, A. S.; Amador, M. M.; Kauzlarich, S. M. Facile Synthesis of Germanium Nanoparticles with Size Control: Microwave versus Conventional Heating. *Chem. Mater.* **2013**, *25* (8), 1416–1422. https://doi.org/10.1021/cm302229b.

(21) Tabatabaei, K.; Holmes, A. L.; Newton, K. A.; Muthuswamy, E.; Sfadia, R.; Carter, S. A.; Kauzlarich, S. M. Halogen-Induced Crystallinity and Size Tuning of Microwave Synthesized Germanium Nanocrystals. *Chem. Mater.* **2019**, *31* (18), 7510–7521. https://doi.org/10.1021/acs.chemmater.9b02225.

(22) Reid, W. E. Some Electrochemical Aspects of Germanium Dissolution. Simultaneous Chemical and Electrochemical Oxidation. *J. Phys. Chem.* **1965**, *69* (7), 2269–2277. https://doi.org/10.1021/j100891a021.

(23) Tabatabaei, K.; Sully, H. R.; Ju, Z.; Hellier, K.; Lu, H.; Perez, C. J.; Newton, K. A.; Brutchey, R. L.; Bridges, F.; Carter, S. A.; Kauzlarich, S. M. Structural Insights on Microwave-Synthesized Antimony-Doped Germanium Nanocrystals. *ACS Nano* **2021**, *15* (1), 1685–1700. https://doi.org/10.1021/acsnano.0c09352.

(24) Newton, K. A.; Ju, Z.; Tabatabaei, K.; Kauzlarich, S. M. Diorganyl Dichalcogenides as Surface Capping Ligands for Germanium Nanocrystals. *ACS Appl. Mater. Interfaces* **2020**. https://doi.org/10.1021/acs.organomet.9b00749.

(25) Alan Esteves, R. J.; Ho, M. Q.; Arachchige, I. U.; Esteves, R. J. A.; Ho, M. Q.; Arachchige, I. U. Nanocrystalline Group IV Alloy Semiconductors: Synthesis and Characterization of Ge1- XSnx Quantum Dots for Tunable Bandgaps. *Chem. Mater.* **2015**, *27* (5), 1559–1568. https://doi.org/10.1021/cm503983b.

(26) Ruddy, D. A.; Erslev, P. T.; Habas, S. E.; Seabold, J. A.; Neale, N. R. Surface Chemistry Exchange of Alloyed Germanium Nanocrystals: A Pathway toward Conductive Group IV Nanocrystal Films. *J. Phys. Chem. Lett.* **2013**, *4* (3), 416–421. https://doi.org/10.1021/jz3020875.

(27) Tallapally, V.; Nakagawara, T. A.; Demchenko, D. O.; Özgür, Ü.; Arachchige, I. U. Ge1- :XSnx Alloy Quantum Dots with Composition-Tunable Energy Gaps and near-Infrared Photoluminescence. *Nanoscale* **2018**, *10* (43), 20296–20305. https://doi.org/10.1039/c8nr04399j.

(28) Mourdikoudis, S.; Liz-Marzán, L. M. Oleylamine in Nanoparticle Synthesis. *Chem. Mater.* **2013**, *25* (9), 1465–1476. https://doi.org/10.1021/cm4000476.

(29) Baranov, D.; Lynch, M. J.; Curtis, A. C.; Carollo, A. R.; Douglass, C. R.; Mateo-Tejada, A. M.; Jonas, D. M. Purification of Oleylamine for Materials Synthesis and Spectroscopic Diagnostics for Trans Isomers. *Chem. Mater.* **2019**, *31* (4), 1223–1230. https://doi.org/10.1021/acs.chemmater.8b04198.

(30) Bernard, A.; Zhang, K.; Larson, D.; Tabatabaei, K.; Kauzlarich, S. M. Solvent Effects on Growth, Crystallinity, and Surface Bonding of Ge Nanoparticles. *Inorg. Chem.* **2018**, *57* (9), 5299–5306. https://doi.org/10.1021/acs.inorgchem.8b00334.

(31) Pescara, B.; Mazzio, K. A.; Lips, K.; Raoux, S. Crystallinity and Size Control of Colloidal Germanium Nanoparticles from Organogermanium Halide Reagents. *Inorg. Chem.* **2019**, *58* (8), 4802–4811. https://doi.org/10.1021/acs.inorgchem.8b03157.

(32) Scherrer, P. Determination of the Internal Structure and Size of Colloid Particles by X-Rays. *Göttinger Nachrichten Gesell* **1918**, *2*, 98–100.

(33) Kumar, K.; Chowdhury, A. Pushing the Limits of Analytical Characterization Tools: How Much Is Too Much? *Handb. Miniaturization Anal. Chem.* **2020**, 239–275.

https://doi.org/10.1016/b978-0-12-819763-9.00011-8.

(34) Matioszek, D.; Ojo, W. S.; Cornejo, A.; Katir, N.; El Ezzi, M.; Le Troedec, M.; Martinez, H.; Gornitzka, H.; Castel, A.; Nayral, C.; Delpech, F. From Rational Design of Organometallic Precursors to Optimized Synthesis of Core/Shell Ge/GeO2 Nanoparticles. *Dalt. Trans.* **2015**, *44* (16), 7242–7250. https://doi.org/10.1039/c5dt00392j.

(35) Kwon, Y.; Kim, S. Indium Phosphide Magic-Sized Clusters: Chemistry and Applications. *NPG Asia Mater.* **2021**, *13* (1), 1–16. https://doi.org/10.1038/s41427-021-00300-4.

(36) Smock, S. R.; Tabatabaei, K.; Williams, T. J.; Kauzlarich, S. M.; Brutchey, R. L. Surface Coordination Chemistry of Germanium Nanocrystals Synthesized by Microwave-Assisted Reduction in Oleylamine. *Nanoscale* **2020**, *12* (4), 2764–2772. https://doi.org/10.1039/c9nr09233a.

(37) Understanding the Impact of Local Structure on Materials for Optoelectronic Applications - ProQuest https://www.proquest.com/docview/2491206104?pq-origsite=gscholar&fromopenview=true (accessed Sep 25, 2021).

(38) Tabatabaei, K.; Holmes, A. L.; Newton, K. A.; Muthuswamy, E.; Sfadia, R.; Carter, S. A.; Kauzlarich, S. M. Halogen-Induced Crystallinity and Size Tuning of Microwave Synthesized Germanium Nanocrystals. *Chem. Mater.* **2019**. https://doi.org/10.1021/acs.chemmater.9b02225.

(39) Guyot-Sionnest, P.; Lhuillier, E.; Liu, H. A Mirage Study of CdSe Colloidal Quantum Dot Films, Urbach Tail, and Surface States. *J. Chem. Phys.* **2012**, *137* (15), 154704. https://doi.org/10.1063/1.4758318.

(40) Cody, G. D. Urbach Edge of Crystalline and Amorphous Silicon: A Personal Review. *J. Non. Cryst. Solids* **1992**, *141* (C), 3–15. https://doi.org/10.1016/S0022-3093(05)80513-7.

(41) Wang, B.; Wong, K. Y.; Yang, S.; Chen, T. Crystallinity and Defect State Engineering in Organo-Lead Halide Perovskite for High-Efficiency Solar Cells. *J. Mater. Chem. A* **2016**, *4* (10), 3806–3812. https://doi.org/10.1039/c5ta09249c.

(42) He, M.; Protesescu, L.; Caputo, R.; Krumeich, F.; Kovalenko, M. V. A General Synthesis Strategy for Monodisperse Metallic and Metalloid Nanoparticles (In, Ga, Bi, Sb, Zn, Cu,

Sn, and Their Alloys) via in Situ Formed Metal Long-Chain Amides. *Chem. Mater.* **2015**, *27* (2), 635–647. https://doi.org/10.1021/cm5045144.

(43) Chen, M.; Feng, Y. G.; Wang, X.; Li, T. C.; Zhang, J. Y.; Qian, D. J. Silver Nanoparticles Capped by Oleylamine: Formation, Growth, and Self-Organization. *Langmuir* **2007**, *23* (10), 5296–5304. https://doi.org/10.1021/la700553d.

(44) Nam, K. M.; Shim, J. H.; Ki, H.; Choi, S. Il; Lee, G.; Jang, J. K.; Jo, Y.; Jung, M. H.; Song, H.; Park, J. T. Single-Crystalline Hollow Face-Centered-Cubic Cobalt Nanoparticles from Solid Face-Centered-Cubic Cobalt Oxide Nanoparticles. *Angew. Chemie - Int. Ed.* **2008**, *47* (49), 9504–9508. https://doi.org/10.1002/anie.200803048.

(45) Xue, D. J.; Wang, J. J.; Wang, Y. Q.; Xin, S.; Guo, Y. G.; Wan, L. J. Facile Synthesis of Germanium Nanocrystals and Their Application in Organic-Inorganic Hybrid Photodetectors. *Adv. Mater.* **2011**, *23* (32), 3704–3707. https://doi.org/10.1002/adma.201101436.

(46) Hiramatsu, H.; Osterloh, F. E. A Simple Large-Scale Synthesis of Nearly Monodisperse Gold and Silver Nanoparticles with Adjustable Sizes and with Exchangeable Surfactants. *Chem. Mater.* **2004**, *16* (13), 2509–2511. https://doi.org/10.1021/cm049532v.

(47) Zhang, D.; Gill, L. A.; Cooks, R. G. Deamination of Protonated Amines to Yield Protonated Imines. *J. Am. Soc. Mass Spectrom.* **1998**, *9* (11), 1146–1157. https://doi.org/10.1016/S1044-0305(98)00093-2.

(48) Thomson, J. W.; Nagashima, K.; Macdonald, P. M.; Ozin, G. A. From Sulfur-Amine Solutions to Metal Sulfide Nanocrystals: Peering into the Oleylamine-Sulfur Black Box. *J. Am. Chem. Soc.* **2011**, *133* (13), 5036–5041. https://doi.org/10.1021/ja1109997.

(49) Park, J. H. J. G. J.; Kang, E.; Son, S. U.; Park, H. M.; Lee, M. K.; Kim, J.; Kim, K. W.; Noh, H. J.; Park, J. H. J. G. J.; Bae, C. J.; Park, J. H. J. G. J.; Hyeon, T. Monodisperse Nanoparticles of Ni and NiO: Synthesis, Characterization, Self-Assembled Superlattices, and Catalytic Applications in the Suzuki Coupling Reaction. *Adv. Mater.* **2005**, *17* (4), 429–434.

(50) Kura, H.; Takahashi, M.; Ogawa, T. Synthesis of Monodisperse Iron Nanoparticles with a

High Saturation Magnetization Using an Fe(CO)x?Oleylamine Reacted Precursor. *J. Phys. Chem. C* **2010**, *114* (13), 5835–5838. https://doi.org/10.1021/jp911161g.

(51) Johnson, O. H. Germanium and Its Inorganic Compounds. *Chem. Rev.* **1952**, *51* (3), 431–469. https://doi.org/10.1021/cr60160a002.

(52) Johnson, W. C.; Sidwell, A. E. Nitrogen Compounds of Germanium. IV. The Action of Ammonia and Amines on Germanium Tetraiodide. *J. Am. Chem. Soc.* **1933**, *55* (5), 1884–1889. https://doi.org/10.1021/ja01332a014.

(53) Thomas, J. S.; Southwood, W. W. Germanium. Part IX. The Action of Amines and of Certain Other Organic Bases on Germanium Tetrachloride. The Structure of Germanium Imide. *J. Chem. Soc.* **1931**, 2083–2097. https://doi.org/10.1039/jr9310002083.

(54) Peng, Y.; Guo, J. D.; Ellis, B. D.; Zhu, Z.; Fettinger, J. C.; Nagase, S.; Power, P. P. Reaction of Hydrogen or Ammonia with Unsaturated Germanium or Tin Molecules under Ambient Conditions: Oxidative Addition versus Arene Elimination. *J. Am. Chem. Soc.* **2009**, *131* (44), 16272–16282. https://doi.org/10.1021/ja9068408.

(55) Gerung, H.; Bunge, S. D.; Boyle, T. J.; Brinker, C. J.; Han, S. M. Anhydrous Solution Synthesis of Germanium Nanocrystals from the Germanium(II) Precursor Ge[N(SiMe3)2]2. *Chem. Commun.* **2005**, No. 14, 1914–1916. https://doi.org/10.1039/b416066e.

(56) Lee, H.; Yoon, D. E.; Koh, S.; Kang, M. S.; Lim, J.; Lee, D. C. Ligands as a Universal Molecular Toolkit in Synthesis and Assembly of Semiconductor Nanocrystals. *Chem. Sci.* **2020**, *11* (9), 2318–2329. https://doi.org/10.1039/c9sc05200c.

Chapter 3

Bi_2Te_3/Sb_2Te_3 core shell lateral heterojunction structure with enhanced thermal conductivity properties

Zheng Ju,[1] *Caitlin Crawford,*[2] *Jesse Adamczyk,*[2] *Eric Toberer*[2] *and Susan M. Kauzlarich**[1]

[1]Department of Chemistry, University of California Davis, One Shields Avenue, Davis, California 95616, United States

[2]Department of Physics, Colorado School of Mines, 1523 Illinois Street, Golden, Colorado 80401, United States

This work has resulted in one paper that is under preparation for submission soon. I performed all the synthesis and most of the characterization of the Bi_2Te_3/Sb_2Te_3 *lateral nanostructures. Collaborators at Colorado School of Mines performed the Van der Pauw resistivity and Hall measurements and Seebeck measurements on all the pressed* Bi_2Te_3/Sb_2Te_3 *pellets.*

Abstract

Thermoelectric materials convert heat energy to electricity, hold promising capabilities of increasing energy waste harvesting and developing sustainable energy utilization. In this work, we successfully synthesized Bi_2Te_3/Sb_2Te_3 (BTST) nanostructured heterojunctions *via* a two-step solution route. Samples with different Sb_2Te_3 to Bi_2Te_3 ratios could be synthesized by controlling the reaction precursors. Scanning electron microscopy images show well-defined hexagonal nanoplates and distinct interfaces between Bi_2Te_3 and Sb_2Te_3. The similarity of the area ratios with the precursor ratios indicates that the growth of the Sb_2Te_3 shell takes place in the lateral rather than vertical direction. Transmission electron microscopy revealed the crystalline nature of as-synthesized Bi_2Te_3 and Sb_2Te_3. Energy dispersive X-ray spectroscopy verified the lateral growth of Sb_2Te_3 shell on Bi_2Te_3. The dried BTST powders were pressed into dense pellets by spark plasma sintering. Thermoelectric properties were measured in two different directions, in-plane and out-of-plane, and are anisotropic due to the nanostructure alignment within the pellets. All samples showed semiconductor character with the electrical resistivity decreasing with increasing temperature. The electrical resistivity decreases with lowering the ratio of Sb_2Te_3 to Bi_2Te_3. Thermal conductivity is also lowered due to interfaces and additional phonon scattering. We show that the out-of-plane direction of the BTST1-3 sample (where 1-3 indicates the ratio of BT to ST) demonstrates a high Seebeck value of 145 μV/K at 500 K which may be attributed to the filtering effect across the heterojunction interfaces. The highest overall *zT* is observed for the BTST1-3 sample on the out-of-plane direction at 500 K. The zT values increase in all range of measured temperature range, indicating a probable higher value at increased temperatures.

3.1. Introduction

Thermoelectric materials, enable the direct energy conversion between heat and electricity, hold promising capabilities of increasing energy waste harvesting and developing sustainable energy utilization. The energy conversion efficiency of thermoelectric devices is expressed as the dimensionless thermoelectric figure of merit $zT = S^2T/\rho\kappa$, in which S is the Seebeck coefficient, ρ the electrical resistivity, κ the total thermal conductivity (with contributions from lattice, κ_{lat}, and electrons, κ_e) and T the absolute temperature. Since S, ρ, and electronic component of κ (κ_e) are inter-related through carrier concentration, enhancing the thermoelectric efficiency (zT) is challenging.

Bi_2Te_3 and Sb_2Te_3 are two small bandgap semiconductors discovered decades ago since 1960,[1–3] and when alloyed or doped are still two of the best room-temperature thermoelectric materials. Over the decades, efforts have been devoted to enhancing the zT of these materials further. Examples include nanostructured Bi_2Te_3 (nanoparticles,[4] nanowires[5] and nanoplates[6]) which show significantly decreased thermal conductivity due to stronger phonon scattering and an enhanced Seebeck effect attributed to quantum confinement.[7,8] Bi_2Te_3 with nanopores show reduced thermal conductivity.[9] Alloying Bi_2Te_3 with Se,[10–14] and Sb_2Te_3 with Bi[15,16] modify the band structure and lead to improvement in overall zT. Dispersing nanoparticles in Bi_2Te_3[17] or Sb_2Te_3[18,19] matrix suppress grain growth, adding new interfaces and defects, which reduced thermal conductivity and enhance the Seebeck coefficient at higher temperature due to carrier filtering effect.

Recently, nanostructured heterojunction structures show combined benefits with enhanced thermoelectric properties attributed to strong energy filtering and phonon scattering.[8,20,21] Different Bi_2Te_3-based heterojunction systems have been studied and show improvement of zT.[22–27] In previous work, Bi_2Te_3 and Bi_2Se_3 core shell heterojunction structures have been synthesized successfully by a solution method with highly improved the power factor ($S^2\sigma$), and reduced thermal conductivities.[28]

Several studies exist on the effect of heterojunction structures on thermoelectric properties; however, few examples of p-n junction heterostructures have been reported. A p-n junction is seldom considered a promising way to improve zT due to the potential of detrimental σ and S. However, introducing an appropriate p-n junction could be beneficial to thermoelectric properties by manipulating carrier concentration to an optimal range. The p-n junction also potentially performs an energy filtering effect which could amplify S and may reduce the lattice thermal conductivity (κ_{lat}) by introducing interfaces. Mixtures of Bi_2Te_3 and Sb_2Te_3 bulk phases demonstrate enhancement on zT with reduced thermal conductivity and enhanced Seebeck coefficient.[29]

Inspired by these reports, we focused on the synthesis of Bi_2Te_3/Sb_2Te_3 heterojunction nanostructures and characterization of the resulting thermoelectric properties. The preferred orientation of the layered nanostructures provides new insight to the transport properties of bulk phases. Bi_2Te_3 and Sb_2Te_3 are both a rhombohedral structure with the same space group ($R\bar{3}m$). The lattice parameters for Bi_2Te_3 and Sb_2Te_3 are $a = b = 4.385$ Å, $c = 30.483$ Å and $a = b = 4.262$ Å, $c = 30.450$ Å, respectively, with a small lattice mismatch for the growth of a heterojunction structure, 2.8% on the a and b directions and 0.11% on the c direction. It has been reported that Bi_2Te_3/Sb_2Te_3 heterojunction structures could be synthesized successfully by a solvothermal method.[30] However, to obtain abundant product for thermoelectric device fabrication and measurement, a scalable reaction with well crystallized nanocomposites is required.

In this work, we report a two-step solution synthesis of highly crystalline Bi_2Te_3/Sb_2Te_3 lateral heterojunction structures with different core/shell (Bi_2Te_3/Sb_2Te_3) ratios. The as-synthesized nanoplates were characterized by powder X-ray diffraction (PXRD), scanning electron microscopy (SEM), transmission electron microscopy (TEM) and energy dispersive X-ray spectroscopy (EDS). The as-synthesized samples were annealed and pressed into pellet by spark plasma sintering (SPS) and their thermoelectric properties were characterized.

3.2. Experimental Section

3.2.1. Synthesis of Bi_2Te_3 Nanoplates

All syntheses of pristine Bi_2Te_3 and Bi_2Te_3/Sb_2Te_3 core-shell nanoplates were carried out by utilizing a bench top solution method. In a typical synthesis of Bi_2Te_3 nanoplates, 12 mmol (5.821 g) bismuth nitrate pentahydrate ($Bi(NO_3)_3 \cdot 5H_2O$, >99.9%, Sigma-Aldrich), 18 mmol (3.988 g) sodium tellurite (Na_2TeO_3, >99%, Sigma-Aldrich) were added into a 1 L 3-neck flask as precursors, and 0.4 g of poly(vinylpyrrolidone) (PVP, MW≈40,000, Sigma-Aldrich) was added and served as surfactant. A 200 mL of 0.375 M NaOH solution in ethylene glycol (EG, Sigma-Aldrich, used as received), which served as both solvent and reducing agent, was slowly poured into the 3-neck flask containing the mixed precursors. The mixture was stirred and sonicated until all precursors dissolved. The clear solution was then heated to 190 ^{o}C in a heating mantle with the flask equipped with a thermometer to monitor temperature and reflux condenser. Argon (Ar) gas flow was applied during the entire synthesis process. After 4.5 hours (including 0.5 h of heating process), the heating mantle was removed, and the finished reaction was naturally cooled to room temperature under Ar(g) flow. The product mixture was evenly distributed into eight 50 mL centrifuge tubes and 25 mL of acetone is added. The solution was centrifuged at 8500 rpm (10016 rcf) at room temperature for 5 min, then the dark supernatant was discarded and the silver-grey precipitate collected at the bottom of centrifuge tube was redispersed in 30 mL of ethanol. The precipitate was then washed with ethanol for two to three times to ensure the removal of all surfactant and unreacted ions. The final precipitate was dispersed in 30 ml ethanol and kept in the centrifuge tube for further reaction and characterizations.

3.2.2. Synthesis of Bi_2Te_3/Sb_2Te_3 Core-Shell Nanoplates

To synthesize Bi_2Te_3/Sb_2Te_3 core-shell hetero-structure, different ratios of as-synthesized Bi_2Te_3 and precursors of Sb_2Te_3 were added. In a typical synthesis of the 1:3 ratio of Bi_2Te_3/Sb_2Te_3 nanoplates, 1.5 mmol as-washed Bi_2Te_3 nanoplates (product collected from 2 centrifuge tubes) were precipitated by centrifugation and redispersed in 30 ml 0.5 M NaOH diethylene glycol solution. 9 mmol (2.690 g) antimony acetate ($Sb(OAc)_3$, >99.5%, Sigma-Aldrich), 13.5 mmol (2.991 g) sodium tellurite (Na_2TeO_3, >99%, Sigma-Aldrich) and 5 g poly(vinylpyrrolidone) (PVP, MW≈40,000, Sigma-Aldrich) were mixed in a one L 3-neck flask adding with 170 ml 0.5 M NaOH diethylene glycol solution and then added to the Bi_2Te_3 solution. The mixed solution was stirred and heated to 70°C to premix and dissolve the precursors. After 30 minutes, the solution was then heated to 215°C for 8 hours. Argon flow and a reflux condenser was equipped during the process. The product was washed with the same procedure as described for Bi_2Te_3.

3.2.3. Spark Plasma Sintering (SPS)

The washed sample was centrifuged. The supernatant decanted and the precipitation in the centrifuge tubes was dried under vacuum to remove all solvent. To totally dry the sample and remove the surfactant, the dried ingots were then placed in an alumina ceramic crucible boat and placed in a tube furnace with Ar flow. The tube furnace was flushed with Ar for 30 min at room temperature and then heated to 315°C and held for one hour. After the heating process, the ingots were then pumped into an Ar-filled glove box and ground into powder by an agate mortar and pestle. A 100-mesh sieve was used to exclude any large pieces, yielding ~3.5 - 5 g of fine powder. The sample was prepared for spark plasma sintering (SPS) and PXRD.

For all samples with different BTST ratio, powder (~4 g) was loaded into a 10-mm-diameter graphite die with graphite plungers and eight sheets of graphite foil on each side to ensure air-free conditions and avoid having the sample stick to the plungers. The die was inserted into a 20-mm-diameter graphite die with graphite plungers and then put into Dr. Sinter-Lab Jr. SPS-2ll LX with a thermocouple inserted into a hole drilled in the side of the die for precise temperature control. The BTST core shell powder was initially cold pressed at 31.8 Mpa for 3 min under ~385 Torr of Ar. After the cold press, the holding pressure was reduced to 19 Mpa. The pressure was increased to 89 MPa over 5 min and held for the remaining 10 min while the die was simultaneously heated from room temperature to 270 °C over 3 min and then to 300 °C over 1 min and held at 300°C for 11 min. The die was naturally cooled after the SPS process and a ~8-mm-thick gray/metallic puck was obtained. The thick puck was firstly cut along the circle plane into a 1-mm-thick disk and a 6-mm-thick pellet. The 6-mm-thick pellet was then cut along the vertical direction of the circle plane to get a 6 mm^2 1-mm-thick square disc. The two sample disks were then prepared for laser flash analysis (LFA), Hall effect, and Seebeck coefficient measurements. Sample density was geometrically determined. All samples were >90% of crystallographic density.

3.2.4. Characterization Methods

PXRD patterns of the as-synthesized solution samples were obtained by drop-casting an ethanol or isopropanol dispersion of nanoplates onto a fused silica holder. PXRD patterns of the as-ground powder were performed by solvent smearing the finely ground powder onto a zero-background diffraction holder. The prepared samples were scanned using Bruker D8 Advance diffractometer (Cu−Kα, 40 kV, 40 mA, $\lambda = 1.5418$ Å) in a 2θ range of 10°− 80°. Electron microscopy analyses on as-synthesized nanoplates were performed using a Thermo Fisher Quattro S SEM at an acceleration voltage at 5 kV and a JEOL JEM 2100F-AC transmission electron microscope (TEM) at an acceleration voltage of 200 kV. The SEM samples were prepared by drop-casting nanoplates solution in isopropanol onto a 1 × 1 cm^2 silicon substrate, followed by drying at room temperature. TEM samples were prepared by drop-casting dilute dispersions of Ge NCs in toluene onto either a continuous carbon film supported by a 400-mesh copper grid, or lacy carbon coated 400 mesh copper grid (Ted Pella). Digital Micrograph software provided by Gatan Inc. was used to capture images. To determine the composition and elemental distribution of a single nanoplate, energy dispersive spectroscopy (EDS) was employed.

Electronic measurements were performed to determine carrier transport. The Seebeck coefficient (S) was measured on a custom apparatus under high vacuum ($<10^6$ Torr) up to 200 ^oC. The quasi-steady slope method was employed to determine the Seebeck coefficient. In addition, both the Hall effect (R_H) and the electrical resistivity (ρ) were measured on a custom-built apparatus to 200 ^oC under same vacuum pressure as that for the Seebeck coefficient meausrement. The van der Pauw method, using nichrome pressure contacts, was used to deduce Hall and conductivity.

Thermal diffusivity was measured on both ~1-mm-thick round pellet and 6 mm^2 1-mm-thick square disc employing a Netzsch LFA 457 laser flash system. The sample discs were polished flat and parallel, sprayed with graphite to ensure laser absorption before the measurement. The thermal conductivity was calculated by $\kappa = D \cdot Cp \cdot \rho$, where D is the thermal diffusivity, Cp is the heat capacity, and ρ is the mass density of the samples. The constant pressure heat capacity (Cp) was estimated from empirical formulas by the Dulong−Petit law, and the density (ρ) values used here were calculated using the Archimedes' method at room temperature.

3.3. Results and Discussions

3.3.1. Nanoplates (NPs)

Bi_2Te_3 NPs with well-defined hexagonal shape were synthesized through a modified polyol method (see Experimental section).[11,13,31,32] The reaction was carried out in a NaOH/EG solution (0.375 M) with 20 ml scale and could be scaled up to 200 ml reaction which gave out around 4.5 g of Bi_2Te_3 with a yield over 95%. Figure 3.1a shows a typical SEM image of the as-synthesized Bi_2Te_3 NPs with well-defined hexagonal shapes and narrow dispersity. Over 150 Bi_2Te_3 NPs were measured and an average lateral size of 0.791 ± 0.113 µm was obtained. The corresponding histogram is shown in Figure 3.2. The purity of Bi_2Te_3 NPs was further characterized by PXRD (Figure 3.1b). In this polyol reaction, tellurium (Te) impurity in the form of nanorods is one common byproduct and controlling the reaction time is critical to synthesize pure and well-shaped Bi_2Te_3 NPs. We noticed that if the reaction time was not enough (less than 4 hours) at the set temperature of 190 oC, Te is present in the final product. Both PXRD patterns and SEM images showed the presence of Te (Figure 3.3a and 3.3b). If the reaction was held at the set temperature for over 6 hours, NPs with nanopores were obtained (Figure 3.4). Bi_2Te_3 NPs with nanopores were reported when the NPs were heated in EG (ethylene glycol).[33] They found that both temperature and reaction time are critical to the formation of the nanopores.[33] This result correlates with our observation in this work, even for the reaction in NaOH/EG solution.

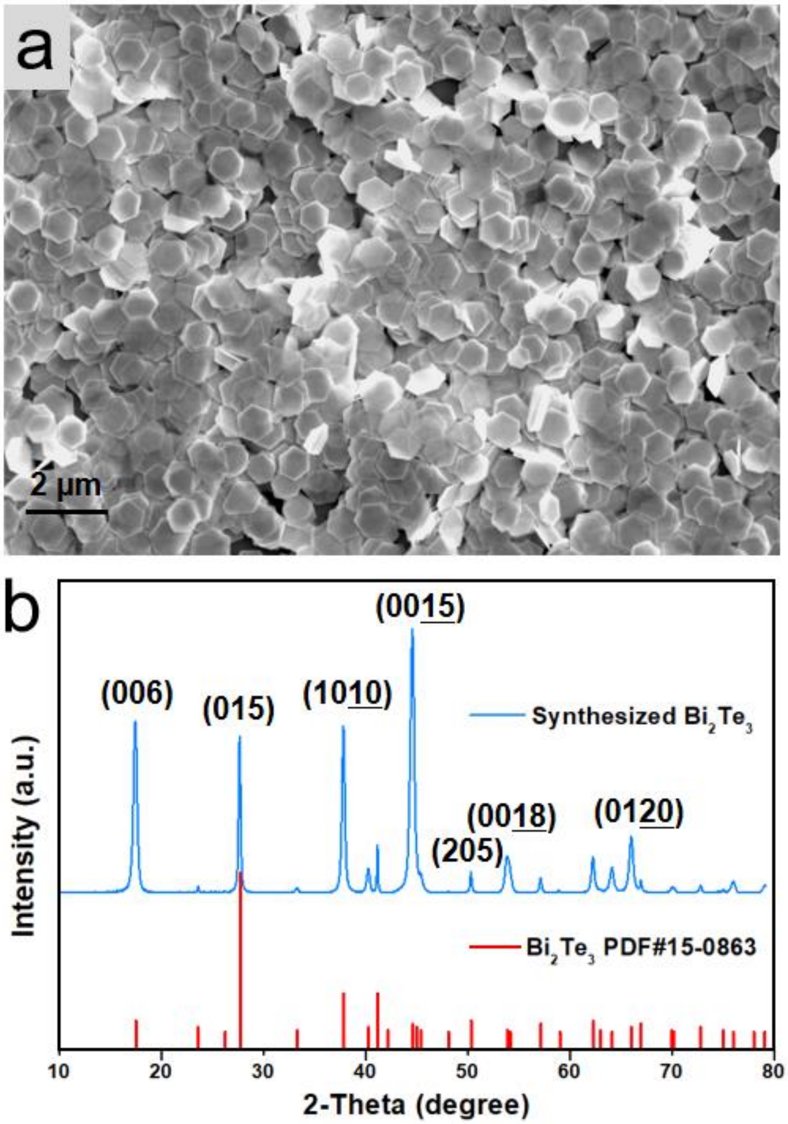

Figure 3.1. a. SEM image of as-synthesized Bi_2Te_3 nanoplates with narrow size distribution. b. XRD pattern of Bi_2Te_3 shows high purity.

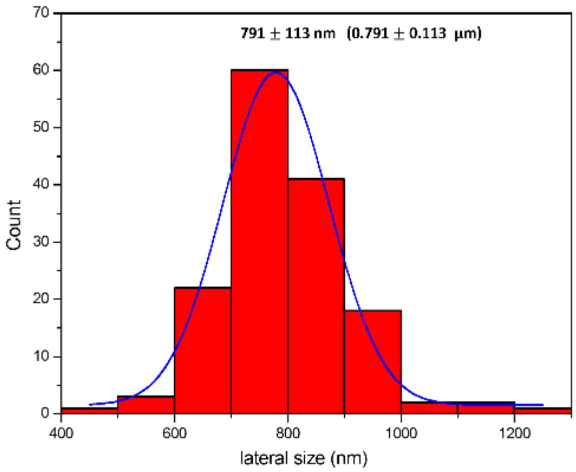

Figure 3.2. Histogram of as-synthesized Bi_2Te_3 nanoplates showing a narrow size distribution.

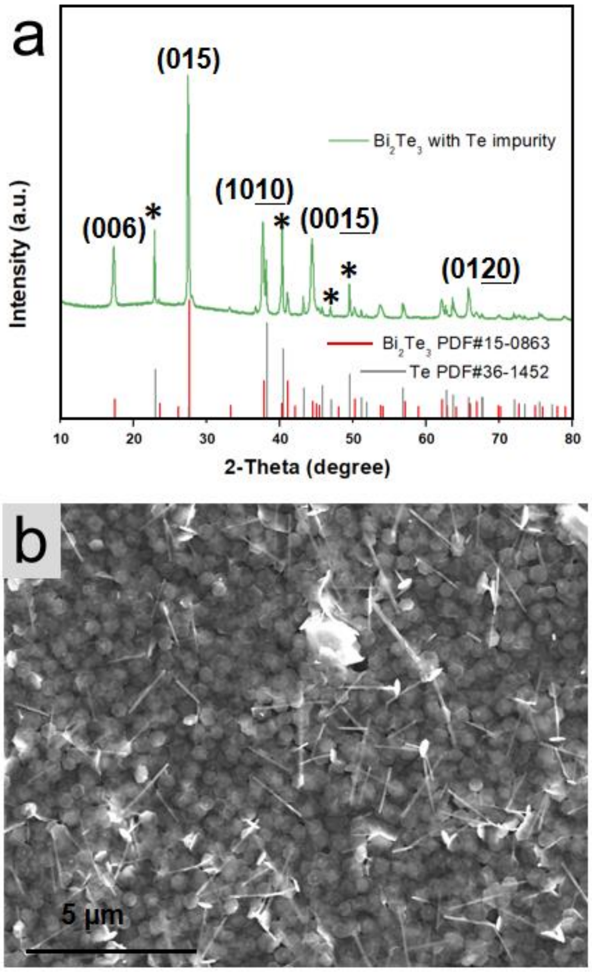

Figure 3.3. a. XRD pattern and b. SEM image of Bi_2Te_3 reaction for times shorter than the critical time and showed an impurity of Te nanorods.

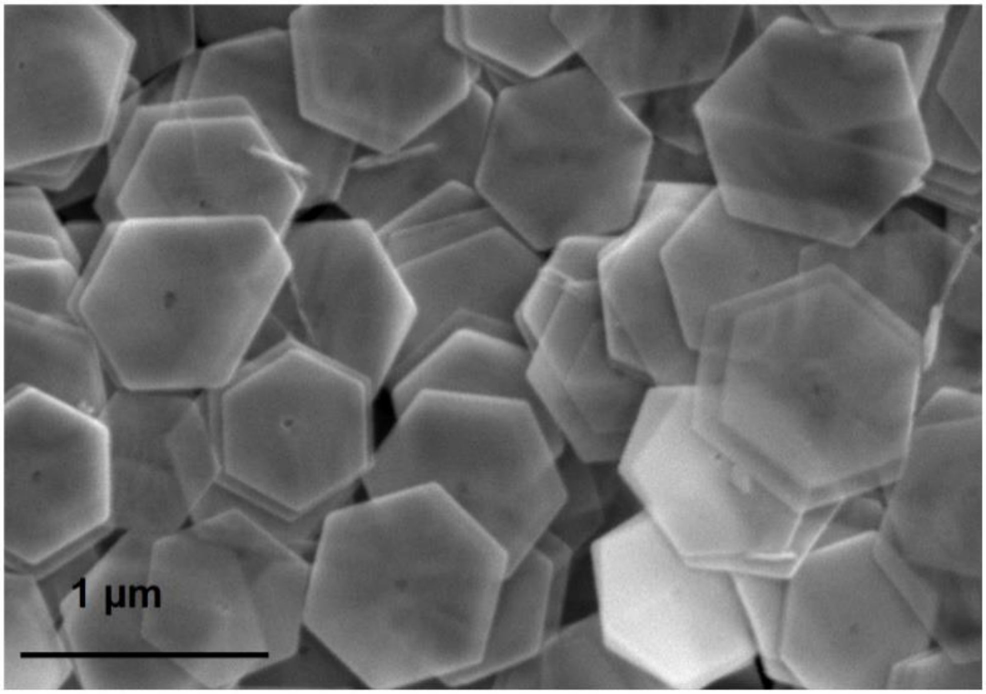

Figure 3.4. SEM image of NPs with nanopores from the reaction where the reaction time was too long.

Both Bi_2Te_3 and Sb_2Te_3 are layer structured materials with rhombohedral crystal structure. The covalently bonded Bi_2Te_3 and Sb_2Te_3 sheets are arranged in quintuple layers. And those quintuple layers are stacked by weak van der Waals interactions along the *c*-axis. The mismatches on the *a* and *b* axis (lateral direction) are less than 3 % and negligible (< 0.1%) on the *c* axis (vertical direction). The isomorphic structure and small lattice mismatch both make epitaxial growth possible.

Bi_2Te_3/Sb_2Te_3 core/shell structures were synthesized starting with as-prepared pure Bi_2Te_3 as the core. In the discussion of these samples, we use BTST1-X to represent the Bi_2Te_3:Sb_2Te_3 samples with different core to shell ratios, where the 'X' is the multiples of the theoretical Sb_2Te_3 precursor amount to that of Bi_2Te_3. Figure 3.5 represents PXRD patterns of all synthesized BTST samples with the ratio from 1-2 to 1-9 and compared with a pure Bi_2Te_3 sample as a reference. No impurities were detected in any of these samples indicating a complete reaction of the shell. A moderate heating with a rate of 5 ~ 7 °C is essential for obtaining a small size distribution.

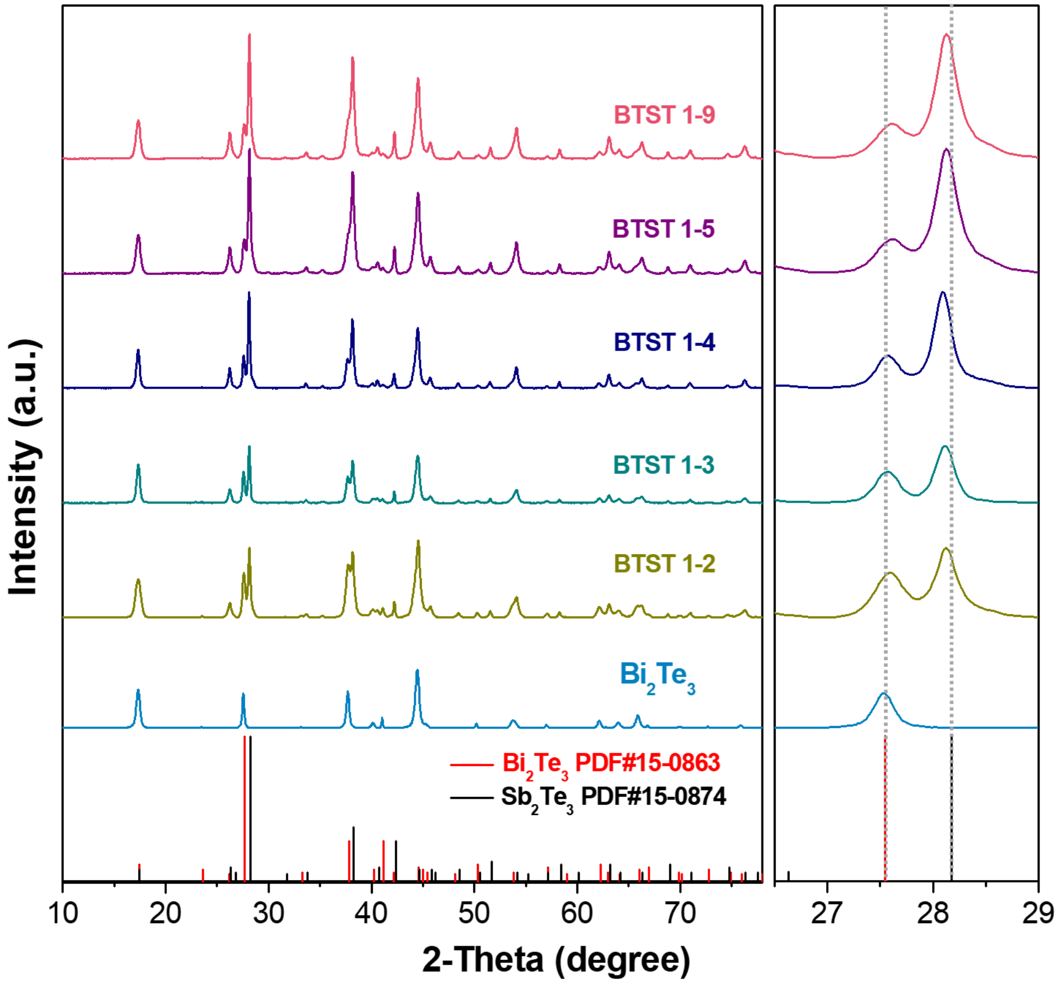

Figure 3.5. Representative XRD pattern of pure Bi_2Te_3 NPs and BTST solution synthesized NPs with different Bi_2Te_3: Sb_2Te_3 ratios with the standard Bi_2Te_3 (PDF#15-0863) and Sb_2Te_3 (PDF#15-0874) XRD patterns as references. An expanded XRD pattern with the range of (27–29°) is shown on the right, and referenced to the pristine structures showing the change of the peak intensities for different Bi_2Te_3: Sb_2Te_3 ratios.

The patterns between the range of 27° - 29° clearly show the relative ratio of Bi_2Te_3:Sb_2Te_3. The red and black vertical lines at the bottom are the standard peak position of the (015) planes belonging to Bi_2Te_3 and Sb_2Te_3, respectively. It can be clearly observed that with increasing amount of Sb_2Te_3 shell, the Sb_2Te_3 peak shifts to higher 2-theta angleand closer to the standard, while the Bi_2Te_3 peak intensity remains the same and shifts slightly to higher 2θ for the higher ratio BTST 1-5 and 1-9 samples. The shifting of the Sb_2Te_3 peak is not consistent with cation diffusion between Bi and Sb. Since the radius of Bi is larger than that of Sb, the cation exchange should induce a shifting to the left (larger unit cell) for Sb_2Te_3 and to the right (smaller unit cell) for Bi_2Te_3. If there was cation diffusion, both should be shifting in a compensating manner. We attribute the left shift of the XRD peak to the lattice expansion of the Sb_2Te_3 shell. When the Sb_2Te_3 grows on the surface of Bi_2Te_3 in the solution, the first few attached atoms of Sb_2Te_3 would expand to match the lattice of Bi_2Te_3, which may cause the lattice expansion of Sb_2Te_3. As the Sb_2Te_3 shell amount increases, the interaction of the Sb_2Te_3 compared to the Bi_2Te_3 decreases and the XRD peak become closer to the standard. This lattice expansion has been observed across the interface between Bi_2Te_3 and Sb_2Te_3 in a similar core/shell structure synthesized *via* a solvothermal method.[30]

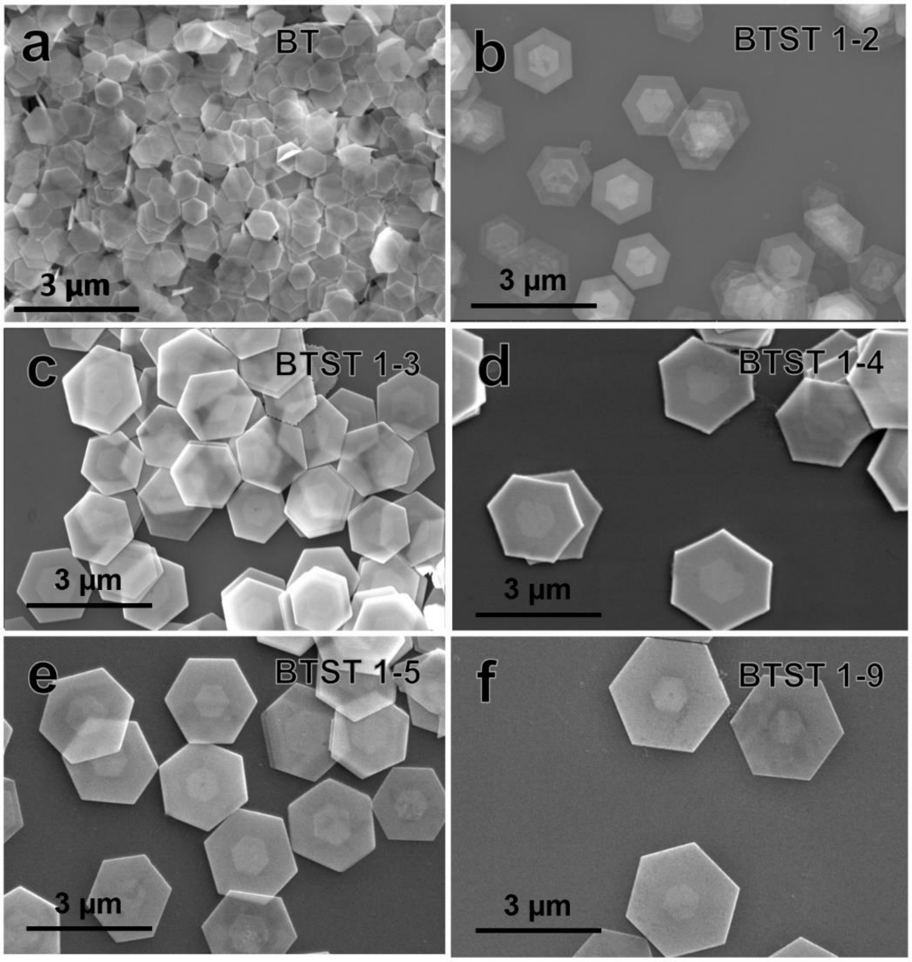

Figure 3.6. SEM images of BTST core-shell NPs with different Bi_2Te_3:Sb_2Te_3 ratios indicated.

SEM images of these core-shell NPs are presented in Figure 3.6. As synthesized core-shell NPs show distinct hexagonal shapes indicating the crystalline nature of the shells. Clear interfaces were observed on almost every single NP, demonstrating the homogeneous growth of the Sb_2Te_3 shell on the a and b crystal directions. The area ratios of the shells to cores are calculated by squaring the lateral length, and are very close to that of the employed precursor amount. Calculated precursor ratios and the area ratios measured on over 50 nanoplates are summarized in Table 3.1. The similarity of the area ratios with the precursor ratios, indicating the growth of the Sb_2Te_3 shell takes place mostly on the lateral direction rather than the vertical of the Bi_2Te_3 plate. This can be explained by the different bond types. Lateral growth forms stronger covalent bonds than the weaker van der Waals interactions that are required for the vertical growth direction. The surfactant, PVP, also facilitate the lateral growth by the attachment to the surface. It has been reported that PVP serves as a surface stabilizer, growth modifier and nanoparticle dispersant under many different conditions.[34] More importantly, it is a shape control agent by binding to some facets and thereby promoting growth of others.[35–37] PVP, as the surfactant, plays an important role in the synthesis of many two dimensional nanostructures.[38–41]

Table 3.1. Stoichiometric (precursor) ratio Bi_2Te_3: Sb_2Te_3 and the core shell NP ratios calculated by the areas from SEM images

Stoichiometric (precursor) ratio Bi_2Te_3: Sb_2Te_3	**Area ratios calculated from SEM images Bi_2Te_3: Sb_2Te_3**
1 : 2	1 : 2.02 (± 0.17)
1 : 3	1 : 3.13 (± 0.34)
1 : 4	1 : 4.05 (± 0.25)
1 : 5	1 : 5.22 (± 0.44)
1 : 9	1 : 9.56 (± 0.87)

Scanning transmission electron microscope (STEM) was employed to further characterize the BTST NPs samples. A sharp contrast of the core and the shell is shown in Figure 3.7a of a BTST 1-3 sample. High resolution TEM (HRTEM) images are taken on both the core and the shell area, which show the highly crystalline nature of Bi_2Te_3 and Sb_2Te_3. The lattice fringes are clearly observed and measured as 0.219 nm and 0.214 nm for core and shell, corresponding to the lattice parameter of $(11\overline{2}0)$ phase of Bi_2Te_3 and Sb2Te3, respectively. We conducted energy dispersive X-ray spectroscopy (EDS) mapping on a single BTST 1-3 core-shell NP. Figure 3.7b-3.7d represent the EDS results showing clear elemental mapping with bismuth located on the core region and antimony mostly on the shell region. Tellurium is uniformly distributed over the entire NP. Selected area EDS spectrum (Figure 3.8) also indicates the Bi_2Te_3 nature of the core and Sb_2Te_3 on the shell with the elemental ratio close to the nominal values. To investigate the sharpness of the interface, a line scan across the NP was taken. As showed in Figure 3.7e, a sharp decrease of bismuth and an increase of antimony are observed in a length scale of 40 nm as the scan crosses the interface region. 4 % of the Sb signals are also detected on the core region, indicating not only lateral growth but also vertical growth of the shell. While there is enough thermal energy, in the form of temperature for this reaction to drive the growth in both directions, the formation of covalent bonds better decreases the overall potential energy. Thus, the lateral growth dominates over the vertical one resulting in a very thin shell of Sb_2Te_3 across the top of the Bi_2Te_3 core.

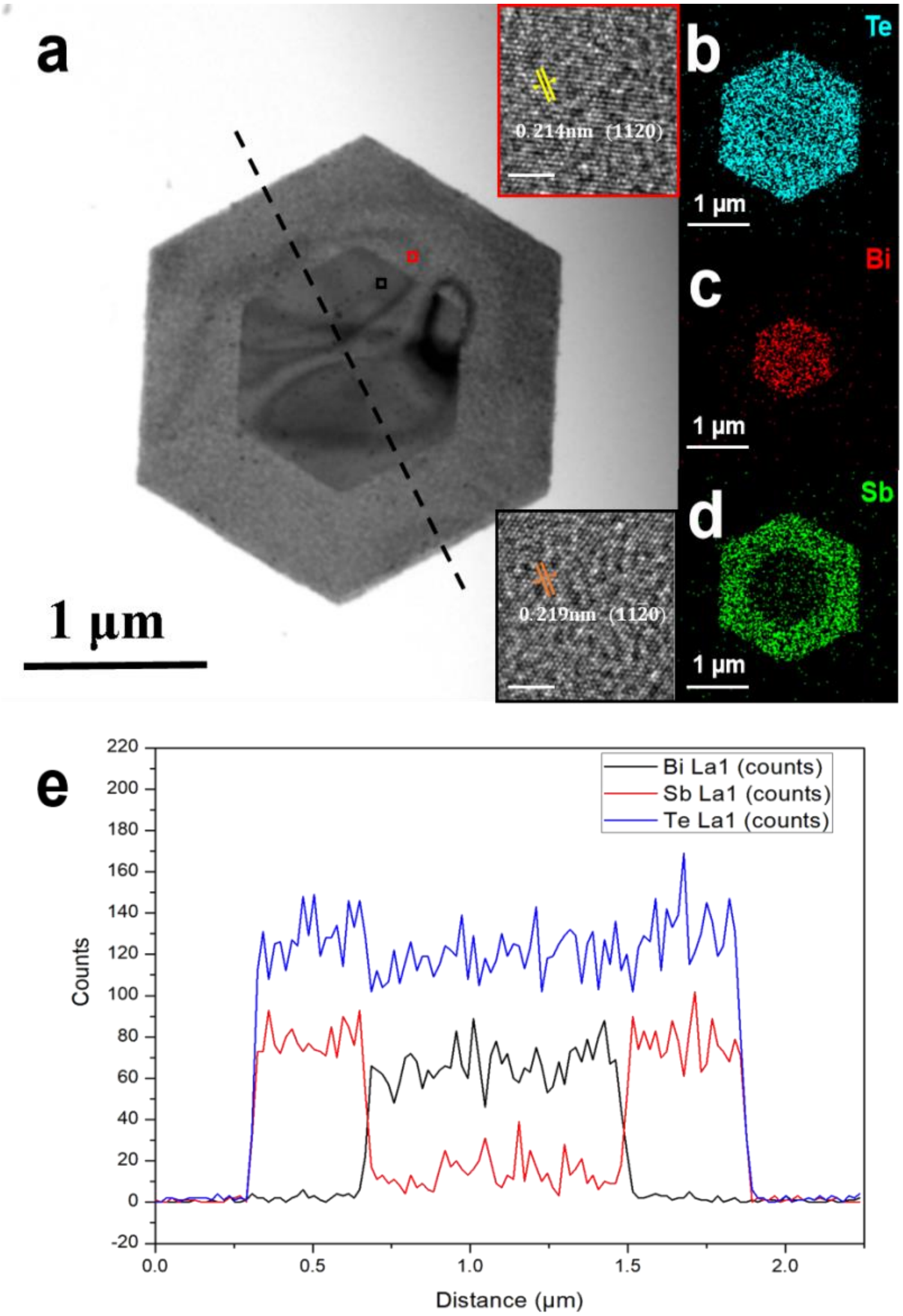

Figure 3.7. (a) EDS mapping image of a typical Bi_2Te_3/Sb_2Te_3 coreshell (BTST1-3) NP. Bismuth is mainly located on the core region and antimony is on the shell region, tellurium is evenly distributed on the entire NP, indicates a lateral heterojunction structure. (b) The line scan EDS across the whole NP. While the scan across the interface of core and shell, a sharp change of bismuth and antimony amounts are observed, indicates the strong sharpness of interface.

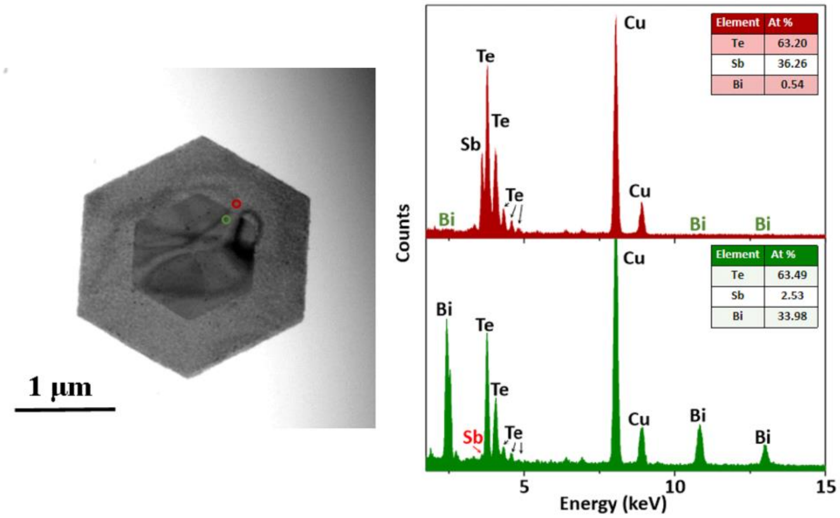

Figure 3.8. Selected area EDS spectrum indicates the Bi_2Te_3 nature of core part (green) and Sb_2Te_3 on the shell (red) with the elemental ratio close to the nominal values.

3.3.2. Characterization of pressed pellet

All synthesized NPs were precipitated by centrifugation, followed with vacuum drying at room temperature and annealed at 315 °C under Ar flow for 60 min in a tube furnace to remove excess surfactant, similar to that described in previous work by Liu *et al.*[11,16] Subsequently, the annealed products (~4 g) were ground into fine powder in an Ar filled glove box with an agate mortar and pestle. The annealed powder was characterized with PXRD, and corresponding patterns are shown in Figure 3.9. The enlarged 2θ range from 27– 29° shows the (015) peaks of Bi_2Te_3 and Sb_2Te_3 from the as-grown solution products (middle) and the annealed samples (right). As shown in the enlarged range, we observed the Sb_2Te_3 peak is well-aligned with the (015) peak, while the Bi_2Te_3 (015) peak shifts to the right with the increasing amount of Sb_2Te_3 shell. This may result from strain release of the Sb_2Te_3 shell structure upon heating, which transfers the strain to the Bi_2Te_3 lattice. If ion migration was happening, the two peaks should be moving closer together in unison.

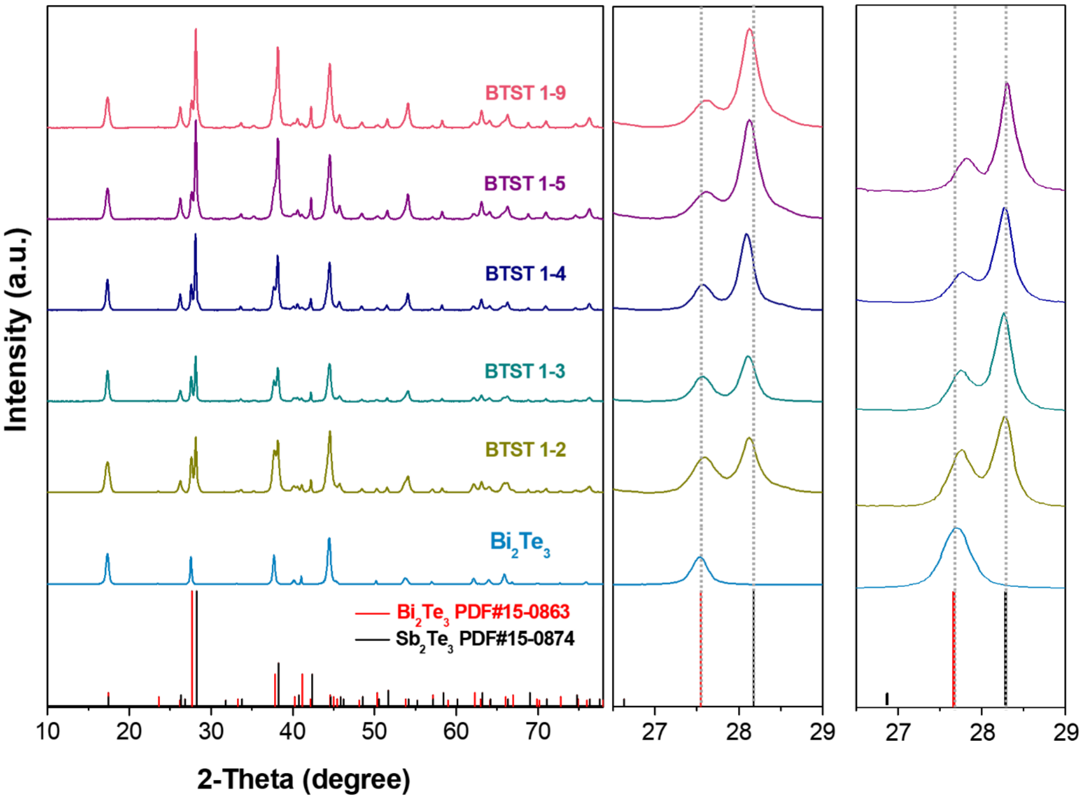

Figure 3.9. Representative XRD pattern of annealed pure Bi_2Te_3 NPs and BTST NPs powders with different Bi_2Te_3: Sb_2Te_3 ratios. The standard Bi_2Te_3 (PDF#15-0863) and Sb_2Te_3 (PDF#15-0874) XRD patterns as references. An enlarged XRD pattern is shown on the right with the range of (27– 29^o) and compared with the XRD of solution synthesized samples in the same range, as shown in the middle.

Wang *et al.* reported in 2018 that $(Bi_2Te_3)_x$-$(Sb_2Te_3)_{1-x}$ performed with the highest figure of merit zT when x = 0.15.[29] Thus, in this work, we start with the core-shell nano heterojunction samples with similar ratios. The as-prepared powders were hot pressed at 400 °C through spark plasma sintering (SPS), resulting in cylindrical pellets. To obtain a dense pellet from the nanostructured powder ~85 MPa was applied during the SPS process. Density of the as-pressed pellets were measured by Archimedes' principle. Densities over 91% were obtained for all pressed samples compared with theoretical density of a mixture of Sb_2Te_3 and Bi_2Te_3 with respective ratios.

Since NPs naturally aligned with preferred orientation,[40] and previous work showed strong anisotropic properties for different directions (parallel and perpendicular to pressure),[11,16,28] we also characterized the as-pressed pellet in both directions, in-plane (lateral) and out-of-plane (vertical). As described in the Experimental section, a cylindrical pellet was cut from the 10 mm diameter sample puck and a square sample cut along the press direction. Therefore, the properties of each sample puck are measured along the (00l) planes for the in-plane direction, while for the out-of-plane direction is vertical to (00l) planes.

XRD patterns of a typical BTST1-3 sample with different directions confirmed the strong preferred orientations with [001] crystallographic direction aligned parallel to the press direction (Figure 3.10a). SEM images of the cross section of consolidated pellet showed layered microstructures, double verified the aligned NPs, shown in Figure 3.10b. Hexagonal nanoplates could be observed in top view of the SEM image (Figure 3.10c) of a cracked pellet indicating the SPS process did not remove the nature of nanoplates of these heterojunction structures.

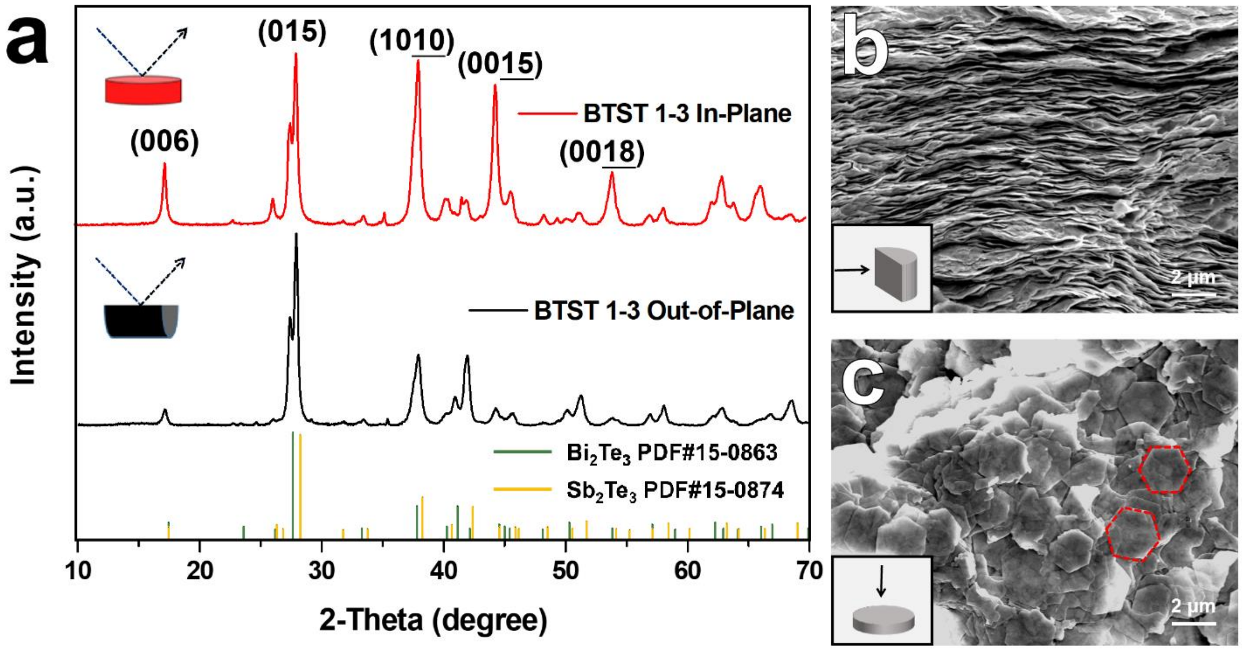

Figure 3.10. (a) XRD patterns for a typical BTST 1-3 sample with the sample oriented in two directions, as diagramed for each diffraction pattern. The black pattern is out-of-plane direction and red is in-plane. (b) A cross view of the SEM image showing the layered stacking of nanoplates with a strong preferred orientation. Scale bar is 2 µm (c) Top view SEM image of a pressed pellet. Some hexagonal nanoplates can be observed (red dashed areas), which indicates the SPS process did not melt the nanoplates.

3.3.3. Thermoelectrical Characterizations

Temperature dependence of electrical resistivity (ρ) and Seebeck coefficient (S) of two directions of BTST 1-3, BTST 1-5, BTST 1-9 and Sb_2Te_3 (ST) samples from room temperature, 300 K, to 500 K are illustrated in Figure 3.11. The carrier concentration (n_H) and the calculated mobility (μ_H) are plotted in Figure 3.12. And thermal conductivity (κ), the total thermal conductivity subtracted the electronic component (κ - κ_e) and the overall thermoelectric figure of merit (zT) of these samples are provided in Figure 3.13.

As shown in Figure 3.11a, all the BTST samples and pure ST sample show the electrical resistivity decreasing with the increasing temperature over the measured temperature range, consistent with a degenerate semiconductor. The pure ST sample only has the interfaces between the nanoplates while in the BTST samples, additional interfaces of the core/shell are added. The electrical resistivity (ρ) is low for the pure ST sample and upon the formation of core/shell interfaces, increases for BTST 1-3, after which all samples decrease systematically with the increasing Sb_2Te_3 amount. Whereas Bi_2Te_3 is generally an n-type semiconductor with the positively charged anti-site defects of Te_{Bi}, Sb_2Te_3 is typical p-type.[42–44] In our BTST samples, carriers of holes from Sb_2Te_3 dominate and make the samples overall p-type. Increasing the Sb_2Te_3 shell introduces more p-type carriers and hence reduces the electrical resistivity.

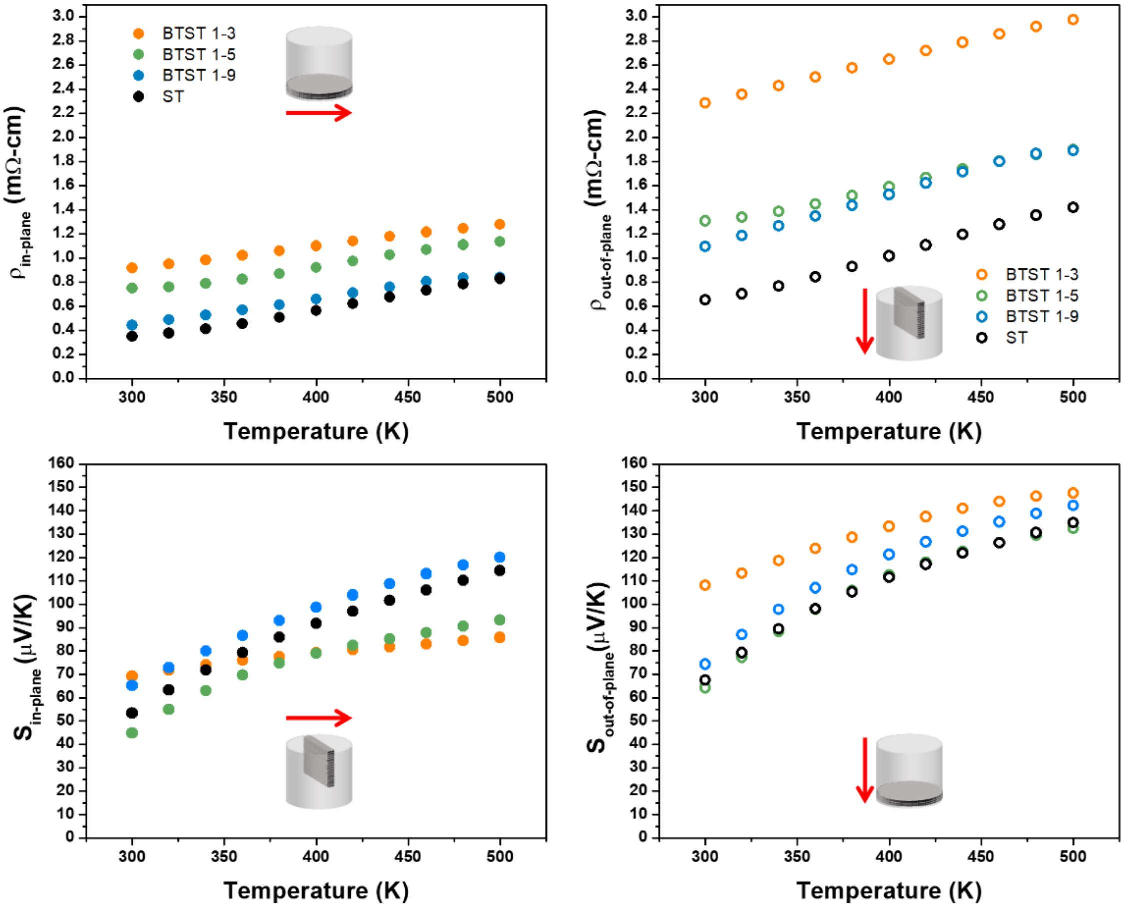

Figure 3.11. Thermoelectric properties of Sb_2Te_3 (ST) and BTST 1-x (x = 3, 5 and 9) samples measured in the in-plane and out-of-plane directions. The measurement direction and sample are schematically shown in the figures. a. In-plane electrical resistivity, $\rho_{in\text{-}plane}$. b. Out-of-plane electrical resistivity, $\rho_{out\text{-}of\text{-}plane}$. c. In-plane Seebeck coefficient, $S_{in\text{-}plane}$. d. Out-of-plane Seebeck coefficient, $S_{out\text{-}of\text{-}plane}$.

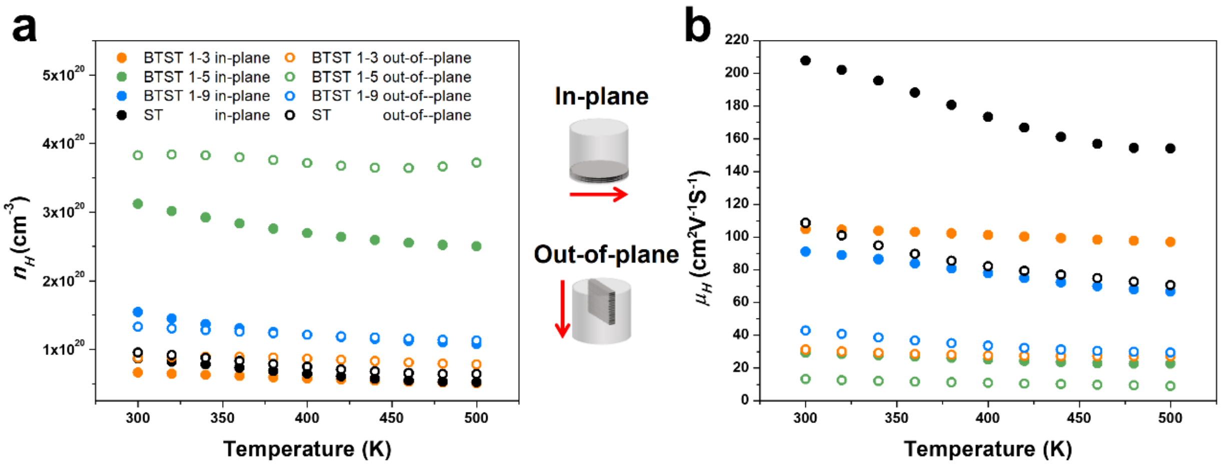

Figure 3.12. Transport properties of Sb_2Te_3 (ST) and BTST 1-x (x = 3, 5 and 9) samples measured in the in-plane and out-of-plane directions. The measurement direction and sample are schematically shown in the figures. a. Carrier concentration, n_H. b. Carrier mobility, μ_H.

As expected, the ρ of the in-plane direction, along the *a*,*b* crystal plane, is almost half that of the out-of-plane direction, along the *c* axis. Similar observations were reported in highly crystallographically textured nanoplate samples.[11,16] The highly aligned nanoplates in the pressed pellet have less interfaces along the in-plane direction. Naturally, out-of-plane samples have larger resistivities than their in-plane counterparts likely due to an increase of scattering as a result of additional interfaces within the system. Both Bi_2Te_3 and Sb_2Te_3 are layered structures with covalently bonded in-plane and weak Van der Waals interactions out-of-plane. Samples with decreasing Sb_2Te_3 ratios yield higher resistivities as evident from BTST 1-3 out-of-plane sample exhibiting a room temperature resistivity near 2.3 mΩ-cm. As the ratio of Sb_2Te_3 to Bi_2Te_3 increases, the resistivity decreases likely due to the increased homogeneity of the system.

The carrier concentrations, n_H, measured by the Van der Pauw method show an unexpected trend. The carrier concentration of the Sb_2Te_3 sample is relatively low for the measured temperature range. While the n_H increases with more Sb_2Te_3 in BTST 1-9 and 1-5 samples, it shows a significant drop in BTST1-3. The n_H increase from ST to BTST1-9 and BTST1-5 samples may be attributed to bipolar conduction: the sum of both the p and n carriers. The drop of n_H in sample BTST 1-3 compared to ST may be attributed to changes in band alignment for the nanostructured BTST sample. In BTST 1-3, the Bi_2Te_3 core may serve as a trap for p carriers and reduced the overall n_H. Further characterization and simulation are required to understand this non-systematic trend of the n_H. The mobility measurement indicates a strong anisotropic transport in the two different directions. The pure Sb_2Te_3 (ST) samples show a high mobility, μ_H, of 207 $cm^2 \cdot V^{-1} \cdot s^{-1}$ in-plane and 108 $cm^2 \cdot V^{-1} \cdot s^{-1}$ out of plane at 300 K. While the other BTST samples demonstrate decreasing mobility attributed to the introduction of heterointerfaces between Bi_2Te_3 and Sb_2Te_3; the anisotropy of the two different directions is conserved.

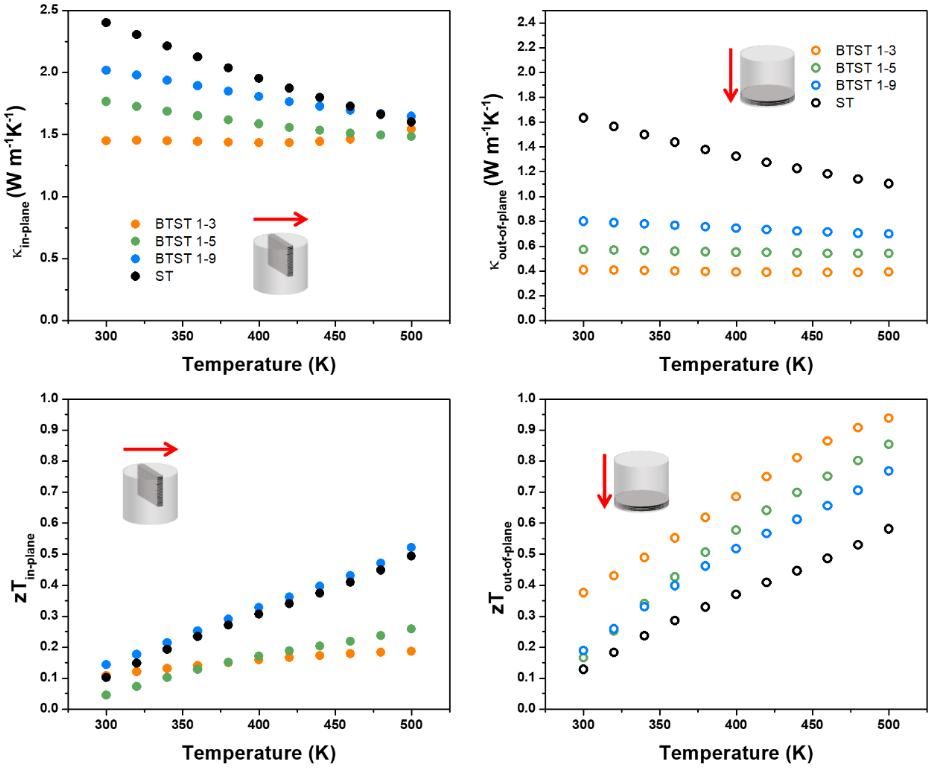

Figure 3.13. Thermoelectric properties of Sb_2Te_3 (ST) and BTST 1-x (x = 3, 5 and 9) pressed samples measured in the in-plane and out-of-plane directions. The measurement direction and sample are schematically shown in the figures. a. In-plane thermal conductivity, $\kappa_{in-plane}$. b. Out-of-plane plane thermal conductivity, $\kappa_{out-of-plane}$. c. In-plane figure of merit, $zT_{in-plane}$. d. Out-of-plane figure of merit, $zT_{out-of-plane}$.

Positive Seebeck coefficient values were obtained in all measured BTST samples over the temperature range, in agreement with the overall p-type character of the Sb_2Te_3 matrix. However, no clear trend could be extracted from the plots, since the Seebeck coefficient, S, not only involves the carrier concentration but also the nanostructure alignment and compositions. The BTST 1-3 sample shows the highest Seebeck value on the out-of-plane direction. This could be attributed to the filtering effect by the p- and n- junction.[29] Similar to what is observed for the electrical resistivity, the Seebeck coefficient is consistently lower for cross-plane samples. This result supports the suggestion provided above that increased scattering interactions are leading to a large change in transport.

With the preferred orientations of the pressed pellets, all samples showed anisotropic transport properties between in-plane and out-of-plane. Unsurprisingly, similar observations are shown for thermal conductivities (κ). The κ measured out-of-plane is significantly lower than that of in-plane with all BTST ratios. For example, BTST 1-5 sample gives a ratio of ~3 of the $\kappa_{\text{in-plane}}/\kappa_{\text{out-of-plane}}$. The κ decreases with the increasing temperature, which can be attributed to the high κ_e at high temperature. Within the measurements along the same directions, lower κ was obtained with lower ratio Sb_2Te_3 to Bi_2Te_3 samples. With lower shell ratios, the overall interfaces in the system increases, and the increased amount of heterojunction interfaces enhanced the phonon scatterings and reduce the thermal conductivity.

Overall, all the different BTST samples measured showed anisotropic properties and enhancement of the overall zT was calculated. BTST 1-9 sample showed a slight enhancement on the overall zT with a value of 0.52 at 500 K along the in-plane direction. BTST 1-3 sample gave out a relatively large increase of zT with a value of 0.94 at 500 K for out-of-plane. This result may be attributed to the high Seebeck coefficient value that derives from a strong filtering effect. Out-of-plane zT

values were systematically higher than that of in-plane *zT* values, due to both the enhanced Seebeck coefficient and decreased thermal conductivity along the out-of-plane direction. All the *zT* values increase in the measured temperature range of 300 - 500 K without reaching a peak point, indicating a possible higher *zT* at a higher temperature.

3.4. Conclusion

This work provides a scalable solution route for the successful synthesis of Bi_2Te_3/Sb_2Te_3 lateral core-shell nanostructured heterojunctions with different ratios. The samples are characterized by XRD and show lattice expansion of Sb_2Te_3 which may be attributed to the lattice mismatch. With annealing, the stress is relieved and transferred to Bi_2Te_3 lattice. SEM and TEM images clearly showed the interfaces between the shell and core. The shell to core ratios calculated by the areas in SEM images indicates the preferred lateral growth *versus* vertical growth. The Bi_2Te_3/Sb_2Te_3 nanostructures in the SPS pressed pellets showed strong preferred orientation which was confirmed by SEM and XRD. The alignment of the nanoplates created anisotropic transport properties: in-plane, and out-of-plane. All samples showed degenerate semiconductor character in measurements. The electrical resistivity and thermal conductivity decreased with increasing the Sb_2Te_3 to Bi_2Te_3 ratio. The Seebeck coefficient depended on both the direction and composition. We found that the out-of-plane direction of the BTST1-3 sample provided a high Seebeck value which could be attributed to the filtering effect across the heterointerfaces. The highest overall *zT* was observed with BTST 1-3 sample on the out-of-plane direction at 500 K. The *zT* values increased over the measured temperature range, indicating a probable higher value at higher temperatures.

3.5. References of Chapter 3

(1) Smith, G. E.; Wolfe, R. Thermoelectric Properties of Bismuth-Antimony Alloys. *J. Appl. Phys.* **1962**, *33* (3), 841–846. https://doi.org/10.1063/1.1777178.

(2) Bergvall, P.; Beckman, O. Thermoelectric Properties of Non-Stoichiometric Bismuth-Antimony-Telluride Alloys. *Solid State Electron.* **1963**, *6* (2), 133–136. https://doi.org/10.1016/0038-1101(63)90006-6.

(3) Walker, P. A. The Thermal Conductivity and Thermoelectric Power of Bismuth Telluride at Low Temperatures. *Proc. Phys. Soc.* **1960**, *76* (1), 113–126. https://doi.org/10.1088/0370-1328/76/1/314.

(4) Scheele, M.; Oeschler, N.; Meier, K.; Kornowski, A.; Klinke, C.; Weller, H. Synthesis and Thermoelectric Characterization of Bi2Te 3 Nanoparticles. *Adv. Funct. Mater.* **2009**, *19* (21), 3476–3483. https://doi.org/10.1002/adfm.200901261.

(5) Zhang, G.; Kirk, B.; Jauregui, L. A.; Yang, H.; Xu, X.; Chen, Y. P.; Wu, Y. Rational Synthesis of Ultrathin N-Type Bi 2Te 3 Nanowires with Enhanced Thermoelectric Properties. *Nano Lett.* **2012**, *12* (1), 56–60. https://doi.org/10.1021/nl202935k.

(6) Son, J. S.; Choi, M. K.; Han, M. K.; Park, K.; Kim, J. Y.; Lim, S. J.; Oh, M.; Kuk, Y.; Park, C.; Kim, S. J.; Hyeon, T. N-Type Nanostructured Thermoelectric Materials Prepared from Chemically Synthesized Ultrathin Bi 2Te 3 Nanoplates. *Nano Lett.* **2012**, *12* (2), 640–647. https://doi.org/10.1021/nl203389x.

(7) Nielsch, K.; Bachmann, J.; Kimling, J.; Böttner, H. Thermoelectric Nanostructures: From Physical Model Systems towards Nanograined Composites. *Advanced Energy Materials*. 2011, pp 713–731. https://doi.org/10.1002/aenm.201100207.

(8) Zhang, G.; Yu, Q.; Wang, W.; Li, X. Nanostructures for Thermoelectric Applications: Synthesis, Growth Mechanism, and Property Studies. *Adv. Mater.* **2010**, *22* (17), 1959–1962. https://doi.org/10.1002/adma.200903812.

(9) Wu, Z.; Mu, E.; Che, Z.; Liu, Y.; Sun, F.; Wang, X.; Hu, Z. Nanoporous (00l)-Oriented Bi2Te3 Nanoplate Film for Improved Thermoelectric Performance. *J. Alloys Compd.* **2020**, *828*, 154239. https://doi.org/10.1016/j.jallcom.2020.154239.

(10) Hong, M.; Chasapis, T. C.; Chen, Z. G.; Yang, L.; Kanatzidis, M. G.; Snyder, G. J.; Zou, J. N-Type Bi2Te3-XSex Nanoplates with Enhanced Thermoelectric Efficiency Driven by Wide-Frequency Phonon Scatterings and Synergistic Carrier Scatterings. *ACS Nano* **2016**, *10* (4), 4719–4727. https://doi.org/10.1021/acsnano.6b01156.

(11) Liu, Y.; Zhang, Y.; Lim, K. H.; Ibáñez, M.; Ortega, S.; Li, M.; David, J.; Martí-Sánchez, S.; Ng, K. M.; Arbiol, J.; Kovalenko, M. V.; Cadavid, D.; Cabot, A. High Thermoelectric Performance in Crystallographically Textured N-Type Bi2Te3- XSex Produced from Asymmetric Colloidal Nanocrystals. *ACS Nano* **2018**, *12* (7), 7174–7184. https://doi.org/10.1021/acsnano.8b03099.

(12) Yan, X.; Poudel, B.; Ma, Y.; Liu, W. S.; Joshi, G.; Wang, H.; Lan, Y.; Wang, D.; Chen, G.; Ren, Z. F. Experimental Studies on Anisotropic Thermoelectric Properties and Structures of N-Type Bi2Te2.7Se0.3. *Nano Lett.* **2010**, *10* (9), 3373–3378. https://doi.org/10.1021/nl101156v.

(13) Soni, A.; Yanyuan, Z.; Ligen, Y.; Aik, M. K. K.; Dresselhaus, M. S.; Xiong, Q. Enhanced Thermoelectric Properties of Solution Grown Bi 2Te 3-XSe x Nanoplatelet Composites. *Nano Lett.* **2012**, *12* (3), 1203–1209. https://doi.org/10.1021/nl2034859.

(14) Li, D.; Qin, X. Y.; Liu, Y. F.; Wang, N. N.; Song, C. J.; Sun, R. R. Improved Thermoelectric Properties for Solution Grown Bi2Te 3-XSex Nanoplatelet Composites. *RSC Adv.* **2013**, *3* (8), 2632–2638. https://doi.org/10.1039/c2ra22562j.

(15) Blank, V. D.; Buga, S. G.; Kulbachinskii, V. A.; Kytin, V. G.; Medvedev, V. V.; Popov, M. Y.; Stepanov, P. B.; Skok, V. F. Thermoelectric Properties of Bi 0.5Sb 1.5Te 3/C 60 Nanocomposites. *Phys. Rev. B - Condens. Matter Mater. Phys.* **2012**, *86* (7), 75426. https://doi.org/10.1103/PhysRevB.86.075426.

(16) Liu, Y.; Zhang, Y.; Ortega, S.; Ibáñez, M.; Lim, K. H.; Grau-Carbonell, A.; Martí-Sánchez, S.; Ng, K. M.; Arbiol, J.; Kovalenko, M. V.; Cadavid, D.; Cabot, A. Crystallographically Textured Nanomaterials Produced from the Liquid Phase Sintering of BixSb2-XTe3 Nanocrystal Building Blocks. *Nano Lett.* **2018**, *18* (4), 2557–2563. https://doi.org/10.1021/acs.nanolett.8b00263.

(17) Zhang, Q.; Ai, X.; Wang, L.; Chang, Y.; Luo, W.; Jiang, W.; Chen, L. Improved Thermoelectric Performance of Silver Nanoparticles-Dispersed Bi2Te3 Composites Deriving from Hierarchical Two-Phased Heterostructure. *Adv. Funct. Mater.* **2015**, *25* (6), 966–976. https://doi.org/10.1002/adfm.201402663.

(18) Ko, D. K.; Kang, Y.; Murray, C. B. Enhanced Thermopower via Carrier Energy Filtering in Solution-Processable Pt-Sb2Te3 Nanocomposites. *Nano Lett.* **2011**, *11* (7), 2841–2844. https://doi.org/10.1021/nl2012246.

(19) Li, J.; Tan, Q.; Li, J. F.; Liu, D. W.; Li, F.; Li, Z. Y.; Zou, M.; Wang, K. BiSbTe-Based Nanocomposites with High ZT: The Effect of SiC Nanodispersion on Thermoelectric Properties. *Adv. Funct. Mater.* **2013**, *23* (35), 4317–4323. https://doi.org/10.1002/adfm.201300146.

(20) Choi, J.; Lee, J. Y.; Lee, S. S.; Park, C. R.; Kim, H. High-Performance Thermoelectric Paper Based on Double Carrier-Filtering Processes at Nanowire Heterojunctions. *Adv. Energy Mater.* **2016**, *6* (9). https://doi.org/10.1002/aenm.201502181.

(21) Mehta, R. J.; Karthik, C.; Singh, B.; Teki, R.; Borca-Tasciuc, T.; Ramanath, G. Seebeck Tuning in Chalcogenide Nanoplate Assemblies by Nanoscale Heterostructuring. *ACS Nano* **2010**, *4* (9), 5055–5060. https://doi.org/10.1021/nn101322p.

(22) Zhang, G.; Fang, H.; Yang, H.; Jauregui, L. A.; Chen, Y. P.; Wu, Y. Design Principle of Telluride-Based Nanowire Heterostructures for Potential Thermoelectric Applications. *Nano Lett.* **2012**, *12* (7), 3627–3633. https://doi.org/10.1021/nl301327d.

(23) Cheng, L.; Chen, Z. G.; Yang, L.; Han, G.; Xu, H. Y.; Snyder, G. J.; Lu, G. Q.; Zou, J. T-Shaped Bi2Te3-Te Heteronanojunctions: Epitaxial Growth, Structural Modeling, and Thermoelectric Properties. *J. Phys. Chem. C* **2013**, *117* (24), 12458–12464. https://doi.org/10.1021/jp4041666.

(24) Wang, W.; Lu, X.; Zhang, T.; Zhang, G.; Jiang, W.; Li, X. Bi2Te3/Te Multiple Heterostructure Nanowire Arrays Formed by Confined Precipitation. *J. Am. Chem. Soc.* **2007**, *129* (21), 6702–6703. https://doi.org/10.1021/ja070976c.

(25) Fang, H.; Feng, T.; Yang, H.; Ruan, X.; Wu, Y. Synthesis and Thermoelectric Properties of Compositional-Modulated Lead Telluride-Bismuth Telluride Nanowire Heterostructures. *Nano Lett.* **2013**, *13* (5), 2058–2063. https://doi.org/10.1021/nl400319u.

(26) Zhang, G.; Wang, W.; Li, X. Enhanced Thermoelectric Properties of Core/Shell Heterostructure Nanowire Composites. *Adv. Mater.* **2008**, *20* (19), 3654–3656. https://doi.org/10.1002/adma.200800162.

(27) Min, Y.; Roh, J. W.; Yang, H.; Park, M.; Kim, S. Il; Hwang, S.; Lee, S. M.; Lee, K. H.; Jeong, U. Surfactant-Free Scalable Synthesis of Bi 2 Te 3 and Bi 2 Se 3 Nanoflakes and Enhanced Thermoelectric Properties of Their Nanocomposites (Adv. Mater. 10/2013) . *Adv. Mater.* **2013**, *25* (10), 1424–1424. https://doi.org/10.1002/adma.201370066.

(28) Min, Y.; Park, G.; Kim, B.; Giri, A.; Zeng, J.; Roh, J. W.; Kim, S. Il; Lee, K. H.; Jeong, U. Synthesis of Multishell Nanoplates by Consecutive Epitaxial Growth of Bi2Se3 and Bi2Te3 Nanoplates and Enhanced Thermoelectric Properties. *ACS Nano* **2015**, *9* (7), 6843–6853. https://doi.org/10.1021/nn507250r.

(29) Wang, X. Y.; Wang, H. J.; Xiang, B.; Fu, L. W.; Zhu, H.; Chai, D.; Zhu, B.; Yu, Y.; Gao, N.; Huang, Z. Y.; Zu, F. Q. Thermoelectric Performance of Sb2Te3-Based Alloys Is Improved by Introducing PN Junctions. *ACS Appl. Mater. Interfaces* **2018**, *10* (27), 23277–23284. https://doi.org/10.1021/acsami.8b01719.

(30) Fei, F.; Wei, Z.; Wang, Q.; Lu, P.; Wang, S.; Qin, Y.; Pan, D.; Zhao, B.; Wang, X.; Sun, J.; Wang, X.; Wang, P.; Wan, J.; Zhou, J.; Han, M.; Song, F.; Wang, B.; Wang, G. Solvothermal Synthesis of Lateral Heterojunction Sb2Te3/Bi2Te3 Nanoplates. *Nano Lett.* **2015**, *15* (9), 5905–5911. https://doi.org/10.1021/acs.nanolett.5b01987.

(31) Hong, M.; Chen, Z. G.; Yang, L.; Zou, J. BixSb2-XTe3 Nanoplates with Enhanced Thermoelectric Performance Due to Sufficiently Decoupled Electronic Transport Properties and Strong Wide-Frequency Phonon Scatterings. *Nano Energy* **2016**, *20*, 144–155. https://doi.org/10.1016/j.nanoen.2015.12.009.

(32) Yang, L.; Chen, Z. G.; Hong, M.; Han, G.; Zou, J. Enhanced Thermoelectric Performance of Nanostructured Bi2Te3 through Significant Phonon Scattering. *ACS Appl. Mater. Interfaces* **2015**, *7* (42), 23694–23699. https://doi.org/10.1021/acsami.5b07596.

(33) Dun, C.; Hewitt, C. A.; Jiang, Q.; Guo, Y.; Xu, J.; Li, Y.; Li, Q.; Wang, H.; Carroll, D. L. Bi2Te3 Plates with Single Nanopore: The Formation of Surface Defects and Self-Repair Growth. *Chem. Mater.* **2018**, *30* (6), 1965–1970. https://doi.org/10.1021/acs.chemmater.7b04985.

(34) Koczkur, K. M.; Mourdikoudis, S.; Polavarapu, L.; Skrabalak, S. E. Polyvinylpyrrolidone (PVP) in Nanoparticle Synthesis. *Dalt. Trans.* **2015**, *44* (41), 17883–17905. https://doi.org/10.1039/c5dt02964c.

(35) Saidi, W. A.; Feng, H.; Fichthorn, K. A. Binding of Polyvinylpyrrolidone to Ag Surfaces: Insight into a Structure-Directing Agent from Dispersion-Corrected Density Functional Theory. *J. Phys. Chem. C* **2013**, *117* (2), 1163–1171. https://doi.org/10.1021/jp309867n.

(36) Wu, X.; Zhao, Y.; Yang, C.; He, G. PVP-Assisted Synthesis of Shape-Controlled CuFeS2 Nanocrystals for Li-Ion Batteries. *J. Mater. Sci.* **2015**, *50* (12), 4250–4257. https://doi.org/10.1007/s10853-015-8977-1.

(37) Kyrychenko, A.; Korsun, O. M.; Gubin, I. I.; Kovalenko, S. M.; Kalugin, O. N. Atomistic Simulations of Coating of Silver Nanoparticles with Poly(Vinylpyrrolidone) Oligomers: Effect of Oligomer Chain Length. *J. Phys. Chem. C* **2015**, *119* (14), 7888–7899. https://doi.org/10.1021/jp510369a.

(38) Guan, G.; Han, M. Y. Functionalized Hybridization of 2D Nanomaterials. *Adv. Sci.* **2019**, *6* (23), 1901837. https://doi.org/10.1002/advs.201901837.

(39) Zhang, Y.; Hu, L. P.; Zhu, T. J.; Xie, J.; Zhao, X. B. High Yield Bi2Te3 Single Crystal Nanosheets with Uniform Morphology via a Solvothermal Synthesis. *Cryst. Growth Des.* **2013**, *13* (2), 645–651. https://doi.org/10.1021/cg3013156.

(40) Ju, Z.; Hou, Y.; Bernard, A.; Taufour, V.; Yu, D.; Kauzlarich, S. M. Ambipolar Topological Insulator and High Carrier Mobility in Solution Grown Ultrathin Nanoplates

of Sb-Doped Bi2Se3. *ACS Appl. Electron. Mater.* **2019**, *1* (9), 1917–1923. https://doi.org/10.1021/acsaelm.9b00415.

(41) He, X.; Zhang, H.; Lin, W.; Wei, R.; Qiu, J.; Zhang, M.; Hu, B. PVP-Assisted Solvothermal Synthesis of High-Yielded Bi 2 Te 3 Hexagonal Nanoplates: Application in Passively Q-Switched Fiber Laser. *Sci. Rep.* **2015**, *5*. https://doi.org/10.1038/srep15868.

(42) Starý, Z.; Horák, J.; Stordeur, M.; Stölzer, M. Antisite Defects in Sb2-XBixTe3 Mixed Crystals. *J. Phys. Chem. Solids* **1988**, *49* (1), 29–34. https://doi.org/10.1016/0022-3697(88)90130-8.

(43) Horák, J.; Čermák, K.; Koudelka, L. Energy Formation of Antisite Defects in Doped Sb2Te3 and Bi2Te3 Crystals. *J. Phys. Chem. Solids* **1986**, *47* (8), 805–809. https://doi.org/10.1016/0022-3697(86)90010-7.

(44) Zhu, T. J.; Hu, L. P.; Zhao, X. B.; He, J. New Insights into Intrinsic Point Defects in V2vi3 Thermoelectric Materials. *Adv. Sci.* **2016**, *3* (7), 1600004. https://doi.org/10.1002/advs.201600004.

(45) Snyder, G. J.; Snyder, A. H.; Wood, M.; Gurunathan, R.; Snyder, B. H.; Niu, C. Weighted Mobility. *Adv. Mater.* **2020**, *32* (25). https://doi.org/10.1002/adma.202001537.

Chapter 4

Ambipolar topological insulator and high-carrier mobility in solution grown ultrathin nanoplates of Sb-doped Bi_2Se_3

Zheng Ju,[a] *Yasen Hou,*[b] *Andrew Bernarda Valentin Taufour,*[b] *Dong Yu,*[b] *and Susan M. Kauzlarich*[*a]

[a] Department of Chemistry, University of California, One Shields Avenue, Davis, California 95616, United States

[b] Department of Physics, University of California, One Shields Avenue, Davis, California 95616, United States

This work has resulted in one publication, listed below. I performed all the synthesis and most of the characterization of the antimony doped Bi_2Se_3 nanoplates. Dr. Yasen Hou from the Physics Department at UC Davis performed electronic measurements on the fabricated devices.

Z. Ju, Y. Hou, A Bernard, V. Taufour, D. Yu, S. M. Kauzlarich, "Ambipolar Topological Insulator and High Carrier Mobility in Solution Grown Ultrathin Nanoplates of Sb-Doped Bi_2Se_3." *ACS Appl. Electron. Mater.* **2019**, 1, 9, 1917-1923

Abstract

Topological insulators (TIs) are a class of materials that can exhibit robust spin polarization at surfaces and have attracted much attention towards spintronic applications. Here, we optimized a solution route to synthesize ultrathin Bi_2Se_3 and Sb-doped Bi_2Se_3 nanoplates with a thickness of 6 - 15 nm and an average lateral size around 5 μm, up to a maximum of 10 μm. Solution chemistry provides high quality nanoplates of TIs with options to manipulate the surface states. We have synthesized Bi_2Se_3 and Sb-doped Bi_2Se_3 and characterized single nanoplates. Sb doping is used to suppress the bulk carriers, and an atomic percentage ~ 6% of Sb is demonstrated by energy dispersive X-ray spectroscopy (EDS). The 2D electron carrier concentration for Sb-doped Bi_2Se_3 nanoplates is lowered to 5.5×10^{12} cm^{-2}, reducing the concentration by a factor of 3 compared to the undoped Bi_2Se_3 nanoplate sample with an average 2D carrier concentration of 16×10^{12} cm^{-2}. At 2 K, pronounced ambipolar field effect is observed on the low-carrier-density Sb-doped Bi_2Se_3 nanoplates, further demonstrating the flexible manipulation of carrier type and concentration for these single-crystal nanoplates. Large out-of-plane magnetoresistance is measured, with a gate tunable phase coherence length.

4.1 Introduction

TIs have attracted a great deal of attention due to their exotic properties and the potential for providing spin-polarization of the carriers at the surface.[1–6] Many novel applications with no analogue among traditional semiconductors are possible such as spintronic devices and new-generation electronic devices.[7,8] To date, existing theories often only consider charge/spin transport at the TI surface at the low impurity density limit. However, high density defects naturally occur in some TI materials, such as Se vacancies and interfacial defects due to surface oxidation of Bi_2Se_3.[9,10] A new mechanism predicts that moderate surface disorder can induce spin accumulation at the TI surfaces.[11] The topological nature of the band structure leads to a transverse spin current through the bulk and spin accumulation at the surface under an external electric field.[11]

Bi_2Se_3 has been studied as a thermoelectric material[1,12–14] and a near infrared transparent conductor[15,16] and more recently as a topological insulator.[6,17] Bi_2Se_3 is of interest because of its simple surface state with a well-defined single Dirac cone and a wide bulk bandgap of 0.3 eV compared with other TIs, and thus is most promising to achieve room temperature spintronic devices. Bi_2Se_3, shown in Figure 4.1a, has a rhombohedral crystal structure of space group $R\bar{3}m$ ($a = b = 4.140$ Å and $c = 28.636$ Å; JCPDF #33-0214) that can be described as a layer-structure where the covalently bonded Bi_2Se_3 sheets are arranged in planar quintuple layers (QLs) of Se(1)-Bi-Se(2)-Bi-Se(1) atoms (with each QL approximately 1 nm thick). The QLs are stacked and connected by weak van der Waals interactions along the *c*-axis.

Three-dimensional TIs have typically been prepared by chemical and physical vapor deposition (CVD and PVD),[18–23] molecular beam epitaxy (MBE)[24–27] and solvothermal methods.[28–31] However, TIs prepared by CVD, PVD methods normally contain excessive bulk carriers with a comparatively higher thickness (over 30 nm).[18,20,22,24,25,32,33] Thinner TI nanostructures have been synthesized by solvothermal routes with small lateral sizes (less than 5 μm). Here, we employ a solution route[16,34] to prepare Bi_2Se_3 nanoplates with a large aspect ratio (6 - 15 nm thick and 1 - 10 μm wide). The small thickness (6 - 15 quintuple layers) reduces the bulk conductivity and allows stronger gate tunability of the Fermi level. To further suppress the bulk conductivity, Bi_2Se_3 is doped with Sb to compensate the excess electrons. Sb has been confirmed as an effective dopant which can significantly reduce carrier concentration without disrupting the topological surface state.[20,30,35] Doping Bi_2Se_3 with Sb in solution environment (without pressure as in a solvothermal environment) is more challenging than vapor deposition methods because of lower reaction temperature. However, it is a low cost, facile, and scalable method capable of producing high quality single nanoplates that allows for further chemical modification. While Sb_2Se_3 exists, it crystallizes in an orthorhombic structure rather than the Bi_2Se_3 rhombohedral crystal structure thereby limiting the solubility of Sb in Bi_2Se_3.[36] In this manuscript, we show that a significant amount of Sb can be doped into Bi_2Se_3 via a mild solution reaction.

4.2 Experimental Section

Pristine Bi_2Se_3 nanoplates were prepared by one pot solution synthesis following the synthesis route from Lin et.al.[16] by using bismuth nitrate pentahydrate ($Bi(NO_3)_3{\cdot}5H_2O$, 0.0970 g, ≥98%, Sigma-Aldrich), sodium selenite (Na_2SeO_3, 0.0517 g, >99%, Sigma-Aldrich) as precursors and poly(vinylpyrrolidone) (PVP, MW≈40,000, 0.22 g, Sigma-Aldrich) as surfactant in 10mL ethylene glycol (EG, Sigma-Aldrich) which serves as both solvent and reducing agent. The mixed solution was sonicated for 10 min, and then heated to 194 ℃ in a 15 mL two-neck flask equipped with thermocouple and reflux condenser in a heating mantle. To synthesize Sb-doped Bi_2Se_3, antimony acetate ($Sb(OAc)_3$, 0.0300 g, >99.5%, Sigma-Aldrich) was added with a reduced amount of $Bi(NO_3)_3{\cdot}5H_2O$ (0.0485 g), while the same synthetic procedure was carried out. After 4 hours, the heating mantle was removed, and the finished reaction was naturally cooled down to room temperature. The mixture was then centrifuged with 30 mL acetone and 10 mL isopropanol at 8500 rpm for 5 min. After the first wash, the precipitate was dispersed back into 40 mL ethanol and washed two more times. The synthesized nanoplates were then dispersed into 10 mL isopropanol for further characterization.

Powder X-ray diffraction was performed on a Bruker D8 Advance diffractometer with Cu $K\alpha$ lines (40 kV, 40 mA). PXRD samples were prepared by dropcasting a small amount of the nanoplates dispersion on a fused silica holder. Electron microscopy analyses on as-synthesized Bi_2Se_3 nanoplates were performed on a Thermo Fisher Quattro S scanning electron microscopy (SEM) at an acceleration voltage at 5 kV and a JEOL JEM 2100F-AC transmission electron microscopy (TEM) at an acceleration voltage of 200 kV. TEM samples were prepared by dropcasting the suspension onto carbon films supported by Cu grids. Nanoplates lie flat on the membrane from the surface tension generated by evaporation of the isopropanol.

As-grown nanoplates in isopropanol were drop-casted onto 300 nm SiO_2 covered Si substrates, where single nanoplate field effect transistor (FET) devices were fabricated using a standard electron beam lithography process. Top metal contacts (5 nm Cr / 90 nm Au) were made using an electron beam evaporator (CHA). Current-voltage curves were measured through a current preamplifier (DL Instruments, model 1211) and a National Instruments (NI) data acquisition system. The magnetoresistance measurements were performed in a Quantum Design Physical Property Measurement System (PPMS).

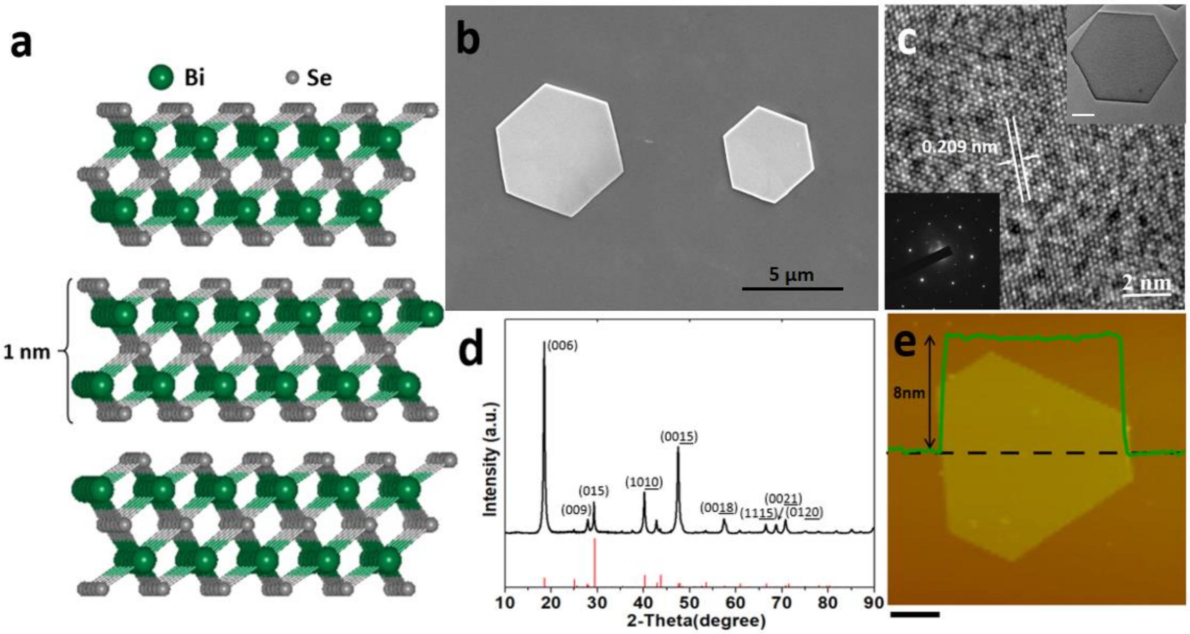

Figure 4.1. (a) A view of the layered rhombohedral structure of Bi_2Se_3 showing the quintuple layers (QLs) of Se(1)-Bi-Se(2)-Bi-Se(1) with a thickness around 1 nm. (b) Scanning electron microscope (SEM) image shows hexagonal shaped Bi_2Se_3 with a lateral dimension around 5 μm and 4 μm. The well resolved edge of nanoplate demonstrates the high crystallinity. (c) HRTEM reveals well crystalline structure of solution synthesized Bi_2Se_3 nanoplate (top right inset) (scale bar, 1 μm). Sharp diffraction spots in the selected area diffraction pattern (bottom-left inset) further confirm the single crystal nature of nanoplate. (d) X-ray diffraction pattern of Bi_2Se_3 nanoplates with strong preferred orientation. The red bars represent characteristic reflections for rhombohedral Bi_2Se_3, PDF #33-0214. (e) Thickness of a typical solution synthesized Sb-doped Bi_2Se_3 nanoplate measured by AFM with a measured height of 8 nm. Scale bar, 1 μm.

4.3 Results and Discussions

The reaction to produce Bi_2Se_3 was optimized the reaction by increasing the temperature to 194 °C and extending reaction time to 4 hours to obtain nanoplates with large lateral sizes. Reaction progress was directly observed as the color of the solution changed from a colloidal white solution to dark gray to highly reflective colloidal gray precipitate, indicating the formation of Bi_2Se_3 nanoplates. The synthesized Bi_2Se_3 nanoplates are thoroughly washed by ethanol or isopropanol to remove excess surface ligands and stored as a stable colloid in isopropanol for further characterization.

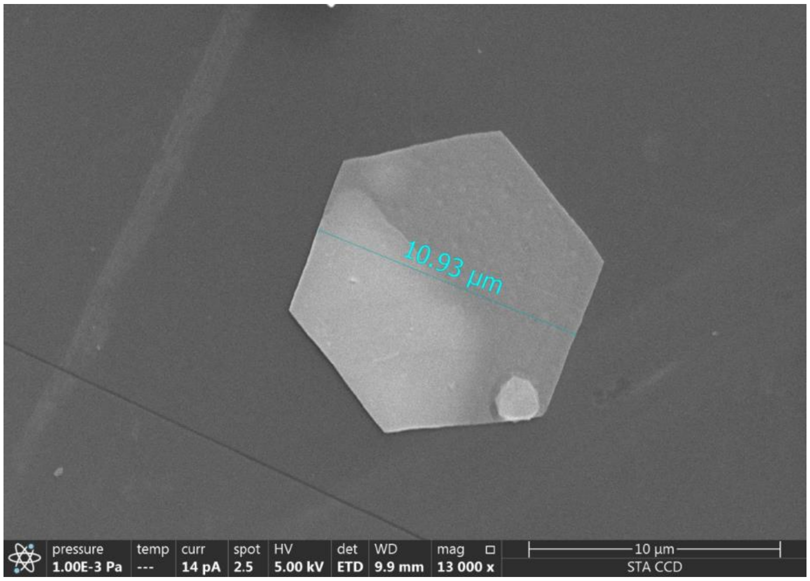

Figure 4.2. Bi_2Se_3 single nanoplate with a lateral size over 10 μm.

Both the SEM and TEMimages show the as-grown nanoplates typically exhibit hexagonal morphology with 120° edge facets and lateral size of 5 - 10 µm as shown in Figure 4.1b, 4.1c inset (top right) and Figure 4.2. The HRTEM image reveals the single-crystalline nature of the nanoplate (Figure 4.1c), also confirmed by the selected area electron diffraction (SAED) pattern Figure 4.1c inset (bottom left). The lattice spacing in HRTEM is ~0.209 nm corresponding to the (110) plane. The phase purity of the products was characterized by X-ray diffraction (XRD). As indicated in Figure 4.1d, the nanoplates obtained by this solution route display a pure rhombohedral phase of Bi_2Se_3 with a space group $R\bar{3}m$. All the major peaks can be indexed to (0001) family and the larger than calculated intensity for the *l* Miller index direction is due to preferred alignment of the nanoplates. The calculated lattice constants of $a = b = 4.153(5)$ Å and $c = 28.612(9)$ Å are in good agreement with the standard literature values ($a = b = 4.140$ Å and $c = 28.636$ Å; JCPDF #33-0214). For the synthesis of Sb-doped Bi_2Se_3, excess Sb precursor was added to overcome the limited solubility in Bi_2Se_3 rhombohedral structure. The final product contains unreacted Se impurity and no other possible impurities such as the orthorhombic form of Bi_2Se_3,[37,38] according to the XRD of the product from the reaction (Figure 4.3). The thicknesses of the doped Bi_2Se_3 nanoplates are measured by atomic force microscopy (AFM) and range from 6 to 15 nm. Figure 4.1e shows an AFM image of a typical nanoplate with a smooth surface, which further demonstrates the surface ligands, such as PVP, have been successfully removed by the washing process.

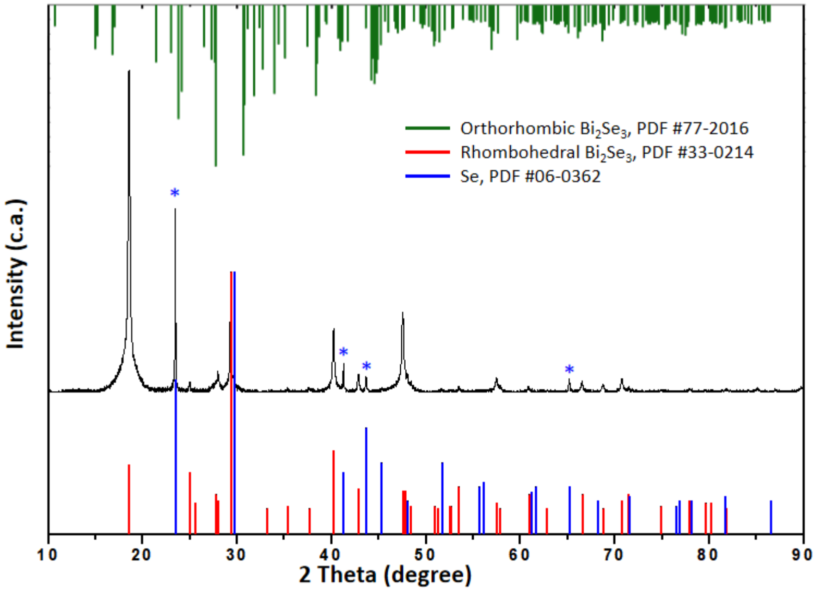

Figure 4.3. Sb-doped Bi_2Se_3 sample with Se impurity (blue star labelled out main peaks from Se).

The energy dispersive spectroscopy (EDS) spectrum obtained for an undoped Bi_2Se_3 single nanoplate shows stoichiometry of Bi:Se ~2:3 (Figure 4.4a), confirming the composition. The EDS spectrum from a single Sb-doped nanoplate shows an Sb atomic percentage of ~ 6% (Figure 4.4b), which is significantly increased compared to nanoplates obtained from solvothermal synthesis,[30] and close to that of vapor-phase-synthesized nanoribbon (~ 7%).[20] We found that the amount of Sb in various nanoplates ranged from 3-6% from the same batch. Further efforts are necessary to ensure a consistent maximum doping of the nanoplates. EDS elemental mapping reveals Se, Bi and Sb are evenly distributed across the entire nanoplate (Figure 4.4c).

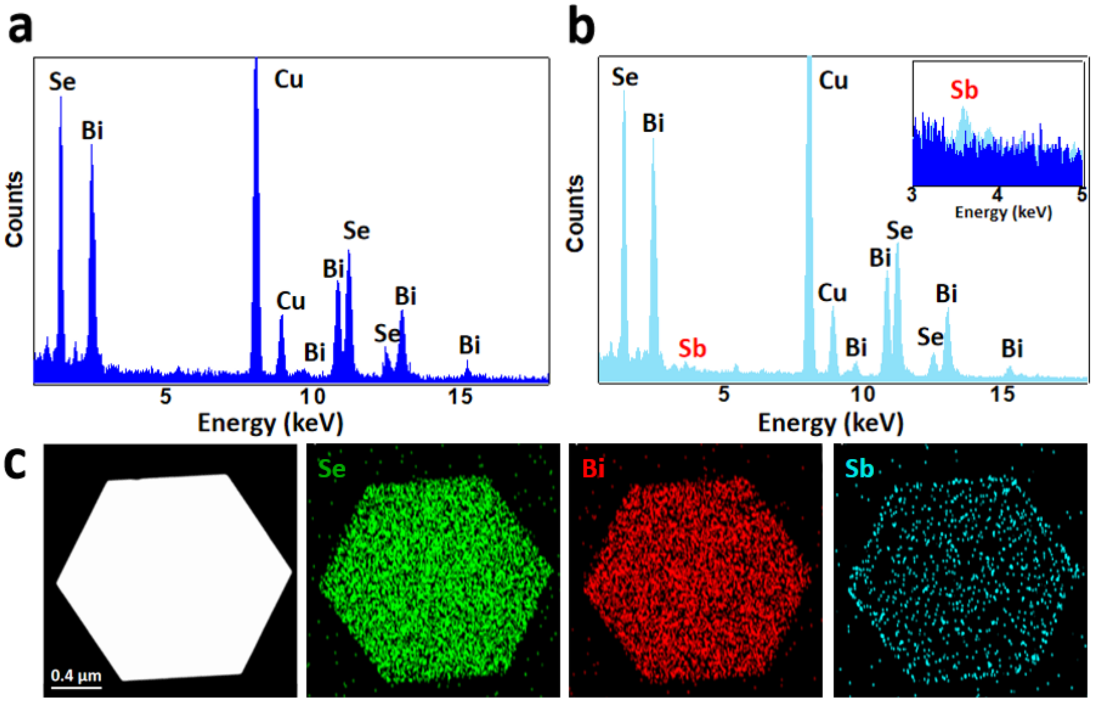

Figure 4.4. (a) EDS spectrum under TEM of a single Bi_2Se_3 nanoplate. (b) EDS spectrum of a Sb-doped Bi_2Se_3 single nanoplate. Inset shows the stacked EDS spectra of Sb-doped and undoped Bi_2Se_3 showing a noticeable Sb peak in Sb-doped sample, corresponding to an atomic concentration of ~6%. Copper signal is from TEM sample grid. (c) Dark-field scanning transmission electron microscopy (DF-STEM) image and EDS elemental mapping of selenium, bismuth and antimony on one Sb-doped Bi_2Se_3 nanoplate, indicating a uniform distribution of the elements.

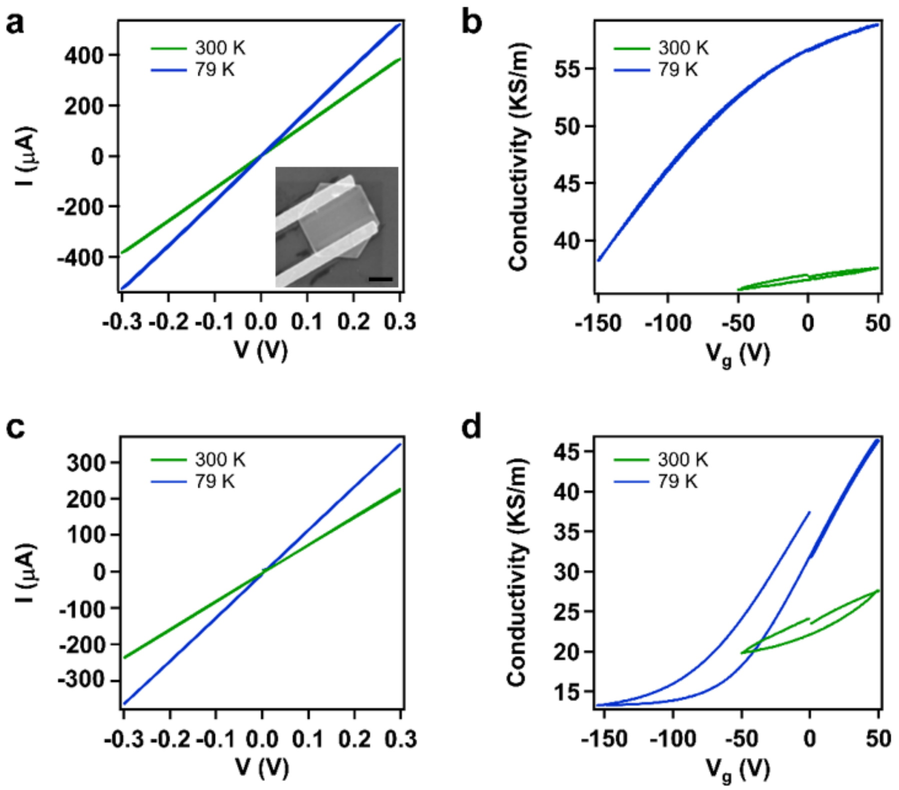

Figure 4.5. Field effect characteristics of undoped and Sb doped Bi_2Se_3 devices. (a) I-V curves for a typical undoped Bi_2Se_3 device (#1) at 300 K and 79 K. Inset is the SEM image of a typical device. Two bright bars are top metal contacts (5 nm Cr / 90 nm Au) deposited on single nanoplate. Scale bar, 2 µm. (b) Gate dependence of conductance at 300 K and 79 K. Field-effect mobility and electron concentration are estimated to be $\mu = 33$ cm^2/Vs, $n_{2D} = 14 \times 10^{12}$ cm^{-2} at 300 K and $\mu = 249$ cm^2/Vs, $n_{2D} = 3 \times 10^{12}$ cm^{-2} at 79 K. (c)-(d) I-V curves and gate dependent conductance for Sb doped Bi_2Se_3 (device #2). Field-effect mobility and electron concentration are estimated to be $\mu = 56$ cm^2/Vs, $n_{2D} = 4.82 \times 10^{12}$ cm^{-2} at 300 K and $\mu = 494$ cm^2/Vs, $n_{2D} = 0.82 \times 10^{12}$ cm^{-2} at 79 K.

Electronic measurements of single nanoplate field effect transistors (FETs) with undoped (device #1) and Sb doped (device #2) Bi_2Se_3 are shown in Figure 4.5. Both devices show linear current-voltage (I-V) curves which indicate ohmic conduction and are more conductive at liquid nitrogen temperature (Figure 4.5a and 4.5c). Conductivity of device #2 shows a strong temperature dependence as shown in Figure 4.6. Contact resistance determined by 3-probe measurements is well below 100 Ω (Figure 4.7). Gate dependence at room temperature indicates both undoped and Sb doped are *n*-type (Figure 4.5b and 4.5d). The carrier concentration of undoped Bi_2Se_3 is double that of Sb doped Bi_2Se_3. As the temperature is lowered to 79K, both devices show stronger gate response (Figure 4.5b and 4.5d). We then extract the field effect mobility and carrier concentration by using a parallel plate capacitance model. Note that this model only provides an estimation of the exact mobility value, because of the fringe effects near the metal contact and the often-irregular shapes of the nanoplate channels. The possible field screening at the SiO_2 nanoplate interface may also lead to an underestimation of the mobility. From this model, the 2D carrier concentration in the Sb doped Bi_2Se_3 nanoplate is as low as 0.82×10^{12} cm^{-2}.

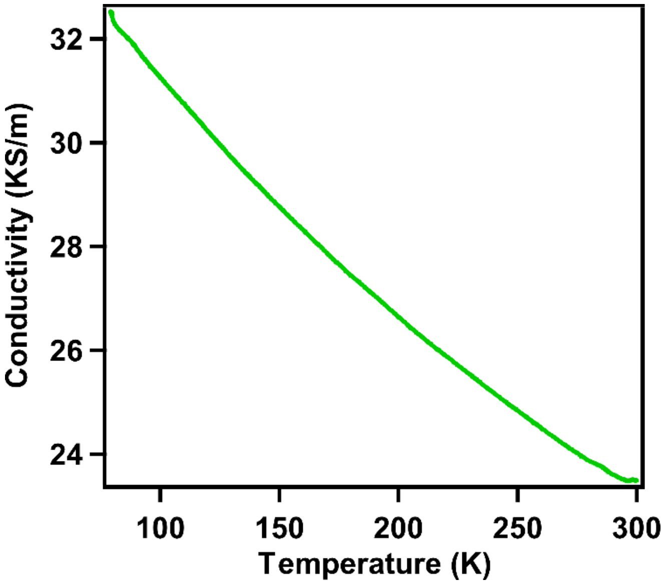

Figure 4.6. Conductivity of device #2 vs temperature from 79 K to 300 K.

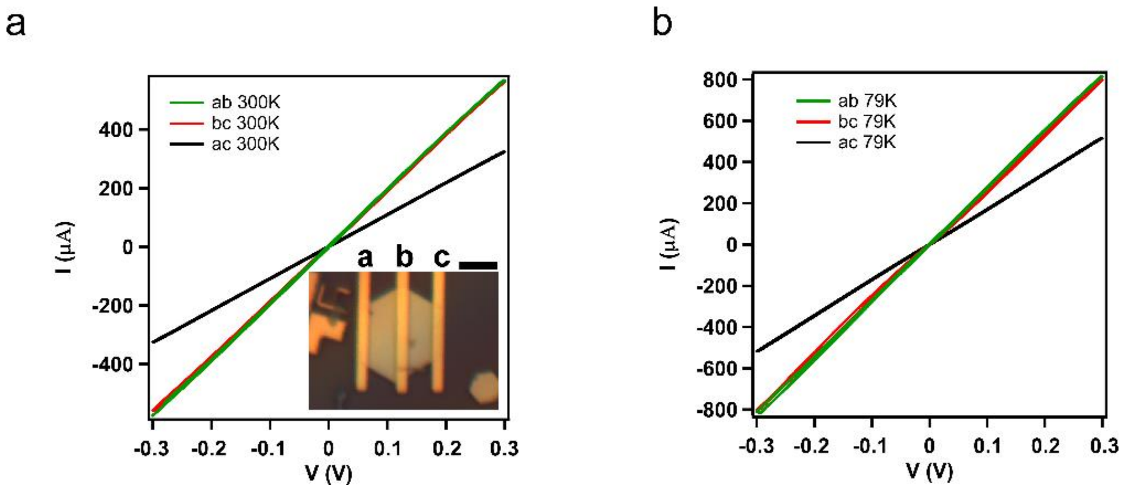

Figure 4.7. 3 probe measurements of contact resistance. (a), IV curves of a three-probe device at 300 K. Inset: optical image of the device. Scale bar: 5 µm. (b) IV curves at 79 K. Contact resistance is calculated by $R_b = (R_{ab} + R_{bc} - R_{ac})/2$. R_b is calculated to be 70 Ω and 90 Ω at 300 K and 79 K, respectively.

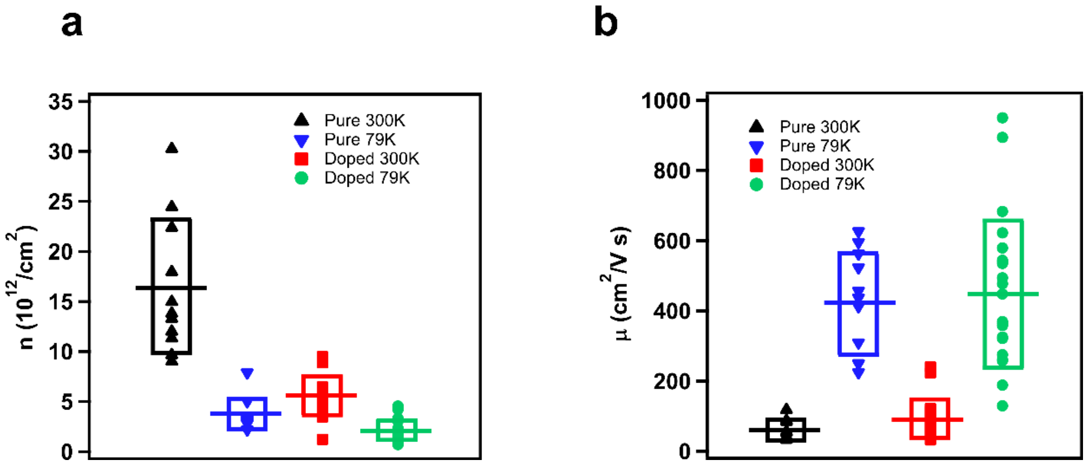

Figure 4.8. (a) Distribution of electron concentration and (b) field effect mobility of undoped and Sb doped Bi_2Se_3 nanoplate devices at 300K and 79K respectively. The horizontal lines indicate the average and the boxes indicate the standard deviation. Sb-doping effectively lowered the electron concentration by half at both 300K and 79K.

Table 4.1. Statistics of Carrier Concentration and Field Effect Mobility of Undoped and Sb-Doped Bi_2Se_3 Devices.

	Undoped Average	Sb doped Average
μ(300K) cm^2/Vs	60 ± 29	94 ± 56
n(300K)×$10^{12}/cm^2$	16.3 ± 2.8	5.5 ± 2.0
μ(79K) cm^2/Vs	422 ± 146	450 ± 212
n(79K) ×$10^{12}/cm^2$	3.7 ± 1.6	2.0 ± 1.1

To further confirm the doping effects, we measured 11 undoped Bi_2Se_3 and 19 Sb-doped Bi_2Se_3 single nanoplate devices. Statistics of carrier mobility and concentration are shown in Figure 4.8 and Table 4.1. On average, as-prepared undoped Bi_2Se_3 nanoplates have a mobility $\mu = 60.4 \pm 28.9$ cm^2/Vs and carrier concentration $n_{2D} = (16.3 \pm 2.8) \times 10^{12}$ cm^{-2} at 300 K, while Sb doped Bi_2Se_3 nanoplates have a mobility $\mu = 93.5 \pm 56$ cm^2/Vs and carrier concentration $n_{2D} = (5.5 \pm 2.0) \times 10^{12}$ cm^{-2}. At low temperature, the field-effect mobility in both types of devices increases greatly up to 10^3 cm^2/Vs for the best devices and the carrier concentration is further reduced. Our data clearly demonstrate that by Sb doping, the carrier concentration of Bi_2Se_3 can be effectively reduced.

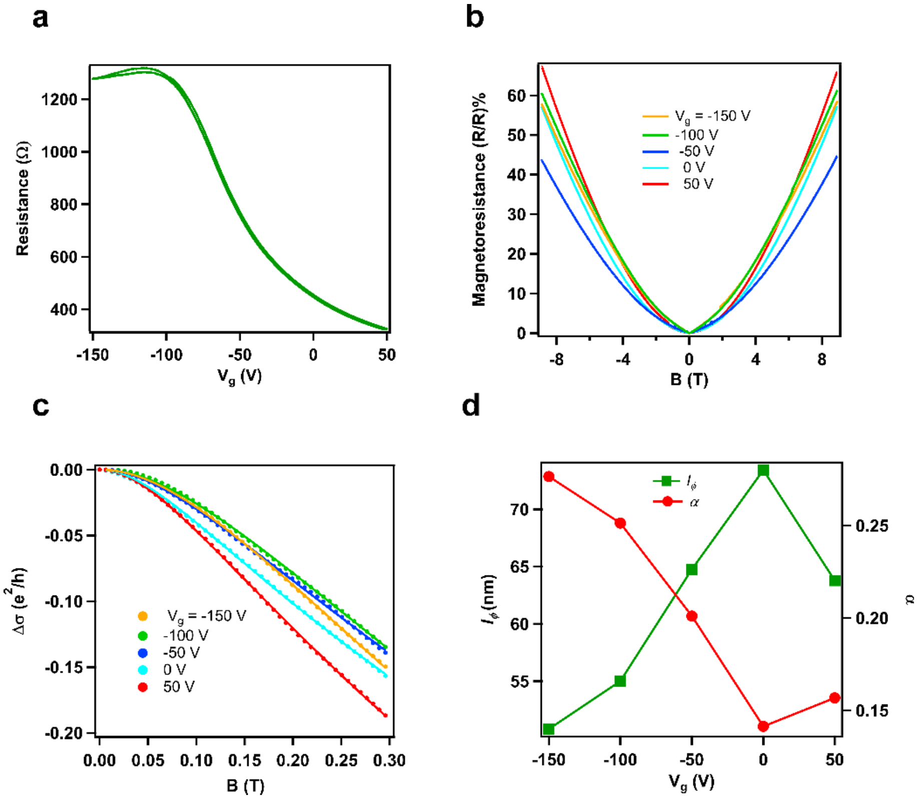

Figure 4.9. (a) Gate voltage dependence of resistance of device #2 at 2 K, which indicates ambipolar conduction. (b) Magnetoresistance of device #2 as a function of out-of-plane magnetic field at various gate voltages at 2 K. (c) Magneto-conductance as a function of magnetic field. Solid lines are fitting curves with the HLN equation. (d) α and phase coherence length l_Φ at different gate voltages. The error bars from fitting are smaller than the size of the data points.

We attribute the lower carrier concentration in Sb-doped Bi_2Se_3 to fewer Se vacancies. Bi_2Se_3 is a heavily doped n-type semiconductor because of the non-stoichiometric composition with a slight deficiency of Se.[30,39,40] The lower carrier concentration in Sb-doped Bi_2Se_3 allows for the observation of an ambipolar gate response at 2K (Figure 4.9). As gate voltage is scanned to -150 V, the device resistance first increases due to the reduction of electron concentration. Maximum resistance is observed at -117 V. As the gate voltage continues to decrease, resistance of the device decreases because of the increasing hole conduction. The gate response is much weaker in the p-type regime as seen in Figure 4.9a. This is not understood but may be caused by lower hole mobility and/or stronger field screening at high gate voltage. The device thickness of this nanoplate is only around 12 nm. It is likely that both top and bottom surfaces are affected by the gate simultaneously.[20] The ambipolar gate response clearly indicates that we can effectively tune the Fermi level from above the Dirac point to below it. Electron concentration as low as n_{2D} = $3.1\times10^{11}/cm^2$ at V_g = -117 V has been realized in this device. This estimated carrier concentration consists of both surface and bulk contributions. The value is comparable with the reported lowest carrier concentrations measured in Bi_2Se_3.[20,41] Such low carrier concentration is essential to minimize bulk transport of TI materials and provides a possible way to study the surface transport of Bi_2Se_3.

Magnetoresistance (MR) measurements are also performed on this device (#2). As can be seen in Figure 4.9b, positive MR responses are observed under all gate voltages, showing weak anti-localization, which is in consistence with the strong spin-orbital coupling in Sb doped Bi_2Se_3. MR as large as 60% is observed at 9 T. According to the Hikami-Larkin-Nagaoka (HLN) theory, for a 2D system, the magneto-conductivity ($\Delta\sigma = \sigma(B) - \sigma(B = 0)$) is given as follows[42]:

$$\Delta\sigma = \alpha \frac{e^2}{2\pi^2\hbar}\left[\ln\frac{\hbar}{4el_\Phi^2 B} - \psi\left(\frac{1}{2} + \frac{\hbar}{4el_\Phi^2 B}\right)\right] \qquad \textbf{Equation 4.1}$$

where l_Φ is the phase coherence length, Ψ is the digamma function, $\hbar$ is the reduced Plank's constant, and α is a fitting parameter that takes a value of 1/2 for a 2D system with strong spin-orbit coupling or the surface of a 3D topological insulator.[42-44] The $\Delta\sigma$ data can be fit with the HLN equation very well under all gate voltages (Figure 4.9c). Phase coherence length extracted from the fitting is around 65 nm, close to previously reported values.[45-48] α obtained from the fitting is around 0.26, which is a value similar to previous studies[43-45,49] and in rough agreement with the symplectic limit. The deviation from 1/2 has been generally attributed to the intermixing between the bulk and surface states[47-50] or sample inhomogeneity.[43] Additionally, the existence of contact resistance may also lead to an underestimation of the fitting parameters.

4.4 Conclusions

In summary, an optimized solution method is utilized to prepare Sb-doped Bi_2Se_3 nanoplates with a lateral size up to 10 μm and as high as 6% doping amount which is close to that of vapor-phase or solvothermal synthesized samples. Sb-doping of Bi_2Se_3 successfully reduced the electron concentration both at room temperature (300 K) and liquid nitrogen temperature (79 K), compared with undoped Bi_2Se_3 nanoplates. A pronounced ambipolar field effect is observed in the Sb-doped Bi_2Se_3 sample, indicating successful Sb incorporation and flexibility to manipulate the Fermi level from above to below the Dirac point. Magnetoresistance up to 60% is observed in ambipolar devices where the phase coherent length is around 10 nm. The solution synthesis of high-quality Sb-doped Bi_2Se_3 nanoplates offers an option for chemically manipulating topological insulators and exploring the properties of single nanoplates with applications in photoelectric[51] and spintronic areas.

4.5 Acknowledgement

Financial support from the NSF (DMR-1709382, DMR-1838532) is gratefully acknowledged. The Advanced Materials Characterization and Testing Lab (AMCaT) of University of California Davis is acknowledged for providing characterization facilities.

4.6 References of Chapter 4

(1) Kong, D.; Cui, Y. Opportunities in Chemistry and Materials Science for Topological Insulators and Their Nanostructures. *Nature Chemistry*. **2011**, *3*, 845–849.

(2) Qi, X. L.; Zhang, S. C. Topological Insulators and Superconductors. *Rev. Mod. Phys.* **2011**, *83* (4), 1057.

(3) Moore, J. E. The Birth of Topological Insulators. *Nature*. **2010**, *464*, 194–198.

(4) Müchler, L.; Zhang, H.; Chadov, S.; Yan, B.; Casper, F.; Kübler, J.; Zhang, S. C.; Felser, C. Topological Insulators from a Chemist's Perspective. *Angew. Chemie - Int. Ed.* **2012**, *51* (29), 7221–7225.

(5) Hasan, M. Z.; Kane, C. L. Colloquium: Topological Insulators. *Rev. Mod. Phys.* **2010**, *82* (4), 3045–3067.

(6) Zhang, H.; Liu, C. X.; Qi, X. L.; Dai, X.; Fang, Z.; Zhang, S. C. Topological Insulators in Bi_2Se_3, Bi_2Te_3 and Sb_2Te_3 with a Single Dirac Cone on the Surface. *Nat. Phys.* **2009**, *5* (6), 438–442.

(7) Žutić, I.; Fabian, J.; Das Sarma, S. Spintronics: Fundamentals and Applications. *Rev. Mod. Phys.* **2004**, *76* (2), 323–410.

(8) Pesin, D.; MacDonald, A. H. Spintronics and Pseudospintronics in Graphene and Topological Insulators. *Nat. Mater.* **2012**, *11* (5), 409–416.

(9) Yashina, L. V.; Sánchez-Barriga, J.; Scholz, M. R.; Volykhov, A. A.; Sirotina, A. P.; Neudachina, V. S.; Tamm, M. E.; Varykhalov, A.; Marchenko, D.; Springholz, G.; Bauer, G.; Knop-Gericke, A.; Rader, O. Negligible Surface Reactivity of Topological Insulators Bi_2Se_3 and Bi_2Te_3 towards Oxygen and Water. *ACS Nano* **2013**, *7* (6), 5181–5191.

(10) Kong, D.; Cha, J. J.; Lai, K.; Peng, H.; Analytis, J. G.; Meister, S.; Chen, Y.; Zhang, H. J.; Fisher, I. R.; Shen, Z. X.; Cui, Y. Rapid Surface Oxidation as a Source of Surface Degradation Factor for Bi_2Se_3. *ACS Nano* **2011**, *5* (6), 4698–4703.

(11) Peng, X.; Yang, Y.; Singh, R. R. P.; Savrasov, S. Y.; Yu, D. Spin Generation via Bulk Spin Current in Three-Dimensional Topological Insulators. *Nat. Commun.* **2016**, *7*, 10878.

(12) Tretiakov, O. A.; Abanov, A.; Murakami, S.; Sinova, J. Large Thermoelectric Figure of Merit for Three-Dimensional Topological Anderson Insulators via Line Dislocation Engineering. *Appl. Phys. Lett.* **2010**, *97* (7), 073108.

(13) Ghaemi, P.; Mong, R. S. K.; Moore, J. E. In-Plane Transport and Enhanced Thermoelectric Performance in Thin Films of the Topological Insulators Bi_2Te_3 and Bi_2Se_3. *Phys. Rev. Lett.* **2010**, *105* (16), 166603.

(14) Wang, S.; Sun, Y.; Yang, J.; Duan, B.; Wu, L.; Zhang, W.; Yang, J. High Thermoelectric Performance in Te-Free $(Bi,Sb)_2Se_3$: Via Structural Transition Induced Band Convergence and Chemical Bond Softening. *Energy Environ. Sci.* **2016**, *9* (11), 3436–3447.

(15) Peng, H.; Dang, W.; Cao, J.; Chen, Y.; Wu, D.; Zheng, W.; Li, H.; Shen, Z. X.; Liu, Z. Topological Insulator Nanostructures for Near-Infrared Transparent Flexible Electrodes. *Nat. Chem.* **2012**, *4* (4), 281–286.

(16) Lin, Z.; Chen, Y.; Yin, A.; He, Q.; Huang, X.; Xu, Y.; Liu, Y.; Zhong, X.; Huang, Y.; Duan, X. Solution Processable Colloidal Nanoplates as Building Blocks for High-Performance Electronic Thin Films on Flexible Substrates. *Nano Lett.* **2014**, *14* (11), 6547–6553.

(17) Xia, Y.; Qian, D.; Hsieh, D.; Wray, L.; Pal, A.; Lin, H.; Bansil, A.; Grauer, D.; Hor, Y. S.; Cava, R. J.; Hasan, M. Z. Observation of a Large-Gap Topological-Insulator Class with a Single Dirac Cone on the Surface. *Nat. Phys.* **2009**, *5* (6), 398–402.

(18) Kong, D.; Dang, W.; Cha, J. J.; Li, H.; Meister, S.; Peng, H.; Liu, Z.; Cui, Y. Few-Layer Nanoplates of Bi_2Se_3 and Bi_2Te_3 with Highly Tunable Chemical Potential. *Nano Lett.* **2010**, *10* (6), 2245–2250.

(19) Cao, H.; Venkatasubramanian, R.; Liu, C.; Pierce, J.; Yang, H.; Zahid Hasan, M.; Wu, Y.; Chen, Y. P. Topological Insulator Bi_2Te_3 Films Synthesized by Metal Organic Chemical Vapor Deposition. *Appl. Phys. Lett.* **2012**, *101* (16), 162104.

(20) Hong, S. S.; Cha, J. J.; Kong, D.; Cui, Y. Ultra-Low Carrier Concentration and Surface-Dominant Transport in Antimony-Doped Bi_2Se_3 Topological Insulator Nanoribbons. *Nat. Commun.* **2012**, *3*, 757.

(21) Guo, Y.; Aisijiang, M.; Zhang, K.; Jiang, W.; Chen, Y.; Zheng, W.; Song, Z.; Cao, J.; Liu,

Z.; Peng, H. Selective-Area van Der Waals Epitaxy of Topological Insulator Grid Nanostructures for Broadband Transparent Flexible Electrodes. *Adv. Mater.* **2013**, *25* (41), 5959–5964.

(22) Brom, J. E.; Ke, Y.; Du, R.; Won, D.; Weng, X.; Andre, K.; Gagnon, J. C.; Mohney, S. E.; Li, Q.; Chen, K.; Xi, X. X.; Redwing, J. M. Structural and Electrical Properties of Epitaxial Bi_2Se_3 Thin Films Grown by Hybrid Physical-Chemical Vapor Deposition. *Appl. Phys. Lett.* **2012**, *100* (16), 162110.

(23) Xu, Z.; Guo, X.; Yao, M.; He, H.; Miao, L.; Jiao, L.; Liu, H.; Wang, J.; Qian, D.; Jia, J.; Ho, W.; Xie, M. Anisotropic Topological Surface States on High-Index Bi_2Se_3 Films. *Adv. Mater.* **2013**, *25* (11), 1557–1562.

(24) Liu, X.; Smith, D. J.; Fan, J.; Zhang, Y. H.; Cao, H.; Chen, Y. P.; Leiner, J.; Kirby, B. J.; Dobrowolska, M.; Furdyna, J. K. Structural Properties of Bi_2Te_3 and Bi_2Se_3 Topological Insulators Grown by Molecular Beam Epitaxy on GaAs(001) Substrates. *Appl. Phys. Lett.* **2011**, *99* (17), 171903.

(25) Schreyeck, S.; Tarakina, N. V.; Karczewski, G.; Schumacher, C.; Borzenko, T.; Brüne, C.; Buhmann, H.; Gould, C.; Brunner, K.; Molenkamp, L. W. Molecular Beam Epitaxy of High Structural Quality Bi_2Se_3 on Lattice Matched InP(111) Substrates. *Appl. Phys. Lett.* **2013**, *102* (4), 041914.

(26) Zhang, Y.; He, K.; Chang, C. Z.; Song, C. L.; Wang, L. L.; Chen, X.; Jia, J. F.; Fang, Z.; Dai, X.; Shan, W. Y.; Shen, S. Q.; Niu, Q.; Qi, X. L., Zhang, S. C.; Ma, X. C.; Xue Q. K. Crossover of the Three-Dimensional Topological Insulator Bi_2Se_3 to the Two-Dimensional Limit. *Nat. Phys.* **2010**, *6* (8), 584–588.

(27) Li, Y. Y.; Wang, G.; Zhu, X. G.; Liu, M. H.; Ye, C.; Chen, X.; Wang, Y. Y.; He, K.; Wang, L. L.; Ma, X. C.; Zhang, H. J.; Dai, X.; Fang, Z.; Xie, X. C.; Liu, Y.; Qi, X. L.; Jia, J. F.; Zhang S. C.; Xue, Q. K. Intrinsic Topological Insulator Bi_2Te_3 Thin Films on Si and Their Thickness Limit. *Adv. Mater.* **2010**, *22* (36), 4002–4007.

(28) Yang, L.; Chen, Z. G.; Hong, M.; Han, G.; Zou, J. Enhanced Thermoelectric Performance of Nanostructured Bi_2Te_3 through Significant Phonon Scattering. *ACS Appl. Mater.*

Interfaces **2015**, *7* (42), 23694–23699.

(29) Zhang, G.; Wang, W.; Lu, X.; Li, X. Solvothermal Synthesis of V-VI Binary and Ternary Hexagonal Platelets: The Oriented Attachment Mechanism. *Cryst. Growth Des.* **2009**, *9* (1), 145–150.

(30) Kong, D.; Koski, K. J.; Cha, J. J.; Hong, S. S.; Cui, Y. Ambipolar Field Effect in Sb-Doped Bi_2Se_3 Nanoplates by Solvothermal Synthesis. *Nano Lett.* **2013**, *13* (2), 632–636.

(31) Liu, X.; Xu, J.; Fang, Z.; Lin, L.; Qian, Y.; Wang, Y.; Ye, C.; Ma, C.; Zeng, J. One-Pot Synthesis of Bi_2Se_3 Nanostructures with Rationally Tunable Morphologies. *Nano Res.* **2015**, *8* (11), 3612–3620.

(32) Andzane, J.; Kunakova, G.; Charpentier, S.; Hrkac, V.; Kienle, L.; Baitimirova, M.; Bauch, T.; Lombardi, F.; Erts, D. Catalyst-Free Vapour-Solid Technique for Deposition of Bi_2Te_3 and Bi_2Se_3 Nanowires/Nanobelts with Topological Insulator Properties. *Nanoscale* **2015**, *7* (38), 15935–15944.

(33) Kunakova, G.; Galletti, L.; Charpentier, S.; Andzane, J.; Erts, D.; Léonard, F.; Spataru, C. D.; Bauch, T.; Lombardi, F. Bulk-Free Topological Insulator Bi_2Se_3 Nanoribbons with Magnetotransport Signatures of Dirac Surface States. *Nanoscale* **2018**, *10* (41), 19595–19602.

(34) Soni, A.; Yanyuan, Z.; Ligen, Y.; Aik, M. K. K.; Dresselhaus, M. S.; Xiong, Q. Enhanced Thermoelectric Properties of Solution Grown $Bi_2Te_{3-x}Se_x$ Nanoplatelet Composites. *Nano Lett.* **2012**, *12* (3), 1203–1209.

(35) Zhang, Y.; Chang, C. Z.; He, K.; Wang, L. L.; Chen, X.; Jia, J. F.; Ma, X. C.; Xue, Q. K. Doping Effects of Sb and Pb in Epitaxial Topological Insulator Bi_2Se_3 Thin Films: An in Situ Angle-Resolved Photoemission Spectroscopy Study. *Appl. Phys. Lett.* **2010**, *97* (19), 194102.

(36) Kong, D.; Chen, Y.; Cha, J. J.; Zhang, Q.; Analytis, J. G.; Lai, K.; Liu, Z.; Hong, S. S.; Koski, K. J.; Mo, S. K.; Hussain, Z.; Fisher, I. R.; Shen, Z. X.; Cui, Y. Ambipolar Field Effect in the Ternary Topological Insulator $(Bi_xSb_{1-x})_2Te_3$ by Composition Tuning. *Nat. Nanotechnol.* **2011**, *6* (11), 705–709.

(37) Patil, N. S.; Sargar, A. M.; Mane, S. R.; Bhosale, P. N. Growth Mechanism and Characterisation of Chemically Grown Sb Doped Bi_2Se_3 Thin Films. *Appl. Surf. Sci.* **2008**, *254* (16), 5261-5265.

(38) Qiu, X.; Burda, C.; Fu, R.; Pu, L.; Chen, H.; Zhu, J. Heterostructured Bi_2Se_3 Nanowires with Periodic Phase Boundaries. *J. Am. Chem. Soc.* **2004**, *126* (50), 16276-16277.

(39) Köhler, H. Conduction Band Parameters of Bi_2Se_3 from Shubnikov-de Haas Investigations. *Phys. Status Solidi* **1973**, *58* (1), 91–100.

(40) Analytis, J. G.; Chu, J. H.; Chen, Y.; Corredor, F.; McDonald, R. D.; Shen, Z. X.; Fisher, I. R. Bulk Fermi Surface Coexistence with Dirac Surface State in Bi_2Se_3: A Comparison of Photoemission and Shubnikov-de Haas Measurements. *Phys. Rev. B - Condens. Matter Mater. Phys.* **2010**, *81* (20), 205407.

(41) Lang, M.; He, L.; Xiu, F.; Yu, X.; Tang, J.; Wang, Y.; Kou, X.; Jiang, W.; Fedorov, A. V.; Wang, K. L. Revelation of Topological Surface States in Bi_2Se_3 Thin Films by in Situ Al Passivation. *ACS Nano* **2012**, *6* (1), 295–302.

(42) Hikami, S.; Larkin, A. I.; Nagaoka, Y. Spin-Orbit Interaction and Magnetoresistance in the Two Dimensional Random System. *Prog. Theor. Phys.* **2005**, *63* (2), 707–710.

(43) Chen, J.; Qin, H. J.; Yang, F.; Liu, J.; Guan, T.; Qu, F. M.; Zhang, G. H.; Shi, J. R.; Xie, X. C.; Yang, C. L.; Wu, K. H.; Li, Y. Q.; Lu, L. Gate-Voltage Control of Chemical Potential and Weak Antilocalization in Bi_2Se_3. *Phys. Rev. Lett.* **2010**, 105 (17), 176602.

(44) Matsuo, S.; Koyama, T.; Shimamura, K.; Arakawa, T.; Nishihara, Y.; Chiba, D.; Kobayashi, K.; Ono, T.; Chang, C. Z.; He, K.; Ma, X. C.; Xue, Q. K. Weak Antilocalization and Conductance Fluctuation in a Submicrometer-Sized Wire of Epitaxial Bi_2Se_3. *Phys. Rev. B - Condens. Matter Mater. Phys.* **2012**, 85 (7), 075440.

(45) Liu, M.; Chang, C. Z.; Zhang, Z.; Zhang, Y.; Ruan, W.; He, K.; Wang, L. L.; Chen, X.; Jia, J. F.; Zhang, S. C.;Xue, Q. K.; Ma, X. C.; Wang, Y. Electron Interaction-Driven Insulating Ground State in Bi_2Se_3 Topological Insulators in the Two-Dimensional Limit. *Phys. Rev. B - Condens. Matter Mater. Phys.* **2011**, 83 (16), 165440.

(46) Tian, J.; Chang, C.; Cao, H.; He, K.; Ma, X.; Xue, Q.; Chen, Y. P. Quantum and Classical Magnetoresistance in Ambipolar Topological Insulator Transistors with Gate-Tunable Bulk and Surface Conduction. *Sci. Rep.* **2014**, 4, 4859.

(47) Cha, J. J.; Kong, D.; Hong, S. S.; Analytis, J. G.; Lai, K.; Cui, Y. Weak Antilocalization in $Bi_2(Se_xTe_{1-x})_3$ Nanoribbons and Nanoplates. Nano Lett. **2012**, 12 (2), 1107–1111.

(48) Steinberg, H.; Laloë, J. B.; Fatemi, V.; Moodera, J. S.; Jarillo-Herrero, P. Electrically Tunable Surface-to-Bulk Coherent Coupling in Topological Insulator Thin Films. *Phys. Rev. B - Condens. Matter Mater. Phys*. **2011**, 84 (23), 233101.

(49) Wang, Z.; Yang, L.; Zhao, X.; Zhang, Z.; Gao, X. P. A. Linear Magnetoresistance versus Weak Antilocalization Effects in Bi_2Te_3. *Nano Res.* **2015**, 8 (9), 2963–2969.

(50) Chen, J.; He, X. Y.; Wu, K. H.; Ji, Z. Q.; Lu, L.; Shi, J. R.; Smet, J. H.; Li, Y. Q. Tunable Surface Conductivity in Bi_2Se_3 Revealed in Diffusive Electron Transport. *Phys. Rev. B - Condens. Matter Mater. Phys.* **2011**, 83 (24), 241304.

(51) Zhang, H.; Zhang, X.; Liu, C.; Lee, S. T.; Jie, J. High-Responsivity, High-Detectivity, Ultrafast Topological Insulator Bi_2Se_3/Silicon Heterostructure Broadband Photodetectors. *ACS Nano* **2016**, *10* (5), 5113–5122.

Appendix

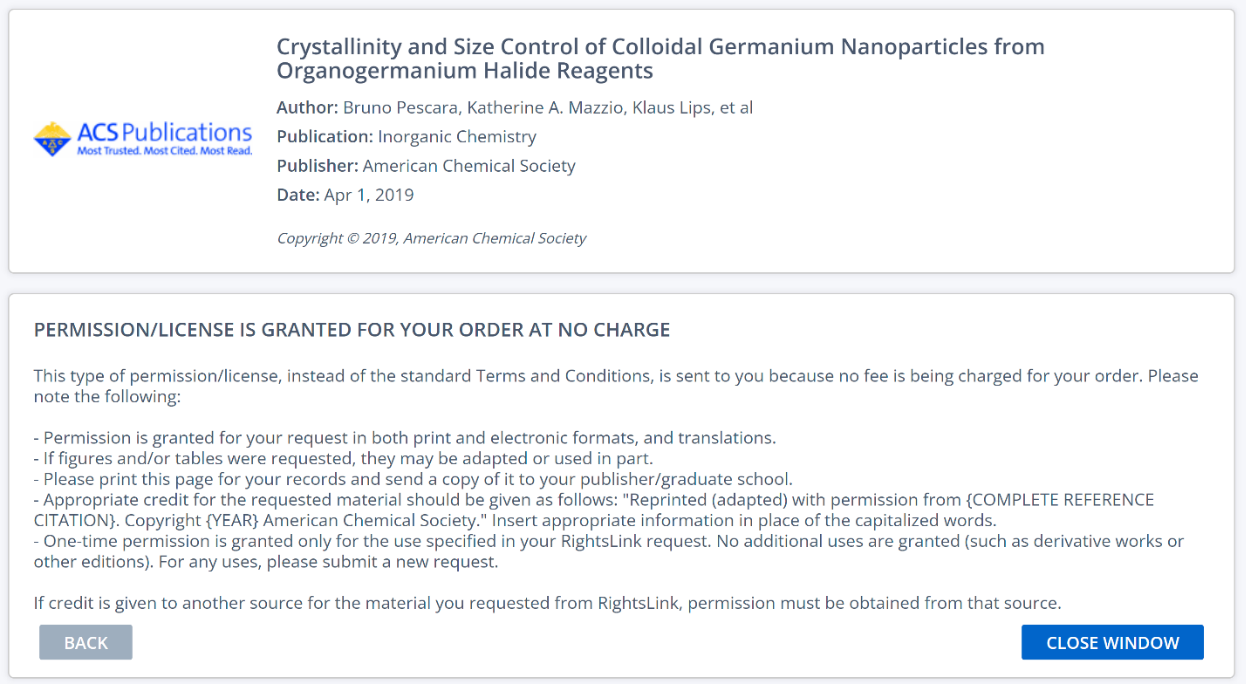

Crystallinity and Size Control of Colloidal Germanium Nanoparticles from Organogermanium Halide Reagents

Author: Bruno Pescara, Katherine A. Mazzio, Klaus Lips, et al

Publication: Inorganic Chemistry

Publisher: American Chemical Society

Date: Apr 1, 2019

Copyright © 2019, American Chemical Society

PERMISSION/LICENSE IS GRANTED FOR YOUR ORDER AT NO CHARGE

This type of permission/license, instead of the standard Terms and Conditions, is sent to you because no fee is being charged for your order. Please note the following:

- Permission is granted for your request in both print and electronic formats, and translations.
- If figures and/or tables were requested, they may be adapted or used in part.
- Please print this page for your records and send a copy of it to your publisher/graduate school.
- Appropriate credit for the requested material should be given as follows: "Reprinted (adapted) with permission from {COMPLETE REFERENCE CITATION}. Copyright {YEAR} American Chemical Society." Insert appropriate information in place of the capitalized words.
- One-time permission is granted only for the use specified in your RightsLink request. No additional uses are granted (such as derivative works or other editions). For any uses, please submit a new request.

If credit is given to another source for the material you requested from RightsLink, permission must be obtained from that source.

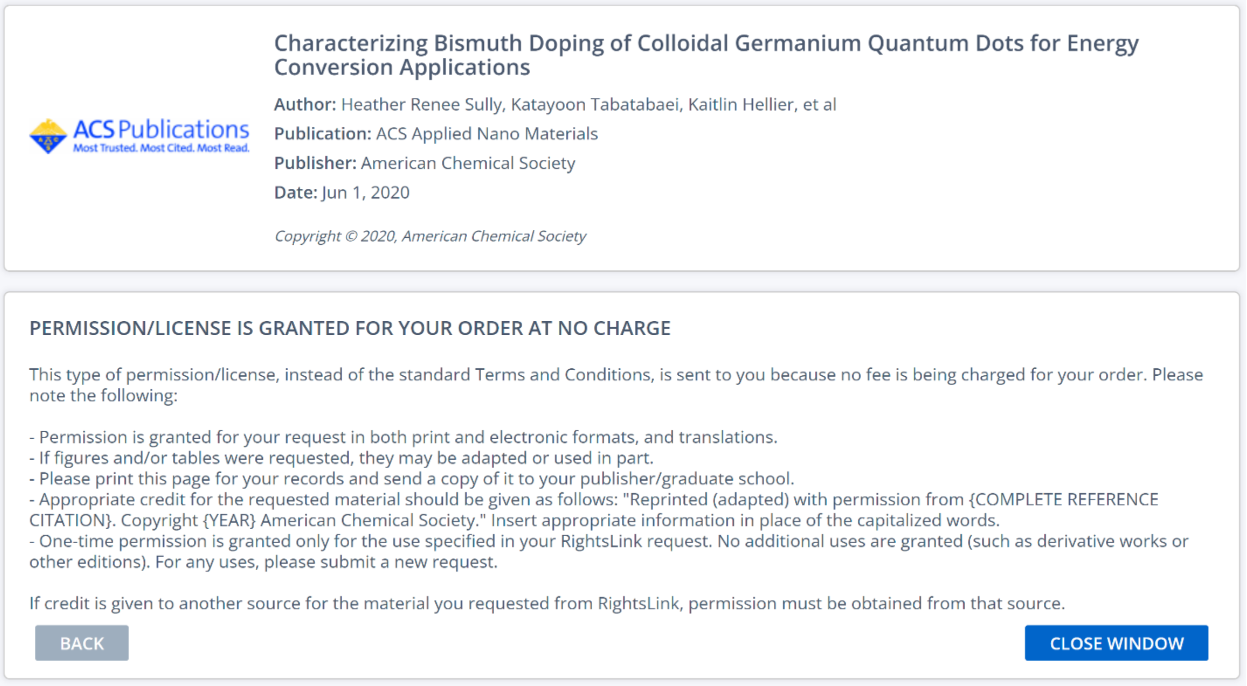

Characterizing Bismuth Doping of Colloidal Germanium Quantum Dots for Energy Conversion Applications

Author: Heather Renee Sully, Katayoon Tabatabaei, Kaitlin Hellier, et al

Publication: ACS Applied Nano Materials

Publisher: American Chemical Society

Date: Jun 1, 2020

Copyright © 2020, American Chemical Society

PERMISSION/LICENSE IS GRANTED FOR YOUR ORDER AT NO CHARGE

This type of permission/license, instead of the standard Terms and Conditions, is sent to you because no fee is being charged for your order. Please note the following:

- Permission is granted for your request in both print and electronic formats, and translations.
- If figures and/or tables were requested, they may be adapted or used in part.
- Please print this page for your records and send a copy of it to your publisher/graduate school.
- Appropriate credit for the requested material should be given as follows: "Reprinted (adapted) with permission from {COMPLETE REFERENCE CITATION}. Copyright {YEAR} American Chemical Society." Insert appropriate information in place of the capitalized words.
- One-time permission is granted only for the use specified in your RightsLink request. No additional uses are granted (such as derivative works or other editions). For any uses, please submit a new request.

If credit is given to another source for the material you requested from RightsLink, permission must be obtained from that source.

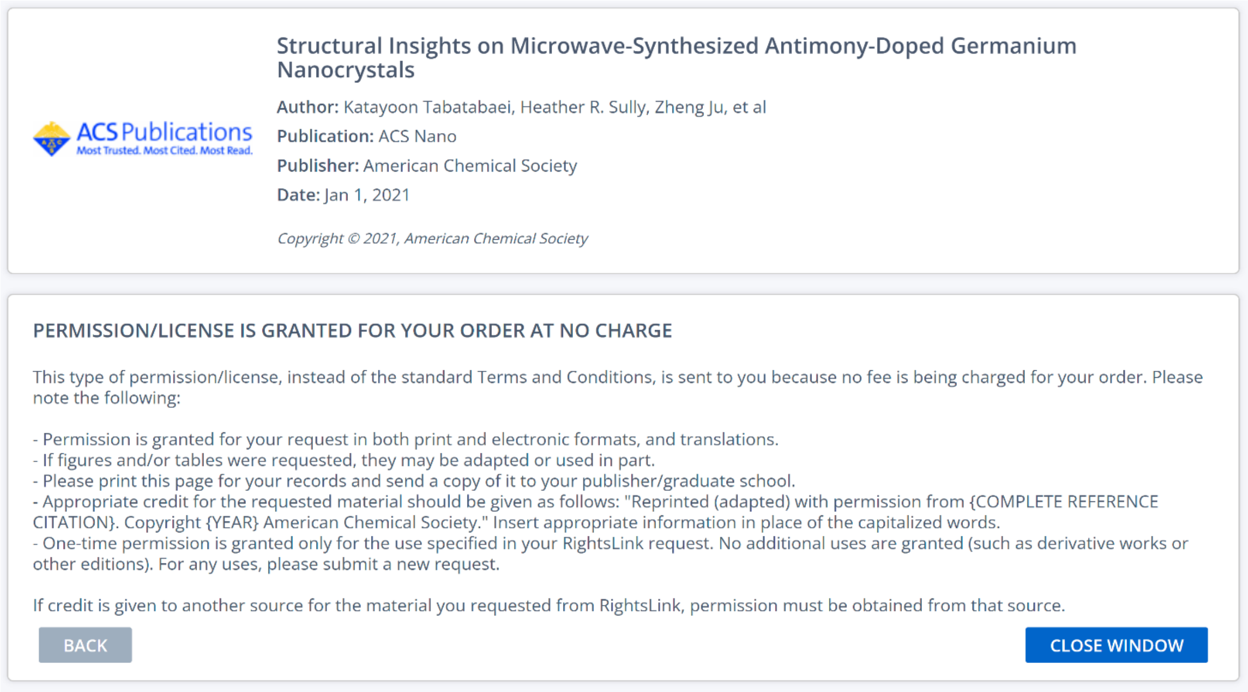

Structural Insights on Microwave-Synthesized Antimony-Doped Germanium Nanocrystals

Author: Katayoon Tabatabaei, Heather R. Sully, Zheng Ju, et al
Publication: ACS Nano
Publisher: American Chemical Society
Date: Jan 1, 2021

Copyright © 2021, American Chemical Society

PERMISSION/LICENSE IS GRANTED FOR YOUR ORDER AT NO CHARGE

This type of permission/license, instead of the standard Terms and Conditions, is sent to you because no fee is being charged for your order. Please note the following:

- Permission is granted for your request in both print and electronic formats, and translations.
- If figures and/or tables were requested, they may be adapted or used in part.
- Please print this page for your records and send a copy of it to your publisher/graduate school.
- Appropriate credit for the requested material should be given as follows: "Reprinted (adapted) with permission from {COMPLETE REFERENCE CITATION}. Copyright {YEAR} American Chemical Society." Insert appropriate information in place of the capitalized words.
- One-time permission is granted only for the use specified in your RightsLink request. No additional uses are granted (such as derivative works or other editions). For any uses, please submit a new request.

If credit is given to another source for the material you requested from RightsLink, permission must be obtained from that source.

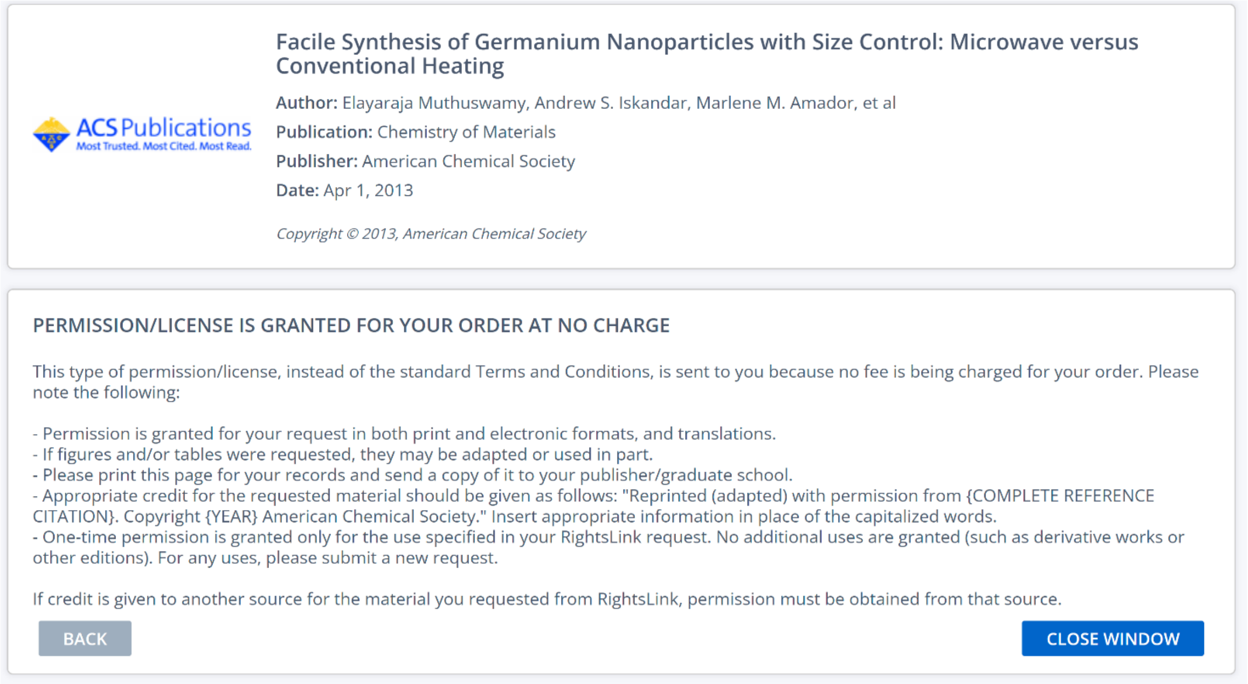

Facile Synthesis of Germanium Nanoparticles with Size Control: Microwave versus Conventional Heating

Author: Elayaraja Muthuswamy, Andrew S. Iskandar, Marlene M. Amador, et al
Publication: Chemistry of Materials
Publisher: American Chemical Society
Date: Apr 1, 2013

Copyright © 2013, American Chemical Society

PERMISSION/LICENSE IS GRANTED FOR YOUR ORDER AT NO CHARGE

This type of permission/license, instead of the standard Terms and Conditions, is sent to you because no fee is being charged for your order. Please note the following:

- Permission is granted for your request in both print and electronic formats, and translations.
- If figures and/or tables were requested, they may be adapted or used in part.
- Please print this page for your records and send a copy of it to your publisher/graduate school.
- Appropriate credit for the requested material should be given as follows: "Reprinted (adapted) with permission from {COMPLETE REFERENCE CITATION}. Copyright {YEAR} American Chemical Society." Insert appropriate information in place of the capitalized words.
- One-time permission is granted only for the use specified in your RightsLink request. No additional uses are granted (such as derivative works or other editions). For any uses, please submit a new request.

If credit is given to another source for the material you requested from RightsLink, permission must be obtained from that source.

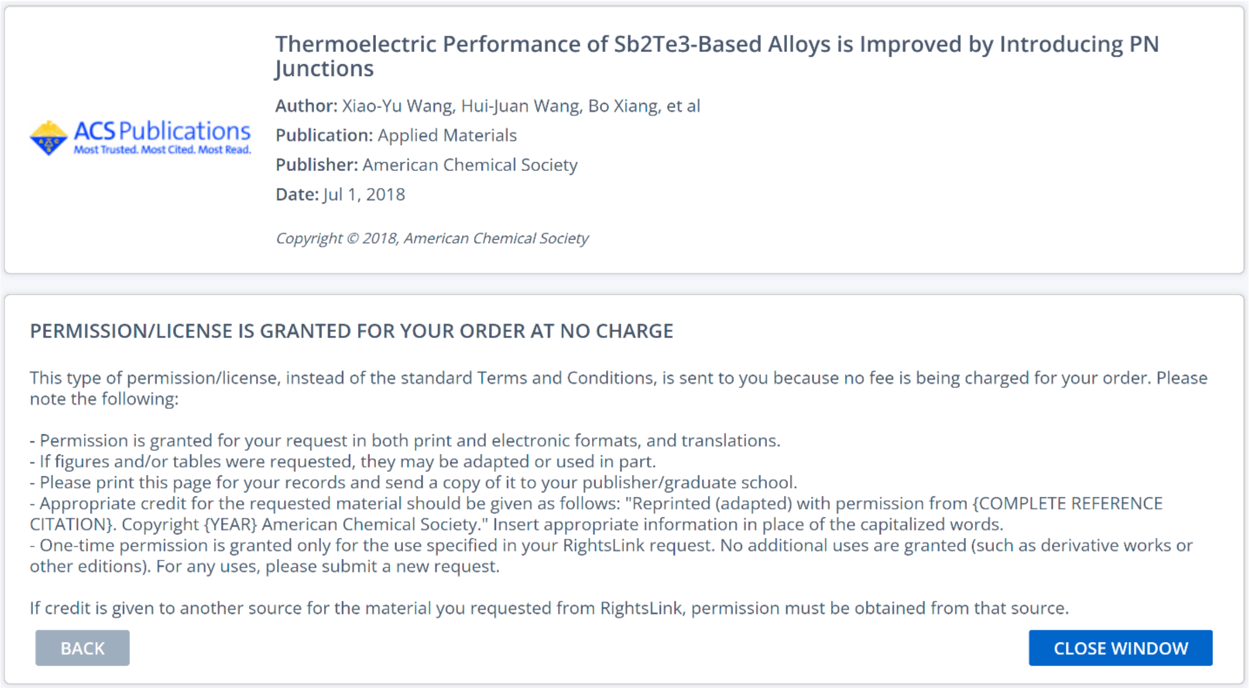

Thermoelectric Performance of Sb2Te3-Based Alloys is Improved by Introducing PN Junctions

Author: Xiao-Yu Wang, Hui-Juan Wang, Bo Xiang, et al

Publication: Applied Materials

Publisher: American Chemical Society

Date: Jul 1, 2018

Copyright © 2018, American Chemical Society

PERMISSION/LICENSE IS GRANTED FOR YOUR ORDER AT NO CHARGE

This type of permission/license, instead of the standard Terms and Conditions, is sent to you because no fee is being charged for your order. Please note the following:

- Permission is granted for your request in both print and electronic formats, and translations.
- If figures and/or tables were requested, they may be adapted or used in part.
- Please print this page for your records and send a copy of it to your publisher/graduate school.
- Appropriate credit for the requested material should be given as follows: "Reprinted (adapted) with permission from {COMPLETE REFERENCE CITATION}. Copyright {YEAR} American Chemical Society." Insert appropriate information in place of the capitalized words.
- One-time permission is granted only for the use specified in your RightsLink request. No additional uses are granted (such as derivative works or other editions). For any uses, please submit a new request.

If credit is given to another source for the material you requested from RightsLink, permission must be obtained from that source.

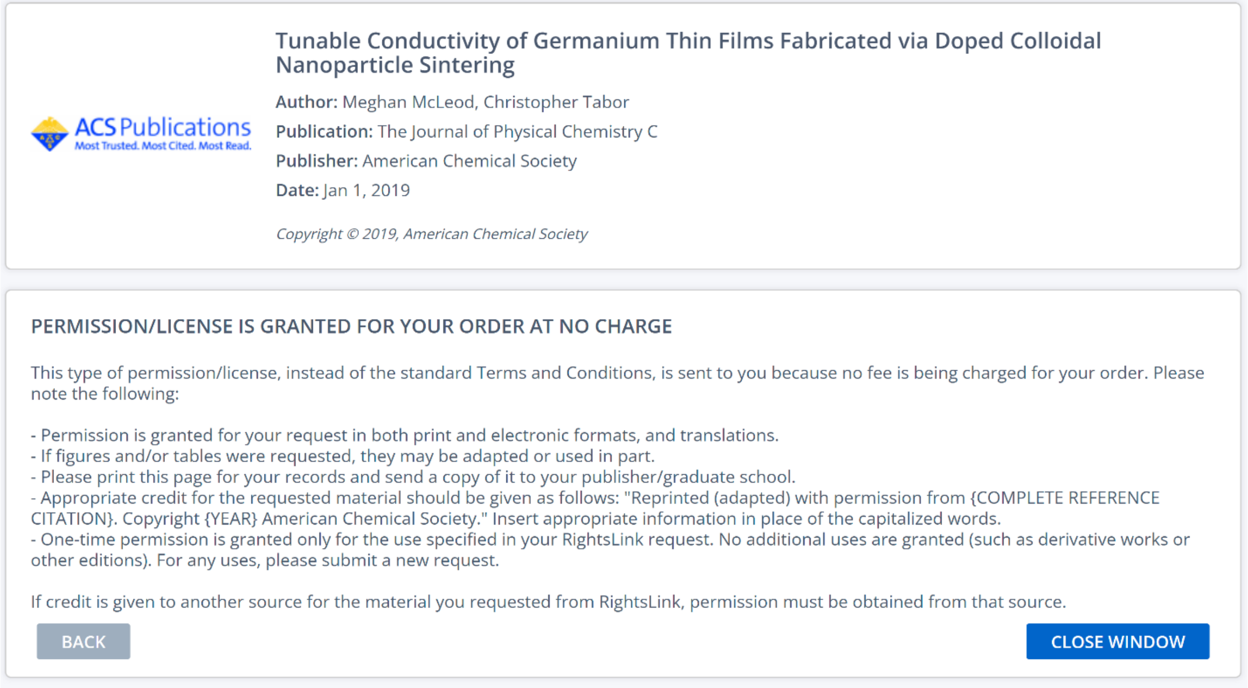

Tunable Conductivity of Germanium Thin Films Fabricated via Doped Colloidal Nanoparticle Sintering

Author: Meghan McLeod, Christopher Tabor

Publication: The Journal of Physical Chemistry C

Publisher: American Chemical Society

Date: Jan 1, 2019

Copyright © 2019, American Chemical Society

PERMISSION/LICENSE IS GRANTED FOR YOUR ORDER AT NO CHARGE

This type of permission/license, instead of the standard Terms and Conditions, is sent to you because no fee is being charged for your order. Please note the following:

- Permission is granted for your request in both print and electronic formats, and translations.
- If figures and/or tables were requested, they may be adapted or used in part.
- Please print this page for your records and send a copy of it to your publisher/graduate school.
- Appropriate credit for the requested material should be given as follows: "Reprinted (adapted) with permission from {COMPLETE REFERENCE CITATION}. Copyright {YEAR} American Chemical Society." Insert appropriate information in place of the capitalized words.
- One-time permission is granted only for the use specified in your RightsLink request. No additional uses are granted (such as derivative works or other editions). For any uses, please submit a new request.

If credit is given to another source for the material you requested from RightsLink, permission must be obtained from that source.

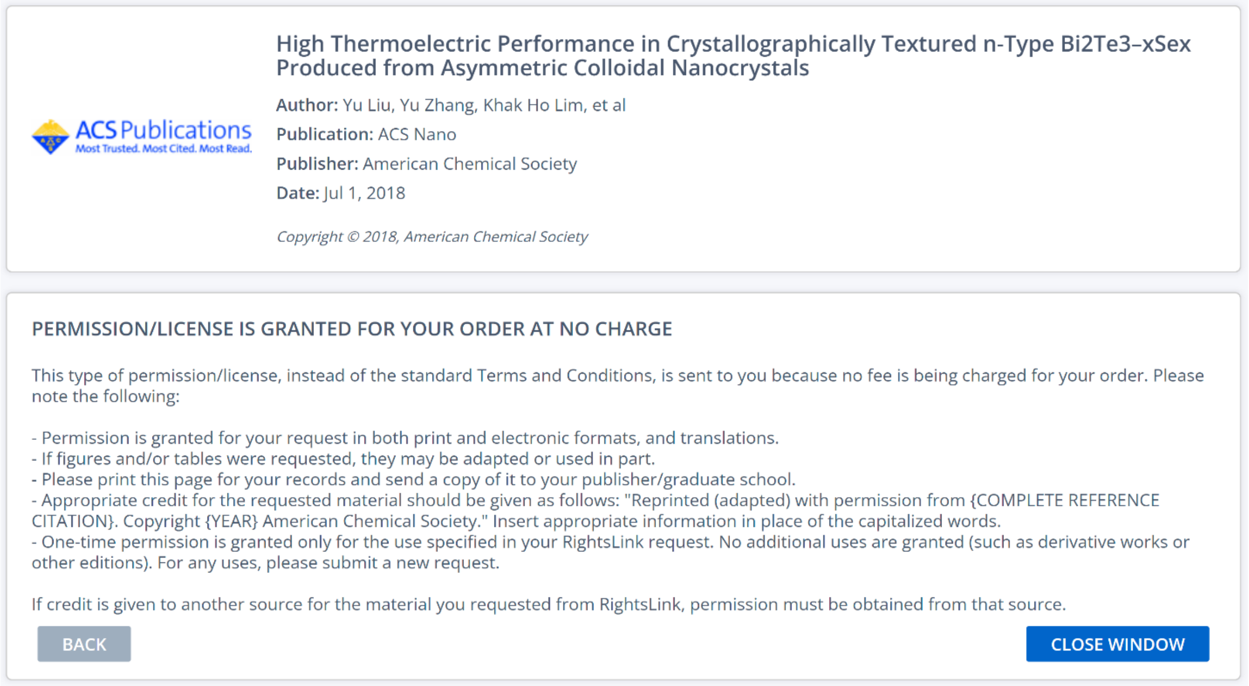

High Thermoelectric Performance in Crystallographically Textured n-Type Bi2Te3–xSex Produced from Asymmetric Colloidal Nanocrystals

Author: Yu Liu, Yu Zhang, Khak Ho Lim, et al
Publication: ACS Nano
Publisher: American Chemical Society
Date: Jul 1, 2018

Copyright © 2018, American Chemical Society

PERMISSION/LICENSE IS GRANTED FOR YOUR ORDER AT NO CHARGE

This type of permission/license, instead of the standard Terms and Conditions, is sent to you because no fee is being charged for your order. Please note the following:

- Permission is granted for your request in both print and electronic formats, and translations.
- If figures and/or tables were requested, they may be adapted or used in part.
- Please print this page for your records and send a copy of it to your publisher/graduate school.
- Appropriate credit for the requested material should be given as follows: "Reprinted (adapted) with permission from {COMPLETE REFERENCE CITATION}. Copyright {YEAR} American Chemical Society." Insert appropriate information in place of the capitalized words.
- One-time permission is granted only for the use specified in your RightsLink request. No additional uses are granted (such as derivative works or other editions). For any uses, please submit a new request.

If credit is given to another source for the material you requested from RightsLink, permission must be obtained from that source.

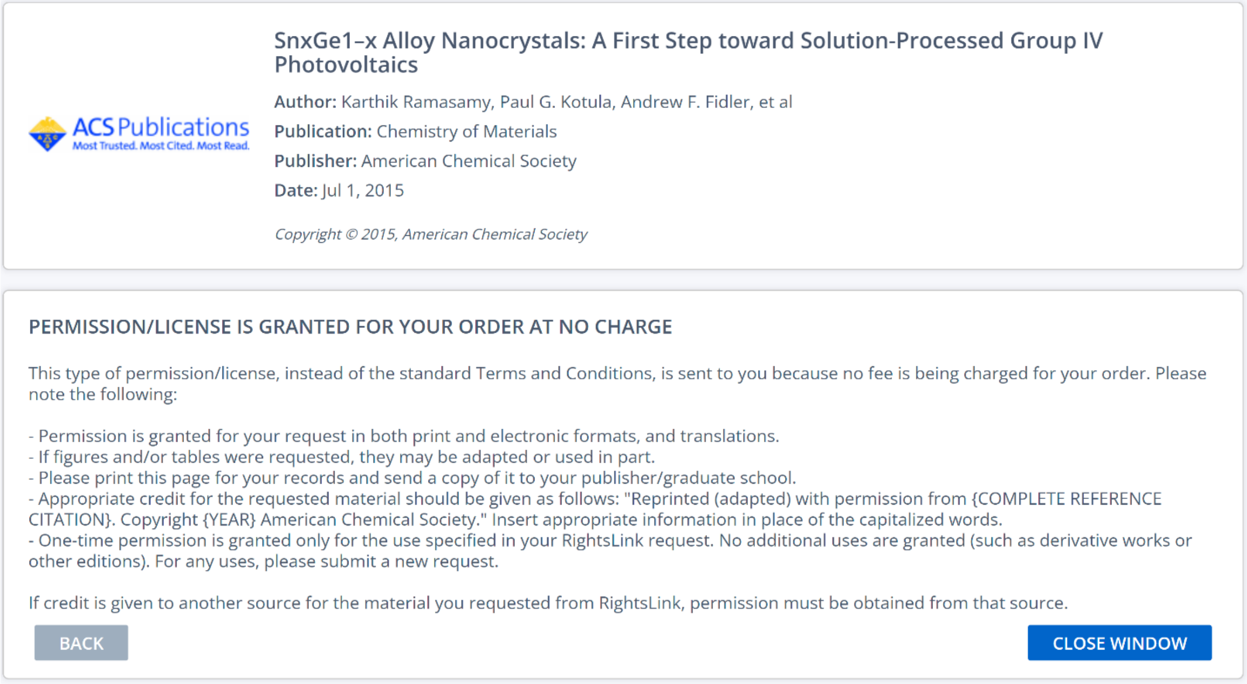

SnxGe1–x Alloy Nanocrystals: A First Step toward Solution-Processed Group IV Photovoltaics

Author: Karthik Ramasamy, Paul G. Kotula, Andrew F. Fidler, et al
Publication: Chemistry of Materials
Publisher: American Chemical Society
Date: Jul 1, 2015

Copyright © 2015, American Chemical Society

PERMISSION/LICENSE IS GRANTED FOR YOUR ORDER AT NO CHARGE

This type of permission/license, instead of the standard Terms and Conditions, is sent to you because no fee is being charged for your order. Please note the following:

- Permission is granted for your request in both print and electronic formats, and translations.
- If figures and/or tables were requested, they may be adapted or used in part.
- Please print this page for your records and send a copy of it to your publisher/graduate school.
- Appropriate credit for the requested material should be given as follows: "Reprinted (adapted) with permission from {COMPLETE REFERENCE CITATION}. Copyright {YEAR} American Chemical Society." Insert appropriate information in place of the capitalized words.
- One-time permission is granted only for the use specified in your RightsLink request. No additional uses are granted (such as derivative works or other editions). For any uses, please submit a new request.

If credit is given to another source for the material you requested from RightsLink, permission must be obtained from that source.

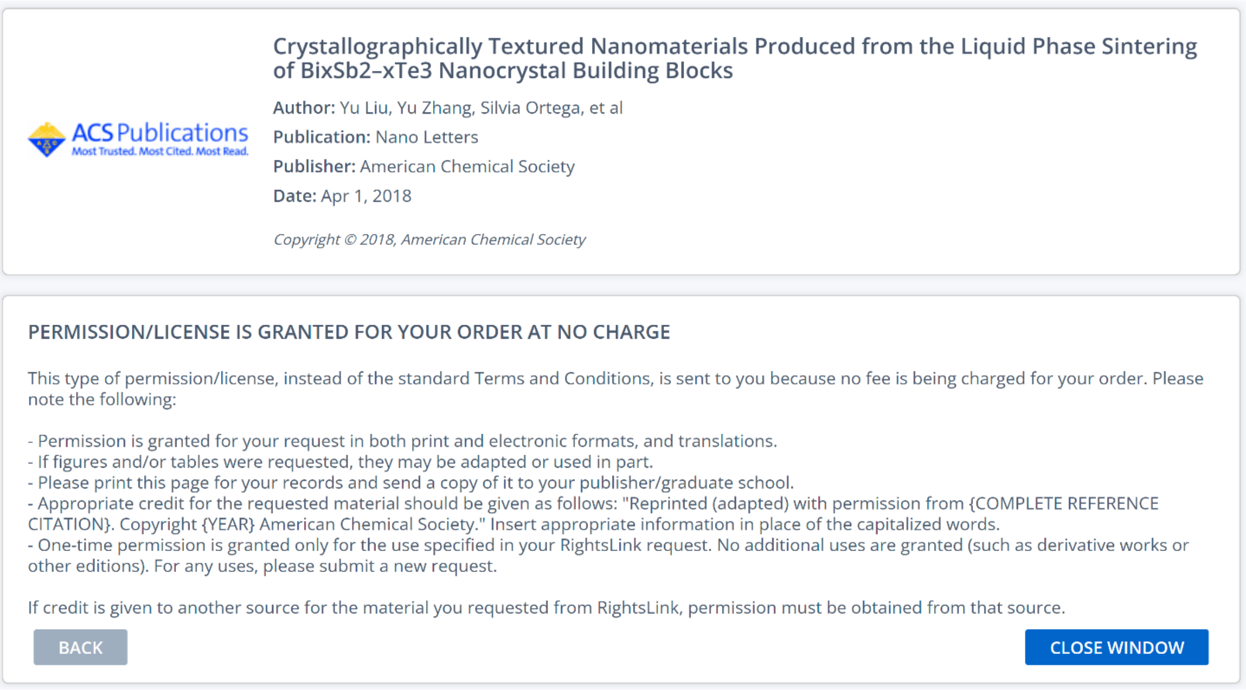

Crystallographically Textured Nanomaterials Produced from the Liquid Phase Sintering of BixSb2−xTe3 Nanocrystal Building Blocks

Author: Yu Liu, Yu Zhang, Silvia Ortega, et al

Publication: Nano Letters

Publisher: American Chemical Society

Date: Apr 1, 2018

Copyright © 2018, American Chemical Society

PERMISSION/LICENSE IS GRANTED FOR YOUR ORDER AT NO CHARGE

This type of permission/license, instead of the standard Terms and Conditions, is sent to you because no fee is being charged for your order. Please note the following:

- Permission is granted for your request in both print and electronic formats, and translations.
- If figures and/or tables were requested, they may be adapted or used in part.
- Please print this page for your records and send a copy of it to your publisher/graduate school.
- Appropriate credit for the requested material should be given as follows: "Reprinted (adapted) with permission from {COMPLETE REFERENCE CITATION}. Copyright {YEAR} American Chemical Society." Insert appropriate information in place of the capitalized words.
- One-time permission is granted only for the use specified in your RightsLink request. No additional uses are granted (such as derivative works or other editions). For any uses, please submit a new request.

If credit is given to another source for the material you requested from RightsLink, permission must be obtained from that source.

Dear Dr. Ju,

Thank you for contacting ACS Publications Support.

Your permission requested is granted and there is no fee for this reuse. In your planned reuse, you must cite the ACS article as the source, add this direct link https://pubs.acs.org/doi/abs/10.1021/acs.chemmater.7b02241, and include a notice to readers that further permissions related to the material excerpted should be directed to the ACS.

If you need further assistance, please let me know.

Best regards,
Ranjith Alexander
~~~~~~
Ranjith Alexander
ACS Publications Support
Customer Services & Information
~~~~~~

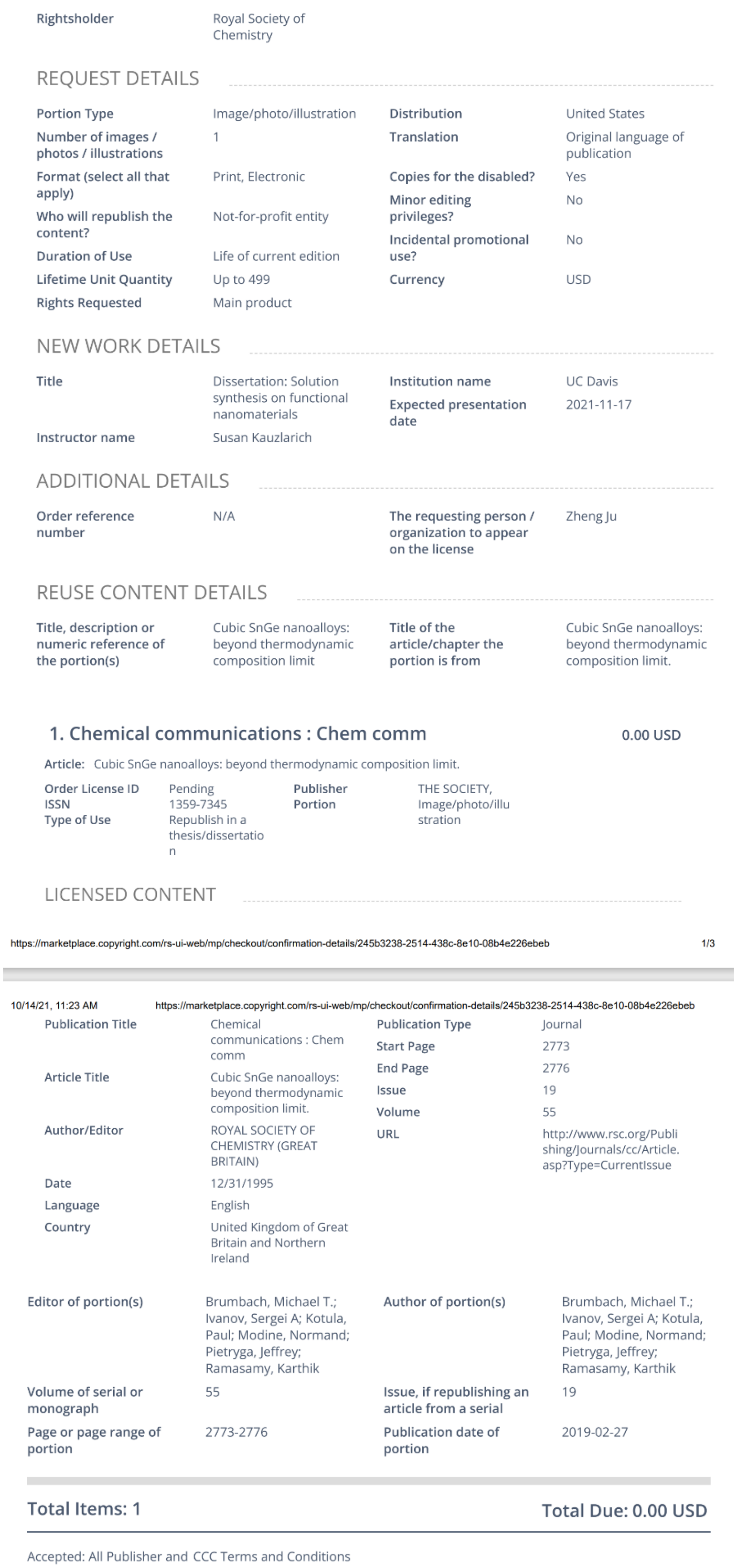

Rightsholder	Royal Society of Chemistry		

REQUEST DETAILS

Portion Type	Image/photo/illustration	**Distribution**	United States
Number of images / photos / illustrations	1	**Translation**	Original language of publication
Format (select all that apply)	Print, Electronic	**Copies for the disabled?**	Yes
Who will republish the content?	Not-for-profit entity	**Minor editing privileges?**	No
Duration of Use	Life of current edition	**Incidental promotional use?**	No
Lifetime Unit Quantity	Up to 499	**Currency**	USD
Rights Requested	Main product		

NEW WORK DETAILS

Title	Dissertation: Solution synthesis on functional nanomaterials	**Institution name**	UC Davis
		Expected presentation date	2021-11-17
Instructor name	Susan Kauzlarich		

ADDITIONAL DETAILS

Order reference number	N/A	**The requesting person / organization to appear on the license**	Zheng Ju

REUSE CONTENT DETAILS

Title, description or numeric reference of the portion(s)	Cubic SnGe nanoalloys: beyond thermodynamic composition limit	**Title of the article/chapter the portion is from**	Cubic SnGe nanoalloys: beyond thermodynamic composition limit.

1. Chemical communications : Chem comm

0.00 USD

Article: Cubic SnGe nanoalloys: beyond thermodynamic composition limit.

Order License ID	Pending	**Publisher**	THE SOCIETY,
ISSN	1359-7345	**Portion**	Image/photo/illustration
Type of Use	Republish in a thesis/dissertation		

LICENSED CONTENT

Publication Title	Chemical communications : Chem comm	**Publication Type**	Journal
		Start Page	2773
		End Page	2776
Article Title	Cubic SnGe nanoalloys: beyond thermodynamic composition limit.	**Issue**	19
		Volume	55
Author/Editor	ROYAL SOCIETY OF CHEMISTRY (GREAT BRITAIN)	**URL**	http://www.rsc.org/Publishing/Journals/cc/Article.asp?Type=CurrentIssue
Date	12/31/1995		
Language	English		
Country	United Kingdom of Great Britain and Northern Ireland		

Editor of portion(s)	Brumbach, Michael T.; Ivanov, Sergei A; Kotula, Paul; Modine, Normand; Pietryga, Jeffrey; Ramasamy, Karthik	**Author of portion(s)**	Brumbach, Michael T.; Ivanov, Sergei A; Kotula, Paul; Modine, Normand; Pietryga, Jeffrey; Ramasamy, Karthik
Volume of serial or monograph	55	**Issue, if republishing an article from a serial**	19
Page or page range of portion	2773-2776	**Publication date of portion**	2019-02-27

Total Items: 1 **Total Due: 0.00 USD**

Accepted: All Publisher and CCC Terms and Conditions